Photo-Activatable Organic and Organometallic Compounds for Enzyme Inhibition and Targeted Drug Delivery

Dissertation

zur

Erlangung der naturwissenschaftlichen Doktorwürde

(Dr. sc. nat.)

vorgelegt der

Mathematisch-naturwissenschaftlichen Fakultät

der

Universität Zürich

von

Philipp Anstätt

aus

Deutschland

Promotionskomitee

Prof. Dr. Gilles Gasser (Vorsitz, Leitung der Dissertation)

Prof. Dr. Roland K. O. Sigel

PD Dr. Bernhard Spingler

Zürich, 2014

Table of Contents

Part I – Photo-Activatable Organic and Organometallic Compounds for Enzyme Inhibition and Targeted Drug Delivery

Part II – Peptide Nucleic Acid for Nanotechnology

Acknowledgments

Help and support from many people went into this thesis. I am indebted and would like to thank:

Prof. Dr. Gilles Gasser for supervising the thesis by providing feedback, leaving enough freedom to test my hypotheses but still making sure things stay on track, and supporting me and my work throughout the whole time. His level of dedication was truly extraordinary.

The members of my PhD committee, Prof. Dr. Roland Sigel and PD Dr. Bernhard Spingler, as well as the reviewer of this thesis, Dr. Sylvestre Bonnet, for their precious time.

All the coworkers in the Gasser group: My fellow PhD students Anna Leonidova, who most directly shared the joys and pains of working with photo-caged compounds, Cristina Mari, who was a great lab mate in our first year in Zurich and organized so many memorable barbecues, Jeannine Hess, who every day positively contributed to the working atmosphere with her unmatched enthusiasm, and Vanessa Pierroz, who had to stem the greatest part of the biological experiments carried out in the group; the Master students, most importantly “my” Master student Angelo Frei, with whom I really enjoyed working, but also all the others, including Assia Nouar, Sandro Konatschnik, Lea Gemperle, Sandra Morard, Seraina Hügli; and of course also the post-docs, Dr. Riccardo Rubbiani (even though he strongly opposed that I finish my thesis), Dr. Tanmaya Joshi, Dr. Malay Patra, and Dr. Giuseppe Martano.

Klemens Koziol, Julien Rehault, and Philip Johnson from the Hamm-group for their support with the fs-laser; especially Klemens made many times adjustments in the laser setup for me… and, not less important, very good margaritas, making the 2014 world cup even more memorable.

The co-authors who have directly contributed to the PNA/nanoparticle research project: Dr. Thibaut Thai and especially Dr. Yuanhui Zheng, who managed to show me all I needed to know about the handling of nanoparticles in a very short time frame, Dr. Alison Funston for guidance and support, and Prof. Dr. Udo Bach for hosting me in his labs and guiding the project.

The co-authors associated with projects in the photo-activation projects: Anna Leonidova, who worked with me on the chemical part, and Vanessa Pierroz for evaluating the cytotoxicity, Bernhard Spingler for solving a crystal structure for Anna, and Dr. Stefano Ferrari for guidance on the cytotoxicity part.

The SF-labs, which became something like my second group over the years.

The mass spectrometry teams in the former institutes of organic and inorganic chemistry.

The people involved in keeping the Graduate School of Chemical and Molecular Science up and running, namely Dr. Sabine Stockhause, Beatrice Spichtig, Dr. Ferdinand Wild (also for the various other tasks he fulfilled), and Roland Sigel. The “aperos” were a great chance to talk to other PhD students, and the financial support to go to conferences were a fantastic opportunity to talk to scientist from other corners of the world (and to travel). Of course also a big thanks to the organizing teams of the graduate school retreats!

The permanent staff of UZH, most notable Hanspeter Stalder and the workshop crew, Manfred Jöhri for IT support, Ramona Erni and Nathalie Melunsky-Fichter for administrative tasks.

Generally, the former Institute of Inorganic Chemistry with its famous “ACI Seminars”, and the newly formed Department of Chemistry. The open mindset and helpfulness of everybody around here make this the by far best department I have worked in.

All the friends which I met at or through University, which helped to balance research and “normal life”. I’m sorry I keep this important point so general and do to not put names here, but I’m too afraid to forget somebody.

My family for their continuous support, which enabled me to gather the education, experience and skills required for this dissertation.

Last and most importantly I’d like to thank my love Anita Schmitz for her scientific and moral support, which went further than it can be described in words.

Summary

In the first part of this PhD thesis entitled *Photo-Activatable Organic and Organometallic Compounds for Enzyme Inhibition and Targeted Drug Delivery*, the main research topic of the dissertation is discussed. As an introduction, a review on organometallic enzyme inhibitors highlights the opportunities that the use of organometallic compounds gives in medicinal chemistry (chapter 1). Several concepts are discussed and explained on basis of literature examples. The topics include: 1) Organometallic compounds as inert scaffolds; 2) Organometallic compounds targeting specific protein residues; 3) Bioisosteric substitution; 4) Novel mechanisms of enzyme inhibition with organometallic compounds; 5) Organometallic compounds as cargo delivers of enzyme inhibitors; 6) Organometallic enzyme inhibitors for theranostic purposes. The following chapters 2 and 3 shift the focus towards light-activatable bioactive compounds. In chapter 2, the acquisition of uncaging quantum yields in the UV-A range is discussed. Surprisingly, the frequently used reference molecule 1-(2-nitrophenyl)ethyl-phosphate ("caged phosphate") leads to vastly wrong uncaging quantum yields (up to an order of magnitude). The correct values could be determined using measurements with classical actinometers based on photo-induced ferrioxalate decomposition and azobenzene photo-isomerization. To elucidate the reason for this inaccuracy, further measurements with 1-(2-nitrophenyl)ethyl-ATP ("caged ATP"), the second important reference molecule for uncaging quantum yields, which is based on the same photo-cage, were undertaken. The data suggest that the broad-band light source originally used to acquire the uncaging quantum yield of caged phosphate is the most likely cause. Thus, a new, convenient, and precise alternative protocol for the determination of uncaging quantum yields at wavelengths around 350 nm was designed based on inexpensive azobenzene. In chapter 3, a more recent variant of light-controlled activation, two-photon uncaging, is applied to spatially and temporally control the activity of an enzyme, namely Cyclooxygenase-2 (COX-2). The advantage of the two-photon mechanism lies in the light that is needed to initiate the uncaging process. Traditional photo-cages rely on activation by UV-light, which can be harmful for biological structures. Two-photon processes on the other hand are initiated by the simultaneous absorption of two photon, each contributing half of the energy. Therefore, firstly the required light is in the near-IR range, which is favorable because it is (almost) not absorbed by biomolecules. Secondly, as the excitation probability depends on the square of the light intensity, three-dimensional selectivity can be accomplished with focused laser beams. Enzyme inhibitors have been de-activated by attaching them to two-photon-cages. The cages have been designed to be modifiable with targeting vectors *via* click-chemistry. The attachment of a targeting peptide has been demonstrated. The enzyme inhibitors could be released not only by irradiation with UV-light, but also by two-photon uncaging upon irradiation with pulsed light in the near-IR range. The successful de- and re-activation of an enzyme inhibitor has been confirmed by a fluorescence-based enzyme inhibition assay. The project described in chapter 4 combines the two concepts of photo-uncaging and the special properties of organometallic compounds. The cytotoxic compound aminoferrocene (**Fc-NH$_2$**) has previously been shown to be unstable under physiological conditions, leading to ferrocenium and free iron ions. Both products catalyze the production of reactive oxygen species (ROS) in cells. Cancer cells are especially vulnerable to ROS since they have inherently elevated ground levels. To deliver **Fc-NH$_2$** to target tissues without prior decomposition, it was protected with two different photo-cages. Both cages have been equipped with a targeting peptide, which was supposed to direct the complex to mitochondria, an organelle particularly prone to alternations of the redox potential. The caging of **Fc-NH$_2$** was realized *via* formation of a carbamate bond. The electronic properties of the bond lead to a stabilization of the organometallic moiety. The uncaging of both **Fc-NH$_2$** derivatives led to the formation of free iron ions. However, the effectivity of this process is very differently between the two caged versions. Cytotoxicity tests against healthy and cancer cell lines in the dark and upon UV-irradiation showed a positive selectivity for both factors. The previously observed differences between the cages also manifested in the biological tests. At the end of the first part of the thesis, chapter 5 presents an outlook for possible future research endeavors.

The second part of the thesis focuses on the use of peptide nucleic acid (PNA) in (bio-)nanotechnology. PNAs are artificial analogues of deoxyribonucleic acid (DNA). The backbone of PNA is made up of a peptide (hence the name), while the backbone of DNA consist of ribose and phosphodiesters. Consequently, PNA is not charged and structurally less flexible than DNA. Both factors contribute to the superior binding strength of PNA to DNA, which surpasses the natural duplex formation. In chapter 6, examples from the literature are highlighted which used PNA for bio-nanotechnology. So far, only relatively few reports in this field have been published. Among the nanoscopic materials which have been functionalized with PNA are silicon nanowires, carbon nanotubes, and nano graphene oxide. The described materials and devices demonstrate the possibilities and advantages of PNA, including the aforementioned superior binding affinity, but also going beyond that, for example by exploiting the uncharged nature in electronic devices. Chapter 7 then deals with a case, in which exactly this property of PNA causes problems. DNA-functionalized gold nanoparticles are already being used for many different applications, ranging from gene regulation to nanofabrication. In almost all cases, the properties of PNA would be of interest. However, the direct functionalization of gold nanoparticles with PNA has not been realized. The combination of both led to destabilization and precipitation of the nanoparticles since the needed repulsion, usually realized through charged species on the particle surface, between the particles was abolished by the uncharged PNAs. A novel step-wise approach which first stabilizes the particles electrostatically and sterically before addition of PNA led to stable particles. To this end, also new thiol linkers, which can be easily employed in solid-phase synthesis, have been designed for the attachment of the PNA to the gold surface. The utilizability of the new PNA-functionalized gold nanoparticles has been demonstrated by sequence specific self-assembly onto PNA-functionalized gold surfaces. The assemblies showed greater coverage densities, i.e. more nanoparticles per surface area unit, than corresponding DNA-functionalize gold nanoparticles. The final chapter 8 outlines possibilities for further research in the field of PNA-based nanotechnology.

Zusammenfassung

Im ersten Teil dieser Doktorarbeit mit dem Titel *Photo-Aktivierbare Organische und Organometallische Verbindungen zur Enzyminhibierung und zum Zielgerichteten Wirkstofftransport* wird das Hauptforschungsthema der Dissertation besprochen. Einleitend wird ein Überblick über organometallische Enzyminhibitoren gegeben, welcher die Möglichkeiten, die die Verwendung organometallischer Verbindungen der medizinischen Chemie bietet, aufzeigt (Kapitel 1). Mehrere Konzepte werden erörtert und basierend auf Beispielen aus der Literatur erklärt. Die Themen umfassen: 1) Organometallische Verbindungen als inerte Gerüste; 2) Organometallische Verbindungen die auf bestimmte Proteinseitenketten abzielen; 3) Bioisosterische Substitution; 4) Neue Mechanismen der Enzyminhibition mit organometallischen Verbindungen; 5) Organometallische Verbindungen als Beförderungsmittel für Enzyminhibitoren; 6) Organometallische Enzyminhibitoren für theragnostische Zwecke. In den folgenden Kapiteln 2 und 3 wird der Fokus auf licht-aktivierbare bioaktive Verbindungen gelenkt. In Kapitel 2 wird die Erfassung von Freisetzungsquantenausbeuten im UV-A Bereich diskutiert. Überraschenderweise liefert das häufig verwendete Referenzmolekül 1-(2-Nitrophenyl)ethyl-phosphat („photoaktivierbares Phosphat“, im englischen „*caged phosphate*“) erheblich falsche Freisetzungsquantenausbeuten (bis zu einer Zehnerpotenz). Die richtigen Werte konnten über Messungen mit klassischen Aktinometern basierend auf der photo-induzierten Zersetzung von Tris(oxalato)ferrat(III) und der Photoisomerisierung von Azobenzol erhalten werden. Um dieser Diskrepanz auf den Grund zu gehen wurde weitere Messungen mit 1-2(-Nitrophenyl)ethyl-ATP („photoaktivierbares ATP“), dem zweiten wichtigen Referenzmolekül für uncaging Quantenausbeuten, welches auf der gleichen photolabilen Gruppe basiert, durchgeführt. Das Datenmaterial legt nahe, dass die ursprünglich zur Erlangung der Freisetzungsquantenausbeuten von photoaktivierbarem Phosphat verwendete breitbandige Lichtquelle die wahrscheinlichste Ursache ist. Daher wurde ein neues, komfortables und genaues alternatives Protokoll für die Bestimmung von Freisetzungsquantenausbeuten für Wellenlängen um 350 nm basierend auf dem preiswerten Azobenzol entworfen. In Kapitel 3 wird eine neuere Variante der Licht-kontrollierten Aktivierung, die Zwei-Photonen-Aktivierung, angewendet um die Aktivität eines Enzymes, der Cyclooxygenase-2 (COX-2), zeitlich und räumlich kontrolliert zu aktivieren. Der Vorteil des Zwei-Photonen Mechanismuses ist hierbei das Licht das zur Einleitung des uncaging Prozesses benötigt wird. Übliche photolabile Gruppen sind auf die Aktivierung mit UV-Licht angewiesen, welches schädlich für biologische Strukturen sein kann. Zwei-Photonen-Prozesse dagegen

werden durch die beinahe gleichzeitige Absorption zweier Photonen angeregt, wobei beide die Hälfte der Energie beisteuern. Daher liegt, erstens, das benötigte Licht im nahen IR Bereich, welches von Vorteil ist, da es (fast) nicht von Biomolekülen absorbiert wird. Zweitens, da die Anregungswahrscheinlichkeit vom Quadrat der Lichtintensität abhängt kann mit einem fokussierten Laserstrahl eine dreidimensionale Selektivität erreicht werden. Enzyminhibitoren wurden durch Anbindung an Zwei-Photonen-Schutzgruppen deaktiviert. Die Schutzgruppen wurden so entworfen, dass sie mittels *Click*-Chemie mit Zielvektoren modifiziert werden konnten. Die Anknüpfung eines Zielprotein wurde vorgeführt. Die Enzyminhibitoren konnten nicht nur durch Bestrahlung mit UV-Licht, sondern auch mit gepulstem Licht im nahen IR Bereich freigesetzt werden. Die erfolgreiche In- und Reaktivierung eines Enzyminhibitors wurde durch ein Fluoreszenz-gestütztes Enzyminhibierungs-Assay bestätigt. Das in Kapitel 4 beschriebene Projekt vereint die beiden Konzepte der Photoaktivierung und die besonderen Eigenschafen von organometallischen Verbindungen. Es hat sich gezeigt, dass die zytotoxische Verbindung Aminoferrocen (**$FcNH_2$**) unter physiologischen Bedingungen instabil ist und in Ferrocenium und freie Eisenionen zerfällt. Beide Produkte katalysieren die Produktion reaktiver Sauerstoff Spezies (ROS, vom englischen *reactive oxygen species*) in Zellen. Krebszellen sind besonders anfällig gegenüber ROS da sie ein von Natur aus höheres Grundlevel besitzen. Um **$FcNH_2$** ohne vorherige Zersetzung zum Zielgewebe zu bringen wurde es mit zwei verschiedenen photolabilen Gruppen geschützt. Beide Schutzgruppen wurden mit Zielpeptiden ausgestattet, die den Komplex zu den Mitochondrien führen sollte, einer Organelle die besonders anfällig für Veränderungen des Redoxpotentials ist. Das schützen von **$FcNH_2$** mit den photolabilen Gruppen wird durch die Bildung einer Carbamat-Bindung realisiert. Die elektronischen Eigenschaften der Bindung führen zu einer Stabilisierung des organometallischen Teils. Die lichtinduzierte Zersetzung beider **$FcNH_2$**-Derivate führte zur Bildung freier Eisenionen. Allerdings ist die Effektivität dieses Prozesses für die beiden lichtlabil geschützten Varianten sehr unterschiedlich. Zytotoxizitätstests mit gesunden und Krebszelllinien im Dunkeln und mit UV-Bestrahlung zeigten positive Selektionen hinsichtlich beider Parameter. Die zuvor beobachteten Unterschiede zwischen den beiden Schutzgruppen zeigte sich auch in den biologischen Tests. Am Ende des ersten Teils der Thesis präsentiert Kapitel 5 Perspektiven für mögliche künftige Forschungsbestrebungen.

Der zweite Teil der Doktorarbeit beschäftigt sich mit der Verwendung von Peptid-Nukleinsäure (PNA) in der (Bio-)Nanotechnologie. PNAs sind künstliche Nachbildungen der Desoxyribonukleinsäure (DNA). Das Rückgrat der PNA besteht aus einem Peptide (daher der Name), wohingegen das Rückgrat der DNA aus Ribose und Phosphodiestern besteht.

Folglich ist PNA ungeladen und strukturell weniger flexibel als DNA. Beide Faktoren tragen zur überlegenen Bindungsstärke der PNA zu DNA bei, welche über der natürlichen Duplexbildung liegt. In Kapitel 6 werden Beispiele aus der Literatur hervorgehoben die PNA für Bio-Nanotechnologie verwendeten. Bisher gibt es nur relativ wenige Berichte auf diesem Gebiet. Zu den nanoskopischen Materialen, die mit PNA funktionalisiert wurden, zählen Silikonnanodrähte, Kohlenstoffnanoröhren und Nanographenoxid. Die beschriebenen Materialien und Objekte zeigen die Möglichkeiten und Vorteile von PNA auf, einschließlich der zuvor erwähnten zuvor erwähnten höheren Bindungsaffinität, aber auch darüber hinaus, zum Beispiel durch Nutzung der Ladungsfreiheit in elektronischen Bauteilen. Kapitel 7 behandelt dann einen Fall, in dem genau diese Eigenschaft der PNA Probleme bereitet. DNA-funktionalisierte Goldnanopartikel werden bereits für viele verschiedene Anwendungen, die von Genregulation bis zur Nanofabrikation reichen, verwendet. In beinahe allen Fällen wären die Eigenschaften von PNA reizvoll. Allerdings wurde die direkte Funktionalisierung von Goldnanopartikeln mit PNA noch nicht verwirklicht. Die Vereinigung beider führte zur Destabilisierung und Präzipitation der Nanopartikel, da die benötigte Abstoßung zwischen den Partikeln, üblicherweise aufgrund geladener Spezies auf der Partikeloberfläche, durch die ungeladenen PNAs aufgehoben wurde. Ein neuer schrittweiser Ansatz, der zunächst die Partikel elektrostatisch und sterisch stabilisiert bevor die PNA zugegeben wird, führte stabilen Partikeln. Zu diesen Zweck wurden ferner neue Thiol-Bindeglieder für die Anbindung der PNA an die Goldoberfläche entwickelt, die bequem in der Festphasensynthese eingesetzt werden können. Die Einsatzfähigkeit der neuen PNA-funktionalisierten Goldnanopartikel wurde anhand von sequenzspezifischer Selbstorganisation auf PNA-funktionalisierten Goldoberflächen bewiesen. Diese Anordnungen zeigten größere Bedeckungsdichten, also mehr Nanopartikel pro Oberflächeneinheit, als entsprechende DNA-funktionalisierten Goldnanopartikel. Das Schlusskapitel 8 umreißt Möglichkeiten für weiterführende Forschung auf dem Gebiet der PNA-basierten Nanotechnologie.

Part I

Photo-Activatable Organic and Organometallic Compounds for Enzyme Inhibition and Targeted Drug Delivery

1 Introduction: Organometallic Complexes as Enzyme Inhibitors: A Conceptual Overview

Philipp Anstaett[a] *and Gilles Gasser*[a]*

[a] Department of Chemistry, University of Zurich, Winterthurerstrasse 190, CH-8057 Zurich, Switzerland.

* Corresponding author: e-mail: gilles.gasser@chem.uzh.ch; Fax: +41 44 635 46 03; Tel: +41 44 635 46 30; homepage: http://www.gassergroup.com.

This chapter has been accepted for publication as chapter in the book *Bioorganometallic Chemistry* (Eds.: G. Jaouen, M. Salmain), John Wiley & Sons Ltd. Copyright © Wiley-VCH Verlag GmbH & Co. KGaA. Reproduced with permission.

1.1 Contributions to the publication

P.A: wrote the first drafts of the subchapters on organometallic compounds as inert structural scaffolds, bioisosteric substitution, and novel mechanisms of enzyme inhibition with organometallic compounds. Furthermore, feedback and suggestions to all subchapters were given.

1.2 Abstract

Enzyme inhibitors represent an important class of drugs currently on the market. Organometallic compounds with their unique properties, compared to purely organic compounds, offer great opportunities to the field of enzyme inhibition. Their additional geometries and electrostatic profiles allow the use of otherwise unavailable binding and interaction modes between the inhibitor and the enzyme. Beyond that, the metal ions can be easily tracked and therefore used for theranostic purposes. For these reasons, great advances have been made in the field of organometallic enzyme inhibitors - the activity of these inorganic inhibitors sometimes even surpasses those of their heavily optimized organic counterparts.

In this chapter, we focus on reviewing and explaining the different concepts that have been applied found valuable for the design and mode of activity of organometallic enzyme inhibitors. More specifically, this chapter discusses the following topics:

1) Organometallic compounds as inert structural scaffolds.

2) Organometallic compounds targeting specific protein residues.

3) Bioisosteric substitution.

4) Novel mechanisms of enzyme inhibition with organometallic compounds.

5) Organometallic compounds as cargo delivers of enzyme inhibitors.

6) Organometallic enzyme inhibitors for theranostic purposes.

Keywords: Bioinorganic chemistry • Organometallic chemical biology • Medicinal organometallic chemistry • Enzyme inhibition.

1.3 Introduction

Enzyme inhibitors are currently playing a crucial role in medicine. A high proportion of the drugs currently reaching the market are exerting their activity by inhibiting an enzyme. For example, the best-selling drug in pharmaceutical history, the lowering blood cholesterol drug Atorvastatin, sold under the trade name Lipitor, is inhibiting an enzyme present in liver tissue.[1] The anticancer drug Imatinib marketed under the trade names Gleevec and Glivec specifically targets a tyrosine kinase. From a medicinal inorganic chemistry perspective, the mechanism of action of several metal-based drugs having reached the market can be linked to enzyme inhibition. Examples of such compounds include the anti-arthritic gold complexes, the antimony-based drugs against leishmaniasis or the arsenic-based drugs against syphilis, trypanososiamis and cancer although the exact mechanism(s) of action of these compounds have not been (yet) fully uncovered. Due to these successful examples, several research groups around the world are currently exploring the possibility of using organometallic compounds to inhibit enzymes involved in diseases. This field of research has been reviewed in detail over the last years.[2–6] In this book chapter, we aim to take an alternative approach by presenting the different concepts employed to achieve enzyme inhibition using organometallic complexes rather than to list all organometallic compounds reported to date which can act as enzyme inhibitors. We will use a few concrete examples to exemplify each concept.

1.4 Organometallic Compounds as Inert Structural Scaffolds for Enzyme Inhibition

Nature evolved proteins, including enzymes, with active sites of very unique and specific shapes and electrostatic surfaces, providing unmatched specificity and catalytic activity for the intended substrates. Obtaining a great selectivity is a challenge in the design of enzyme inhibitors. These small molecules have to match the interaction pattern dictated by the active pocket in order to effectively bind to and block the activity of an enzyme. For this task, the greater the chemical space used in the search of an inhibitor is, the greater are the chances to find a “perfect” inhibitor. Thus, the use of metal complexes greatly increases the structural possibilities to form enzyme inhibitors. Additional metal-specific geometries, such as square-planar or octahedral, can be indeed exploited. Moreover, unique bond lengths and bond polarities, which are unavailable to purely organic compounds, further increase the potential associated with the use of metal compounds as enzyme inhibitors. There are several examples in the literature describing organometallic enzyme inhibitors which have been built around an inert metal center and this topic has been previously reviewed.[7,8] The most extensively studied organometallic complexes are undoubtedly the kinase inhibitors developed by the group of Meggers. Below, we highlight the range of opportunities that has been opened up with the use of metal centers as inert scaffolds, on basis of this work.

Protein kinases are enzymes which catalyze the attachment of phosphate groups to proteins, thereby regulating their function. Hundreds of different subtypes are known, usually phosphorylating only a few specific substrates. Consequently, protein kinases are involved in many cellular pathways, including, but not exclusively, ones up-regulated in cancer tissues leading to their uncontrolled growth. Therefore, selective protein kinase inhibitors represent attractive targets for drug discovery, e.g. as anticancer agents (see introduction).

The common phosphate source of all protein kinases is ATP (Figure 1 a)), whose terminal phosphate group is transferred to the respective substrates. The ATP binding pocket is the main target for protein kinase inhibitors.[9] As there are more than 500 human kinase genes,[10] which have a structurally highly conserved ATP binding pocket, it is essential, and particularly difficult, to design inhibitors with high specificity for a particular kinase subtype.

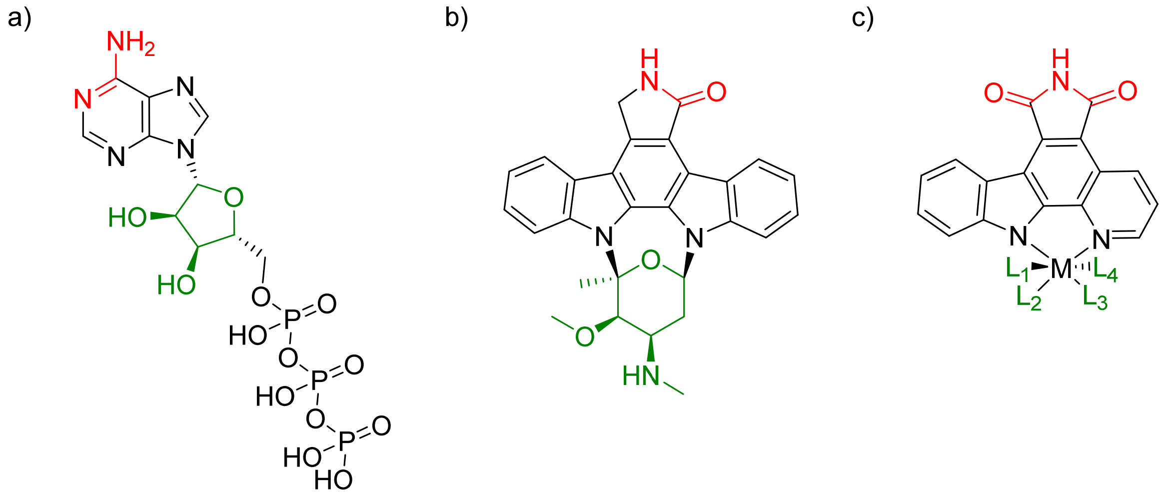

Figure 1. Structure of a) ATP; b) Staurosporine; c) Staurosporine-inspired octahedral metal complex with variable ligands L_1-L_4. The colors indicate the parts of the respective molecules that occupy the same spatial position in the binding pocket of the protein kinases; the red parts show the parts involved in hydrogen bonding to corresponding amino acids, the green parts occupy an area allowing for secondary interactions potentially leading to subtype specificity.

Staurosporine (Figure 1 b)) is a natural alkaloid which inhibits protein kinases with low nanomolar IC_{50} values, but which possesses only low subtype specificity.[11] It binds to the ATP binding site of kinases, which is very similar among the different subtypes. Within the ATP binding site, the lactam (the red part in Figure 1 b)) forms two hydrogen bonds to the protein, as adenine does in the case of ATP.[12] The glycosyl unit in staurosporine (green part in Figure 1 b)) replaces the ribose part of ATP. This part of the inhibitor was found to be less important for the binding affinity of staurosporine to the active site of kinases.[13] On the basis of those observations, Meggers and co-workers designed their organometallic kinase inhibitors. They envisaged keeping the general structure of staurosporine. However, they modified it in a way that it could serve as a ligand for metal complexation (Figure 1c)). Hence, the initial affinity towards protein kinases would be conserved. The remaining open coordination sites of the metal ion then give the opportunity to introduce additional ligands, *inter alia* replacing the glycosyl moiety present in staurosporine. These ligands were later shown to influence the specificity, but also to some extend the affinity of the metal-containing inhibitors to certain kinase subtypes (see below).

Accordingly, ruthenium complexes such as **1** were synthesized and their binding affinity towards protein kinases was investigated (Figure 2).[14] **1** has been found to be over 100 times more potent against the kinase GSK-3 than staurosporine and more than 50 times more potent than the pyridocarbazole ligand by itself.

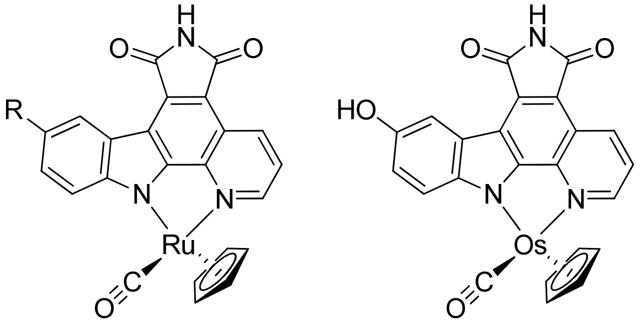

1 R=OH
2 R=H

3

Figure 2. Isostructural ruthenium and osmium complexes with pyridocarbazole ligand.

A cocrystal structure of the protein kinase Pim-1 and **1** showed that the complex **1** binds to the ATP binding site in a homologous manner to staurosporine (Figure 3).[15] Previously, a Lineweaver-Burke analysis, which is a kinetic method allowing the distinction of competitive and non-competitive binding modes, was performed for the ruthenium complex **2**, revealing an ATP-competitive binding mode.[16] Both findings together clearly show that Meggers' organometallic staurosporine-derivatives, like staurosporine itself, bind to the ATP binding pocket of kinases. The cyclopentadienyl moiety and particularly the carbonyl ligand of **1** occupy positions within the ATP binding pocket which are not accessible to purely organic molecules due to the specific geometric properties of the metal complex. For example, as can be seen in the cocrystal structure of **1** with Pim-1, the CO ligand of **1** is involved in dipolar interactions with the glycine-rich loop of Pim-1.[15] This interaction seems to be of

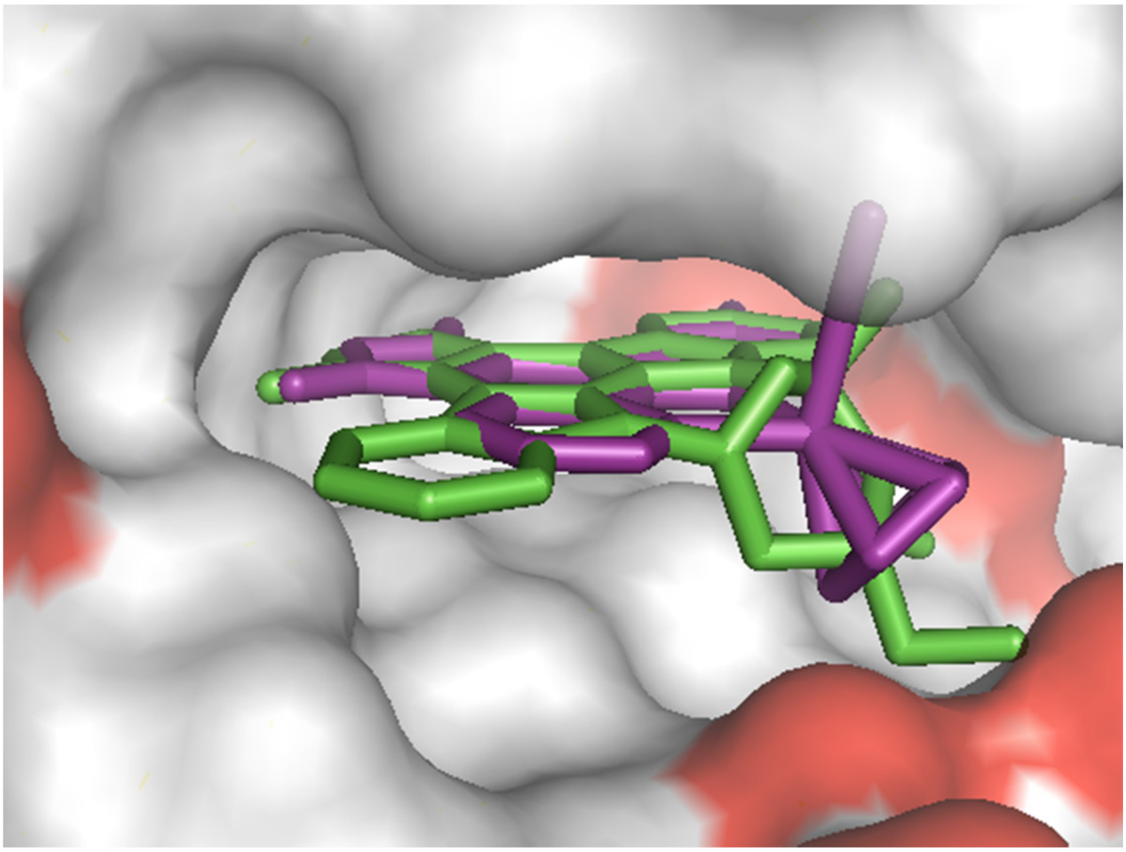

Figure 3. Ruthenium complex **1** (purple; PDB code 2BZI) and staurosporine (green; PDB code 1YHS) inside the ATP binding pocket of Pim-1.[15,17] Both inhibitors occupy a similar spatial position and exhibit homologous interactions to the enzyme.

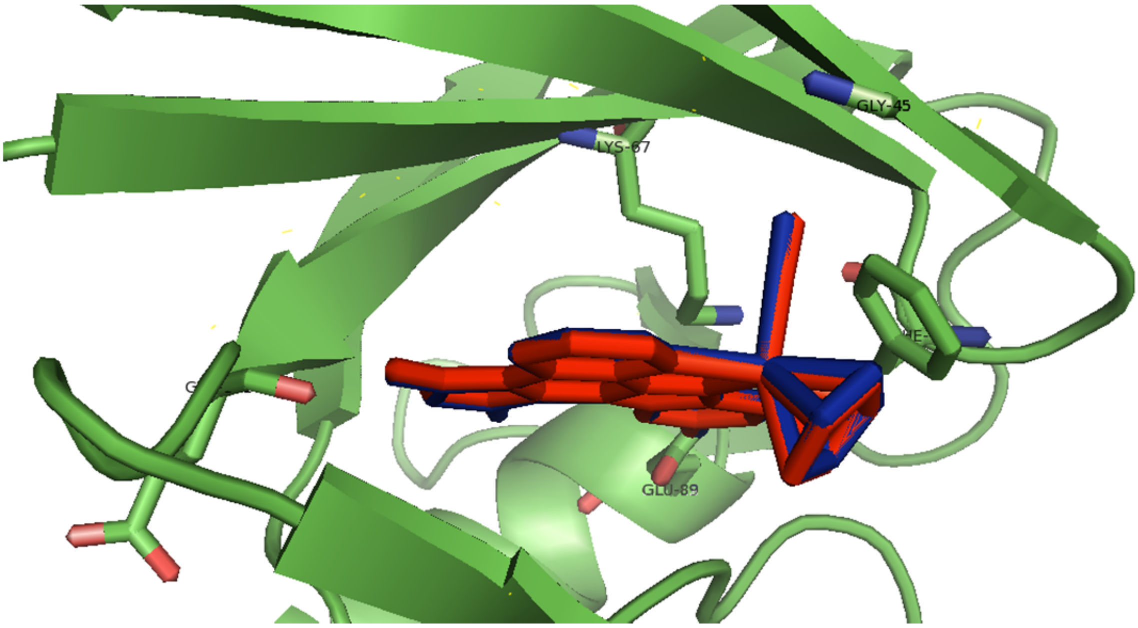

Figure 4. Superimposed cocrystal structures of Pim-1 (green) with **1** (red; PDB code 2BZI)[15] and with **3** (blue; PDB code 3BWF).[18] The amino acid residues involved in the most important interactions with the inhibitors are shown as stick models.[17]

great significance for the subtype specificity towards Pim-1 and GSK3, which possess similar glycine-rich loops. Similar observations were made for other related organometallic kinase inhibitors,[15,18–22] and, to date, all specific organometallic inhibitors found for those enzymes carry this CO ligand. Worthy of note, a CO ligand, unlike an organic carbonyl group in a molecule, is not polar.[22] Hence, the electronic properties responsible for the favorable interactions of the CO ligand of Meggers' enzyme inhibitors with the protein cannot be imitated by organic carbonyl groups. Due to their unique geometric and electronic characteristics, only other organometallic inhibitors are, to the best of our knowledge, known to establish comparable interactions with the glycine-rich loop of protein kinases, introducing hence this great selectivity.[19]

The metal center of **1** appears to be unable to directly interact with the protein as the metal is "protected" by its ligands. In order to further confirm that the role of the metal is solely of structural nature, an complex isosteric to **1**, namely the osmium complex **3** was prepared.[18] In contrast to their geometry, the redox potentials of the two metal complexes are different. Hence, if the metal has a purely structural role the bioactivity should remain unaffected, while any additional influences should alter the activity profile. Cocrystal structures of Pim-1 with **1** and **3** show nearly identical binding geometries and interactions for both complexes (Figure 4). *In vitro* studies, such as the anticancer activity in 1205 Lu melanoma cells and the activation of Wnt signaling as result of inhibition of GSK-3β in human embryonic kidney cells (HEK293OT), also verified the almost identical biological activity of both compounds **1** and **3**, thus clearly demonstrating the purely structural role of the metal center.

Nevertheless, the change of the metal center in this type of inhibitors can lead to an overall different affinity and selectivity pattern among protein kinases. Apart from ruthenium(II)[8,14,15,20–32] and osmium(II),[18] iridium(III),[19,33–36] platinum(II),[37] and rhodium(III)[36,38,39] have also served as metal centers for kinase inhibitors. Such swaps can lead to several consequences depending on the metal ion chosen. Firstly, due to the different electronic properties of the metal ions, different synthetic pathways might be employed to prepare the complexes and thus ease the screening of large compound libraries (*vide infra*). Secondly, a swap of the metal center can, in contrast to the isosteric replacement of ruthenium with osmium discussed above, lead to a different overall complex geometry, which can alter the affinity and selectivity for certain kinases. In accordance with these points, the change from one metal center to another is an option worth considering, as it opens up new avenues for molecular diversity.

Although tetrahedral half-sandwich complexes have geometries which can hardly be mimicked by organic compounds (*vide supra*), octahedrally substituted complexes are even more intriguing as they offer additional geometric complexity.[19,20,25,32,33,35,38–40] The consequences of this become striking if the number of possible stereoisomers is taken into consideration: a tetrahedral center can form up to two enantiomers, octahedral centers can form up to 30 stereoisomers. Meggers coined the term "octasporines" for this group of compounds, as they feature an octahedral coordination sphere and are derived from staurosporine. Notably, the group of octasporines is not limited to organometallic compounds, but also includes classical inorganic complexes, such as **4** (see Figure 5). Compounds **4–7** (Figure 5) nicely demonstrate the tremendous impact of the geometric complexity on biological systems. Despite their similar general arrangement, all of these complexes are highly selective inhibitors of different protein kinase subtypes (Figure 5 and 6).[19,33] It has to be noted that already most of the tetrahedral metal complexes also show high subtype selectivities which surpass many organic inhibitors.

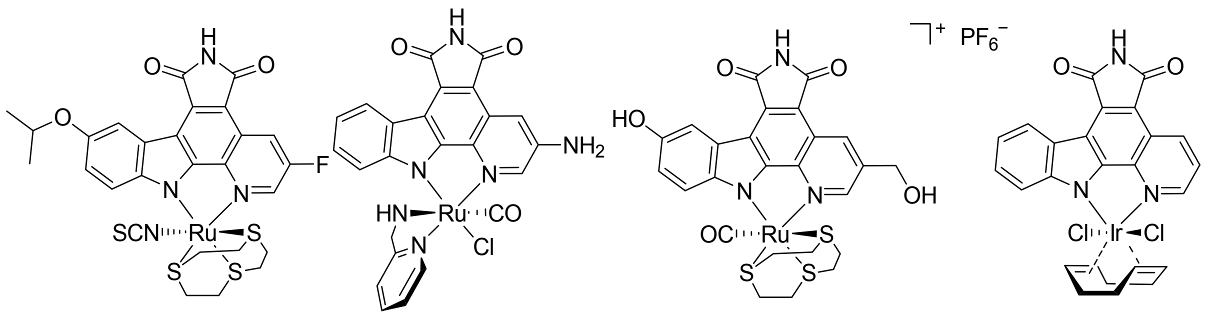

4
DAPK1 inhibitor
2.0 nM

5
GSK3α inhibitor
0.9 nM

6
Pim-1 inhibitor
0.075 nM

7
FLT4 inhibitor
123 nM

Figure 5. Octasporines with distinct selectivity profiles.

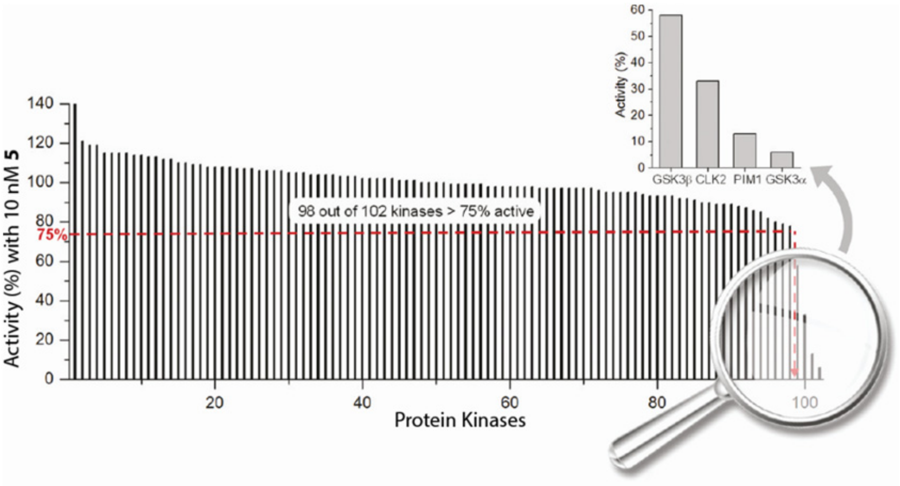

Figure 6. Selectivity of **5** in a screening against 102 kinases. Adapted with permission from ref. [19]. Copyright 2011 American Chemical Society.

The great structural variability gained by the multiple ligands around the metal center can be exploited for Structure Activity Relationship (SAR) studies. The synthesis of complexes with labile ligands allows for rapid screening of different ligands around the metal center as it is the case for the ruthenium complex **8** (Figure 7).[25,37,38] For example, **6** is a selective Pim-1 inhibitor (IC_{50} = 0.075 nM), while **4** is selective for DAPK1 (IC_{50} = 2.0 nM). Replacement of the CO ligand, which is a common motif for Pim-1 selective inhibitors, with a NCS ligand changes the selectivity towards DAPK1. The switch in selectivity is due to the interaction of the respective ligands with the glycine-rich loop of the respective enzymes. In the case of DAPK1, compared to other kinases such as Pim-1, the glycine-rich loop provides more space and can therefore accommodate the larger thiocyanato ligand.

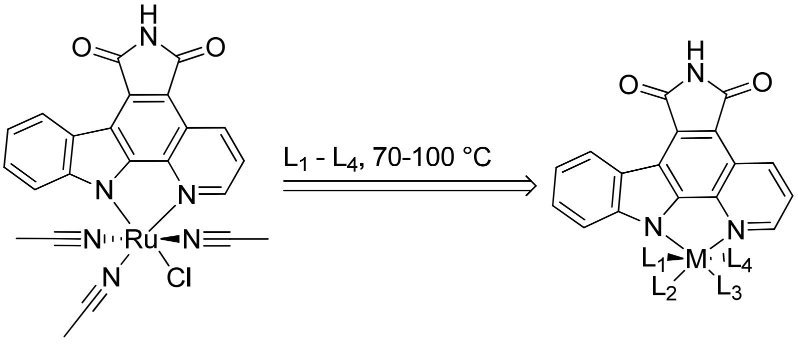

8

Figure 7. Precursor complex **8** can be used to create libraries of complexes carrying different ligands L_1-L_4 by substituting labile ligands at elevated temperatures.[25]

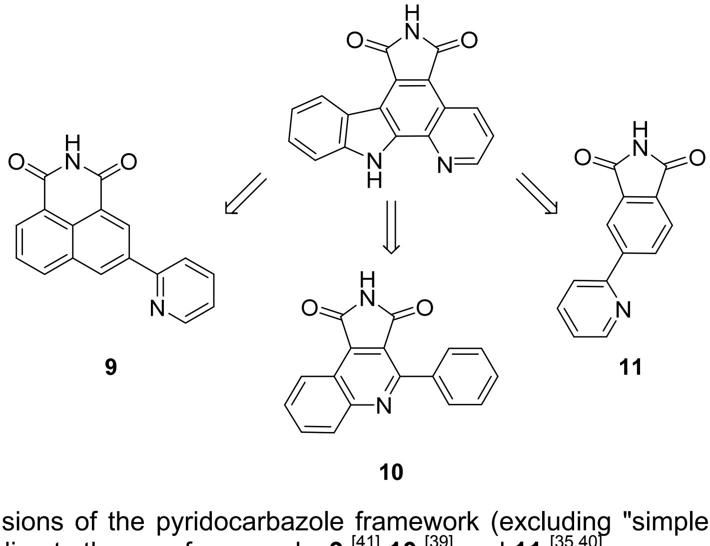

9 **10** **11**

Figure 8. Major revisions of the pyridocarbazole framework (excluding "simple" substitutions of the pyridocarbazole) leading to the new frameworks **9**,[41] **10**,[39] and **11**.[35,40]

Apart from exchanging ligands around the metal center, the ligands themselves can also be modified as part of the screening process to obtain the best enzyme inhibition possible. This is in line with conventional medicinal chemistry approaches. For example, the pyridocarbazole ligand has been substituted with a variety of functional groups.[28,42] A library of 68 amides has been screened, which was synthesized from a ruthenium(II) complex carrying a NHS active ester modified cyclopentadienyl ligand.[26] More recently, even the pyridocarbazole unit, which has been the essential part of almost all enzyme inhibitors previously developed by Meggers and co-workers, has been substantially modified (**9–11** in Figure 8).[35,39,40] In all cases, it was shown that the ligand modification leads to substantially different affinity and/or selectivity profiles. In this regard, the complexes behave like "traditional" fully organic enzyme inhibitors.

The impressive scope of the above described system can be seen by the number of different kinases that can be targeted by these various complexes. It includes GSK3α,[16,42] GSK3β,[27,43] Pim1,[25,38] Pim2,[21] PAK1,[20,40] MST1,[23] BRAF,[30] PI3Kγ,[31] FLT4,[33,34] TrkA,[29] DAPK1,[19] MYLK,[41] PKCδ,[39] among others (Figure 9). This is a result of the extensive variation possibilities gained by using inert metal centers as scaffolds for ligands, which can be altered or exchanged – in addition to the metal itself. However, the complete biological consequences of the changes in the ligand or metal center have to be considered. Changes in the electronic properties of the metal ion lead to different excited state energies, possibly introducing previously unavailable (side-)reactivity.[34,44] Such drastic changes in complex stability can completely change the modes of action of the metal complexes. For example, ruthenium(II) complex **12** possesses, additionally to the protein kinase inhibition, light-activatable properties which can lead to apoptosis.[34] It was indeed recently found that light irradiation of **12** leads to a ligand exchange generating complex **13** (see Scheme 1). The exact cellular pathway leading to apoptosis is not known, but kinase dependence has been ruled out. Nevertheless, metal centers can serve as inert structural elements giving access to geometries that are not available for purely organic compounds. It is expected that the concept of metal complexes as inert scaffolds for enzyme inhibition purposes will become increasingly important in the future, leading to more agents with unprecedented affinity and selectivity.

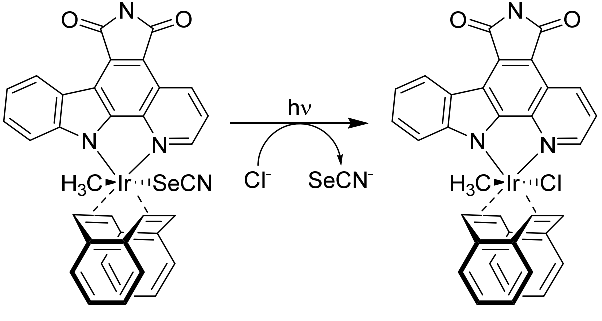

12 **13**

Scheme 1. Photo-induced exchange of the SeCN ligand of **12** with a chloride leads to metal complex **13** which can induce apoptosis via a kinase independent pathway.

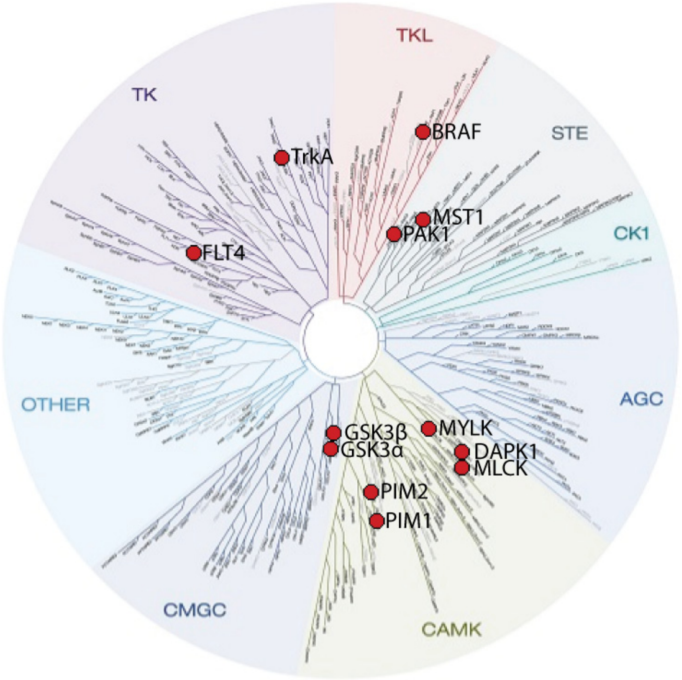

Figure 9. Binding selectivities of selected Meggers-type kinase inhibitors within the human kinase dendrogram which displays the evolutionary relationship between kinases. Adapted with permission from ref. [41]. Copyright 2011 American Chemical Society.

1.5 Organometallic Compounds targeting Specific Protein Residues

One of the most used and effective methods to inhibit enzymes using organometallic complexes, and more generally metal complexes, is by covalent coordination of a metal center to a residue of a specific amino acid involved in the catalytic activity of the enzyme (at active or allosteric sites). This metal coordination renders the enzyme inactive, usually in an irreversible manner (see Scheme 2 for an example with a tyrosine phosphatase and a gold organometallic complex inhibitor[45]). More specifically, the catalytic mechanism of tyrosine phosphatases relies on the transfer of a phosphate group from the substrate to a cysteine residue in the catalytic site (Scheme 2, path (a)). The covalent coordination of the gold center to the cysteine residue allows for the irreversible inhibition of the tyrosine phosphatase (Scheme 2, path (b)).

To achieve such an inhibition, the organometallic compound should ideally have several features:

1) The complex has to be designed in a way that a ligand exchange is possible as for the gold complex in Scheme 2 where a chloride ligand is exchanged by the sulfur of the cysteine residue.

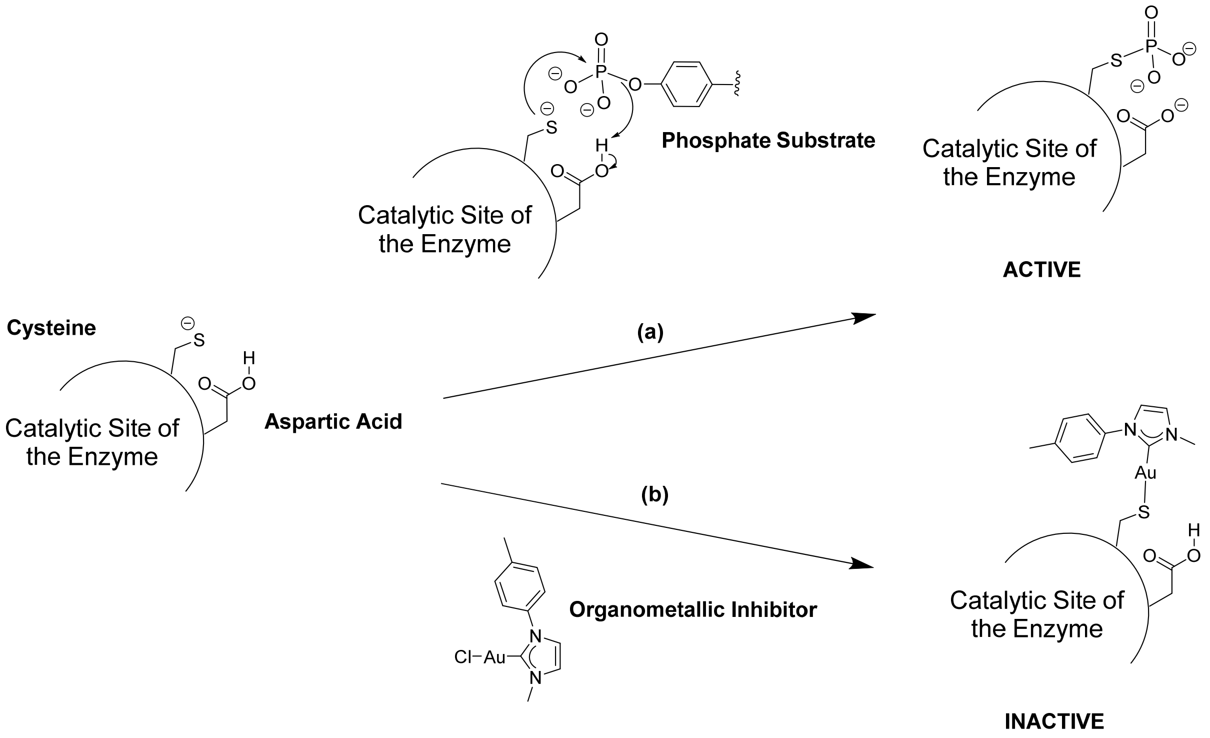

Scheme 2. Simplified depiction of the catalytic mechanism (path (a)) and covalent inhibition (path (b)) of a tyrosine phosphatase.

2) The complex must be specific for an amino acid residue. This means that the metal ion has to be carefully selected. For example, if a cysteine residue is targeted, a (relatively) soft metal ion such as Au(I) or Pt(II) has to be chosen (see also point 3).

3) The complex has to be stable enough to reach its anticipated target. In other words, the ligand must stabilize the complex but has to be labile enough! This “ideal” reactivity can be achieved by fine-tuning of the metal-ligand interaction. As an example of this improved kinetic stability, Berners-Price and co-workers demonstrated that Au(I) *N*-heterocyclic carbene (NHC) complexes such as **14** shown in Figure 10 could display a high kinetic stability in presence of thiols.[46] Interestingly, the authors showed that their complexes were much more reactive (rate constants 20 to 80-fold higher) towards selenocysteine (Sec) than to cysteine (Cys).[46] This difference was explained by the difference in p*K*a values of the two amino acids (Cys = 8.5;[47] Sec = 5.2[48]). At pH = 7.2, the selenol is fully ionized while the thiol is not, facilitating the attack of the selenium to the gold cation.[46] Importantly, these lipophilic, cationic Au(I) complexes selectively induced apoptosis in cancer cells but not in normal cells.[46]

4) The complex should be selective for a specific enzyme. To date, as mentioned by Dyson in a recent review, this endeavor has never been achieved.[6] The metal complexes are targeting several enzymes instead of a single enzyme. In the case of Au(I) complexes, in addition to the targeted enzymes thioredoxin reductases (TrxRs), cysteine proteases,

kinases and glutathione S-transferases (GST P1-1), these compounds were also shown to inhibit other cysteine-containing proteins such as serum albumin.[6] However, the quest of highly selective enzyme inhibitor is a topic of intensive investigations and researchers from all around the globe are becoming closer and closer to achieve this important aim. For example, Ott *et al*. have recently demonstrated that both the enzymatic inhibition and enzyme selectivity of NHC-Au-L complexes could be tuned by subtle ligand modifications (L = Cl (**15**), PPh_3 (**16**) or NHC (**17**); see Figure 10 for the structures).[49] More specifically, the authors showed that the more stable the Au-L bond was (**15** < **16** < **17**), the less reactive the complex was towards enzyme inhibition. However, a higher selectivity could be achieved when the Au-L bond is extremely stable.[49] For example, the most stable complex **17** was much more selective to TrxR than for glutathione reductase (GR) and glutathione peroxidase (GPx).[49] These findings on gold compounds, although obtained on isolated enzymes, are extremely promising and it can be anticipated that even more selective organometallic-based inhibitors will be discovered in the near future.

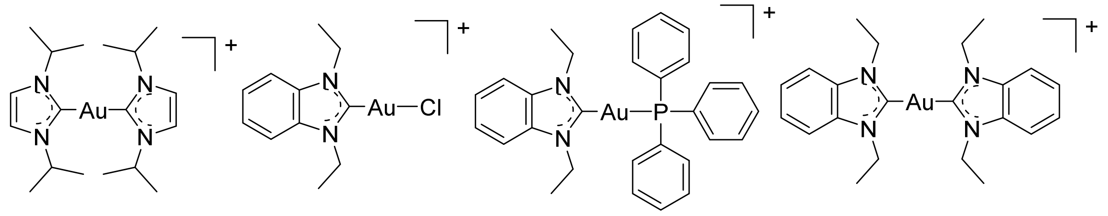

14 **15** **16** **17**

Figure 10. Structure of Au(I) *N*-heterocyclic carbene complexes.

Below, we will not review all organometallic complexes which inhibit enzymes by covalent coordination of a metal center to an amino acid residue, we send the reader to specific reviews and book chapters.[3,4,6,50,51] We will rather highlight an extension of the concept presented in this section. As mentioned above (point 4)), ideally, an organometallic complex should be selective for an enzyme and hence not inhibit several enzymes. As a first step towards solving this problem, Metzler-Nolte *et al*. recently reported the preparation of organometallic Au(I)-peptide bioconjugates which act as TrxR inhibitors.[52] More specifically, the authors envisaged to selectively bring different organometallic Au(I) complexes to a specific cellular organelle, namely mitochondria, which are known to host the targeted enzyme. For this purpose, they coupled, using a [3 + 2] cycloaddition reaction, tetrapeptides which have been previously shown by Szeto[53] and Kelley[54] to cross cell membranes and accumulate in mitochondria.[52] Examples of Au(I) peptide conjugates prepared in their work are presented in Figure 11. As desired, the metal conjugates **18–20** displayed prolonged stability in the presence of one equivalent of cysteine.[52] Worthy of note, the authors could demonstrate an interesting selectivity of their metal-containing bioconjugates for the selenocysteine-containing TrxR over the cysteine-containing GR with EC_{50} values for TrxR lower by at least one order of magnitude compared to the EC_{50} values for GR. The inhibition of TrxR is of high relevance since this enzyme plays an important role in the cellular and mitochondrial redox system.[52] It has been described that TrxR was responsible for the antiproliferative activity of gold compounds.[55]

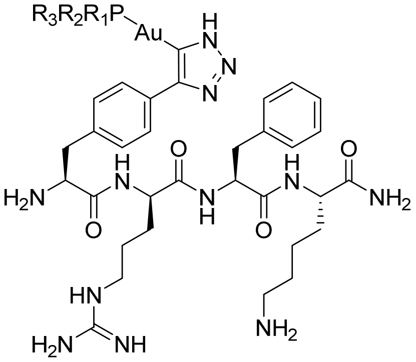

R_1=R_2=R_3=Ph (**18**)
R_1=Ph, R_2=R_3=Et (**19**)
R_1=R_2=R_3=Et (**20**)

Figure 11. Structures of organometallic Au(I)-peptide bioconjugates prepared by Metzler-Nolte *et al.*[52]

1.6 The Bioisosteric Substitution

Although still not fully obvious for part of the drug design community, many organometallic complexes can be handled in presence of oxygen and water just like "normal" organic compounds. Therefore, additionally to screening the substitution on a drug candidate with organic groups (e.g. methyl, ethyl, isopropyl or phenyl), organometallic moieties like ferrocenyl or ruthenocenyl could (should?) be employed during this screening as well. This would allow for the exploration of additional structures which can possibly occupy the binding pocket of an enzyme in a more efficient manner than purely organic inhibitors. The idea of adding organometallic moieties to enhance the activity of enzyme inhibitors is not new. Already in the 1970's, Edwards *et al.* prepared ferrocenyl substituted penicillin and cephalosporin derivatives, which showed high antibacterial activity.[56] In this section, we will explain, on the basis of examples from recent literature, how to design organometallic enzyme inhibitors starting from known bioactive organic molecules.

Starting from pre-existing organic enzyme inhibitors, a straight-forward manner to introduce organometallic moieties is to make use of so-called bioisosteric substitutions. Bioisosteric groups exhibit similar biological effects as a result of their structural resemblance. Most prominently in terms of organometallic chemistry, ferrocenyl moieties are, despite their three-dimensional rather than flat structure, classified as bioisosteric to phenyl. Ferrocene has therefore been extensively used in medicinal chemistry.[57] Ferrocene derivatives have been tested for their toxicity against various cancer cell lines as well as for their antimicrobial activity. However, in most cases, the exact mechanism of action has not been identified. In this section, we will focus on examples in which the mechanism clearly involves inhibition of an enzyme.

Histones are proteins which are responsible for packing and ordering DNA in the nucleus. They are inherently basic and therefore positively charged at physiological pH. The charge state of histones controls their binding strength to DNA and can be altered by changing their degree of acetylation. Histone deacetylases (HDACs) catalyze the removal of negatively charged acetyl groups from the ε-lysine tails of histone proteins utilizing a catalytic zinc ion.[58] Negatively charged DNA then tightly wraps around the positively charged histone core leading to transcriptional silencing of genes. Different subtypes of HDACs control the acetylation of different histones leading to different changes in the transcription. Class I HDACs, comprising HDAC1, 2, 3 and 8, are often overexpressed in cancer tissues and are linked to circumvention of apoptosis and progression of cancer.[59] Subtype specific HDAC inhibitors are therefore subject of ongoing research as anticancer agents.[60]A number of HDAC inhibitors have been found to feature an aryl “cap” combined with a zinc binding motif, such as hydroxamic acid. Vorinostat **21** (Suberoylanilide hydroxamic acid, SAHA) is a representative of this class and is marketed as Zolinza for the treatment of cutaneous T-cell lymphoma (Scheme 3).[61]

Making use of the bioisosteric substitution paradigm, Spencer *et al*. designed N^1-hydroxy-N^8-ferrocenyloctanediamide **22** (Jay Amin hydroxamic acid, abbreviated JAHA) along with other similar derivatives (Scheme 3).[62,63] Docking studies with **22**, starting from a cocrystal structure of Vorinostat **21** with HDAC8[64] supported the expectation of homologous binding interactions.[62] The hydroxylamines of both **21** and **22** interact with the catalytic zinc of the enzyme and the amides of **21** and **22** form an hydrogen bond with an aspartic acid of HDAC8. The ferrocene unit of **22** occupies a part of the binding pocket of HDAC8 which is known to be malleable. Indeed, **22** inhibits class I HDACs with nanomolar affinity (*in vitro* assays). The docking results are in agreement with the experimentally obtained IC_{50} values for **21** and **22** with HDACs (including HDAC8). The series of different ferrocene-containing derivatives all showed selectivity for class I and IIb over class IIa HDACs. The IC_{50} obtained

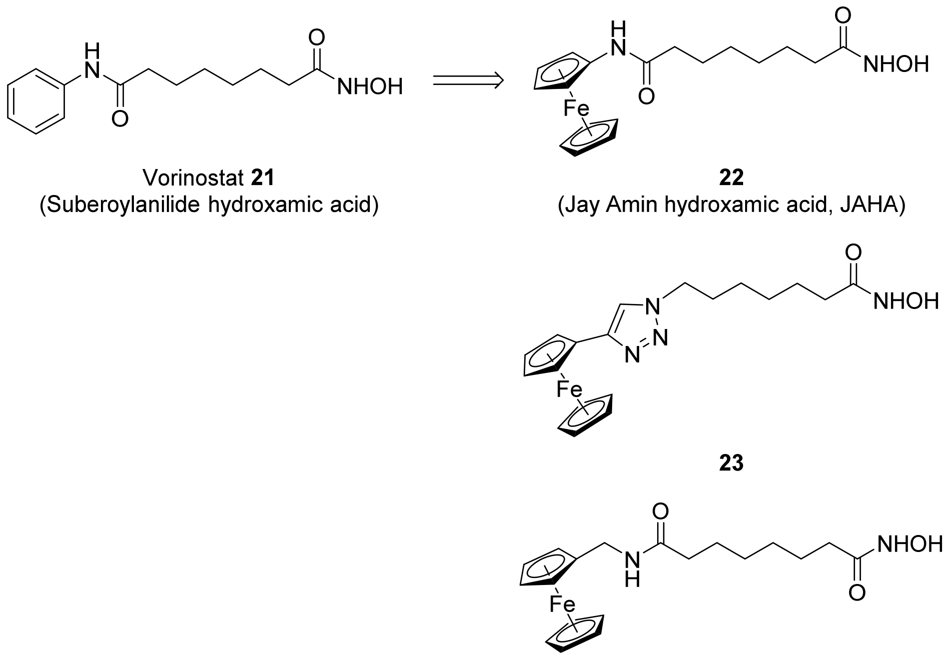

Vorinostat **21**
(Suberoylanilide hydroxamic acid)

22
(Jay Amin hydroxamic acid, JAHA)

23

24

Scheme 3. Structures of the clinical HDAC inhibitor Vorinostat and of ferrocene derivatives which have been designed by bioisosteric substitution of the aromatic moiety.

values surpass the affinity of Vorinostat for certain HDAC subtypes with inhibition levels in the subnanomolar range for the class IIb HDAC6. Cytotoxicity investigations further showed that **22** is inhibiting growth of MCF7 breast cancer cells. Triazole derivatives such as **23** were also shown to inhibit HDACs with low nanomolar IC_{50} values. However, the biological potential of these compounds, as evaluated *in vivo* in *Xenopus laevis*, falls short of this finding.[63] This was attributed to their inferior cellular uptake due to their poor membrane permeability caused by the ferrocene and triazole moieties present in **23**.

22 and **24** were also tested for their ability to inhibit cell growth of triple-negative breast cancer cell line MDA-MB231 *in vitro*.[65] These cells lack receptors for estrogen, progesterone, and epidermal growth factor. They are very aggressive and have a high malignant potential.[66] Despite the similar activity profiles against the pure HDACs, out of **22** and **24**, only **22** shows significant activity against MDA-MB231. The mechanisms involved in the cytotoxicity of **22** towards MDA-MB231 cells were further investigated. Unfortunately, Vorinostat **21** was not tested in the same study, hence complicating direct comparison to **22**. Nevertheless, the cytotoxic effects found for **22** are similar to those observed for **21** in other studies, although partially on different cancer tissues cells.[67]

It has to be noted, that the replacement of phenyl derivatives in known drugs with ferrocene can also have non-desired effects going up to the abolition of the activity of the parent compound. For example, the fungicide fluconazole has been modified to incorporate a ferrocene unit instead of the difluorophenyl moiety (Scheme 4).[68] **25** does not inhibit fungal growth, neither on fluconazole resistant, nor on non-resistent yeast stems – it even stimulates growth under certain conditions.

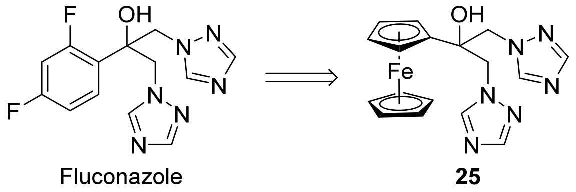

Scheme 4. Fungicide Fluconazole and its ferrocene derivative **25**.

In contrast to the examples highlighted above, in the following examples, organometallic moieties were introduced into enzyme inhibitors without replacing a specific bioisosteric group, such as a phenyl moiety. Carbonic anhydrase (CA) is an enzyme which catalyzes decomposition of carbonic acid to water and carbon dioxide: $H_2CO_3 \rightleftharpoons H_2O + CO_2$.[69,70] There are several CA isozymes involved in different cellular processes. Inhibitors of CAs are in clinical use as diuretics, for gastric and duodenal ulcers, neurological disorders, osteoporosis, and others.[71] In order to control the biological effect of these inhibitors, subtype specificity is essential. In this regard, subtype hCA IX is of interest as it is overexpressed in cancer tissues and only very little expressed in normal tissues.[72]

Benzenesulfonamides, or more generally arylsulfonamides, are a class of carbonic anhydrase inhibitors which consist of a sulfonamide attached to an aromatic moiety, classically a benzyl ring.[69–71] The deprotonated sulfonamide coordinates the catalytically active Zn^{2+} in the substrate binding pocket of the enzyme (see Figure 12). Many different additional substituents are tolerated on the aromatic system as can be seen by the broad range of structures of carbonic anhydrase inhibitors in clinical use including dichlorophenamide, brinzolamide, and acetazolamide (Figure 13).

Poulsen and co-workers have studied the effect of ferrocene and ruthenocene as substituents on benzenesulfonamides (Figure 13).[74] Metallocene derivatives **26**–**29** all showed good binding affinity towards CAs. Ruthenocene derivative **27** was the most active compound against the relevant carbonic anhydrase hCA IX, surpassing the clinically available sulfonamides. Four cocrystal structures of **26**–**29** with hCA II showed the expected coordination of the sulfonamide group to the catalytic Zn^{2+} center of the enzyme (see Figure 12 with **27** as an example).[73] The metallocenes are oriented towards the exterior of the binding pocket and form hydrophobic interactions with the surrounding amino acid residues. Notably, the metal centers are not directly interacting with the enzyme. An observed

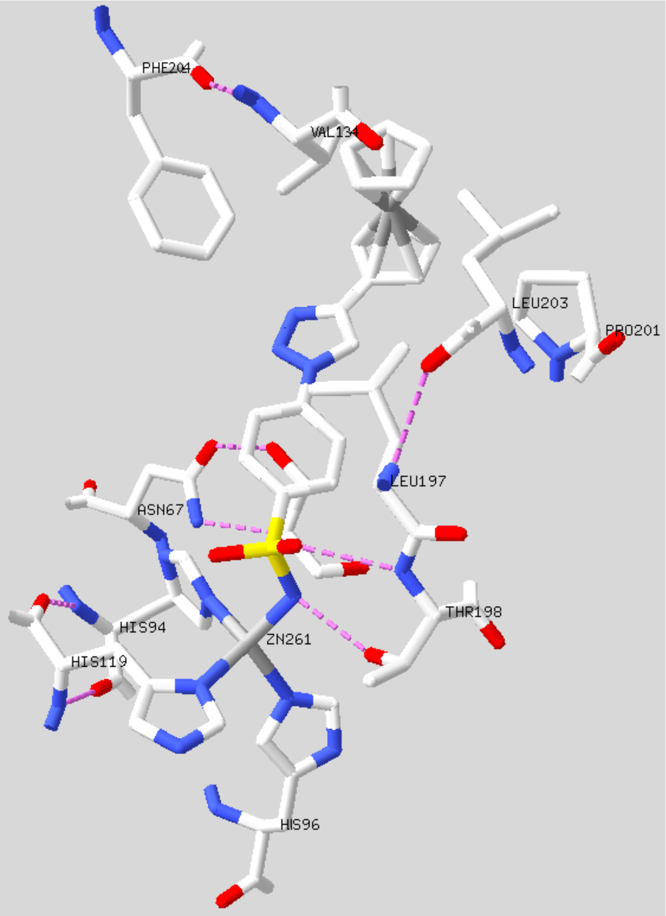

Figure 12. Cocrystal structure of sulfonamide ruthenocene derivative **27** bound to carbonic anhydrase hCAII (PDB: 3P44).[73] Only amino acid residues close enough for interactions with the ligand and Zn^{2+} are shown. Hydrogen bonds are depicted as pink dotted lines, carbon in white, oxygen in red, nitrogen in blue, metals in grey. Protons are omitted for clarity.

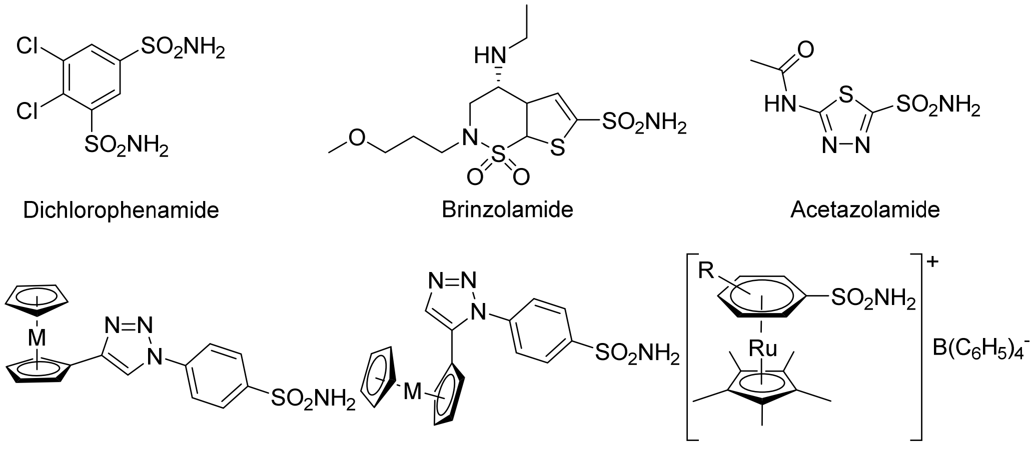

Dichlorophenamide

Brinzolamide

Acetazolamide

M = Fe **26**
Ru **27**

M = Fe **28**
Ru **29**

30

Figure 13. Therapeutic (top) and organometallic (bottom) arylsulfonamide carbonic anhydrase inhibitors.

difference in binding strength between ruthenocene and ferrocene derivatives is therefore thought to be due to the different size of the metals which makes the Cp-Cp distances slightly longer for the ruthenocenes.

Interestingly, organometallic fragments have also been directly attached to the aromatic pharmacophore (**30** in Figure 13).[75] Presumably for steric reasons, these compounds were less active than their benzenesulfonamide ligands.

1.7 Novel Mechanisms of Enzyme Inhibition with Organometallic Compounds

The structural modification of a known organic drug with an organometallic fragment can dramatically alter its mode of action. A prominent example to demonstrate this fact is ferrocifen. Ferrocifen is a ferrocenyl derivative of the anticancer drug tamoxifen.[76] It was found to have an additional mode of action compared to its parent organic compound, which is based on the oxidation of the iron present in ferrocifen. Below, we will focus our attention to the case of hexacarbonyl[2-propyn-1-ylacetylsalicylate]dicobalt (Co-AAS, **31**; see Figure 14).

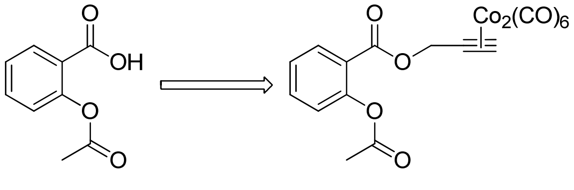

ASS
Aspirin

Co-ASS
31

Figure 14. Antiproliferative compound hexacarbonyl[2-propyn-1-ylacetylsalicylate]dicobalt (Co-ASS, **31**) and its parent drug, aspirin (ASS).

More than 15 years ago, Jung and co-workers reported the synthesis of the dicobalthexacarbonyl derivative **31** (Co-ASS) of the well-known analgesic aspirin (acetylsalicylic acid, abbreviated ASS).[77] Non-steroidal anti-inflammatory drugs (NSAIDs) such as ASS are known to bind to cyclooxygenases (COXs). This family of enzymes is responsible for the formation of prostaglandin H_2 from arachidonic acid. Three subtypes of COX are known, namely COX-1, COX-2, and COX-3 which is a splice variant of COX-1. COX-1 is constitutionally expressed, while COX-2 is overexpressed in many cancer cell lines. ASS is a selective inhibitor of the COX-1 subtype and its analgetic and anti-aggregating effects stem from this interaction.

Co-ASS **31** has been shown to be toxic towards several cancer cell lines, including 3677 human melanoma and H2981 lung adenocarcinoma cancer cell lines,[77] LAMA-84 and

K-562 leukemia cells,[78] as well as MCF-7 and MDA-BM 231 human breast cancer cells.[79] For classical NSAIDs including aspirin, there are still debates whether they are effective against cancer, and if so, by which mechanism(s).[80,81] However, ASS has been clearly proven to be ineffective in all screenings against the cancer cell lines in which **31** has shown to be active. There has been great interest in understanding the molecular mechanism(s) responsible for the cytotoxicity of **31**. Below, we discuss the reasons for the spectacular changes in cytotoxic activity between Co-ASS **31** and ASS.

By analogy to the known effects of ASS, the inhibition efficiency of both COX subtypes has been evaluated for a series of dicobalthexacarbonyl complexes. The inhibition constants of **31** for COX-1 and COX-2 are lower than those for ASS.[79] Interestingly, **31** binds equally strongly to COX-2 and COX-1, while ASS is known to bind only strongly to COX-1. As the binding pocket of COX-2 is bigger than the one of COX-1, the bulkiness of the $Co_2(CO)_6$ group could explain this shift in selectivity. Importantly, comparison of the COX inhibition among dicobalt hexacarbonyl complexes **31**- **34** (Figure 15) with their order of cytotoxic strength revealed that a higher inhibition strength towards COX correlates with a higher cytotoxicity. COX inhibition is therefore thought to be (part of) the mode of action of this class of compounds.

ASS is known to deactivate COX by irreversibly acetylating serine 530 in the active site of COX-1,[82] and correspondingly serine 516 in COX-2.[83] Hence, Ott and co-workers were interested in the potential of Co-ASS **31** to acetylate COX.[83] The exact acetylation sites of COX-2 after incubation with Co-ASS were examined by LC-ESI tandem mass spectrometry. In contrast to ASS, incubation with Co-ASS did not lead to acetylation of serine 516, but to acetylation of several lysine residues, namely lysine 166, lysine 346, lysine 432 and lysine 598 (see Figure 16). Lysine 346 is part of the entrance channel of the active site and thus acetylation could hinder the access of the substrate. Lysine 166 and lysine 432 are close to the heme prosthetic group, and therefore acetylation of these residues could abolish the function of the protein. In analogy to ASS, these modifications can be assumed to be irreversible. In summary, Co-ASS **31** leads to acetylation of COX, however, at different sites than ASS. Nevertheless, these acetylations are certainly involved in the inactivation of the COX enzymes.

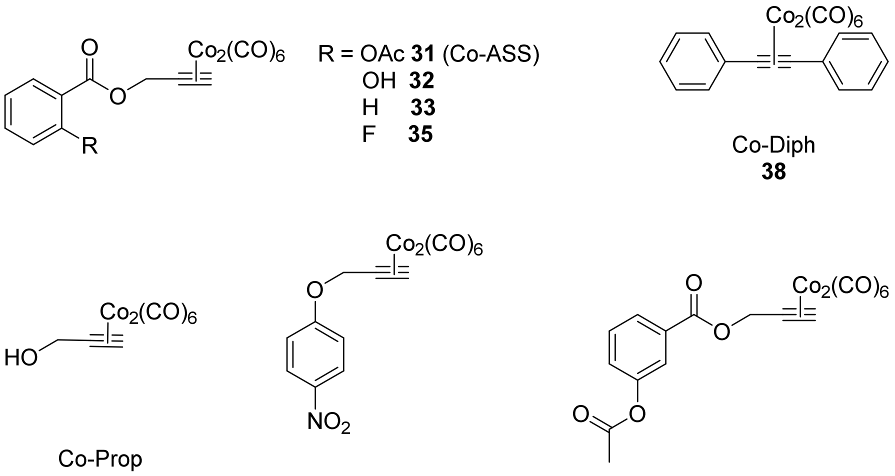

Figure 15. Co-ASS **31** and derivatives Co-Prop **34**, [84] Co-Diph **38**[84], and the salicylates **32**, **33**, **35**, **36**[79] and **44**.[85]

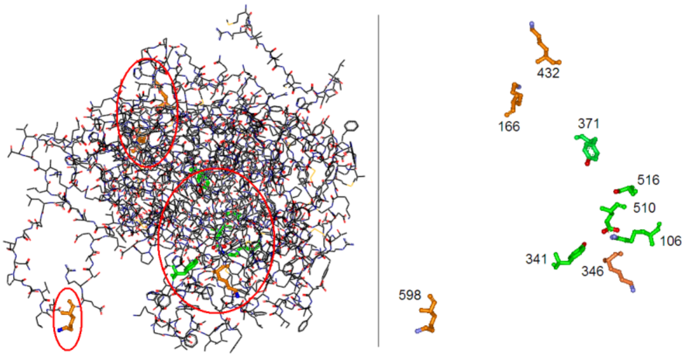

Figure 16. Acetylation sites of COX-2 due to incubation with Co-ASS **31**. Figure reproduced with permission from ref. [83]. Copyright © 2009 WILEY-VCH Verlag GmbH & Co. KGaA, Weinheim.

Interestingly, **32**, which lacks the acetyl moiety present in Co-ASS **31** and ASS and, thus, cannot acetylate COX, is still inhibiting COX.[86] However, the presence of the organometallic moiety in Co-ASS enables to postulate several alternative modes of COX inhibition. It has been shown that both the alkyne ligand and the Co cluster by themselves are not effective antiproliferative agents.[86] However, if the salicylate ligand acts as a carrier to bring the organometallic cluster to the COX binding pocket, the $Co_2(CO)_6$ moiety could exert an enzyme inhibition activity as previously demonstrated by Jaouen and co-workers with the interaction of the $Co_2(CO)_6$ motif with an amino acid residue inside a protein binding pocket.[87] In this work, the authors designed the organometallic hexacarbonyl[ethinyl-estradiol]dicobalt **37**, a derivative of 17α-ethinylestradiol, to bind to estrogen hormone receptors to deactivate them (Scheme 5).[87] Indeed, the $Co_2(CO)_6$ moiety of **37** could react with a close-by nucleophilic cysteine moiety inside the binding pocket of the estrogen receptor in a Nicholas-type reaction *via* formation of a reactive carbocation binding covalently to the receptor.[88] In analogy, a similar reactivity pattern has to be considered as mode of action of Co-ASS **31**. However, the overall structure of **31** is significantly less favorable for the formation of a carbocation than the structure of **37**.[87,89,90] Furthermore, the structurally related cobalt complex **38** (Figure 15), which is cytotoxic, does not contain any methylene groups enabling the formation of a carbocation species.[78] Another indicator against the reactive carbocation hypothesis is the absence of Nicholas-like reactions when incubating **31** with nucleophilic thiols.[91] In summary, a COX inhibition mechanism based on the formation of a reactive carbocation species seems extremely unlikely for **31**.

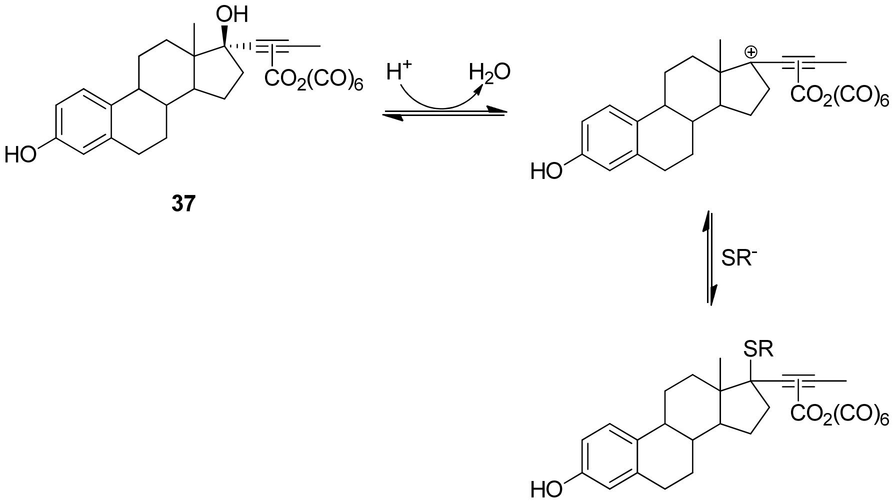

Scheme 5. Hexacarbonyl[ethinylestradiol]dicobalt **37**, its potential formation of a carbocationic species and subsequent reaction with a thiolate.[87,90]

Depending on the substituents on the alkynyl ligand, $Co_2(CO)_6$ moieties can release carbon monoxide.[92] The COX enzymes contain a heme prosthetic group which is essential for electron transfer between the protein and the physiological substrate arachidonic acid. Since the heme group is known to bind CO, a CO dependent mechanism seems appealing. The influence of the alkyne substituents on the CO release of dicobalt hexacarbonyl alkyne complexes is significant, leading either to compounds which are stable or to compounds with rapid CO release rates ($t_{1/2}$ = 1.1 min).[92] Indeed, decomposition of the $Co_2(CO)_6$ moiety of **31** has been observed after treatment with thiols.[91] On the other hand, UV/vis and HPLC analysis of **31** incubated in EMEM cell culture medium containing fetal calf serum did not clearly show any decomposition of **31** within 24 h.[91] Notably, other metal-based ASS-derivatives without CO ligands, namely copper and silver derivatives, were also shown to have antiproliferative properties.[93] Based on these findings, CO release could potentially play a role in the activity of Co-ASS **31** although there is no clear evidence to date.

As presented above, an interaction between **31** and COX enzymes seems likely to be involved in the cytotoxic activity observed. The higher inhibition efficiency of COX and the altered subtype specificity of **31** compared to its parent drug ASS could explain the differences in activity on cancer cell lines. Furthermore, the aforementioned molecular mechanisms could be amplified by a greater cellular uptake and accumulation of the compound in cells. The lipophilicity of the $Co_2(CO)_6$ moiety is typically higher than the lipophilicity of the alkyne ligand by itself.[79,94] This might play an important role in the bioactivity of **31** since a greater lipophilicity often leads to a better cellular uptake through the hydrophobic cellular membrane. Indeed, for the $Co_2(CO)_6$-modified 5-alkynyl-2'-deoxyuridines **39** and **40** (Figure 17) a correlation between cellular uptake, which was determined by measuring the intracellular cobalt content *via* atomic absorption spectroscopy, and their cytotoxicity in MCF-7 and MDA-MB 231 breast cancer cells has been demonstrated.[94]

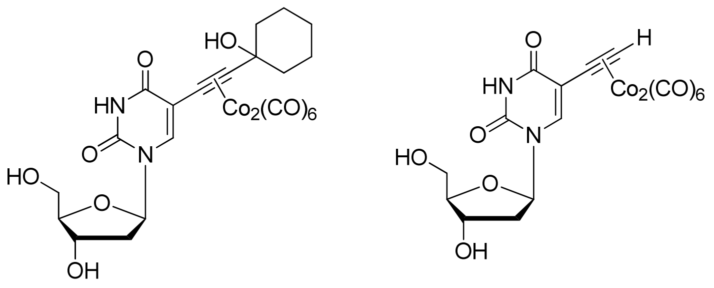

39 **40**

Figure 17. Dicobalt hexacarbonyl derivatives of 5-alkynyl-2'-deoxyuridine.[94]

A similar trend has been observed for the only moderately cytotoxic fructopyranose derivatives **41–43** (Figure 18).[95] For these compounds, it was found that the cytotoxicity depends on the degree of acetalization of the hydroxyl groups of the sugar which is directly responsible for the lipophilicity of the compounds. The cellular uptake was found to correlate with both cytotoxicity and lipophilicity.

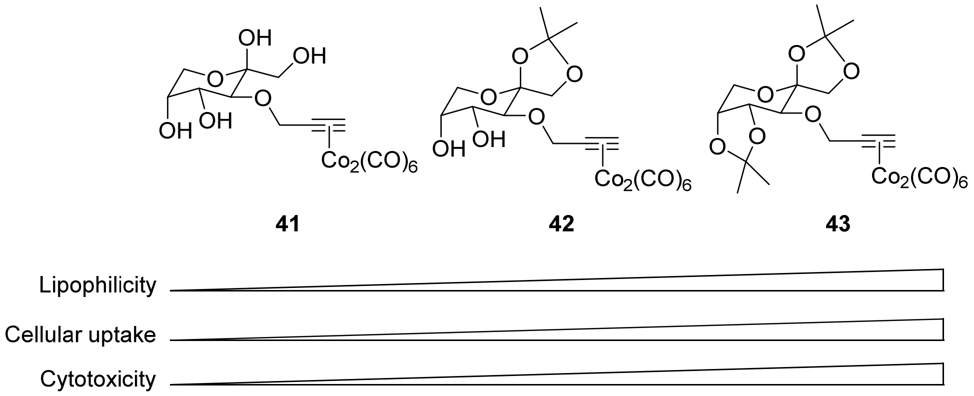

Figure 18. Dicobalt hexacarbonyl derivatives of fructopyranose **41**, **42**, and **43**. The degree of acetylation determines the lipophilicity and correlates with their cytotoxicity in MCF-7 breast cancer cells. [95]

Gust and co-workers showed by analysis of HPLC retention times that the coordination of the $Co_2(CO)_6$ cluster fragment to ASS derivatives indeed increases their lipophilicity.[79] Additionally, it was found that the accumulation grade of **31**, i.e. the resulting concentration of **31** inside cells, is six times higher for **31** than for cisplatin. However, comparison of Co-ASS **31** with the potential metabolite Co-Prop **34** and the pseudo-dimer **38** (Figure 15) revealed a lack of correlation between lipophilicity, cellular uptake, and cytotoxicity in leukemia cells.[78] A more extensive study with other salicylate cobalt derivatives confirmed this finding.[79] Thus, the lipophilicity and cellular uptake of cobalthexacarbonyl derivatives of ASS seem unrelated to their cytotoxicity.

Some doubt about a pathway based purely on COX inhibition came from a recent report on other metal cluster ASS derivatives. Compounds with structures corresponding to **31** with $Co_4(CO)_{10}$ or $Ru_3(CO)_9$ clusters showed lower COX-inhibition efficiencies than **31**, but similar inhibition of cell growth.[96] Simple COX inhibition seems not to be exclusively the reason for the activity of **31**. Further investigations for alternative mechanisms of action for the cytotoxicity of **31** are therefore discussed below.

Since the great success of the inorganic anti-cancer drug cisplatin, metal-based drug candidates are suspected to interfere with DNA, e.g. by direct coordination. Incubation of salmon testes DNA with **31**–**36** showed efficient DNA association for all compounds.[79] Indeed, the attachment was more efficient than for cisplatin. Even more effective was the precursor $Co_2(CO)_8$. This suggests that the interaction with DNA results from the cobalt-alkyne moiety. However, a correlation between the efficiency of DNA association and cytotoxicity could not be found. Moreover, after incubation with cobalt salicylates, the nuclei of both MCF-7 and MDA-BM 231 cells did not contain significant amounts of cobalt, as determined by atomic absorption spectroscopy.[79] Cell cycle analysis of MDA-MB 231 cells after incubation with **44** (Figure 15) revealed an increased amount of cells in the S phase, and less in the G_2/M phase.[85] This means that the cells underwent DNA duplication but did not divide afterwards. Since DNA synthesis appears to function normally, an interaction of **44** with the DNA is very unlikely. Overall, the *in vitro* studies exclude DNA binding to be part of the mechanism of action of dicobalt hexacarbonyl salicylates, including **31**.

Of note, due to the high cytotoxicity against the human breast cancer cell lines MCF-7 and MDA-MB-231 with IC_{50} values of less than 2 µM, the possibility of an interaction of **31** with the estrogen receptor was also investigated.[79] The binding efficiency was very low and the hypothesis was dismissed.

Furthermore, the redox system of the cell could be influenced by the cobalt cluster. **31** has been shown to form disulfides when treated with thiols such as glutathione or cysteine.[91]

The activity of glutathione reductase is a very sensitive indicator for the redox state within cells. It has been shown that glutathione reductase activity was not influenced by **34**, **31**, ASS, or the alkyne ligand of **31**.[79] A mechanism of action based on changing the redox state of the cell can therefore be excluded.

All in all, the combination of the results presented above suggests that several mechanisms are responsible for the cytotoxicity observed for **31**. The inhibition of the COX enzymes is most likely one of them, but both the NSAID as well as the organometallic moiety could have additional activities. The cytotoxicity of celecoxib, a COX-2 specific NSAID, in cancer cell lines which lack COX,[81] as well as the cytotoxicity of $Co_2(CO)_6$ modified peptides, which clearly do not interact with COX,[97] underline that additional mechanisms of action are likely. The case as a whole illustrates that the search for the exact mechanism of action of a complex can be very tedious and the use of organometallic complexes brings even more possibilities for modes of action. This is not a disadvantage though! As shown in the case of the ferrocifens or the antimalarial drug candidate ferroquine the additional activities gained with organometallic compounds can be used to circumvent resistances of purely organic enzyme inhibitors, or even establish an inhibitory activity.

1.8 Organometallic Compounds as Cargo Delivers of Enzyme Inhibitors

A very recent and innovative concept using organometallic-based assemblies for enzyme inhibition purposes has been described by Therrien *et al*. In their work, the authors employed water-soluble organometallic cages to deliver biologically active compounds to cancer cells.[98] An example of one of their constructs is shown in Figure 19. These cages presents two main interests in the field of medicinal chemistry: 1) Despite containing several aromatic moieties, these cages are water soluble as they are usually highly charged, which offers the opportunity to bring very lipophilic compounds into cells; 2) They allow a selective increase of the cellular uptake of the biologically active compounds into cancer cells thank to the enhanced permeability and retention effect (EPR effect). This effect discovered by Matsumura and Maeda in 1986 describes the ability of large molecules to accumulate much more in solid tumors than in healthy tissues.[99] Diverse types of compounds were encapsulated into the organometallic cages including photosensitizers,[100] antiproliferative agents,[101] fluorescent agents,[102] dendrimers[103] and recently enzyme inhibitors.[104,105] For the latter, two different kinds of enzyme inhibitors were encapsulated into the organometallic

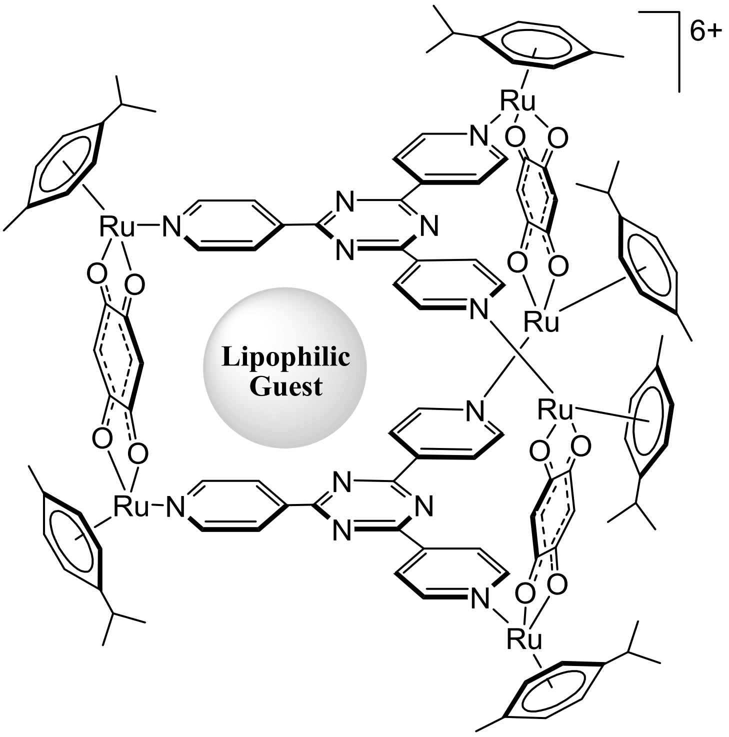

Figure 19. Structure of a water-soluble organometallic cage which can be used to deliver lipophilic guests.

drug used against colorectal cancer Floxuridine which is an irreversible inhibitor of thymidylate synthase; 2) antiproliferative ruthenium arene complexes from the so-called RAPTA family (see Figure 20 for the chemical structures of these compounds). More specifically about this class of compounds, the organometallic RAPTA complexes from the Dyson group are very promising anticancer drug candidates. RAPTA stands for Ruthenium Arene PTA whereby PTA is the abbreviation for the ligand 1,3,4-triaza-7-phosphatricyclo-[3.3.1.1]decane present in all complexes of this family. RAPTA-C (Figure 20) is one of the most famous examples of this family. The exact mechanism of action of RAPTA-C, and in general from all this class of compounds, is not understood in a definitive manner. However, it is clear that these compounds have a fully different behavior compared to cisplatin which targets DNA. At this stage of the research, enzyme binding is the most probable explanation for the activity of the RAPTA complexes.[51] It was indeed demonstrated that such compounds form adducts with proteins[106] and that the reactivity of RAPTA-C and cisplatin in the presence of proteins was much different.[107]

To allow a stable encapsulation of these two types of enzyme inhibitors into their organometallic cages, Therrien and co-workers connected them to pyrene derivatives (Figure 21). The encapsulation of the pyrenyl group into the cage is driven by hydrophobicity

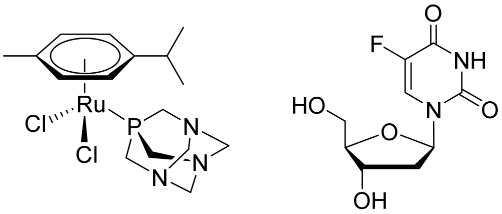

RAPTA-C **Floxuridine**

Figure 20. Structures of the anticancer drug candidate RAPTA-C and of the FDA approved anticancer drug Floxuridine.

and π-π interactions. Of note, the successful encapsulation of the compounds was confirmed by diverse NMR, X-ray crystallography and ESI-MS techniques. In the case of the Ru arene complexes, an increase in cytotoxicity on four different human cancer cell lines was observed for **45–47** (Figure 21) when these compounds were encapsulated. These observations reinforce the postulate that the encapsulation increases the cellular uptake.[105] This effect was clearly demonstrated by monitoring the fluorescence of the pyrenyl moiety. An increase of uptake by a factor of two was determined for complex **45**. Of note, the cage itself employed in this work was found to be highly cytotoxic and even in some cases more toxic than the encapsulated pyrenyl-arene ruthenium complex system itself. This intrinsic toxicity of the cage can be potentially beneficial, provided the cage is selectively delivered to cancer cells. In the case of the caged Floxuridine derivatives, an important difference in cytotoxicity between the cage and the encapsulated pyrenyl-enzyme inhibitor was observed. Hence, all encapsulated pyrenyl-Floxuridine system studied were found to be more toxic than the empty cages alone.[104] Importantly, as anticipated by the authors, the host-guest complexes were found to be highly water-soluble contrary to the Floxuridine compounds used in the clinic.[104]

In a similar line of thought to what has been presented above, namely the delivery of known enzyme inhibitors into cancer cells using organometallic cages, the Dyson group coupled, for example, the glutathione S-transferase (GST) inhibitor ethacrynic acid (EA) to two RAPTA derivatives (**48** and **49**, Figure 22).[108,109] In this work, in addition to the enzyme inhibition by the known inhibitor, the authors also anticipated to engender an inhibition by the organometallic delivery compound used to bring the enzyme inhibitor to the cancer cells (*dual cytotoxic mode of action*). More specifically, knowing that EA, which has been investigated as a potential anticancer drug,[110] binds competitively to the hydrophobic cosubstrate (H-site) of GST and that the RAPTA compounds react with soft nucleophilic centers (e.g. thiol groups), the authors postulated that **48** and **49** could bind to the enzyme at the H-site and could also interact with the two reactive cysteine residues present in

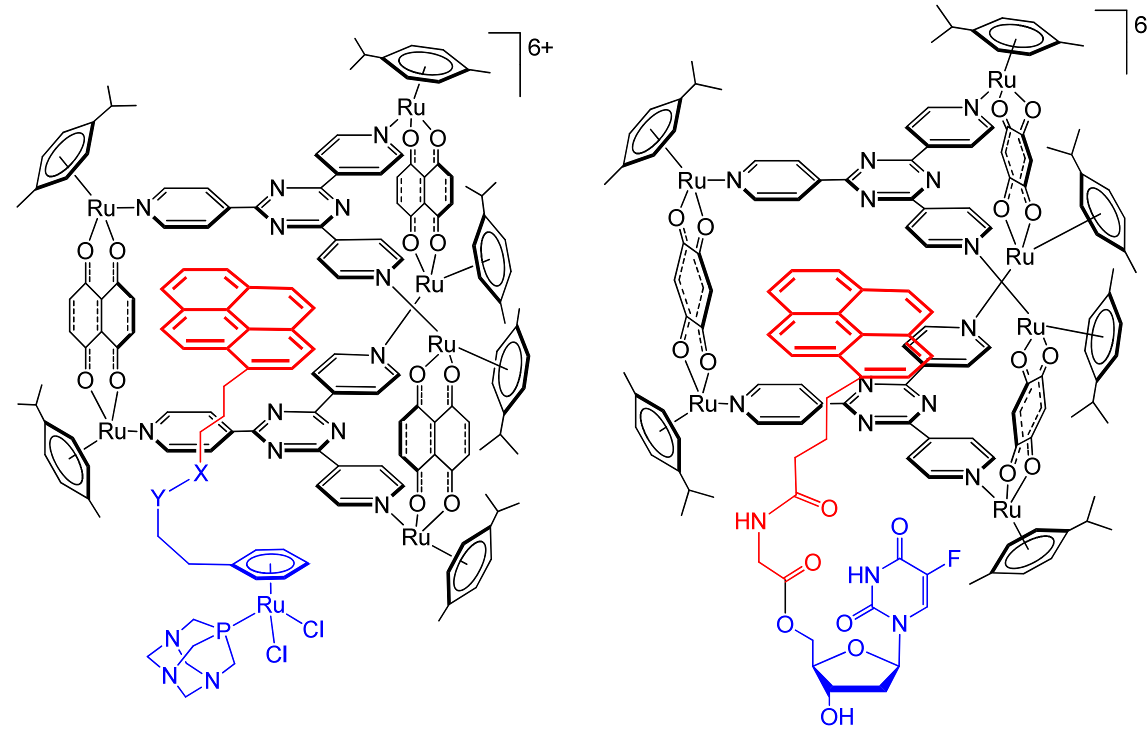

X = CH_2; Y = O (**45**), X= CO; Y = NH (**46**) or X = CO; Y = O (**47**)

Encapsulated Pyrenyl-Arene Ruthenium Complexes **Encapsulated Pyrenyl-Floxuridine**

Figure 21. Structures of the encapsulated pyrenyl-arene ruthenium complexes and of pyrenyl-Floxuridine of Therrien *et al*.

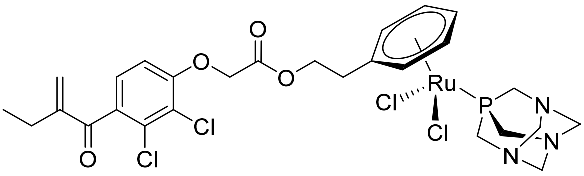

48

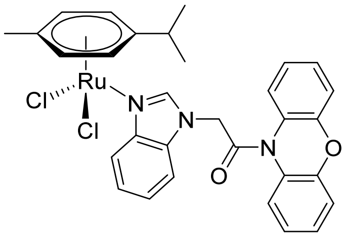

50

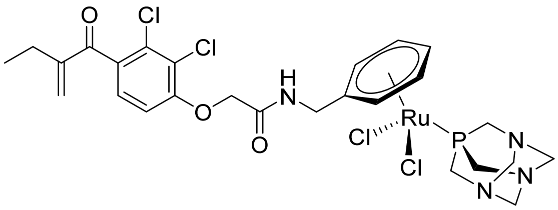

49

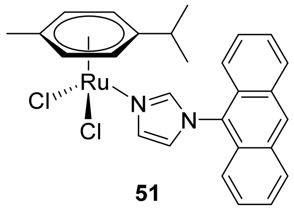

51

Figure 22. Structures of Ru organometallic complexes containing an EA moiety (**48** and **49**) or phenoxazine- (**50**) and anthracene-based (**51**) ligands.

GST P1-1.[108,111] As anticipated, **48** and **49** were found to bind the catalytic H-site but also to have inhibition constants on GST P1-1 three or four times lower than EA. This observation clearly demonstrates that the ruthenium centers of **48** and **49** are involved in the inhibition of

GST P1-1. This was confirmed by X-ray crystallography and ESI-MS measurements. Hence, **49** was found to decompose, over a period of time, into EA and a ruthenium derivative. This cleavage is assumed to occur by virtue of a possible allosteric effect or simply due to binding of the EA moiety present in **49** to the H-site of GST.[108]

The same research group coupled phenoxazine-[112] (**50**) and anthracene-based (**51**) multidrug resistance (MDR) modulator ligands to Ru organometallic complexes (Figure 22).[113] More specifically, the inhibition of P-glycoprotein (Pgp), which is a plasma membrane protein responsible for drug efflux from cells and which is implicated in MDR was studied.[111,114] The combination of the selectivity of ruthenium complexes towards cancer cells and the ability of the phenoxazine and anthracene derivatives for Pgp inhibition was found to lead to a *synergistic effect*. The coordination of the anthracene-based ligand to the Ru complex (**51**) resulted indeed in an enhancement of the cytotoxicity as well as of the inhibition of Pgp, compared to the anthracene-based ligand itself.[113] The other newly formed complexes in this study such as **50** were found to be also generally more cytotoxic than their MDR modulator ligands. However, they inhibited in a lesser extend Pgp than the original Pgp inhibitor derivatives used as ligands.[113] Interestingly, it could be demonstrated with fluorescence measurement that **51** was accumulating in cell nuclei thank to the presence of the fluorescent anthracene group in **51**. This observation correlates well with the results obtained by ^{3}H-thymidine incorporation assay which suggests inhibition of DNA synthesis as possible mechanism of cytotoxic action. All in all, these latest results indicate that, although Pgp inhibition was confirmed *in vitro*, the main mechanism of action of **51** could be independent from inhibition of efflux proteins.[113] Of note, Hartinger, Arion and Keppler used a similar strategy to couple ruthenium or osmium organometallic complexes to flavonoids derivatives which are known to inhibit human topoisomerases,[115,116] paullone derivatives

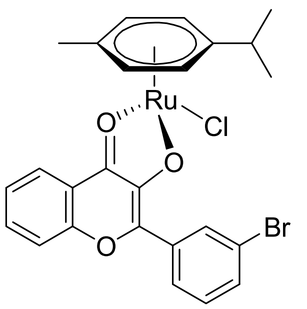

52
Flavonoid-derivative-containing Ru complex

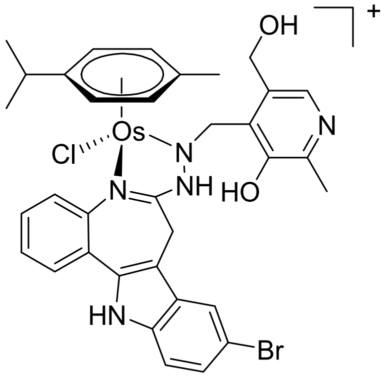

53
Paullone-derivative-containing Os complex

Figure 23. Structures of two Ru and Os organometallic complexes containing flavonoid (**52**)[116] and paullone (**53**)[117] derivatives.

which are known to inhibit cyclin-dependent kinase (CDK) glycogen synthase kinase-3 inhibitors and mitochondrial malate dehydrogenase,[117,118] 3-(1*H*-benzimidazol-2-yl)-1*H*-quinoxalin-2-one bearing pharmacophoric groups of known protein kinase inhibitors[119] or [3-(1*H*-benzimidazol-2-yl)-1*H*-pyrazolo[3,4-*b*]pyridines (and indolo[3,2-*d*]benzazepines derivatives which are known CDK inhibitors (see Figure 23 for two examples of such compounds).[120] It must be however stated that for none of these compounds it was proven that the enzyme inhibitors were actually released in cells, although it is reasonable to anticipate that release will ultimately happen.

1.9 Organometallic Enzyme Inhibitors for Theranostic Purposes

The idea of having a drug (or two very similar drugs) which can be used for both diagnostic and therapeutic purposes is extremely appealing, not to say the holy grail of researchers in drug discovery! This strategy is called theranostics. This term is a portmanteau of the words therapy and diagnostics. For this purpose, a potential approach is the use of a bioconjugate that contains a ligand that can be coordinated to an element which is known to have two different radioisotopes. One of them should have the right radionuclear properties to be used for diagnosis and the other one for therapy. Hence, by designing a single bioconjugate incorporating a ligand suitable for one element, diagnosis and therapy could be undertaken.[121] Among the different elements of the periodic table, potential dual candidates are ^{64}Cu-^{67}Cu, ^{123}I-^{131}I and ^{86}Y-^{90}Y. Note that due to their comparable chemical behaviors, ^{111}In and the more “exotic” ^{177}Lu have been proposed as alternatives to ^{90}Y due to the high-radiation energy of the latter. However, an important drawback of these duos is the production of the radioisotopes. A synchrotron is indeed required. A more favorable option is the use of the ^{99m}Tc-^{188}Re matched pair. The ^{99m}Tc radioisotope has ideal radio-nuclear properties for diagnostic purposes and is available from a commercial ^{99}Mo/^{99m}Tc generator. It is the reason why this radionuclide is used in over 90% of nuclear medicine scans.[122] Furthermore, its third row congener, Re, has relatively similar chemistry to that of Tc (although the kinetic behaviour and stability in the higher oxidation states is somewhat different[123,124]) and has two particle-emitting radioisotopes (^{188}Re and ^{186}Re). One of those is of particular interest for therapy due to its specific activity, namely ^{188}Re ($t_{1/2}$ = 16.98 h, β = 2.12 MeV, γ = 155 keV).[125] Importantly, in the view of easy clinical applications, ^{188}Re can be produced conveniently using a ^{188}W/^{188}Re generator. In addition, the non-radioactive isotopes of Re (^{185}Re and ^{187}Re) provide a model for the chemistry of both the radioactive analogues. With this concept in mind, several groups have embarked into this field of research using the so-called bifunctional chelator (BFC) approach (see Figure 24 for an example). In the BFC approach, a metal chelator is linked via a spacer to a targeting vector whose role is to bring the radionuclide to a specific location (e.g. an over-expressed receptor).

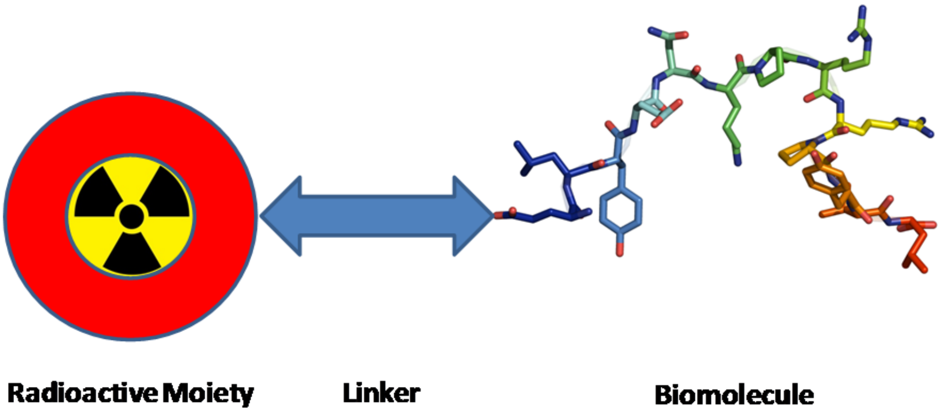

Figure 24. Schematic representation of the BFC approach using the peptide neurotensin as an example of biomolecule (PDB code: 2LNE).

To date, no such dual ^{99m}Tc/^{188}Re theranostic bioconjugates have entered into the market. Furthermore, with regard to the topic of this book chapter, in most of the radioactive conjugates currently approved for diagnostic or therapeutic purposes, and more generally in the clinical pipeline, the target of the radiolabeled bioconjugate is not an enzyme but a specific receptor (e.g. somatostatin receptor, epidermal growth factor receptor (EGFR), etc.). In this context, Alberto *et al*. recently developed a fully novel theranostic concept related to enzyme inhibition. They envisaged preparing, for therapeutic purposes, an enzyme inhibitor containing a cold Re atom. The diagnostic counterpart to this Re complex was anticipated to be a ^{99m}Tc analogue that could be easily synthesised *via* the $[^{99m}Tc(CO)_3(H_2O)_3]^+$ precursor which is generated using the Isolink® kit “Carbonyl Labeling Agent”.[123] The enzymes targeted in their study were carbonic anhydrases (CAs). This family of enzymes, which holds 16 different isozymes, catalyses the formation of carbonic acid from water and CO_2 (see also section 3 of this chapter). Importantly, from a drug discovery point of view, the two human CAs, namely hCA IX and hCA XII, are known to be over-expressed in a large number of hypoxic tumors, mostly in the perinecrotic areas.[126] These two isozymes are therefore interesting targets for both cancer diagnosis and therapy. With this in mind, Alberto and co-workers synthesised a small series of arylsulfonamide, -sulfamide and -sulfamate based compounds with the $[(Cp\text{-}R)Re(CO)_3]$ motif (**54–57**, Figure 25)[127] knowing that unsubsituted sulfonamides and their bioisosters (sulfamates and sulfamites) bind to the Zn(II) ion of the active site of CA by substitution of the non-proteinogenic zinc ligand to generate a tetrahedral adduct[4,69,128] and, importantly, that metal complexes and notably organometallic compounds have been previously shown to be excellent candidates as CA inhibitors (see also section 4 of this chapter).[4,5,129]

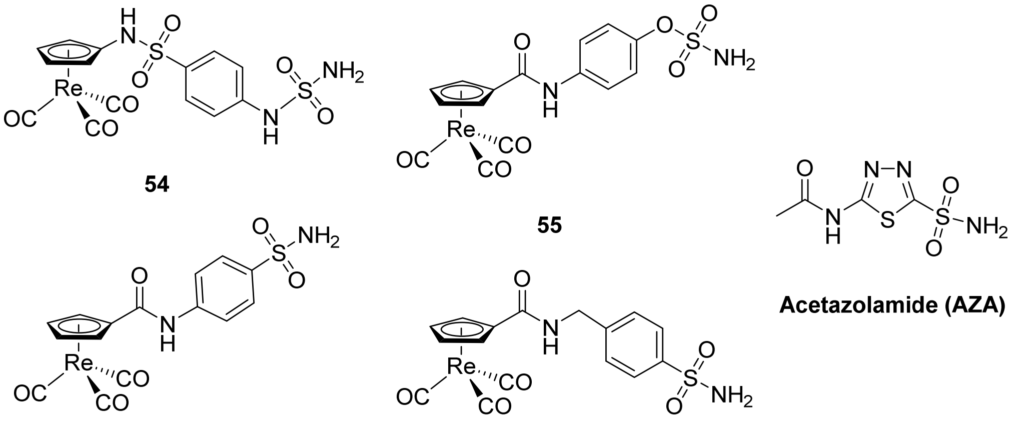

54

55

56

57

Acetazolamide (AZA)

Figure 25. Structures of Re-containing CA inhibitors prepared by Alberto *et al.*[127] and of the drug Acetazolamide (**AZA**).

Of the four compounds prepared in their laboratories, **54** was found to be of particular interest. **54** inhibits CA II, CA XII and CA XIV in the low nanomolar range similarly to the known CA inhibitor acetazolamide (AZA) which is an approved drug against a range of conditions including glaucoma, abnormal retention of fluids, epileptic seizures, etc.[130] However, as can be seen in Figure 26, **54** has a much more pronounced selectivity pattern over the range of the twelve CA isozymes studied in this work compared to AZA. The enhanced selectivity of **54** was proposed to be due to a better space occupancy as previously described by Meggers *et al.* with kinase inhibitors or by Paulsen and co-workers with CA inhibitors (see sections 2 and 4 of this chapter). [25,73] Of great importance from a pharmaceutical point of view, **54** inhibits much more hCA IX, which is overexpressed in certain tumors, than the physiologically dominant hCA II.[127]

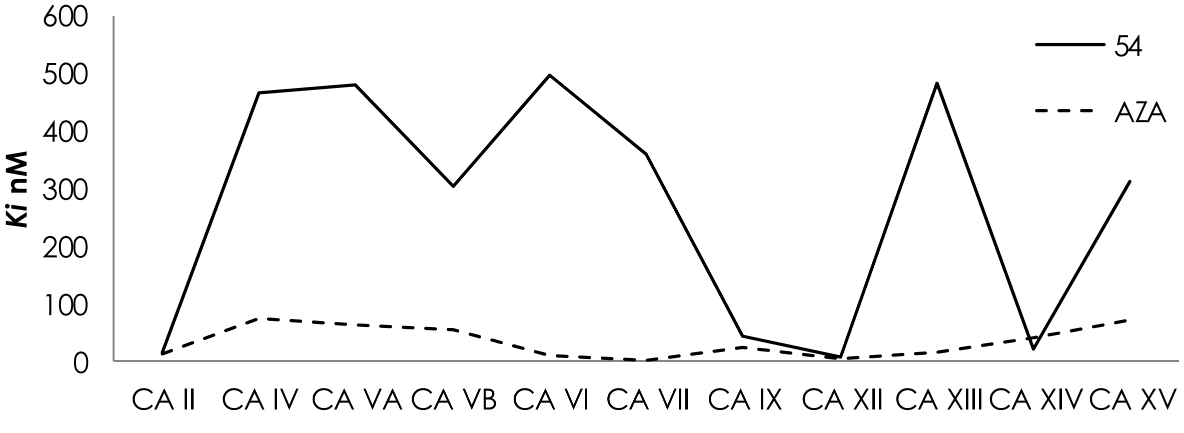

Figure 26. Comparison of the inhibition constants of **54** and AZA over a range of isozymes of hCAs.

The authors of the study could also demonstrate by X-ray crystallography that one of their organometallic CA inhibitors, namely **57**, was indeed able to bind to hCA II. As shown in Figure 27, **57** binds its target in a similar manner than other CA inhibitors by coordinating the Zn atom of the active site of hCA II through the deprotonated nitrogen of arylsulfonamide. As in the case of Meggers' kinase inhibitors and of Paulsen's CA inhibitors, the metal ion is not playing a direct role in the binding of the inhibitor to the enzyme. The organometallic part $CpRe(CO)_3$ is neither interacting with the protein nor with water molecules. However, a hydrophobic interaction between the $CpRe(CO)_3$ moiety and three amino acids (phenylalanine 131, leucine 198 and proline 202) was observed (Figure 27).

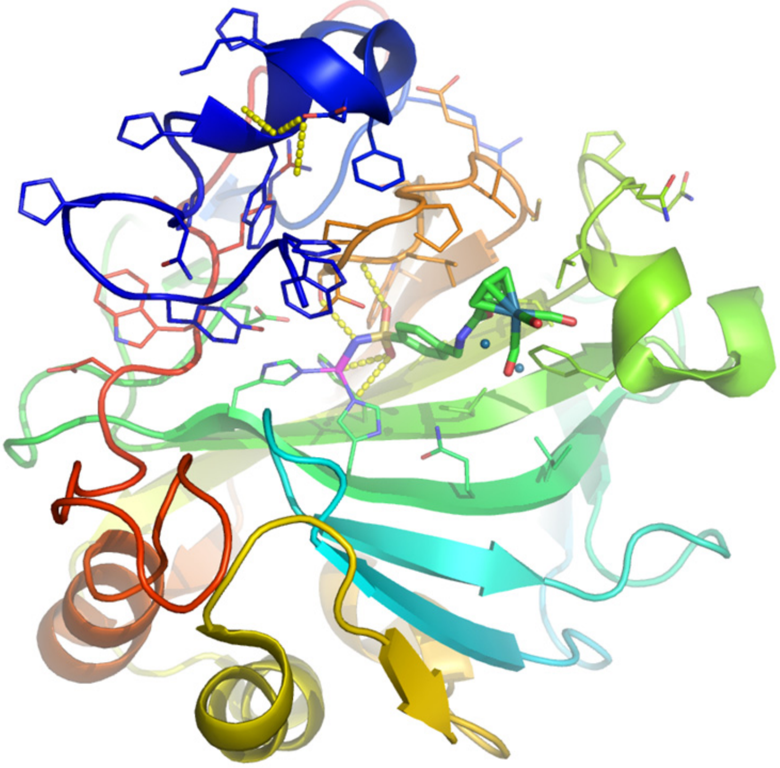

Figure 27. Crystal structure of complex **57** ⊂ hCA II (PDB code: 3RJ7). The Rhenium CA inhibitor **57** coordinates the Zn atom (in magenta) of the active site of hCA II through the deprotonated nitrogen of arylsulfonamide. The Zn atom is bound to three histidines.

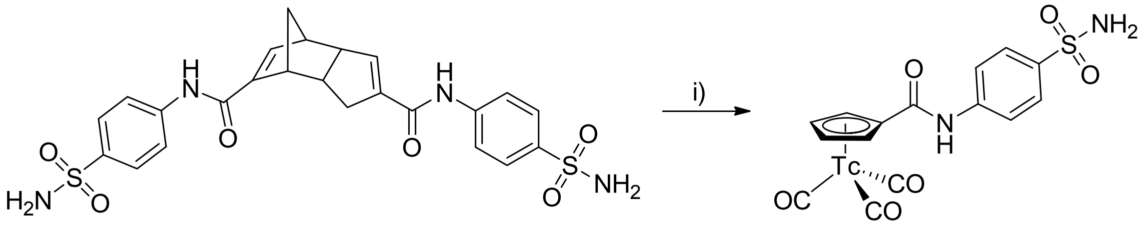

Scheme 6. Synthetic procedure for the ^{99m}Tc analogue of **56**, namely **58**; i) Isolink kit "Carbonyl Labeling Agent", $[^{99m}TcO_4]^-$.

In order to confirm the theranostic concept of their project, Alberto *et al.* had still to demonstrate that a ^{99m}Tc analogue of their Re-containing CA inhibitors could be easily prepared in water since the $^{99m}TcO_4^-$ is eluted from the $^{99}Mo/^{99m}Tc$ generator as a saline solution from the generator. Towards this aim, as presented in Scheme 6 with the ^{99m}Tc analogue of **56** (**58**) as an example, they prepared the ^{99m}Tc complex by reacting $[^{99m}TcO_4]^-$ with the dicyclopentadienyl dimer **59** that they had initially synthesized. The authenticity of **58** was then confirmed by comparison of the HPLC retention times of **58** (γ trace) and **56** (UV trace). As mentioned by the authors, this concept can be extended to any enzyme inhibitor and holds therefore great promises.

1.10 Conclusion

The increasing demand in specific enzyme inhibitors by the pharmaceutical industry for the development of new drugs is a fantastic opportunity for bioorganometallic chemists to display the full potential of their compounds in medicinal chemistry. As explained in this chapter, one important advantage of organometallic compounds compared to purely organic ones lies in the additional geometric and electrostatic profiles that can be created. This can be exploited by “simple” bioisosteric derivatization of a known enzyme inhibitor, or by designing new inert organometallic scaffolds. As nicely demonstrated with the work of Meggers on kinase inhibitors, by using the unique physico-chemical properties of such complexes, higher enzyme specificity can be obtained compared to when purely organic compounds are employed. Importantly, this specificity can be found to be useful not only for drug development reasons but also in the field of chemical biology where such inhibitors are highly valued to understand cellular processes. For instance, two of Meggers’ Ru(II) organometallic complexes are currently commercially available as GSK3 and Pim-1 inhibitors. Moreover, the reactivity of metal centers of organometallic compounds as well as their electrochemical properties can also be exploited for enzyme inhibition purposes. For example, metal centers can covalently bind to certain protein residues or release bio-active compounds, allowing for modes of enzyme inhibition for which no resistances are known to date. Moving beyond therapeutic uses, the metal ions present in organometallic complexes can be tracked by various analytical methods, making them valuable diagnostic tools. We are optimistic that the various advantages that organometallic compounds yield will soon lead to news exciting advances in the field of medicinal chemistry and chemical biology.

1.11 Acknowledgments

This work is funded by the Swiss National Science Foundation (SNSF Professorship PP00P2_133568 to G.G.), the Stiftung für wissenschaftliche Forschung of the University of Zurich, and the University of Zurich. The authors thank Dr. Daniel Can and Prof. Alberto for providing us with raw data for the preparation of Figure 26 as well as Prof. Christian Hartinger, Dr. Henrik Braband, Prof. Ingo Ott, Prof. Ian Fairlamb, Prof. Bruno Therrien, Prof. Fabio Zobi and Anita Schmitz for helpful discussions.

1.12 Abbreviations

ASS	Acetylsalicylic acid, aspirin
ATP	Adenosine triphosphate
AZA	Acetazolamide
BFC	Bifunctional chelator
CA	Carbonic anhydrase
CDK	cyclin-dependent kinase
COX	Cyclooxygenase
Cp	Cyclopentadienyl
Cys	Cysteine
DNA	Deoxyribonucleic acid
EA	Ethacrynic acid
EGFR	Epidermal growth factor receptor
EPR effect	Enhanced permeability and retention effect
ESI-MS	Electron Spray Ionization – Mass Spectrometry
FDA	Food and Drug Administration
GPx	Glutathione peroxidase
GR	Glutathione reductase
GST	Glutathione S-transferase
HDAC	Histone deacetylase
HPLC	High performance liquid chromatography
IC50	Inhibitory concentration 50
JAHA	Jay Amin hydroxamic acid
L	Ligand
LC-ESI	Liquid chromatography – electron spray ionization (mass spectrometry)
MDR	Multidrug resistance
NHC	N-heterocyclic carbene
NMR	Nuclear Magnetic Resonance
NSAID	Non-steroidal anti-inflammatory drugs
PDB	Protein database
Pgp	P-glycoprotein
RAPTA	Ruthenium Arene PTA whereby PTA is the abbreviation for the ligand 1,3,4-triaza-7-phosphatricyclo-[3.3.1.1]decane
SAHA	Suberoylanilide hydroxamic acid
SAR	Structure activity relationship
Sec	selenocysteine
TrxR	thioredoxin reductase
UV/vis	Ultraviolet/visible light

1.13 References and Notes

[1] Associated Press, *Lipitor becomes world's top-selling drug*, *Crain's New York Business*, **2011**.

[2] A. Y. Louie, T. J. Meade, *Chem. Rev.* **1999**, *99*, 2711–2734.

[3] E. Meggers, *Chem. Commun.* **2009**, 1001–1010.

[4] G. Gasser, N. Metzler-Nolte in *Bioinorganic Medicinal Chemistry* (Ed.: E. Alessio), Wiley-VCH Verlag GmbH & Co. KGaA, **2011**.

[5] M. Patra, G. Gasser, *ChemBioChem* **2012**, *13*, 1232–1252.

[6] K. J. Kilpin, P. J. Dyson, *Chem. Sci.* **2013**, *4*, 1410–1419.

[7] S. Mulcahy, E. Meggers in *Topics in Organometallic Chemistry* (Eds.: G. Jaouen, N. Metzler-Nolte), Springer Berlin Heidelberg, **2010**.

[8] E. Meggers, G. E. Atilla-Gokcumen, H. Bregman, J. Maksimoska, S. P. Mulcahy, N. Pagano, D. S. Williams, *Synlett* **2007**, *2007*, 1177,1189.

[9] a) P. Cohen, *Nat. Rev. Drug Discov.* **2002**, *1*, 309–315; b) C. García-Echeverría, P. Traxler, D. B. Evans, *Med. Res. Rev.* **2000**, *20*, 28–57; c) P. A. Cole, A. D. Courtney, K. Shen, Z. Zhang, Y. Qiao, W. Lu, D. M. Williams, *Acc. Chem. Res.* **2003**, *36*, 444–452.

[10] G. Manning, D. B. Whyte, R. Martinez, T. Hunter, S. Sudarsanam, *Science* **2002**, *298*, 1912–1934.

[11] a) S. Omura, Y. Iwai, A. Hirano, A. Nakagawa, J. Awaya, H. Tsuchya, Y. Takahashi, R. Masuma, *J. Antibiot.* **1977**, *30*, 275–282; b) T. Tamaoki, H. Nomoto, I. Takahashi, Y. Kato, M. Morimoto, F. Tomita, *Biochem. Biophys. Res. Commun.* **1986**, *135*, 397–402; c) L. Prade, R. A. Engh, A. Girod, V. Kinzel, R. Huber, D. Bossemeyer, *Structure* **1997**, *5*, 1627–1637; d) L. M. Toledo, N. B. Lydon, *Structure* **1997**, *5*, 1551–1556; e) G. Caravatti, T. Meyer, A. Fredenhagen, U. Trinks, H. Mett, D. Fabbro, *Bioorg. Med. Chem. Lett.* **1994**, *4*, 399–404.

[12] A. M. Lawrie, M. E. M. Noble, P. Tunnah, N. R. Brown, L. N. Johnson, J. A. Endicott, *Nat. Struct. Mol. Biol.* **1997**, *4*, 796–801.

[13] H. Hu, *Drug Discov. Today* **1996**, *1*, 438–447.

[14] D. S. Williams, G. E. Atilla, H. Bregman, A. Arzoumanian, P. S. Klein, E. Meggers, *Angew. Chem. Int. Ed.* **2005**, *44*, 1984–1987.

[15] J. É. Debreczeni, A. N. Bullock, G. E. Atilla, D. S. Williams, H. Bregman, S. Knapp, E. Meggers, *Angew. Chem. Int. Ed.* **2006**, *45*, 1580–1585.

[16] H. Bregman, D. S. Williams, G. E. Atilla, P. J. Carroll, E. Meggers, *J. Am. Chem. Soc.* **2004**, *126*, 13594–13595.

[17] L. L. Schrödinger, *The PyMOL Molecular Graphics System, Version 1.3r1*, **2010**.

[18] J. Maksimoska, D. S. Williams, G. E. Atilla-Gokcumen, K. S. M. Smalley, P. J. Carroll, R. D. Webster, P. Filippakopoulos, S. Knapp, M. Herlyn, E. Meggers, *Chem. Eur. J.* **2008**, *14*, 4816–4822.

[19] L. Feng, Y. Geisselbrecht, S. Blanck, A. Wilbuer, G. E. Atilla-Gokcumen, P. Filippakopoulos, K. Kräling, M. A. Celik, K. Harms, J. Maksimoska et al., *J. Am. Chem. Soc.* **2011**, *133*, 5976–5986.

[20] J. Maksimoska, L. Feng, K. Harms, C. Yi, J. Kissil, R. Marmorstein, E. Meggers, *J. Am. Chem. Soc.* **2008**, *130*, 15764–15765.

[21] A. N. Bullock, S. Russo, A. Amos, N. Pagano, H. Bregman, J. É. Debreczeni, W. H. Lee, F. v. Delft, E. Meggers, S. Knapp, *PLoS ONE* **2009**, *4*, e7112 EP -.

[22] G. E. Atilla-Gokcumen, L. Costanzo, E. Meggers, *JBIC, J. Biol. Inorg. Chem.* **2011**, *16*, 45-50.
[23] R. Anand, J. Maksimoska, N. Pagano, E. Y. Wong, P. A. Gimotty, S. L. Diamond, E. Meggers, R. Marmorstein, *J. Med. Chem.* **2009**, *52*, 1602–1611.
[24] G. E. Atilla-Gokcumen, N. Pagano, C. Streu, J. Maksimoska, P. Filippakopoulos, S. Knapp, E. Meggers, *ChemBioChem* **2008**, *9*, 2933–2936.
[25] H. Bregman, P. J. Carroll, E. Meggers, *J. Am. Chem. Soc.* **2006**, *128*, 877–884.
[26] H. Bregman, E. Meggers, *Org. Lett.* **2006**, *8*, 5465–5468.
[27] E. Meggers, G. E. Atilla-Gokcumen, K. Grundler, C. Frias, A. Prokop, *Dalton Trans.* **2009**, 10882–10888.
[28] N. Pagano, J. Maksimoska, H. Bregman, D. S. Williams, R. D. Webster, F. Xue, E. Meggers, *Org. Biomol. Chem.* **2007**, *5*, 1218–1227.
[29] C. Streu, L. Feng, P. J. Carroll, J. Maksimoska, R. Marmorstein, E. Meggers, *Inorg. Chim. Acta* **2011**, *377*, 34–41.
[30] P. Xie, C. Streu, J. Qin, H. Bregman, N. Pagano, E. Meggers, R. Marmorstein, *Biochem.* **2009**, *48*, 5187–5198.
[31] P. Xie, D. S. Williams, G. E. Atilla-Gokcumen, L. Milk, M. Xiao, K. S. M. Smalley, M. Herlyn, E. Meggers, R. Marmorstein, *ACS Chem. Biol.* **2008**, *3*, 305–316.
[32] L. Zhang, P. Carroll, E. Meggers, *Org. Lett.* **2004**, *6*, 521–523.
[33] A. Wilbuer, D. H. Vlecken, D. J. Schmitz, K. Kräling, K. Harms, C. P. Bagowski, E. Meggers, *Angew. Chem. Int. Ed.* **2010**, *49*, 3839–3842.
[34] A. Kastl, A. Wilbuer, A. L. Merkel, L. Feng, P. Di Fazio, M. Ocker, E. Meggers, *Chem. Commun.* **2012**, *48*, 1863–1865.
[35] S. Blanck, Y. Geisselbrecht, K. Kraling, S. Middel, T. Mietke, K. Harms, L.-O. Essen, E. Meggers, *Dalton Trans.* **2012**, *41*, 9337–9348.
[36] Y. Geldmacher, M. Oleszak, W. S. Sheldrick, *Inorg. Chim. Acta* **2012**, *393*, 84–102.
[37] D. S. Williams, P. J. Carroll, E. Meggers, *Inorg. Chem.* **2007**, *46*, 2944–2946.
[38] S. Dieckmann, R. Riedel, K. Harms, E. Meggers, *Eur. J. Inorg. Chem.* **2012**, *2012*, 813–821.
[39] S. Mollin, S. Blanck, K. Harms, E. Meggers, *Inorg. Chim. Acta* **2012**, *393*, 261–268.
[40] S. Blanck, J. Maksimoska, J. Baumeister, K. Harms, R. Marmorstein, E. Meggers, *Angew. Chem. Int. Ed.* **2012**, *51*, 5244–5246.
[41] S. Blanck, T. Cruchter, A. Vultur, R. Riedel, K. Harms, M. Herlyn, E. Meggers, *Organometallics* **2011**, *30*, 4598–4606.
[42] G. E. Atilla-Gokcumen, D. S. Williams, H. Bregman, N. Pagano, E. Meggers, *ChemBioChem* **2006**, *7*, 1443–1450.
[43] N. Pagano, E. Y. Wong, T. Breiding, H. Liu, A. Wilbuer, H. Bregman, Q. Shen, S. L. Diamond, E. Meggers, *J. Org. Chem.* **2009**, *74*, 8997–9009.
[44] A. Kastl, S. Dieckmann, K. Wähler, T. Völker, L. Kastl, A. L. Merkel, A. Vultur, B. Shannan, K. Harms, M. Ocker et al., *ChemMedChem* **2013**, n/a.
[45] D. Krishnamurthy, M. R. Karver, E. Fiorillo, V. Orrú, S. M. Stanford, N. Bottini, A. M. Barrios, *J. Med. Chem.* **2008**, *51*, 4790–4795.
[46] J. L. Hickey, R. A. Ruhayel, P. J. Barnard, M. V. Baker, S. J. Berners-Price, A. Filipovska, *J. Am. Chem. Soc.* **2008**, *130*, 12570–12571.
[47] R. E. Benesch, R. Benesch, *J. Am. Chem. Soc.* **1955**, *77*, 5877–5881.
[48] R. E. Huber, R. S. Criddle, *Arch. Biochem. Biophys.* **1967**, *122*, 164–173.

[49] R. Rubbiani, S. Can, I. Kitanovic, H. Alborzinia, M. Stefanopoulou, M. Kokoschka, S. Mönchgesang, W. S. Sheldrick, S. Wölfl, I. Ott, *J. Med. Chem.* **2011**, *54*, 8646–8657.

[50] a) L. Oehninger, R. Rubbiani, I. Ott, *Dalton Trans.* **2013**, *42*, 3269–3284; b) W. Liu, R. Gust, *Chem. Soc. Rev.* **2013**, *42*, 755–773; c) I. Bratsos, T. Gianferrara, E. Alessio, C. G. Hartinger, M. A. Jakupec, B. K. Keppler in *Bioinorganic Medicinal Chemistry* (Ed.: E. Alessio), Wiley-VCH Verlag GmbH & Co. KGaA, **2011**; d) S. J. Berners-Price in *Bioinorganic Medicinal Chemistry* (Ed.: E. Alessio), Wiley-VCH Verlag GmbH & Co. KGaA, **2011**; e) K. M. Hindi, M. J. Panzner, C. A. Tessier, C. L. Cannon, W. J. Youngs, *Chem. Rev.* **2009**, *109*, 3859–3884; f) I. Ott, *Coord. Chem. Rev.* **2009**, *253*, 1670–1681.

[51] A. Casini, C. Hartinger, A. Nazarov, P. Dyson in *Topics in Organometallic Chemistry* (Eds.: G. Jaouen, N. Metzler-Nolte), Springer Berlin Heidelberg, **2010**.

[52] S. D. Koster, H. Alborzinia, S. Can, I. Kitanovic, S. Wolfl, R. Rubbiani, I. Ott, P. Riesterer, A. Prokop, K. Merz et al., *Chem. Sci.* **2012**, *3*, 2062–2072.

[53] H. H. Szeto, *AAPS J.* **2006**, *08*, E277-E283.

[54] K. L. Horton, K. M. Stewart, S. B. Fonseca, Q. Guo, S. O. Kelley, *Chem. Biol.*, *15*, 375–382.

[55] a) A. Bindoli, M. P. Rigobello, G. Scutari, C. Gabbiani, A. Casini, L. Messori, *Coord. Chem. Rev.* **2009**, *253*, 1692–1707; b) R. Rubbiani, I. Kitanovic, H. Alborzinia, S. Can, A. Kitanovic, L. A. Onambele, M. Stefanopoulou, Y. Geldmacher, W. S. Sheldrick, G. Wolber et al., *J. Med. Chem.* **2010**, *53*, 8608–8618.

[56] a) E. I. Edwards, R. Epton, G. Marr, *J. Organomet. Chem.* **1975**, *85*, C23; b) E. I. Edwards, R. Epton, G. Marr, *J. Organomet. Chem.* **1976**, *122*, C49; c) E. I. Edwards, R. Epton, G. Marr, *J. Organomet. Chem.* **1976**, *107*, 351–357; d) E. I. Edwards, R. Epton, G. Marr, *J. Organomet. Chem.* **1979**, *168*, 259–272.

[57] a) L. V. Snegur, V. N. Babin, A. A. Simenel, Y. S. Nekrasov, L. A. Ostrovskaya, N. S. Sergeeva, *Russ. Chem. Bull.* **2010**, *59*, 2167-2178; b) N. Metzler-Nolte, M. Salmain in *Ferrocenes* (Ed.: P. Štěpnička), John Wiley & Sons, Ltd, **2008**; c) D. R. van Staveren, N. Metzler-Nolte, *Chem. Rev.* **2004**, *104*, 5931–5986; d) E. A. Hillard, A. Vessières, G. Jaouen in *Topics in Organometallic Chemistry* (Eds.: G. Jaouen, N. Metzler-Nolte), Springer Berlin Heidelberg, **2010**.

[58] a) C. Choudhary, C. Kumar, F. Gnad, M. L. Nielsen, M. Rehman, T. C. Walther, J. V. Olsen, M. Mann, *Science* **2009**, *325*, 834–840; b) J. D. Best, N. Carey, *Drug Discov. Today* **2010**, *15*, 65–70.

[59] G. P. Delcuve, D. H. Khan, J. R. Davie, *Expert Opin. Ther. Targets* **2013**, *17*, 29–41.

[60] P. A. Marks, *Expert Opin. Invest. Drugs* **2010**, *19*, 1049–1066.

[61] a) P. A. Marks, R. Breslow, *Nat. Biotechnol.* **2007**, *25*, 84–90; b) B. S. Mann, J. R. Johnson, M. H. Cohen, R. Justice, R. Pazdur, *Oncologist* **2007**, *12*, 1247–1252.

[62] J. Spencer, J. Amin, M. Wang, G. Packham, S. S. S. Alwi, G. J. Tizzard, S. J. Coles, R. M. Paranal, J. E. Bradner, T. D. Heightman, *ACS Med. Chem. Lett.* **2011**, *2*, 358–362.

[63] J. Spencer, J. Amin, R. Boddiboyena, G. Packham, B. E. Cavell, S. S. Syed Alwi, R. M. Paranal, T. D. Heightman, M. Wang, B. Marsden et al., *Med. Chem. Commun.* **2012**, *3*, 61–64.

[64] J. R. Somoza, R. J. Skene, B. A. Katz, C. Mol, J. D. Ho, A. J. Jennings, C. Luong, A. Arvai, J. J. Buggy, E. Chi et al., *Structure* **2004**, *12*, 1325–1334.

[65] M. Librizzi, A. Longo, R. Chiarelli, J. Amin, J. Spencer, C. Luparello, *Chem. Res. Toxicol.* **2012**, *25*, 2608–2616.

[66] a) O. Gluz, C. Liedtke, N. Gottschalk, L. Pusztai, U. Nitz, N. Harbeck, *Ann. Oncol.* **2009**, *20*, 1913–1927; b) A. L. Gartel, C. Feliciano, A. L. Tyner, *Oncol. Res.* **2003**, *13*, 405–408; c) C. Luparello, F. David, G. Campisi, R. Sirchia, *Biol. Chem.* **2003**, *384*, 965–975.

[67] a) L. Huang, A. B. Pardee, *Mol. Med.* **2000**, *6*, 849–866; b) L. Xu, R. Tong, D. M. Cochran, R. K. Jain, *Cancer Res.* **2005**, *65*, 5711–5719; c) Y. Dai, M. Rahmani, P. Dent, S. Grant, *Mol. Cell. Biol.* **2005**, *25*, 5429–5444; d) P. Portanova, T. Russo, O. Pellerito, G. Calvaruso, M. Giuliano, R. Vento, G. Tesoriere, *Int. J. Oncol.* **2008**, *33*, 325–331; e) J. Li, R. Liu, Y. Lei, K. Wang, Q. C. Lau, N. Xie, S. Zhou, C. Nie, L. Chen, Y. Wei et al., *Autophagy* **2010**, *6*, 711–724; f) A. Yamamoto, Y. Tagawa, T. Yoshimori, Y. Moriyama, R. Masaki, Y. Tashiro, *Cell Struct. Funct.* **1998**, *23*, 33–42; g) Y.-L. Liu, P.-M. Yang, C.-T. Shun, M.-S. Wu, J.-R. Weng, C.-C. Chen, *Autophagy* **2010**, *6*, 1057–1065; h) N. Gammoh, Du Lam, C. Puente, I. Ganley, P. A. Marks, X. Jiang, *Proc. Natl. Acad. Sci. USA* **2012**, *109*, 6561–6565.

[68] C. Biot, N. François, L. Maciejewski, J. Brocard, D. Poulain, *Bioorg. Med. Chem. Lett.* **2000**, *10*, 839–841.

[69] C. T. Supuran in *Carbonic Anhydrase: Its Inhibitors and Activators* (Eds.: A. Scozzafava, C. T. Supuran, J. Conway), CRC Press, **2004**.

[70] C. T. Supuran, A. Scozzafava, *Bioorg. Med. Chem.* **2007**, *15*, 4336–4350.

[71] C. T. Supuran, A. Scozzafava, *Expert Opin. Ther. Pat.* **2000**, *10*, 575–600.

[72] C. T. Supuran, F. Briganti, S. Tilli, W. R. Chegwidden, A. Scozzafava, *Bioorg. Med. Chem.* **2001**, *9*, 703–714.

[73] A. J. Salmon, M. L. Williams, A. Hofmann, S.-A. Poulsen, *Chem. Commun.* **2012**, *48*, 2328–2330.

[74] A. J. Salmon, M. L. Williams, A. Innocenti, D. Vullo, C. T. Supuran, S.-A. Poulsen, *Bioorg. Med. Chem. Lett.* **2007**, *17*, 5032–5035.

[75] B. T. Loughrey, M. L. Williams, P. C. Healy, A. Innocenti, D. Vullo, C. T. Supuran, P. G. Parsons, S.-A. Poulsen, *J. Biol. Inorg. Chem.* **2009**, *14*, 935–945.

[76] a) U. Schatzschneider, N. Metzler-Nolte, *Angew. Chem. Int. Ed.* **2006**, *45*, 1504–1507; b) G. Jaouen, S. Top, A. Vessieres, G. Leclercq, M. J. McGlinchey, *Curr. Med. Chem.* **2004**, *11*, 2505–2517.

[77] M. Jung, D. E. Kerr, P. D. Senter, *Arch. Pharm. Pharm. Med. Chem.* **1997**, *330*, 173–176.

[78] I. Ott, B. Kircher, R. Gust, *J. Inorg. Biochem.* **2004**, *98*, 485–489.

[79] I. Ott, K. Schmidt, B. Kircher, P. Schumacher, T. Wiglenda, R. Gust, *J. Med. Chem.* **2005**, *48*, 622–629.

[80] a) D. J. E. Elder, A. Hague, D. J. Hicks, C. Paraskeva, *Cancer Res.* **1996**, *56*, 2273–2276; b) P. C. Elwood, A. M. Gallagher, G. G. Duthie, L. A. J. Mur, G. Morgan, *Lancet* **11**, *373*, 1301–1309; c) M. K. Jones, H. Wang, B. M. Peskar, E. Levin, R. M. Itani, I. J. Sarfeh, A. S. Tarnawski, *Nat. Med.* **1999**, *5*, 1418–1423.

[81] C. Waskewich, R. D. Blumenthal, H. Li, R. Stein, D. M. Goldenberg, J. Burton, *Cancer Res.* **2002**, *62*, 2029–2033.

[82] A. L. Blobaum, L. J. Marnett, *J. Med. Chem.* **2007**, *50*, 1425–1441.

[83] I. Ott, B. Kircher, C. P. Bagowski, D. H. W. Vlecken, E. B. Ott, J. Will, K. Bensdorf, W. S. Sheldrick, R. Gust, *Angew. Chem. Int. Ed.* **2009**, *48*, 1160–1163.

[84] H. Greenfield, H. W. Sternberg, R. A. Friedel, J. H. Wotiz, R. Markby, I. Wender, *J. Am. Chem. Soc.* **1956**, *78*, 120–124.

[85] S. D. Schimler, D. J. Hall, S. L. Debbert, *J. Inorg. Biochem.* **2013**, *119*, 28–37.

[86] K. Schmidt, M. Jung, R. Keilitz, B. Schnurr, R. Gust, *Inorg. Chim. Acta* **2000**, *306*, 6–16.

[87] A. Vessières, S. Top, C. Vaillant, D. Osella, J.-P. Mornon, G. Jaouen, *Angew. Chem.* **1992**, *104*, 790–792.

[88] R. F. Lockwood, K. M. Nicholas, *Tetrahedron Lett.* **1977**, *18*, 4163–4165.

[89] a) D. Osella, F. Galeotti, G. Cavigiolio, C. Nervi, K. I. Hardcastle, A. Vessières, G. Jaouen, *Helv. Chim. Acta* **2002**, *85*, 2918–2925; b) O. Kuhn, D. Rau, H. Mayr, *J. Am. Chem. Soc.* **1998**, *120*, 900–907.

[90] D. Osella, M. Ravera, C. Nervi, G. Cavigiolio, M. Vincenti, A. Vessieéres, G. Jaouen, *Eur. J. Inorg. Chem.* **2000**, *2000*, 491–497.

[91] I. Ott, R. Gust, *Biometals* **2005**, *18*, 171-177.

[92] A. J. Atkin, S. Williams, P. Sawle, R. Motterlini, J. M. Lynam, I. J. S. Fairlamb, *Dalton Trans.* **2009**, 3653–3656.

[93] G. Rubner, K. Bensdorf, A. Wellner, S. Bergemann, R. Gust, *Arch. Pharm. Pharm. Med. Chem.* **2011**, *344*, 684–688.

[94] C. D. Sergeant, I. Ott, A. Sniady, S. Meneni, R. Gust, A. L. Rheingold, R. Dembinski, *Org. Biomol. Chem.* **2008**, *6*, 73–80.

[95] I. Ott, T. Koch, H. Shorafa, Z. Bai, D. Poeckel, D. Steinhilber, R. Gust, *Org. Biomol. Chem.* **2005**, *3*, 2282–2286.

[96] G. Rubner, K. Bensdorf, A. Wellner, B. Kircher, S. Bergemann, I. Ott, R. Gust, *J. Med. Chem.* **2010**, *53*, 6889–6898.

[97] M. A. Neukamm, A. Pinto, N. Metzler-Nolte, *Chem. Commun.* **2008**, *0*, 232–234.

[98] a) B. Therrien in *Topics in Current Chemistry* (Eds.: M. Albrecht, E. Hahn), Springer Berlin Heidelberg, **2012**; b) B. Therrien, *Eur. J. Inorg. Chem.* **2009**, *2009*, 2445–2453; c) G. S. Smith, B. Therrien, *Dalton Trans.* **2011**, *40*, 10793–10800.

[99] Y. Matsumura, H. Maeda, *Cancer Res.* **1986**, *46*, 6387–6392.

[100] F. Schmitt, J. Freudenreich, N. P. E. Barry, L. Juillerat-Jeanneret, G. Süss-Fink, B. Therrien, *J. Am. Chem. Soc.* **2011**, *134*, 754–757.

[101] a) N. P. E. Barry, O. Zava, W. Wu, J. Zhao, B. Therrien, *Inorg. Chem. Commun.* **2012**, *18*, 25–28; b) B. Therrien, G. Süss-Fink, P. Govindaswamy, A. K. Renfrew, P. J. Dyson, *Angew. Chem. Int. Ed.* **2008**, *47*, 3773–3776.

[102] a) K. Suntharalingam, A. Łęczkowska, M. A. Furrer, Y. Wu, M. K. Kuimova, B. Therrien, White, Andrew J. P., R. Vilar, *Chem. Eur. J.* **2012**, *18*, 16277–16282; b) O. Zava, J. Mattsson, B. Therrien, P. J. Dyson, *Chem. Eur. J.* **2010**, *16*, 1428–1431.

[103] a) A. Pitto-Barry, N. P. E. Barry, O. Zava, R. Deschenaux, P. J. Dyson, B. Therrien, *Chem. Eur. J.* **2011**, *17*, 1966–1971; b) A. Pitto-Barry, N. P. E. Barry, O. Zava, R. Deschenaux, B. Therrien, *Chem. Asian J.* **2011**, *6*, 1595–1603.

[104] J. W. Yi, N. P. E. Barry, M. A. Furrer, O. Zava, P. J. Dyson, B. Therrien, B. H. Kim, *Bioconjugate Chem.* **2012**, *23*, 461–471.

[105] M. A. Furrer, F. Schmitt, M. Wiederkehr, L. Juillerat-Jeanneret, B. Therrien, *Dalton Trans.* **2012**, *41*, 7201–7211.

[106] A. Casini, G. Mastrobuoni, W. H. Ang, C. Gabbiani, G. Pieraccini, G. Moneti, P. J. Dyson, L. Messori, *ChemMedChem* **2007**, *2*, 631–635.

[107] A. Casini, C. Gabbiani, E. Michelucci, G. Pieraccini, G. Moneti, P. Dyson, L. Messori, *J. Biol. Inorg. Chem.* **2009**, *14*, 761-770.

[108] W. H. Ang, L. J. Parker, A. De Luca, L. Juillerat-Jeanneret, C. J. Morton, M. Lo Bello, M. W. Parker, P. J. Dyson, *Angew. Chem. Int. Ed.* **2009**, *48*, 3854–3857.

[109] W. H. Ang, A. De Luca, C. Chapuis-Bernasconi, L. Juillerat-Jeanneret, M. Lo Bello, P. J. Dyson, *ChemMedChem* **2007**, *2*, 1799–1806.

[110] H.-W. Lo, F. Ali-Osman, *Curr. Opin. Pharmacol.* **2007**, *7*, 367–374.

[111] G. Gasser, I. Ott, N. Metzler-Nolte, *J. Med. Chem.* **2011**, *54*, 3–25.

[112] K. N. Thimmaiah, J. K. Horton, R. Seshadri, M. Israel, J. A. Houghton, F. C. Harwood, P. J. Houghton, *J. Med. Chem.* **1992**, *35*, 3358–3364.

[113] C. A. Vock, W. H. Ang, C. Scolaro, A. D. Phillips, L. Lagopoulos, L. Juillerat-Jeanneret, G. Sava, R. Scopelliti, P. J. Dyson, *J. Med. Chem.* **2007**, *50*, 2166–2175.

[114] M. Melchart, P. J. Sadler in *Bioorganometallics* (Ed.: G. Jaouen), Wiley-VCH Verlag GmbH & Co. KGaA, **2006**.

[115] a) A. Kurzwernhart, W. Kandioller, C. Bartel, S. Bachler, R. Trondl, G. Muhlgassner, M. A. Jakupec, V. B. Arion, D. Marko, B. K. Keppler et al., *Chem. Commun.* **2012**, *48*, 4839–4841; b) A. Kurzwernhart, W. Kandioller, E. A. Enyedy, M. Novak, M. A. Jakupec, B. K. Keppler, C. G. Hartinger, *Dalton Trans.* **2013**, *42*, 6193–6202.

[116] A. Kurzwernhart, W. Kandioller, S. Bächler, C. Bartel, S. Martic, M. Buczkowska, G. Mühlgassner, M. A. Jakupec, H.-B. Kraatz, P. J. Bednarski et al., *J. Med. Chem.* **2012**, *55*, 10512–10522.

[117] W. F. Schmid, R. O. John, V. B. Arion, M. A. Jakupec, B. K. Keppler, *Organometallics* **2007**, *26*, 6643–6652.

[118] a) G. Mühlgassner, C. Bartel, W. F. Schmid, M. A. Jakupec, V. B. Arion, B. K. Keppler, *J. Inorg. Biochem.* **2012**, *116*, 180–187; b) V. B. Arion, A. Dobrov, S. Goschl, M. A. Jakupec, B. K. Keppler, P. Rapta, *Chem. Commun.* **2012**, *48*, 8559–8561.

[119] W. Ginzinger, G. Mühlgassner, V. B. Arion, M. A. Jakupec, A. Roller, M. Galanski, M. Reithofer, W. Berger, B. K. Keppler, *J. Med. Chem.* **2012**, *55*, 3398–3413.

[120] a) I. N. Stepanenko, A. Casini, F. Edafe, M. S. Novak, V. B. Arion, P. J. Dyson, M. A. Jakupec, B. K. Keppler, *Inorg. Chem.* **2011**, *50*, 12669–12679; b) I. N. Stepanenko, M. S. Novak, G. Mühlgassner, A. Roller, M. Hejl, V. B. Arion, M. A. Jakupec, B. K. Keppler, *Inorg. Chem.* **2011**, *50*, 11715–11728; c) L. Filak, G. Mühlgassner, M. Jakupec, P. Heffeter, W. Berger, V. Arion, B. Keppler, *J. Biol. Inorg. Chem.* **2010**, *15*, 903-918.

[121] C. S. Cutler, H. M. Hennkens, N. Sisay, S. Huclier-Markai, S. S. Jurisson, *Chem. Rev.* **2012**, *113*, 858–883.

[122] R. Dilworth, Jonathan, J. Parrott, Suzanne, *Chem. Soc. Rev.* **1998**, *27*, 43–55.

[123] R. Alberto, H. Braband in *Comprehensive Inorganic Chemistry II (Second Edition)* (Eds.: J. Reedijk, K. Poeppelmeier), Elsevier, Amsterdam, **2013**.

[124] S. R. Banerjee, J. W. Babich, J. Zubieta, *Chem. Commun.* **2005**, 1784–1786.

[125] C. L. Ferreira, S. R. Bayly, D. E. Green, T. Storr, C. A. Barta, J. Steele, M. J. Adam, C. Orvig, *Bioconjugate Chem.* **2006**, *17*, 1321–1329.

[126] a) C. C. Wykoff, Beasley, Nigel J. P., P. H. Watson, K. J. Turner, J. Pastorek, A. Sibtain, G. D. Wilson, H. Turley, K. L. Talks, P. H. Maxwell et al., *Cancer Res.* **2000**, *60*, 7075–7083; b) V. Alterio, M. Hilvo, A. Di Fiore, C. T. Supuran, P. Pan, S. Parkkila, A. Scaloni, J. Pastorek, S. Pastorekova, C. Pedone et al., *Proc. Natl. Acad. Sci. USA* **2009**, *106*, 16233–16238; c) D. Vullo, A. Innocenti, I. Nishimori, J. Pastorek, A. Scozzafava, S. Pastoreková, C. T. Supuran, *Bioorg. Med. Chem. Lett.* **2005**, *15*, 963–969.

[127] D. Can, B. Spingler, P. Schmutz, F. Mendes, P. Raposinho, C. Fernandes, F. Carta, A. Innocenti, I. Santos, C. T. Supuran et al., *Angew. Chem. Int. Ed.* **2012**, *51*, 3354–3357.

[128] C. T. Supuran, *Nat. Rev. Drug Discov.* **2008**, *7*, 168–181.

[129] a) F. W. Monnard, T. Heinisch, E. S. Nogueira, T. Schirmer, T. R. Ward, *Chem. Commun.* **2011**, *47*, 8238–8240; b) V. Akurathi, L. Dubois, N. G. Lieuwes, S. K. Chitneni, B. J. Cleynhens, D. Vullo, C. T. Supuran, A. M. Verbruggen, P. Lambin, G. M. Bormans, *Nucl. Med. Biol.* **2010**, *37*, 557–564.

[130] Rimmer, R. Dale, H. Richter, P. C. Ford, *Inorg. Chem.* **2009**, *49*, 1180–1185.

2 Caged Phosphate and the Slips and Misses in Determination of Quantum Yields for UV-A Induced Photouncaging

*Philipp Anstaett,[a] Anna Leonidova[a] and Gilles Gasser[a]**

[a] Department of Chemistry, University of Zurich, Winterthurerstrasse 190, CH-8057 Zurich, Switzerland.

* Corresponding author: e-mail: gilles.gasser@chem.uzh.ch; Fax: +41 44 635 46 03; Tel: +41 44 635 46 30; homepage: http://www.gassergroup.com.

This chapter has been accepted for publication in *ChemPhysChem* (DOI: 10.1002/cphc.201402547). Copyright © 2014 WILEY-VCH Verlag GmbH & Co. KGaA, Weinheim. Reproduced with permission.

A commentary[1] and a reply to it[2] were published afterwards to further elaborate the topic.

2.1 Contributions to the publication

P.A. designed the experiments, and carried them out together with A.L. The first draft of the manuscript was written by P.A.

2.2 Abstract

The quantum yields for uncaging reactions are in most cases determined relative to other uncaging reactions, often of 1-(2-nitrophenyl)ethyl-phosphate ("caged phosphate"). Herein, we demonstrate that the quantum yields acquired using this method can be off by an order of magnitude at the typical irradiation wavelengths around 350 nm and describe an easy-to-use alternative procedure using inexpensive azobenzene.

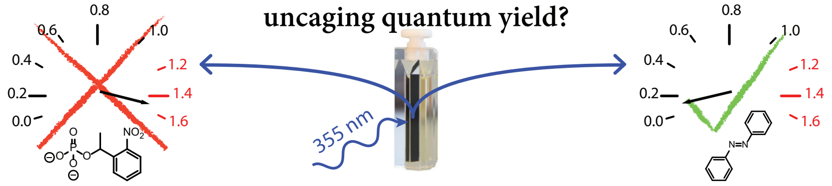

Keywords: Azo compounds • Caged compounds • Photochemistry • Photouncaging • Quantum Yield.

2.3 Article

The release of bioactive compounds upon light irradiation has been coined "uncaging". The method has been extensively applied, especially for studies on molecular processes in biology.[3] One of the first demonstrations of this technique was the uncaging of adenosine triphosphate (ATP) for studying the Na:K pump of human red blood cell ghosts.[4] However, although caging substances has since become an established method, the determination of uncaging efficiencies is still not trivial. Even today, more than 30 years later, reports on convenient methods to determine these quantum yields are being published.[5] Standard actinometry protocols which utilize for example ferrioxalate[6] or phenylglyoxylic acid[7] for determining the total number of photons reaching the sample can be employed. However, they often require several milliliters of concentrated solutions. More conveniently, the photolysis rate of the caged compound in question and of a caged compound with a known quantum yield can be compared without having to calculate the total photon flux. The advantage is that no compromise on the technical setup has to be made regarding volume or dilution of sample and reference. Caged compounds are often the result of a tedious synthesis and, therefore, are used as sparingly as possible. When using other caged compounds for comparison purposes, both reference and sample can be measured in small-volume cuvettes and in highly dilute solutions. Plots of the percentage of remaining cage against the irradiation time/dose can then be used to compute the uncaging quantum yields by multiplying the quotient of the slopes with the known quantum yield of the reference molecule. To this end, 1-(2-nitrophenyl)ethyl-phosphate ("caged phosphate")[4] or 1-(2-nitrophenyl)ethyl-ATP ("caged ATP")[4,8] have been extensively used (Figure 1 a). The quantum yield of caged phosphate has been reported to be 0.54 ± 0.04 as the average of two measurements with individual values of 0.50 and 0.58,[4] referencing to ferrioxalate actinometry.[9] The illumination setup featured a light source with a peak wavelength of 342 nm and half-bandwidth of 60 nm. For caged ATP, a quantum yield of 0.63 has been reported using a 150 W xenon arc lamp with a Corning 9863 glass band-pass filter (300–350 nm),[8] referencing to caged phosphate.[4] The choice of the reference compound depends therefore on the irradiation wavelength one wishes to apply. Caged ATP is used as reference for irradiation at 313 nm.[5] Caged phosphate in phosphate buffered saline (PBS) has often been used as a reference for the determination of uncaging quantum yields around an irradiation wavelength of 350 nm, for example when using a Rayonet photo-reactor with light bulbs emitting at a center wavelength of 350 nm and a half-bandwidth of approximately 36 nm (see Figure S1 in the Supporting Information, SI, for an emission spectrum).[10,11,12] It has been assumed that caged phosphate has the same uncaging quantum yield under these irradiation conditions as at 342 nm (*vide supra*).[4] To the best of our knowledge, no uncaging action spectrum of caged phosphate has been determined. However, the uncaging action spectrum of the caged ATP, which relies on the same photocaging group, shows a difference of approximately 30% between 342 nm and 355 nm (Figure 2).[13,14] It therefore appears questionable if the quantum yield at 350 nm is the same as at 342 nm. Furthermore, data presented by Baldwin and coworkers suggest that the photolysis of caged phosphate at 308 or 355 nm gave a significantly lower quantum yield,[15] *i.e.* the maximum amount of released phosphate upon photolysis, compared to the value by Kaplan and coworkers upon irradiation at around 342 nm.[4] Taking these findings into consideration, a proper determination of the uncaging quantum yield of caged phosphate upon irradiation at around 350 nm is missing.

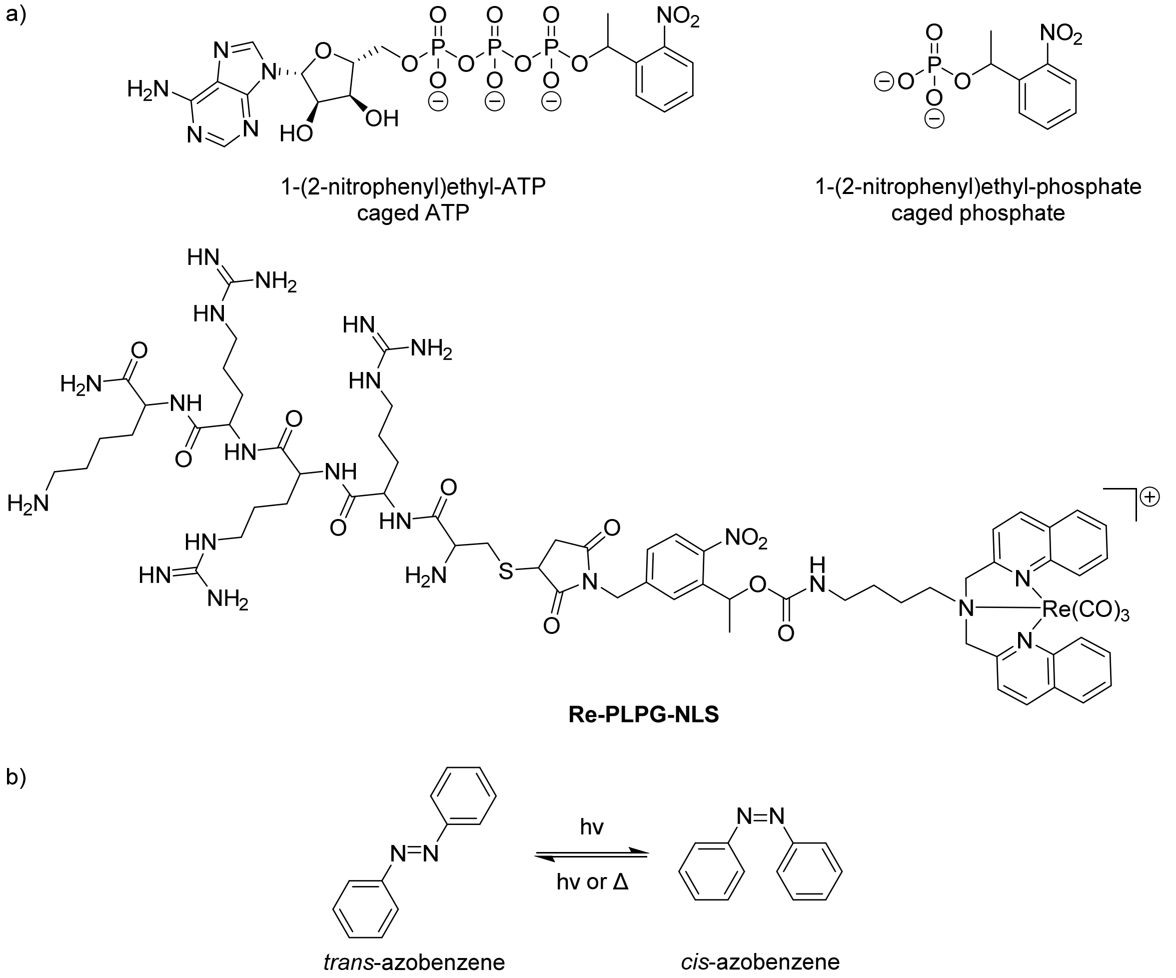

Figure 1. a) Caged compounds used in this study. Caged ATP and caged phosphate are often used as references for the determination of uncaging quantum yields. **Re-PLPG-NLS** is a recently reported caged compound with cytotoxic activity upon light irradiation;[16] b) *trans-cis* isomerization of azobenzene. The process can be monitored by UV/Vis spectroscopy or analytical HPLC with UV detection.

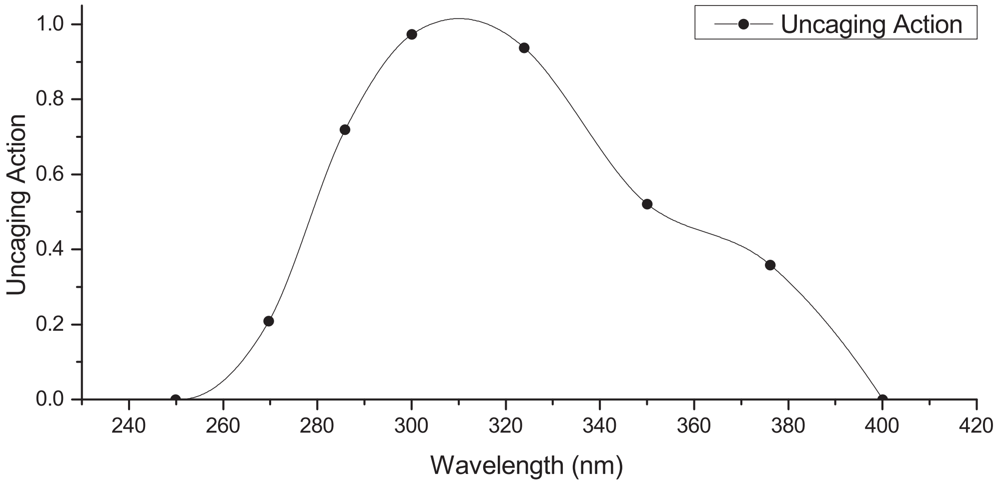

Figure 2. Normalized uncaging action spectrum of caged ATP. General conditions: pH=7.4, 200 W mercury lamp equipped with a monochromator, amount of free ATP determined by a luciferase assay. Adapted from [14], copyright 1998, with permission from Elsevier.

To evaluate the uncaging quantum yield of caged phosphate upon irradiation around 350 nm, experiments using ferrioxalate as reference were carried out. To gain the most precise and transferable data possible, measurements were performed using a Nd:YAG laser frequency-tripled to emit at 355 nm which was part of a laser flash photolysis spectrometer. Such setups have been used for the investigation of uncaging processes.[8,17,18,19] The monochromatic light has the advantage of being more reproducible between setups of different research groups. Using a standard ferrioxalate actinometry procedure,[20] the total photon flux per laser shot was hence determined. Based on this, the fraction of photons absorbed by the caged compound, and the rate of uncaging of caged phosphate, the uncaging quantum yield of the latter was calculated. It was found to be merely 0.04, only 8% of the assumed 0.54.

An additional referencing system based on azobenzene was designed to verify the low quantum yield. The *cis*-*trans* isomerization of azobenzene is a known actinometer in methanol (Figure 1 b) and it has been used before for the determination for uncaging quantum yields, but at other wavelengths and without description of the exact protocol.[12,21] Depending on the irradiation wavelength used, complicated mathematical procedures are required to determine the photon flux.[20,22,23] At wavelengths greater than approximately 340 nm, there is no total absorption of all photons due to insufficiently low molar absorptivity of both azobenzene isomers and hence, the total photon flux cannot be determined directly. However, we found that a protocol based on the irradiation of a dilute solution of azobenzene can be applied (see SI for details). This protocol can generally be adapted for the determination of uncaging quantum yields. Shortly, dilute solutions of *trans*-azobenzene and the caged compound in question were separately irradiated under identical conditions with the laser at 355 nm. Subsequent comparison of the reaction rates leads directly to the quantum yield for the uncaging process, similarly to and with the same advantages as using another caged compound as reference (*vide supra*). As an additional benchmark the total photon flux was determined based on the isomerization of azobenzene under consideration of the fraction of absorbed photons. The procedure leads, within the typical error range of 10%,[4,5,24,25] to the same total photon flux as ferrioxalate. For the determination of the photo-uncaging quantum yields the total number of photons is not required, in contrast to the ferrioxalate method. The quantum yields of uncaging processes can be easily computed by direct comparison of the uncaging rate with the isomerization rate of solutions with the same optical densities. The resulting uncaging quantum yield for caged phosphate relative to azobenzene is 0.036 and therefore in line with the values obtained using ferrioxalate actinometry.

The current literature does not offer a straight-forward explanation for this drastic difference. To shed some light on possible reasons the uncaging quantum yield of caged ATP was determined in the same way and found to be 0.02. Based on the uncaging action spectrum of caged ATP (Figure 2) and the uncaging quantum yield at 313 nm,[8] again a more than tenfold higher quantum yield was expected. As result of these findings, we suspect that shorter wavelength light in the originally used broadband light source led to faster uncaging and therefore overestimation of the quantum yield of caged phosphate. As caged ATP was referenced to it, the inaccuracy was carried on. In order to avoid such problems monochromatic light sources, which are nowadays ubiquitous, should be used for the determination of quantum yields.

Recently, our group started investigating the uncaging of inert bioactive metal complexes.[16,26] To illustrate the dramatic effect that the above findings have on the determination of uncaging quantum yields of new compounds, solutions of the caged compound **Re-PLPG-NLS** (see Figure 1 a) in PBS were tested against caged phosphate, ferrioxalate, and the azobenzene protocol (Table 1). Caged phosphate was used for irradiation with the laser setup at 355 nm as well as the often used Rayonet UV-reactor setup with a center wavelength of 350 nm (*vide supra*). In both cases, **Re-PLPG-NLS** was uncaging approximately three times as fast as caged phosphate. This would correspond to an uncaging quantum yield of 1.62 in the UV-reactor and 1.39 with the laser setup (Table 1, Entries A and B), respectively. With today's understanding of the nitrobenzyl-uncaging mechanism, it is physically impossible to achieve uncaging quantum yields greater than 1.[7,8,11,18,19,21,27] The moderate difference between the two values obtained relative to ferrioxalate or azobenzene can be explained by two reasons:1) The presence of shorter wavelength light in the emission spectrum of the UV-reactor; these photons are very likely more efficiently inducing uncaging (compare Figure 2); 2) the inherently low accuracy in quantum yield determinations; errors of 10-20% are generally accepted.[4,5,24] The ferrioxalate and azobenzene methods were only applied upon laser irradiation at 355 nm, as the broad emission spectrum of the UV reactor inevitably leads to errors such as 1). Using the ferrioxalate method,[20] a quantum yield of merely 0.11 for **Re-PLPG-NLS** was determined (Table 1, Entry C). Similarly, the azobenzene protocol led to an uncaging quantum yield of 0.10 (Table 1, Entry D). In summary, the quantum yield obtained with caged phosphate as reference deviates more than tenfold from the actual values.

Table 1. Quantum yield of **Re-PLPG-NLS** relative to different reference molecules.

Entry	Irradiation Condition[a]	Reference Molecule	Corresponding Quantum Yield
A	UV	Caged phosphate	1.62
B	Laser	Caged phosphate	1.30
C	Laser	Ferrioxalate	0.11
D	Laser	Azobenzene	0.10

[a] For detailed experimental descriptions corresponding to the indicated irradiation conditions, see SI. In short, UV reactor: Rayonet RMR-200 photo reactor, light bulbs with peak wavelength of 350 nm; laser: Nd:YAG laser frequency-tripled to 355 nm. All experiments were carried out in PBS except for the azobenzene experiments, which were carried out in methanol.

The herein described azobenzene protocol is experimentally very convenient. Its flexibility regarding the concentration of the used solutions and the fractions of irradiated solution, for example due to different flask geometries, was investigated. To this end, measurements in different cuvettes, *i.e.* with different path lengths and window sizes, were compared (see SI for details). It was found that the relative uncaging rates of azobenzene and the caged compounds were, as expected, independent from the absolute concentration and fraction of irradiated solutions, as long as the conditions were identical for all samples. The azobenzene-based protocol for the acquisition of uncaging quantum yields therefore combines the experimental ease of relative methods (referencing to other caged compounds) with the precision of experimentally inflexible absolute methods (actinometers like ferrioxalate). It should be noted however, that the temperature should not exceed typical room temperatures to avoid temperature-induced isomerization of azobenzene.[22]

In summary, we could demonstrate using two independent protocols, that caged phosphate, although frequently used by scientists working with caged compounds, is not an appropriate reference for the determination of uncaging quantum yields around 350 nm using the literature value reported at 342 nm. Comparison of the values obtained for **Re-PLPG-NLS** with caged phosphate and with two other references showed a more than tenfold deviation.

Caged ATP showed the same trend as caged phosphate at an irradiation wavelength of 355 nm. To obtain the correct uncaging quantum yields, a protocol based on the well-understood photochemical *cis-trans* isomerization of azobenzene can be applied. This protocol allows for convenient, inexpensive, and accurate determination of uncaging quantum yields for irradiation wavelengths around 355 nm. Given the great popularity of cage compounds in chemical biology and this wavelength range for studying them, the presented findings will undoubtedly have an important impact on this research field.

2.4 Acknowledgements

This work was supported by the Swiss National Science Foundation (Professorship N° PP00P2_133568 and Research Grants N° 200021_129910 and N° 200020_146776 to G.G.), the University of Zurich (G.G.) and the Stiftung für Wissenschaftliche Forschung of the University of Zurich (G.G.).

2.5 Supporting Information

2.5.1 Materials and Instrumentation

UV/Vis spectroscopy was performed on PerkinElmer Lambda 25 and Varian Cary 100 instruments. ^{1}H and ^{13}C NMR spectra were recorded on Bruker Avance (400 and 500) spectrometers. ^{13}C NMR measurements were carried out as ^{13}C {H}. NMR spectra were referenced to the residual solvent signal. HPLC measurements were performed on a VWR Hitachi Chromaster system with 5110 pump, 5210 autosampler, 5310 column oven, and 5430 diode array detector. The method was run on a Macherey-Nagel EC 250/3 NUCLEOSIL 100-5 C18 with a flow of 1mL min^{-1}, 0.1% TFA in water : acetonitrile, 0 min: 90:10, 27 min: 0:100, 31 min: 0:100, 36 min: 99:1, 38 min: 99:1, 40 min: 90:10, 41 min: 90:10. LC-MS spectra were measured on an Acquity from Waters system equipped with a PDA detector and an auto sampler coupled to a Bruker Daltonics HCT 6000 mass spectrometer. LC-MS was run using an Agilent Zorbax 300SB-C18 analytical column (3.5 µm particle size, 300 Å pore size, 150 × 4.6 mm). The LC run (flow rate: 0.5 mL min^{-1}) was performed with a linear gradient of A (double distilled water containing 0.1% v/v formic acid) and B (acetonitrile containing 0.1% v/v formic acid); t = 0 min, 5% B; t=3 min, 5% B; t=17 min, 100% B; t=20 min, 100% B; t = 25 min, 5% B. Experiments in the UV-reactor were undertaken in a Rayonet RMR-200 photo-reactor, using 6 bulbs emitting around 350 nm (see Figure S1 for a detailed emission spectrum). The irradiation power was checked with an X11 optometer (Gigahertz-Optik) and determined to be 42 W m^{-2} at the center of the reactor. The temperature inside the reactor was 30 °C. Experiments with laser irradiation were undertaken using an Edinburgh Instruments LP920 laser flash photolysis setup with a Continuum Surelight Nd:YAG laser, frequency-tripled to generate monochromatic (i.e. bandwidth of less than 1 nm) light with a wavelength of 355 nm. The laser was slightly misaligned to reach a suitable irradiation power. As every misalignment results in a slightly different amount of photons reaching the sample, measurements belonging together were performed on the same day.

All used solvents were HPLC grade, water was doubly distilled. 1-(2-nitrophenyl)ethyl-phosphate ("caged phosphate") was prepared as described in the literature.[28] The analytical data matched what was reported before.[4,28] Potassium trioxalatoferrate(III) trihydrate ("ferrioxalate") was purchased from Alfa Aesar, 1,10-phenantroline (anhydrous, 99%) from ABCR (Germany), sodium acetate (anhydrous, 98.5%) from Fluka (Switzerland), sulfuric acid (95-97%) from Merck (Germany), NPE-caged-ATP (10 mM in H_2O) from Jena Bioscience GmbH (Germany), azobenzene (ANALPEST quality) from Sigma-Aldrich

(Switzerland). The purity, especially the absence of the *cis* isomer was checked by ^{1}H and ^{13}C NMR spectroscopy and HPLC (see below). All commercial chemicals were used without further purification. All experiments were performed in triplicate at room temperature, except for the ones in the UV-reactor (see above).

Additional analytical data for *trans*-azobenzene: $\varepsilon(\lambda = 236\ \text{nm}) = 9581 \pm 233\ \text{M}^{-1}\text{cm}^{-1}$, $\varepsilon(\lambda = 355\ \text{nm}) = 2992 \pm 89.4\ \text{M}^{-1}\text{cm}^{-1}$. HPLC: $t_R = 18.23$ min.

Additional analytical data for *cis*-azobenzene: HPLC: $t_R = 13.26$ min.

2.5.2 Methods

Table of Variables and Units

In all equations consistent units have to be used. The units below only represent a few of the possible choices.

Table S1. Overview over variables, their meaning, and their associated units.

Variable	Representing…	Exemplary Units
A	Area of peak	%, mAU s
k	"Rate constant"	s^{-1}, J^{-1} cm²
x	Irradiation dose or time	s, min, J cm^{-2}, laser shots
ϕ	Quantum yield	Dimensionless
D	Absorbed light dose	J, J cm^{-2}
λ	Wavelength	nm
E_λ	Emission intensity at wavelength λ	Dimensionless (relative), J cm^{-2}
F	Fraction of absorbed photons	Dimensionless
A_λ	Absorbance at wavelength λ	%, mAU
N	Amount of substance	Mol
V	Volume	L
l	Length (of path through cuvette)	cm

UV-Reactor Experiments

The caged compound solutions were prepared by starting from 20 mM DMSO stock solutions, and diluting them with “Dulbecco’s PBS modified, without calcium and magnesium” (PAA Laboratories GmbH, Pasching/Austria, part of GE Healthcare, pH=7.2) to an OD(λ=350 nm)=0.2. The solutions were placed in a fluorescence cuvette (1x1 cm) at the center of the reactor and irradiated for certain time intervals. The progress of the uncaging reaction was monitored by LC-MS analysis and integration of the corresponding peak of the UV chromatogram. The percentage of remaining caged compound was plotted as a function of irradiation dose and was fitted by a single exponential (first order kinetics law):

$$A = A_0 \times e^{-kx}$$

with A being the area of the peak after irradiation dose x, A_0 being the area before the irradiation, k being the coefficient defining the rate of the process, and x being the irradiation dose or time (see Figure S6 and Figure S7). Either the time or dose has to be chosen for all calculations. The initial slopes of the fitted curves were determined because there no competing chromophores, i.e. the products of the reaction, influence the reaction. The slope is used to calculate the quantum yields by the following formula:

$$\phi_{sample} = \phi_{reference} \times \frac{slope_{sample}}{slope_{reference}} \times \frac{D_{reference}}{D_{sample}}$$

with ϕ being the corresponding quantum yields, and D being the respective absorbed light doses:

$$D = \int E_{\lambda} \times F \, d\lambda$$

with E_{λ} being the wavelength dependent emission intensity of the light source (see Figure S1) and F being the fraction of absorbed photons as defined by:

$$F = 1 - 10^{-A_{\lambda}}$$

with A_{λ} being the absorbance at wavelength λ.

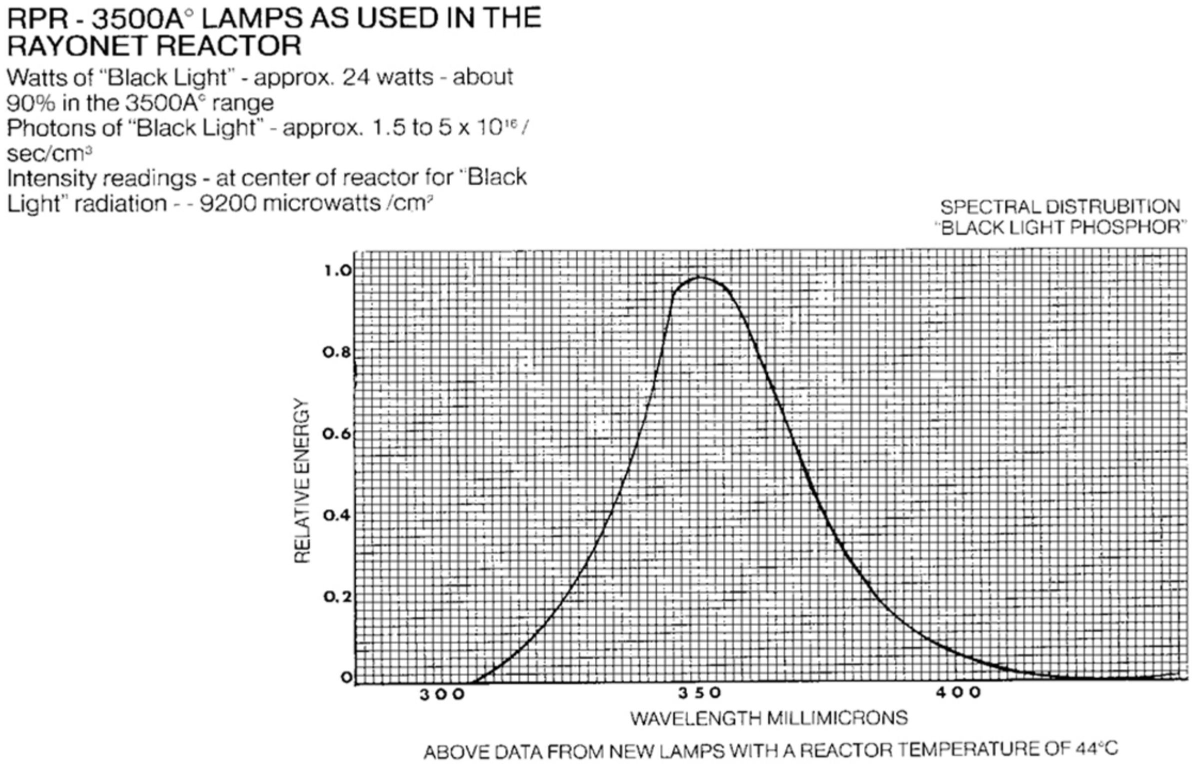

RPR - 3500A° LAMPS AS USED IN THE RAYONET REACTOR

Watts of "Black Light" - approx. 24 watts - about 90% in the 3500A° range
Photons of "Black Light" - approx. 1.5 to 5 x 10^{16}/ sec/cm^3
Intensity readings - at center of reactor for "Black Light" radiation - - 9200 microwatts /cm^2

ABOVE DATA FROM NEW LAMPS WITH A REACTOR TEMPERATURE OF 44°C

Figure S1. Normalized emission spectrum of UV lamps. Reprinted with permission from Southern New England Ultraviolet Co Inc., Branfort, CT, USA.

Laser Experiments

500 µL of sample solutions with an OD(λ=355 nm)=0.2 along the 0.2 cm path of a Starna 28F/Q/10 cuvette (2x10 mm fluorescence cuvette, 700 µL maximum volume) were irradiated for certain time intervals, characterized by a certain number of laser shots. The progress of the uncaging reaction was monitored as described above for **RE-PLPG-NLS**, caged phosphate, and caged ATP, except for the following. As lower conversion points could be monitored by this irradiation method, linear fits of the decomposition of the first 20% were sufficient to determine the uncaging rates. Exponential fits were not needed. The monitoring of ferrioxalate and azobenzene was done as described below.

The following procedure can be used to calculate the uncaging quantum yields if 1) the same cuvette with 2) the same filling level for all measurements (to ensure the same fraction of molecules being irradiated) and 3) the graphs have been brought to the same units (e.g. percent of remaining caged compound or amount of converted compound (in moles)):

$$\phi_{sample} = \phi_{reference} \times \frac{slope_{sample}}{slope_{reference}} \times \frac{F_{reference}}{F_{sample}}$$

with F being the fraction of absorbed photons by the corresponding substance. For ferrioxalate actinometry experiments described herein, $F_{reference} = 1$. For dilute samples, the fraction of absorbed photons F is defined as described in the UV-reactor section. Consequently, the factor $\frac{F_{reference}}{F_{sample}} = 1$ if the absorbances of the reference and the sample are identical at λ=355 nm.

Ferrioxalate Actinometry

Ferrioxalate actinometry was performed as described by Montalti.[20] In short, 3.00 mL of a ferrioxalate solution (0.012 M in 0.05 M H_2SO_4) were irradiated in a fluorescence cuvette (10x10 mm, 3.5 mL volume, Starna 23/Q/10) as described above. Less than 10% of the ferrioxalate complex should be destroyed during the irradiation. 0.50 mL of a 1,10-phenanthroline (0.1 weight-% in acetate buffer made from 225 g sodium acetate trihydrate / 1 L 0.5 M H_2SO_4) were added and the solution well mixed. Absorbance at 510 nm was directly measured. All data points were acquired as triplicates, plotted against the irradiation amount, and fitted with a linear function (see Figure S8).

In the following, the calculation of the total photon flux in general is described and exemplified with the data presented in Figure S8. The slope of the fitting function ($\Delta A_{510\,nm}$) was used to determine the amount of freed Fe^{2+} per laser shot:

$$\frac{n(Fe^{2+})}{laser\ shot} = \frac{V \times \Delta A_{510\,nm}}{l \times \varepsilon_{510\,nm}} = \frac{0.00350\,L\ \times 0.02712}{1\,cm\ \times 11100\,\frac{L}{mol \times cm}} = 8.55 \times 10^{-9} mol$$

with V being the volume of solution taken for determination of the absorbance, l being the path length of the cuvette, and $\varepsilon_{510\,nm}$ being the molar absorptivity of $Fe(phen)_3^{2+}$ at λ=510 nm. The number of photons per laser shot is then:

$$\frac{n(h\nu)}{laser\ shot} = \frac{n(Fe^{2+})}{laser\ shot\ \times\ \phi} = \frac{8.55 \times 10^{-9} mol}{1.25} = 6.84 \times 10^{-9} mol$$

with ϕ being the quantum yield of the Fe^{2+} production at 355 nm, which is 1.25.

Azobenzene Actinometry

trans-Azobenzene was dissolved in methanol to a concentration of 3.36x10^{-4} M. The absorbance of the solution was determined in a Starna 28F/Q/10 cuvette (2x10 mm fluorescence cuvette, 700 µL maximum volume) to be OD(λ=355 nm)=0.20. 500 µL ($n(azobenzene) = 1.68 \times 10^{-7}\ mol$) of the solution were irradiated. All data points were acquired as triplicates, plotted against the irradiation amount, and fitted with a linear function (Figure S9).

The slope of the fitting function was determined to be 5.19796×10^{-4}. Consequently, a fraction of

$$\frac{5.19796 \times 10^{-4}}{0.200} = 0.00260 = 0.260\%$$

of *trans*-azobenzene was converted to *cis*-azobenzene with each laser shot. The backwards reaction of *cis*-azobenzene to *trans*-azobenzene can be neglected, as less than the first 10% of conversion have been taken into account and the absorbance of *cis*-azobenzene is significantly lower at λ=355 nm than the absorbance of *trans*-azobenzene. This hypothesis is generally correct as long as the reaction rate does not change over time, i.e. the plotted curve remains linear. The amount of generated *cis*-azobenzene is given by:

$$n(cis\text{–}\,azobenzene) = (fraction\ of\ azobenzene\ converted) \times n(azobenzene)$$
$$= 0.00260 \times 1.68 \times 10^{-7} mol = 4.37 \times 10^{-10} mol$$

with $n(azobenzene)$ being the total amount of azobenzene. The fraction of absorbed photons F is:

$$F = 1 - 10^{-A_{350\,nm}} = 1 - 10^{-0.200} = 0.370$$

The amount of photons can then simply be expressed as:

$$\frac{n(hv)}{laser\ shot} = \frac{n(cis - azobenzene)}{\phi_{\ trans\rightarrow cis} \times F} = \frac{4.37 \times 10^{-10} mol}{0.15 \times 0.370} = 7.89 \times 10^{-9} mol$$

with $\phi_{\ trans\rightarrow cis}$ being the quantum yield for the *trans*→*cis* photoisomerization, which can be assumed to be 0.15 between 334 and 365 nm.[20]

Comparison of Ferrioxalate and Azobenzene Actinometry

The mean value of the azobenzene and ferrioxalate measurements for the determination of photon flux is 7.36x10^{-9} (±10%).

Comparison for Azobenzene Referencing for the Use of Different Cuvettes and Concentrations

Measurements for azobenzene-isomerization and uncaging of caged phosphate were repeated in a 100 µL cuvette (1 cm x 0.2 cm, Hellma 105.202-QS). The absorbance was adjusted to OD(λ=355 nm)=0.2 along the 1 cm path and irradiation took place along the 2 mm path length. The sample concentrations were thus lower by a factor of 5, compared to the measurements described above, due to the different path lengths in absorbance measurements. Due to the smaller total sample volume, the fraction of actually irradiated azobenzene molecules is greater than in the case of the 700 µL cuvette. Consequently, the isomerization rate differed from the previous measurements by a factor of 3. However, the ratio between the uncaging rate of caged phosphate and the isomerization of azobenzene remained constant, and hence the determined uncaging quantum yield for caged phosphate did not change either.

2.5.3 UV/Vis Spectroscopy

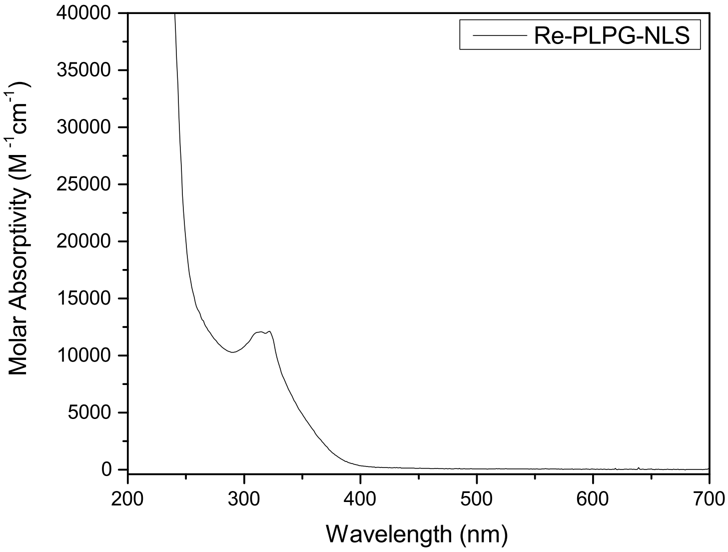

Figure S2. UV/Vis spectrum of Re-PLPG-NLS in phosphate buffered saline.

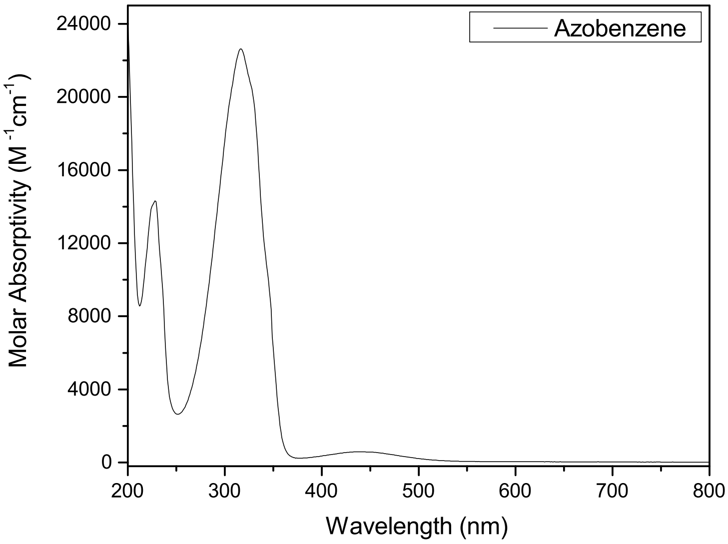

Figure S3. UV/Vis spectrum of *trans*-azobenzene in methanol.

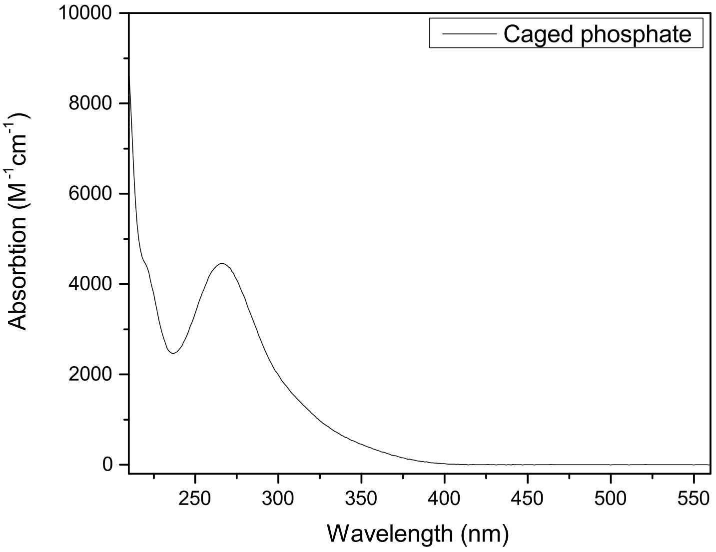

Figure S4. UV/Vis spectrum of caged phosphate in phosphate buffered saline.

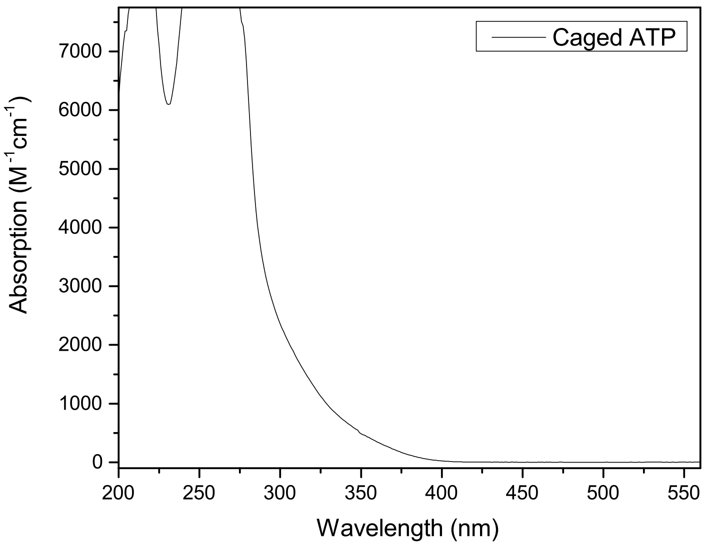

Figure S5. UV/Vis spectrum of caged ATP in phosphate buffered saline.

2.5.4 Representative Uncaging Graphs

A representative graph for uncaging of **Re-PLPG-NLS** relative to azobenzene upon laser irradiation has recently been published by our group.[16]

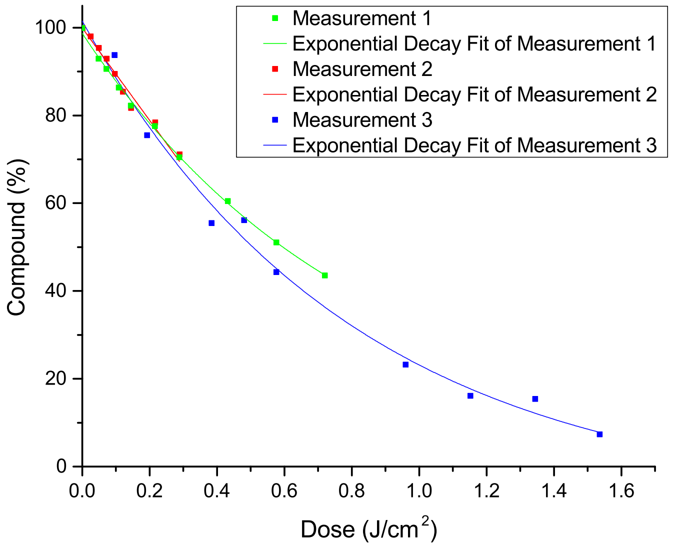

Figure S6. Percentage of remaining caged phosphate as a function of light dose. The data was acquired by irradiation with the UV reactor.

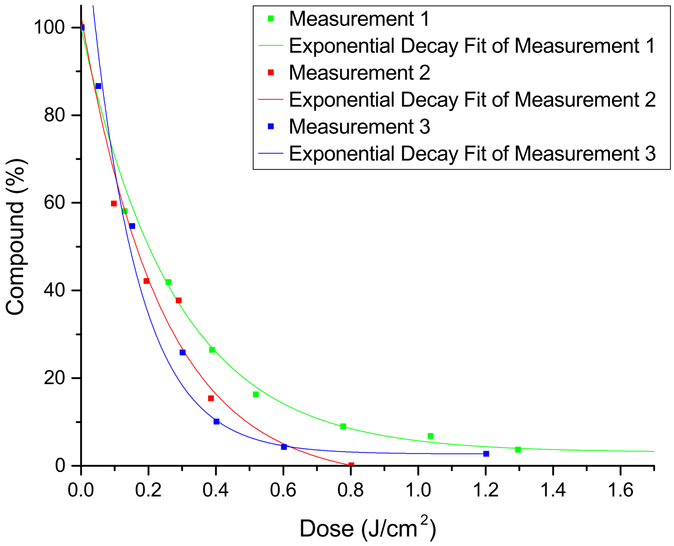

Figure S7. Percentage of remaining Re-PLPG-NLS as function of light dose. The data was acquired by irradiation with the UV reactor.

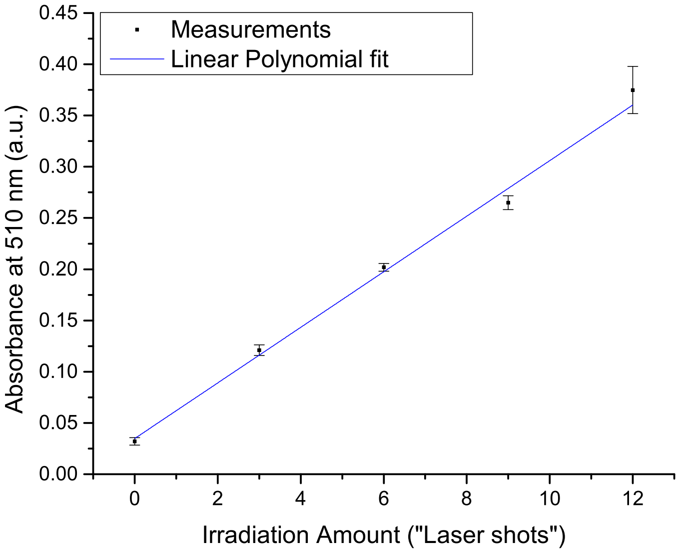

Figure S8. Absorbance at 510 nm, attributable to Fe(phen)$_3$, as function of irradiation amount. The data was acquired by irradiation with the laser. Values for the fit: $A_{510\,nm} = 0.0348 + 0.02712 \times (irradiation\ amount)$. R²=0.99, error for intercept: 0.00521, error for slope: 0.00107.

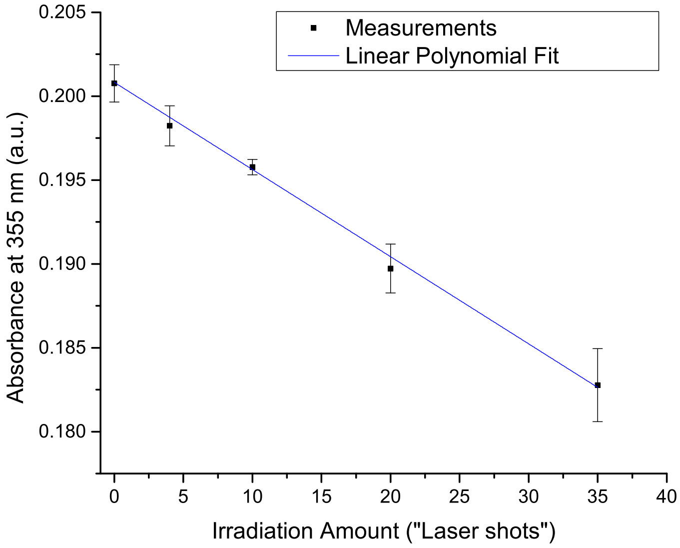

Figure S9. Absorbance at 355 nm, attributable to *trans*-azobenzene, as function of irradiation amount. The data was acquired by irradiation with the laser. Values for the fit: $A_{355\,nm} = 0.20083 - 5.19796 \times 10^{-4} \times (irradiation\ amount)$. R²=0.99. Error for intercept: 2.9205×10^{-4}, error for slope: 2.48257×10^{-5}.

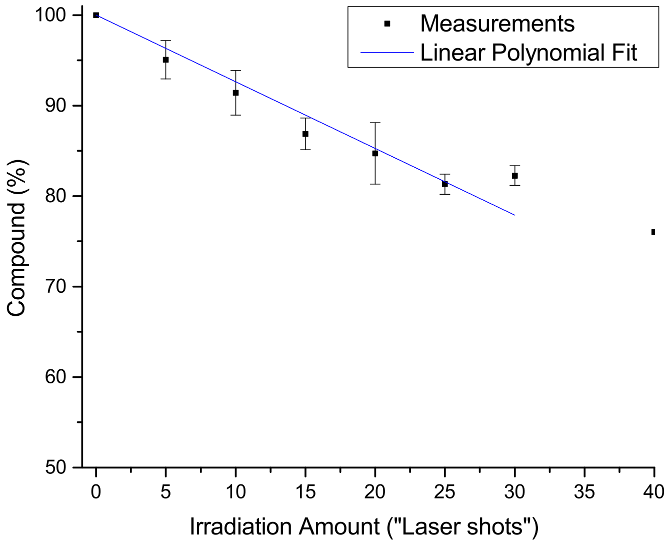

Figure S10. Percentage of remaining caged phosphate as a function of irradiation amount. The data was acquired by irradiation with the laser. Note, that this graph has been acquired on a different day using a different laser power than the exemplary graphs for azobenzene and ferrioxalate depicted above. Values for the fit: $Compound(\%) = 100 - 0.73693 \times (irradiation\,amount)$. R²=0.99. The intercept was fixed to 100, error for slope: 0.04031.

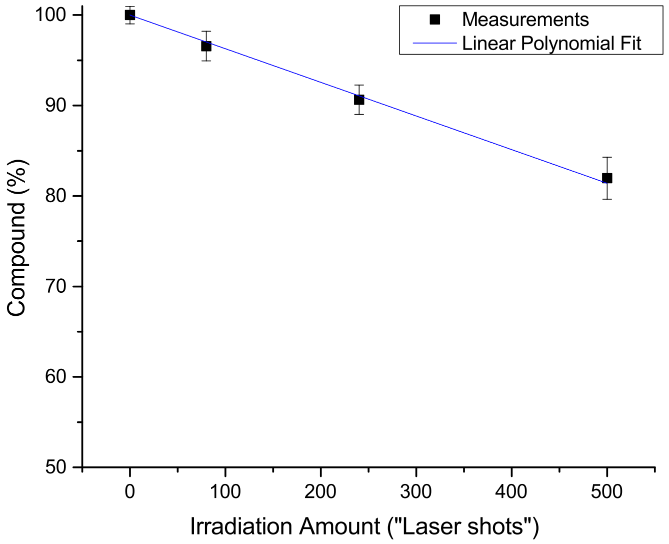

Figure S11. Percentage of remaining caged ATP as a function of irradiation amount. The data was acquired by irradiation with the laser. Note, that this graph has been acquired on a different day using a different laser power than the exemplary graphs for azobenzene and ferrioxalate depicted above. Values for the fit: $Compound(\%) = 100 - 0.03719 \times (irradiation\,amount)$. R²=0.99. The intercept was fixed to 100, error for slope: 0.0009947.

The following graphs have been acquired pairwise on the same day with the same laser power and are thus directly comparable (S12 with S13 and S14 with S15).

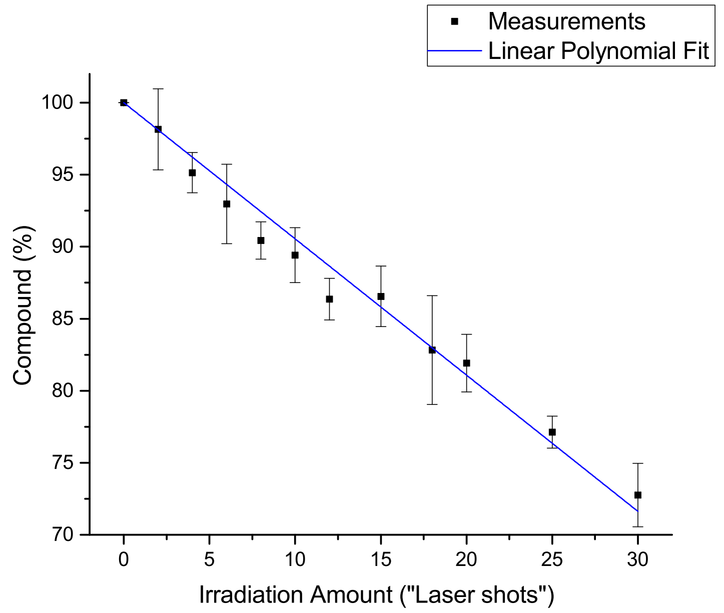

Figure S12. Percentage of remaining *trans*-azobenzene, as determined by monitoring the absorbance at 355 nm, and plotted as function of irradiation amount. The data was acquired by irradiation with the laser. Values for the fit: $Compound(\%) = 100 - 0.94571 \times (irradiation\ amount)$. R²=0.99. Error for intercept: 8.43882×10^{-4}, error for slope: 0.02649.

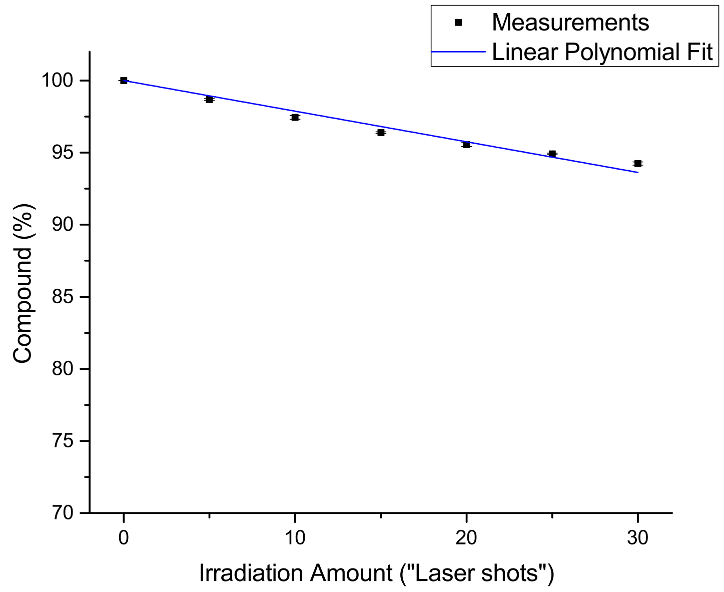

Figure S13. Percentage of remaining caged phosphate as a function of irradiation amount. The data was acquired by irradiation with the laser. Values for the fit: $Compound(\%) = 99.99983 - 0.21237 \times (irradiation\ amount)$. R²=0.99. Error for intercept: 0.00563, error for slope: 0.00878.

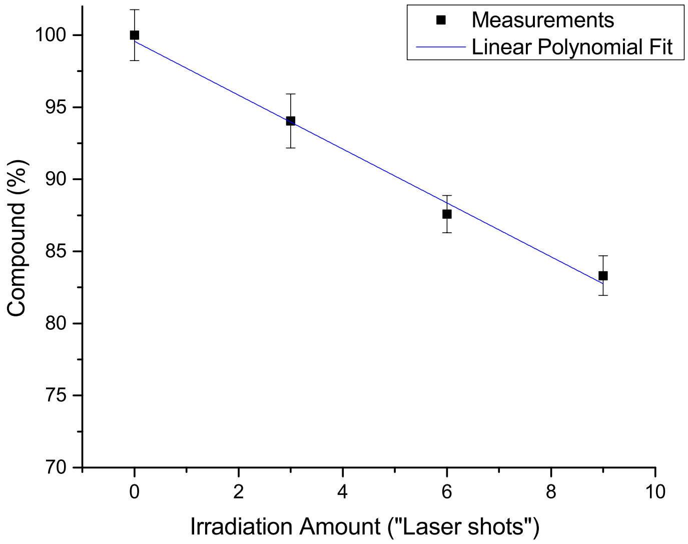

Figure S14. Percentage of remaining *trans*-azobenzene, as determined by monitoring the absorbance at 355 nm, and plotted as function of irradiation amount. The data was acquired by irradiation with the laser. Values for the fit: $Compound(\%) = 99.57124 - 1.86924 \times (irradiation\ amount)$. R²=0.99. Error for intercept: 0.78914, error for slope: 0.12679.

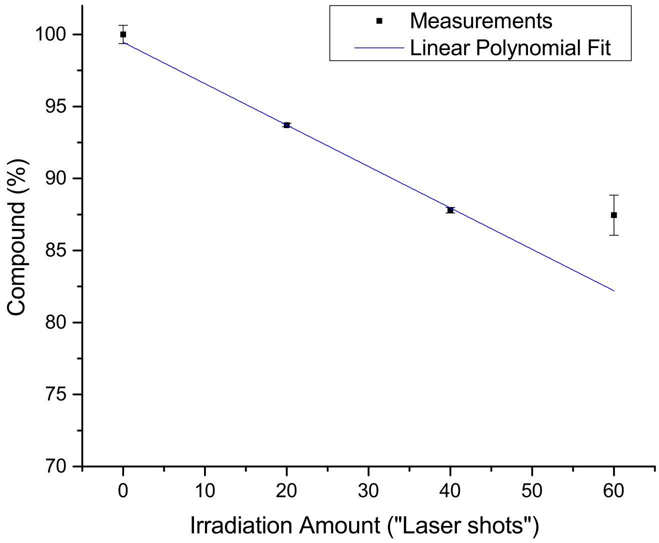

Figure S15. Percentage of remaining caged ATP as a function of irradiation amount. The data was acquired by irradiation with the laser. Values for the fit: $Compound(\%) = 99.45488 - 0.28753 \times (irradiation\ amount)$. R²=0.98. Error for intercept: 0.75399, error for slope: 0.02816.

2.6 References and Notes

[1] J. E. T. Corrie, J. H. Kaplan, B. Forbush, D. C. Ogden, D. R. Trentham, *ChemPhysChem* **2015**, DOI: 10.1002/cphc.201402808.

[2] P. Anstaett, A. Leonidova, E. Janett, C. G. Bochet, G. Gasser, *ChemPhysChem* **2015**, DOI: 10.1002/cphc.201500178.

[3] a) G. Marriott (Ed.) *Methods in Enzymology: Caged Compounds*, Academic Press, **1998**; b) G. Bort, T. Gallavardin, D. Ogden, P. I. Dalko, *Angew. Chem. Int. Ed.* **2013**, *52*, 4526–4537; c) G. C. R. Ellis-Davies, *Nat. Meth.* **2007**, *4*, 619–628; d) P. Klán, T. Šolomek, C. G. Bochet, A. Blanc, R. Givens, M. Rubina, V. Popik, A. Kostikov, J. Wirz, *Chem. Rev.* **2012**, *113*, 119–191; e) G. Mayer, A. Heckel, *Angew. Chem. Int. Ed.* **2006**, *45*, 4900–4921; f) C. Brieke, F. Rohrbach, A. Gottschalk, G. Mayer, A. Heckel, *Angew. Chem. Int. Ed.* **2012**, *51*, 8446–8476; g) L. Zayat, O. Filevich, L. M. Baraldo, R. Etchenique, *Phil. Trans. R. Soc. A* **2013**, *371*.

[4] J. H. Kaplan, B. Forbush, J. F. Hoffman, *Biochem.* **1978**, *17*, 1929–1935.

[5] A. Specht, F. Bolze, J. F. Nicoud, M. Goeldner in *Methods in Molecular Biology* (Ed.: M. R. Banghart), Humana Press, **2013**.

[6] a) M. J. G. Fernandes, S. P. G. Costa, M. S. T. Goncalves, *New J. Chem.* **2013**, *37*, 2369–2376; b) D. P. Kennedy, D. C. Brown, S. C. Burdette, *Org. Lett.* **2010**, *12*, 4486–4489; c) C. Gwizdala, C. V. Singh, T. R. Friss, J. C. MacDonald, S. C. Burdette, *Dalton Trans.* **2012**, *41*, 8162–8174.

[7] T. Solomek, S. Mercier, T. Bally, C. G. Bochet, *Photochem. Photobiol. Sci.* **2012**, *11*, 548–555.

[8] J. W. Walker, G. P. Reid, J. A. McCray, D. R. Trentham, *J. Am. Chem. Soc.* **1988**, *110*, 7170–7177.

[9] C. G. Hatchard, C. A. Parker, *Proc. R. Soc. A* **1956**, *235*, 518–536.

[10] a) G. C. Ellis-Davies, J. H. Kaplan, *Proc. Natl. Acad. Sci. USA* **1994**, *91*, 187–191; b) K. L. Ciesienski, L. M. Hyman, D. T. Yang, K. L. Haas, M. G. Dickens, R. J. Holbrook, K. J. Franz, *Eur. J. Inorg. Chem.* **2010**, 2224–2228; c) K. L. Ciesienski, K. L. Haas, K. J. Franz, *Dalton Trans.* **2010**, *39*, 9538–9546; d) A. Barth, J. E. T. Corrie, *Biophys. J.* **2002**, *83*, 2864–2871; e) K. L. Ciesienski, K. L. Haas, M. G. Dickens, Y. T. Tesema, K. J. Franz, *J. Am. Chem. Soc.* **2008**, *130*, 12246–12247; f) R. Sreekumar, Y. Q. Pi, X. P. Huang, J. W. Walker, *Bioorg. Med. Chem. Lett.* **1997**, *7*, 341–346.

[11] J. E. T. Corrie, A. Barth, V. R. N. Munasinghe, D. R. Trentham, M. C. Hutter, *J. Am. Chem. Soc.* **2003**, *125*, 8546–8554.

[12] M. Gaplovsky, Y. V. Il'ichev, Y. Kamdzhilov, S. V. Kombarova, M. Mac, M. A. Schworer, J. Wirz, *Photochem. Photobiol. Sci.* **2005**, *4*, 33–42.

[13] L. G. Herbette, *Ph.D. Thesis*, University of Pennsylvania, Ann Arbor, **1980**.

[14] J. A. McCray in *Methods in Enzymology: Caged Compounds* (Ed.: G. Marriott), Academic Press, **1998**.

[15] a) J. E. Baldwin, A. W. McConnaughie, M. G. Moloney, A. J. Pratt, S. Bo Shin, *Tetrahedron* **1990**, *46*, 6879–6884; b) Unfortunately, the authors did not clarify in the publication which wavelength was used. Personal correspondence could not clarify this matter.

[16] A. Leonidova, V. Pierroz, R. Rubbiani, Y. Lan, A. G. Schmitz, A. Kaech, R. K. O. Sigel, S. Ferrari, G. Gasser, *Chem. Sci.* **2014**, 4044–4056.

[17] a) J. A. McCray, L. Herbette, T. Kihara, D. R. Trentham, *Proc. Natl. Acad. Sci. USA* **1980**, *77*, 7237–7241; b) J. P. Y. Kao, S. Muralidharan in *Methods in Molecular Biology* (Ed.: M. R. Banghart), Humana Press, **2013**.

[18] R. W. Yip, D. K. Sharma, R. Giasson, D. Gravel, *J. Phys. Chem.* **1985**, *89*, 5328–5330.

[19] R. W. Yip, Y. X. Wen, D. Gravel, R. Giasson, D. K. Sharma, *J. Phys. Chem.* **1991**, *95*, 6078–6081.

[20] M. Montalti, A. Credi, L. Prodi, M. T. Gandolfi, *Handbook of photochemistry*, CRC Press (Taylor & Francis Group), Boca Raton, FL, **2006**.

[21] M. Schwörer, J. Wirz, *Helv. Chim. Acta* **2001**, *84*, 1441–1458.

[22] H. J. Kuhn, S. E. Braslavsky, R. Schmidt, *Pure Appl. Chem.* **2004**, *76*, 2105–2146.

[23] a) G. Gauglitz, S. Hubig, *J. Photochem.* **1981**, *15*, 255–257; b) G. Gauglitz, S. Hubig, *J. Photochem.* **1985**, *30*, 121–125; c) G. Persy, J. Wirz, *EPA Newsl.* **1987**, *29*, 45–6.

[24] I. Aujard, C. Benbrahim, M. Gouget, O. Ruel, J.-B. Baudin, P. Neveu, L. Jullien, *Chem. Eur. J.* **2006**, *12*, 6865–6879.

[25] Sources of errors include the accuracies of the UV absorbance measurements, the linear fits, and inaccuracies in the quantum yields reported in the literature for the reference molecules.

[26] T. Joshi, V. Pierroz, C. Mari, L. Gemperle, S. Ferrari, G. Gasser, *Angew. Chem. Int. Ed.* **2014**, *53*, 2960–2963.

[27] a) Y. V. Il'ichev, M. A. Schwörer, J. Wirz, *J. Am. Chem. Soc.* **2004**, *126*, 4581–4595; b) A. Barth, J. E. T. Corrie, M. J. Gradwell, Y. Maeda, W. Mäntele, T. Meier, D. R. Trentham, *J. Am. Chem. Soc.* **1997**, *119*, 4149–4159; c) Y. V. Il'ichev, J. Wirz, *J. Phys. Chem. A* **2000**, *104*, 7856–7870.

[28] K. Fendler, E. Grell, M. Haubs, E. Bamberg, *EMBO J.* **1985**, *4*, 3079–3085.

3 Two-Photon Uncageable Enzyme Inhibitors with Additional Targeting as Probes for Chemical Biology

P. Anstaett[a] and G. Gasser[a]*

[a] Department of Chemistry, University of Zurich, Winterthurerstrasse 190, CH-8057 Zurich, Switzerland.

* Corresponding author: e-mail: gilles.gasser@chem.uzh.ch; Fax: +41 44 635 46 03; Tel: +41 44 635 46 30; homepage: http://www.gassergroup.com.

This chapter is based on a submission for publication in *Chemical Communications* on 21.07.2014.

3.1 Contributions to the publication

P.A. performed the experiments and wrote the first draft of the manuscript.

3.2 Abstract:

Two-photon cages have been synthetically modified to allow for attachment of enzyme inhibitors *via* an alcohol or carboxylic acid function. The cages furthermore can be conjugated to a targeting vector using click chemistry. Most importantly, the control of enzyme activity is being directly demonstrated with a caged cyclooxygenase-2 inhibitor.

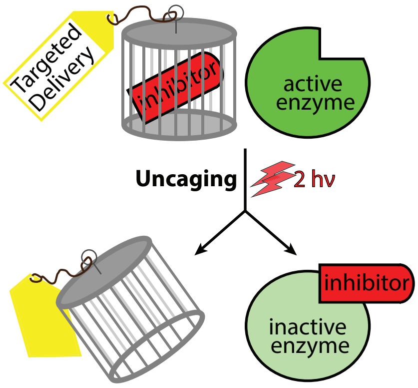

3.3 Article

Enzymes are one of the largest families of proteins and play a vital role in many biological signaling pathways and metabolic processes. However, even in cases where the reaction catalyzed by the enzyme is known, exploring its full significance within its biological network context remains challenging to date.[1,2] In order to gain more insight into the exact functions and effects of enzymes within their biological network, temporal and spatial control over their activity is needed. The use of light in this context is extremely appealing since it is known to not bias biological systems at certain wavelengths and doses.[3,4] Despite the enormous impact that such a discovery would have, the examples of specific enzyme inhibitors whose activity can be turned on on demand using light are extremely scarce. Photoswitchable inhibitors have been recently reported for acetylcholinesterase.[5] However, this concept requires the design of completely new compounds with special properties and is likely impossible in many instances.[6] Furthermore, the effects of common drugs cannot be investigated by this technique as they are not photoswitchable. Nanoscopic carrier systems with the ability to release their cargo upon light irradiation have recently been reported.[7] However, macromolecular approaches are fundamentally different and less controllable than ones relying on small molecules.[8]

A potential alternative to control the biological activity of a biomolecule using light is through (photo-)caging. In this case, a photo-labile protecting group is attached to a crucial functional group of a biomolecule thereby deactivating its biological function. Upon irradiation with UV light, the original bioactive compound is released and its bioactivity hence restored. This technique has been successfully applied in chemical biology to understand or modulate biological processes.[4,9] For example, we recently reported the successful single-photon caging/uncaging of metal complexes to control their anti-cancer activity.[10] However, the use of light in the UV range is problematic since it is absorbed by biomolecules and is known to damage them. Over the last few years, new cages have been developed, which can be cleaved by two-photon excitation upon irradiation in the near-IR range.[11] This quantum mechanical phenomenon allows the excitation of a molecule by near-simultaneous absorption of two photons. Each of these two photons only needs half the power, respectively twice the wavelength that single photon excitation would require. The light is therefore not absorbed by biomolecules, making it less harmful and allowing for deeper tissue penetration. An additional advantage of the two-photon process is the better spatial resolution stemming from the need of high photon densities for this phenomenon to occur. In combination with focused lasers, this leads to a subcellular three-dimensional resolution. Consequently, two-photon uncaging facilitates chemical biological investigations with unprecedented precision in temporal (femtosecond scale) and spatial (femtoliter scale)[12] dimensions. This has already led to many important discoveries, especially in the field of neuroscience, where it has been employed for the release of neurotransmitters.[13] Nevertheless, the impact of two-photon uncaging on other fields, such as the aforementioned investigations on enzymes, is limited so far. A few caged enzyme inhibitors with the potential to be two-photon-uncaged have been reported.[14–17] For those compounds, either no biological two-photon experiments were performed,[16] the irradiation times needed were very long (several hours),[14,15] the inhibition change upon uncaging was only moderate,[14] or the uncageable concentrations were physiologically irrelevant.[17] Herein, we report an important step towards applicability of two-photon uncageable for studying enzyme function. The design, synthesis and physicochemical properties of a two-photon uncaging platform, which can be used for studying enzyme function in a time and space controlled manner are described. We caged two drugs which selectively inhibit cyclooxygenase 2 (COX-2), namely Celecoxib and Lumiracoxib. Celecoxib is FDA-approved for use against the localized disease arthritis and has been shown to have anticancer activity. Lumiracoxib had been approved for the treatment of arthritis as well, but has no anticancer activity. The differences in the physiological effect are so far not understood because of the multitude of interdependent effects triggered by COX inhibition,[1] and caged probes could help elucidating these differences. The two drugs have to be caged *via* different functional groups. This has been realized by adjusting the respective functional group on the cage, namely an alcohol for Lumiracoxib and a carboxylic acid for Celecoxib. Of high interest, the cage structures can furthermore be decorated with a targeting moiety. This is demonstrated by the attachment of a peptide, which specifically directs the cage towards cancer cells. The targeting could be used in chemical biological investigations to study the influence of biodistribution on the function of the inhibitor. The potential to control the activity of an enzyme by a targeted two-photon caged enzyme inhibitor is being demonstrated in an *in vitro* assay. Enzyme activity assays have been shown to be good benchmarks for caged inhibitors in UV-uncaging experiments.[18]

Based on a two-photon cage developed by Goeldner and co-workers,[19] which has already been used on HeLa cells,[20] we developed cages **1** and **2** (see Scheme 1). The syntheses are described in the Supporting Information. The carboxylic acid of Lumiracoxib and sulfonamide function of Celecoxib were caged to the alcohol and carboxylic acid moieties of **1** and **2**, respectively, to give caged Lumiracoxib **3** and caged Celecoxib **4**. Other cage structures with carboxylic acid attachment groups have been reported before,[21] but to the best of our knowledge, **2** is the first biphenyl nitro cage capable of caging *via* a carboxylic acid function. The biphenyl-core of both cages is substituted with a tetraethylene glycol chain

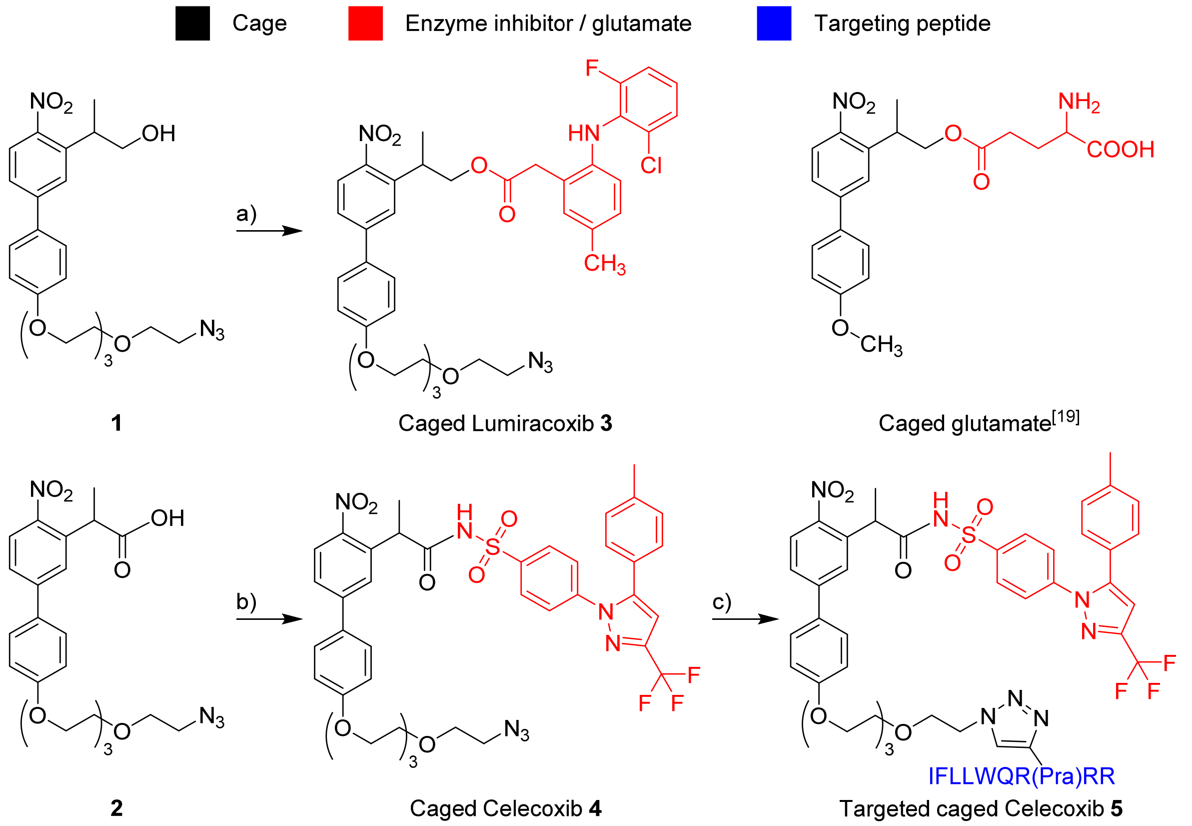

Scheme 1. Caging of the COX-2 selective inhibitors Lumiracoxib (top) and Celecoxib (bottom), exemplary attachment of a targeting peptide to caged Celecoxib (bottom right), and the previously reported caged glutamate (top right).[19] Reaction conditions: a) *N*,*N'*-dicyclohexylcarbodiimide, DMAP, Lumiracoxib, CH_2Cl_2, 0 °C to rt, 20 h, 80%; b) 1-(3-Dimethylaminopropyl)-3-ethylcarbodiimide hydrochloride, DMAP, Celecoxib, CH_2Cl_2, rt, 2 h, 54%; c) $CuSO_4$, sodium ascorbate, IFLLWQR(Pra)RR, THF/H_2O 2:1, rt to 60 °C, 30 h. DMAP: 4-dimethylaminopyri-dine; Pra: (S)-2-amino-4-pentynoic acid.

to increase solubility in aqueous media, a critical parameter for the hydrophobic two-photon cages, as well as membrane permeability.[22] The terminal azide group can be used to additionally attach any alkyne-containing targeting biomolecules *via* click chemistry. This gives the opportunity to target the biological effect with two orthogonal methods, *i.e.* 1) by directing the caged compound towards the intended tissue with the targeting vector and 2) by light activation. Importantly, the attachment of the targeting moiety to the caged compounds is by design the last step in the synthesis and hence conveniently adjustable to different cellular or subcellular units. To exemplify this, a peptide which binds to annexin-1 and has been shown to function as a targeting moiety towards certain cancer cells,[23] has been attached to caged Celecoxib **4**, producing targeted caged Celecoxib **5** (see Scheme 1).

The caged compounds **3**, **4**, and **5** were photo-physically investigated and the results are summarized Table 1. Notably, although photo-degradation of azides to reactive nitrene groups has been reported[24] we never observed such reactions for **3** or **4**, neither upon UV nor fs-pulsed near-IR irradiation. The caged glutamate by Goeldner *et al.* (Scheme 1) has been shown to have a quantum yield of 0.1 at 313 nm, relative to 1-(2-nitrophenyl)ethyl-ATP (caged ATP).[19] We determined the single photon uncaging quantum yields upon irradiation with a frequency-tripled Nd-YAG laser at 355 nm with azobenzene as reference, as discussed in our recent article on the accurate determination of uncaging quantum yields.[25–27] For **3**, which links the bio-active compound also via an ester to the same cage chromophore, a similar uncaging quantum yield of 0.094 was determined. **4**, which has a sulfonamide as linking group, has a significantly lower quantum yield of 0.013. The quantum yield of **5** is with 0.0047 in the range of **4**, but still smaller. This difference demonstrates a moderate effect of the targeting moiety on the single-photon uncaging. Low single-photon uncaging rates are in principle desired since unwanted photolysis under ambient conditions is suppressed. However, in this case, the differences between the compounds are mostly due to the chemical reactions following photo-excitation since the biphenylnitro core is the same for all three compounds. Consequently, also lower two-photon uncaging action cross-sections ($\delta_a\Phi_u$) can be expected for **4** and **5**, compared to **3**. These properties were determined upon irradiation at 800 nm with a fs-pulsed laser with a 5 kHz repetition rate using the known reference 7-hydroxycoumarin-4-ylmethyl acetate.[28,29] As expected, the uncaging action cross-sections $\delta_a\Phi_u$ of **4** (0.063 GM) and **5** (0.053 GM) were found to be lower than the one of **3** (0.37 GM). Importantly, the attachment of the targeting peptide was found to not majorly influence the two-photon uncaging efficiency. As for the single photon uncaging, the value for **3** is in the same range as the one for caged glutamate.[19] Notably, the two-photon uncaging action cross-section of a dye attached to the same biphenylnitro cage core has been shown to be more than an order of magnitude greater at wavelengths around 740 nm.[20] However, tissue transparency is better at 800 nm than at 740 nm and therefore an even more useful wavelength with respect to future applications.[30]

Table 1. Photophysical uncaging properties of the caged compounds **3**, **4**, **5** and of the literature-known caged glutamate.[19]

Compound	**ϕ (λ=355 nm)^a**	**$\delta_a\Phi_u$ (λ=800 nm)^b**
Caged glutamate	0.1 (313 nm)	0.45 GM
3	0.094 ±0.02	0.37 ±0.04 GM
4	0.013 ±0.001	0.063 ±0.008 GM
5	0.0047 ±0.0004	0.053 ±0.008 GM

[a] Acquired with a Nd-YAG laser, relative to the photoisomerizaion of azobenzene;[25–27] [b] Acquired with a fs-pulsed laser with 5 kHz repetition rate relative to 7-hydroxycoumarin-4-ylmethyl acetate; [28,29] for details on both methods, see Supporting Information.

In a study which investigated two-photon uncaging at 740 nm, it has been stated that two-photon uncaging action cross-sections of at least 0.1 GM are required for biological applications.[28] Accordingly, the two-photon uncaging of **4** and **5** would be insufficient for biological studies. However, the minimum value certainly depends on the wavelength, which was 740 nm in the previous study, and most likely also on additional laser properties, such as the repetition rate of the laser. Most two-photon uncaging studies used lasers with MHz repetition rates.[29,31] However, 10^3 smaller repetition rates (kHz), like in this study, have also been used before.[19] With the same average powers and peak lengths, the peak photon densities differ therefore by the same factor of 10^3. Thus, the commonly quoted paradigm that two-photon uncaging only occurs in the focal point of a laser beam is not generally true. Indeed, we and others[19] found that with the laser beam used for this study it was not necessary to focus since the photon density was sufficient with a collimated beam. These observations raise the question if biologically relevant uncaging is still possible with two-photon uncaging cross-sections below 0.1 GM at 800 nm. To this end, the inhibition potential of COX-2 by the caged compounds **4** and **5**, whose uncaging efficiencies are clearly below 0.1 GM, was tested with a fluorescent inhibitor screening assay (see Figure 1). The irradiation time was chosen to be 15 min since this time frame has been used in biological studies before.[22,32] Notably, this time is significantly shorter than what was required in other reports on uncaging of drugs.[14,15,33] To test if the high photon densities influence biomolecules, the enzyme was irradiated using these experimental conditions and its activity tested in comparison to a non-irradiated sample. The activity of the enzyme was found to be unaffected by the pulsed laser light. In addition, Celecoxib was irradiated. No decomposition could be detected by HPLC analysis and its inhibitory potential towards COX-2 remained unchanged at around 60-70 nM. Likewise, solutions of the caged compounds **4** and **5** were tested. Before uncaging, no inhibition of COX-2 could be detected within the limits given by the solubility of the caged compounds. After 15 min of irradiation, the uncaging progress was around 70% for **4** and 40% for **5**. The amount of free Celecoxib was determined by HPLC. The IC_{50} values relative to the released Celecoxib are for both **4** and **5** identical to the non-caged Celecoxib. Relative to the caged starting materials, the IC_{50} values are slightly higher due to the incomplete release in the given timeframe. Nevertheless, at least five- and ten-fold increases for **4** and **5**, respectively, were observed.

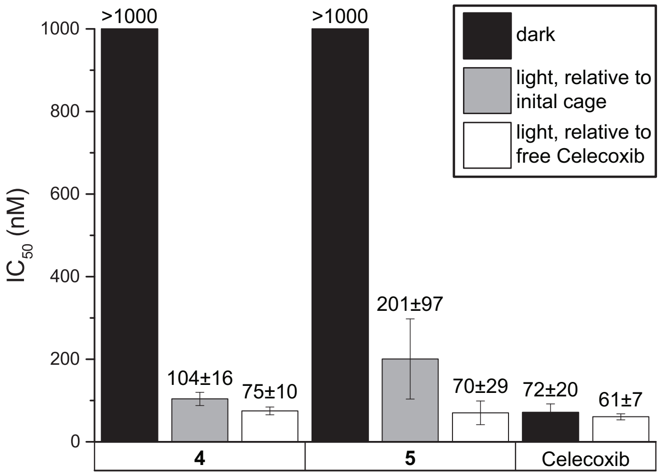

Figure 1. Inhibition constants of Celecoxib, **4**, and **5**, without and upon irradiation with a pulsed laser at 800 nm for 15 min. The values are relative to the concentrations of caged compound, or released Celecoxib, as indicated. For details, see Supporting Information.

In summary, we could demonstrate that targetable two-photon uncaging can be employed to control enzyme activity. The two drugs Celecoxib and Lumiracoxib, which both selectively inhibit COX-2, were deactivated by conjugation to a targetable cage. A targeting peptide could be attached to the cage without significantly altering the uncaging efficiency. The uncaging process was shown to be adequate for controlling the inhibition of an enzyme in an *in vitro* assay. The concept holds great promise for the future, not only for chemical biological studies on enzyme function, but potentially also for applications in therapeutic targeted drug delivery. Currently, Photodynamic Therapy (PDT) is the most prominent method which utilizes light for the treatment of different skin conditions, certain types of cancer,[34] and its potential against infective diseases is currently being explored.[35] PDT depends on the generation of reactive oxygen species, especially singlet oxygen. However, many cancerous tissues are hypoxic and therefore oxygen-independent phototherapies could advance therapy tremendously.[36] We believe that therapeutic two-photon uncaging, with the ability to activate virtually any drug without depending on additional factors such as oxygen, could therefore further promote non-invasive light based therapies.

3.4 Acknowledgments

This work was supported by the Swiss National Science Foundation (Professorship N° PP00P2_133568 and Research Grants N° 200021_129910 and N° 200020_146776 to G.G.), the University of Zurich (G.G.) and the Stiftung für Wissenschaftliche Forschung of the University of Zurich (G.G.). The authors would like to thank Peter Hamm, Julien Réhault and especially Klemens Koziol for help and support with the two-photon uncaging experiments, and Anita G. Schmitz for helpful discussions.

3.5 Supporting Information

3.5.1 Instrumentation and Materials

^{1}H, ^{13}C and ^{19}F NMR spectra were recorded on Bruker Avance (400 and 500) spectrometers. ^{13}C and ^{19}F NMR measurements were carried out as ^{13}C {H} and ^{19}F {H}, respectively. ^{1}H and ^{13}C NMR spectra were referenced to the residual solvent signal, the ^{19}F spectrum to CCl_3F. IR spectra were acquired on a Perkin-Elmer Spectrum 2 FT-IR, UV/Vis spectra on a Varian Cary 100 instrument. High resolution ESI-MS spectra were measured with a Bruker ESQUIRE-LC quadrupole ion trap instrument and MALDI-MS spectra on a Bruker Autoflex I. Preparative HPLC purification was carried out with a Varian ProStar with two solvent delivery modules, an UV/Vis detector and an Agilent PrepHT 300 SB-C18 column. Analytical HPLC traces were acquired on a VWR Hitachi Chromaster with a 5110 pump system, a 5260 auto sampler, a 5310 column oven, a 5430 diode array detector, and a Macherey-Nagel EC 250/3 NUCLEOSIL 100-5 C18 column. Microwave heated reactions were carried out in an Anton Paar Monowave 300. Single-Photon uncaging was performed with an Edinburgh Instruments LP920 laser flash photolysis setup with a Continuum Surelight Nd:YAG laser, frequency-tripled to generate light with a wavelength of 355 nm. Two-photon uncaging was carried out using using a Ti:sapphire amplifier system (Spitfire Pro, 5 kHz, 90 fs, 800 µJ per pulse; Spectra-Physics). Chemicals were acquired from Sigma-Aldrich, Acros, and TCI Europe. Celecoxib was acquired from AK Scientific, Inc. (Union City, CA, USA) and Lumiracoxib was acquired from Kemprotec Ltd. (Cumbria, UK). Amino acids were acquired from Bachem (Bubendorf, Switzerland), and Iris-Biotech (Marktredwitz, Germany). The Tentagel S Ram resin for the peptide synthesis was acquired from Rapp Polymers (Tübingen, Germany). Enzyme inhibition was tested using the “COX Fluorescent Inhibitor Screening Assay Kit” from Cayman Chemical Company (Ann Harbor, MI, USA) according to the manual. The fluorescence measurements were carried out with a Molecular Devices SpectraMax m2E microplate reader.

3.5.2 Methods

Single Photon Uncaging Quantum Yields

The single photon uncaging quantum yields were determined as described by us earlier.[25–27] In short, the samples were dissolved in a 1:1 mixture of acetonitrile and phosphate buffer saline (pH=7.2, 20 mM) to have an optical density OD(λ=355 nm) = 0.2. The samples were irradiated for certain intervals with an Edinburgh Instruments LP920 laser flash photolysis setup with a Continuum Surelight Nd:YAG laser, frequency-tripled to generate light with a wavelength of 355 nm. The laser was slightly misaligned to reach a suitable irradiation power. A fresh aliquot was used for each irradiation. The percentage of remaining caged compound was determined by peak integration of analytical HPLC UV-traces and setting the value in relation to the value obtained without irradiation. The percentage values were plotted against the irradiation, and the slope m_{sample} of the curve was determined for the linear range (approx. the first 20% of decomposition). As reference, *trans*-azobenzene was dissolved in methanol to the same OD(λ=355 nm) = 0.2. The irradiation was carried out as described for the uncaging samples. Subsequently, the absorbance was determined at 355 nm and the percentage of remaining *trans*-azobenzene was plotted against the irradiation. The slope $m_{reference}$ of the curve was determined for the linear range (approx. the first 20% of decomposition). Exemplary uncaging plots including linear fits are shown in the section below. Comparison of the slopes of the curves gave the uncaging quantum yields of the caged compounds under consideration of the number of molecules with the following formula:

$$\phi_{sample} = \phi_{reference} \times \frac{n_{sample,0} \times m_{sample}}{n_{reference,0} \times m_{referece}}$$

At least three independent sets of measurements were averaged to obtain the single-photon uncaging quantum yields.

Exemplary uncaging plots:

For an azobenzene-isomerization plot, the reader is referred to our recent publication on this topic.[25]

The data sets of the individual compounds plotted below have not been recorded on the same day and the slopes therefore cannot be compared to one another.

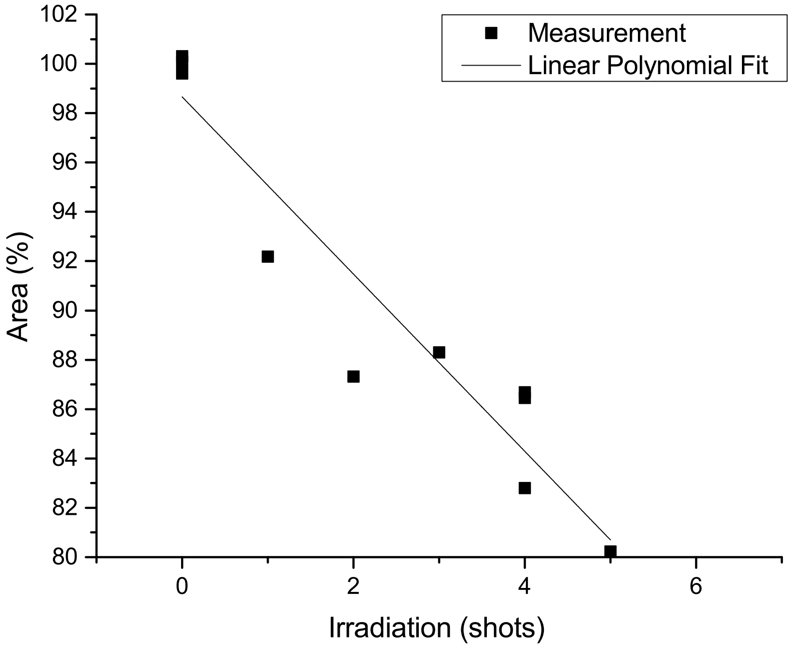

Figure S1. Single-photon uncaging of **3**. Values for the fit: $y = 96.659 - 3.592 x$; $R^2 = 0.91$.

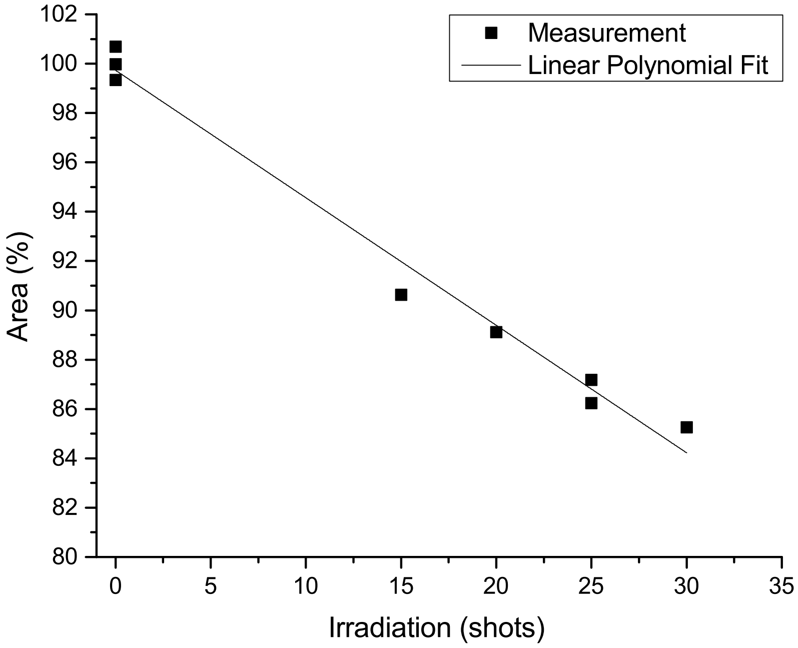

Figure S2. Single-photon uncaging of **4**. Values for the fit: $y = 99.732 - 0.5170 x$; $R^2 = 0.99$.

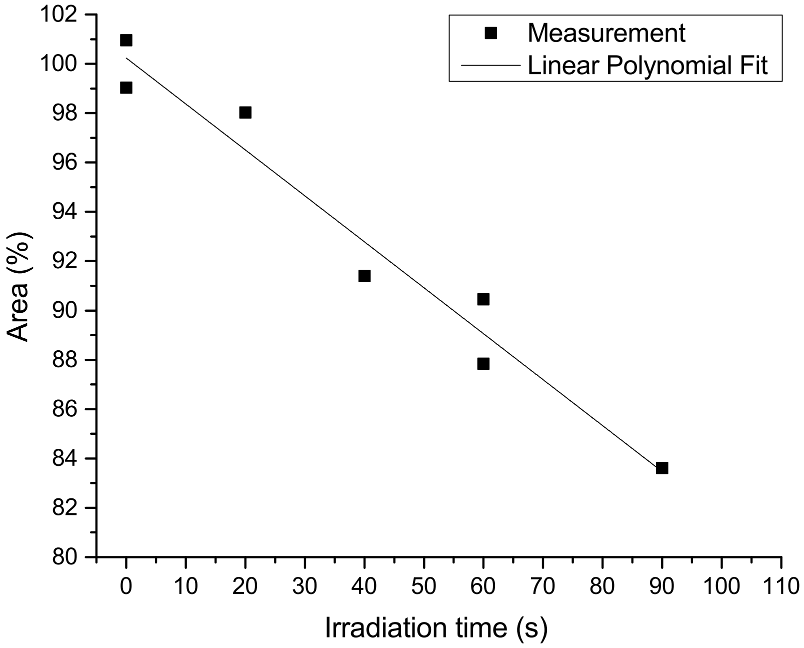

Figure S3. Single-photon uncaging of **5**. Values for the fit: y = 100.24 - 0.1863 x; R² = 0.96.

Two-Photon Uncaging Action Cross-Sections

The two-photon uncaging action cross-sections were determined as previously described.[19,29] In short, the samples were dissolved in a 1:1 mixture of acetonitrile and phosphate buffer saline (pH=7.2, 20 mM) to have an optical density OD(λ=400 nm)=0.2. As reference, 7-hydroxycoumarin-4-ylmethyl acetate[28] was dissolved in a 1:1 mixture of acetonitrile and phosphate buffer saline (pH=7.2, 20 mM) to have OD(λ=400 nm)=0.2. The respective solutions were separately illuminated for certain time intervals in Hellma 105.202-QS cuvettes (window size 2.5x2 mm², 50 µL volume, 10 mm light path). A fresh aliquot was used for each irradiation. An amplified Ti:sapphire laser system was used to obtain 90 fs pulses centered at 800 nm with a 5 kHz repetition rate. The intensity was reduced to 40 to 100 µJ using a neutral density filter. The beam diameter was reduced to only illuminate the cuvette window by the use of a telescope. The disappearance of the caged compounds was detected by integration of the peaks in the UV traces of analytical HPLC measurements and plotted against the irradiation time. Exemplary plots including linear fits are shown in the section below. The slopes of these curves were used to calculate the two-photon uncaging action cross-sections, according to the following formula:

$$\phi_{sample} = \phi_{reference} \times \frac{slope_{sample}}{slope_{reference}}$$

At least three independent sets of measurements were averaged to obtain the two-photon uncaging action cross-section.

Exemplary uncaging plots:

The data sets of the individual compounds plotted below have not been recorded on the same day and the slopes therefore cannot be compared to one another.

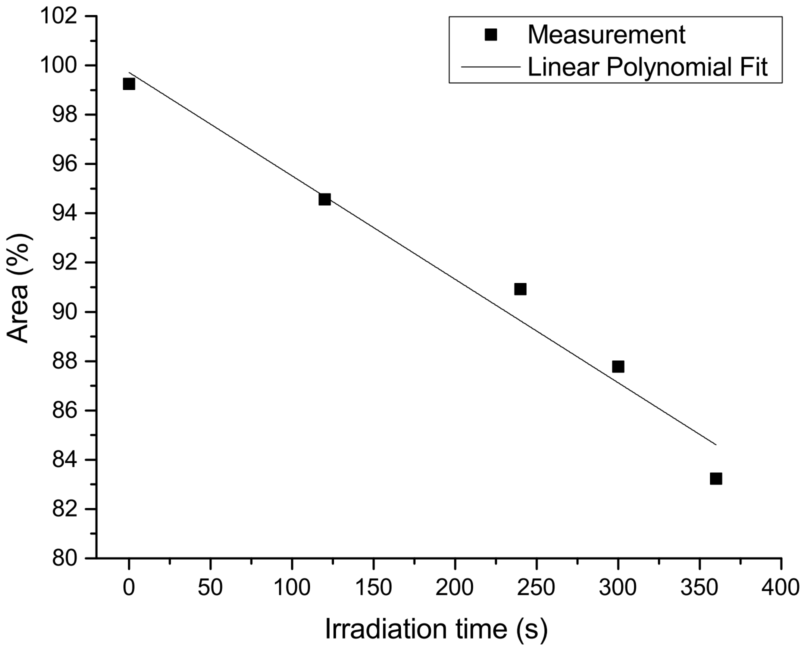

Figure S4. Two-photon uncaging of **CouOAc**. Values for the fit: y = 99.71 - 0.04197 x; R² = 0.97.

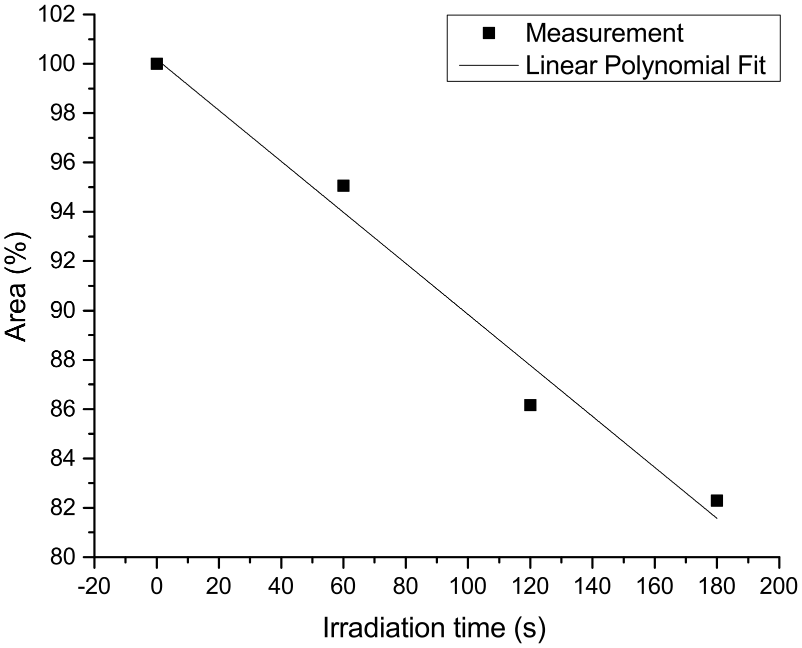

Figure S5. Two-photon uncaging of **3**. Values for the fit: y = 100.18 - 0.1034 x; R² = 0.98.

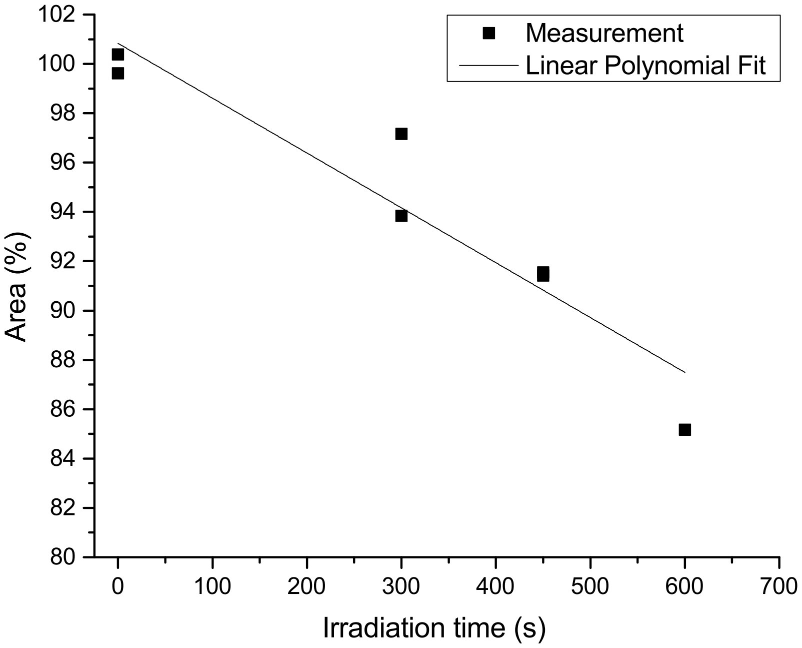

Figure S6. Two-photon uncaging of **4**. Values for the fit: y = 100.83 - 0.0222 x; R² = 0.90.

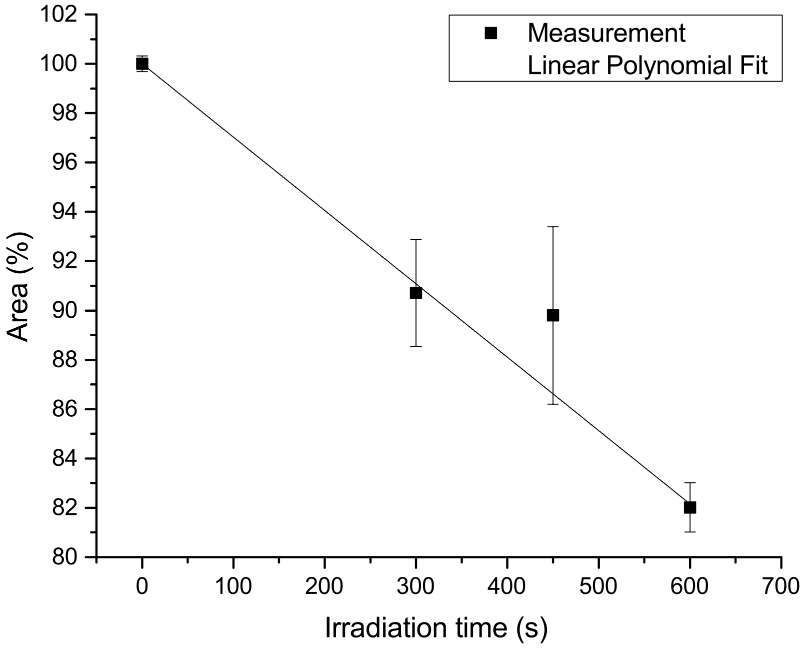

Figure S7. Two-photon uncaging of **5**. Values for the fit: y = 100.02 - 0.0297 x; $R^2 = 0.99$.

Enzyme Inhibition Assays

Enzyme inhibition was tested using the “COX Fluorescent Inhibitor Screening Assay Kit” from Cayman Chemical Company (Ann Harbor, MI, USA). All experiments were performed at least as duplicates of duplicates. The assay was carried out as described in the manufacturer’s manual, with the following adjustments.

The incubation time for all samples was 20 min, as opposed to the 5 min period recommended in the manual.

For the experiments in which the COX-2 enzyme was irradiated, 10 µL of ready-to-use diluted COX-2 solution was further diluted with COX-FIS Assay Buffer 1x diluted to 50 µL and subsequently irradiated in a Hellma 105.202-QS cuvette as described above for the acquisition of two-photon uncaging cross-sections. The power was adjusted to values of 180-200 µJ with neutral density filters. The solution was then transferred to the 96-well plate. The amount of buffer used for this determination was reduced by 40 µL to compensate for the additional volume due to the diluted the enzyme solution. As reference, the same procedure was done without irradiating. A decrease in COX-2 activity was observed for both the irradiated and non-irradiated samples, which could be due to aggregation effects in the cuvette. The effect was identical for both the irradiated and the non-irradiated enzyme samples.

Below, exemplary enzyme activity plots of irradiated and non-irradiated caged compounds are shown.

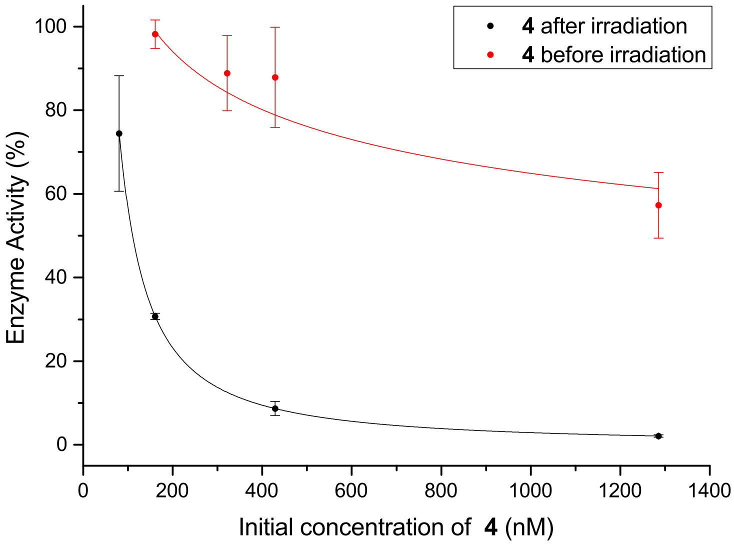

Figure S8. Enzyme inhibition of caged Celecoxib **4** before and after irradiation at 800 nm with a pulsed laser.

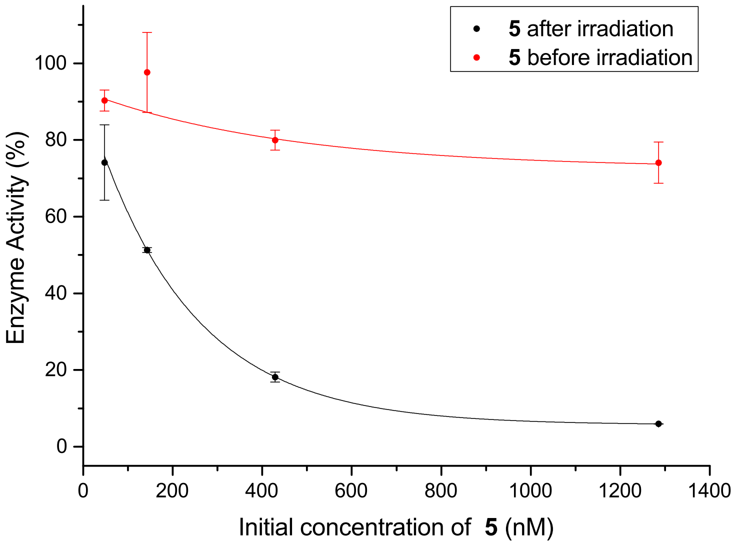

Figure S9. Enzyme inhibition of caged Celecoxib **4** before and after irradiation at 800 nm with a pulsed laser.

3.5.3 Syntheses

Overview over Synthetic Steps not Depicted in the Article

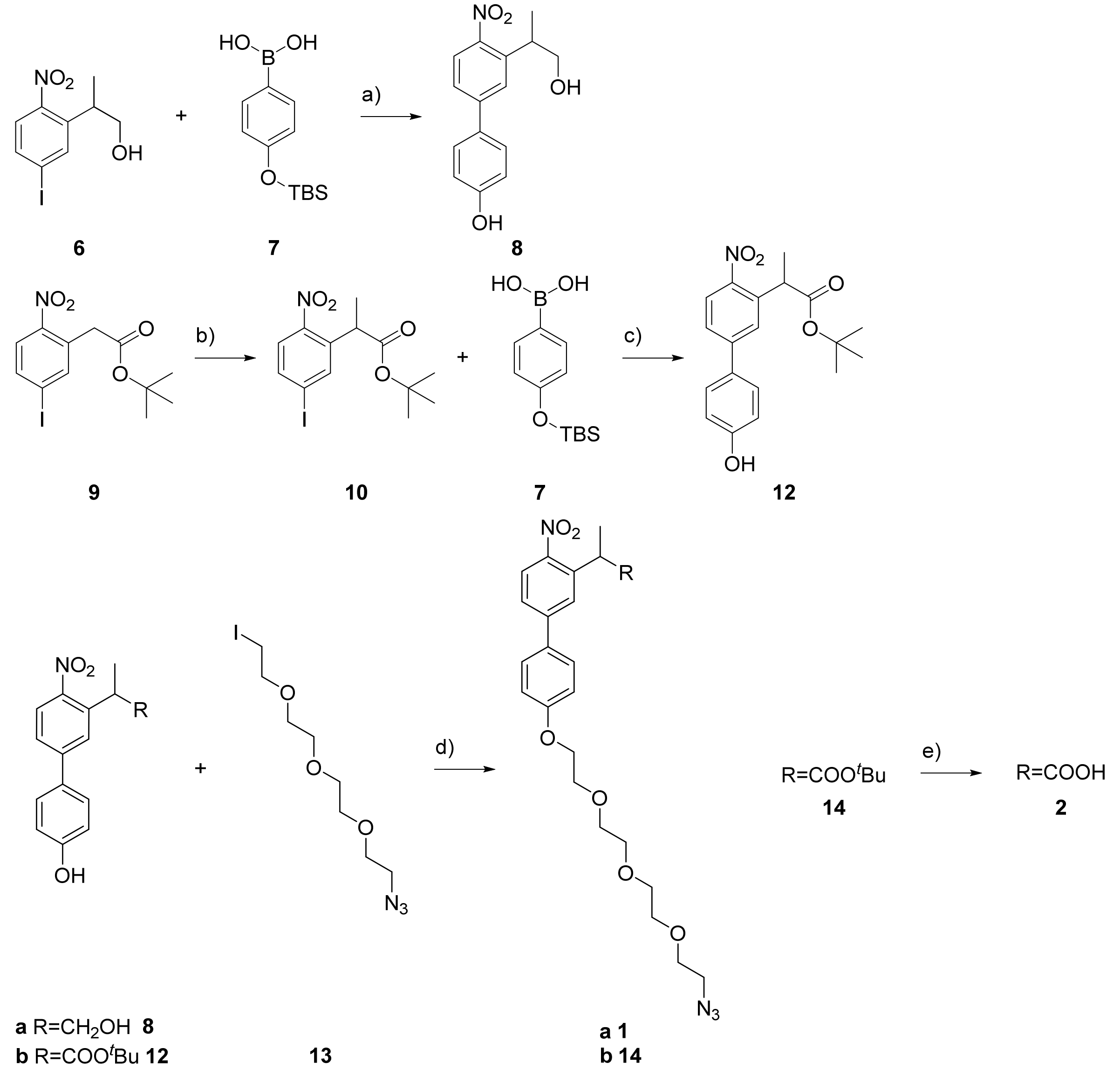

Scheme S1. Synthetic steps not depicted in the main article; procedures: a) 1. Pd(PPh_3)$_4$, Na_2CO_3, toluene, 90 °C, 16 h, 2. Tetrabutylammonium fluoride, THF, rt, 2 h, 98%; b) CH_3I, NaH, THF, 0 °C → rt, 64 h, 45%; c) Pd(PPh_3)$_4$, Na_2CO_3, water, toluene, 95 °C, 17 h, 2. Tetrabutylammonium fluoride, THF, rt, 3 h, 84%; d) K_2CO_3, MeOH, microwave, 100 °C, 10 h, a: 78%, b: 51%; e) Trifluoroacetic acid, CH_2Cl_2, rt, 20 h, 100%.

Compound 6

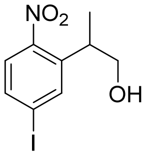

The title compound was prepared as described by Bühler *et al.*[37] The analytical data matched what was reported there.

Compound 7

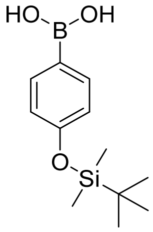

The title compound was prepared as described by Jeanjot *et al.*[38] The analytical data matched what was reported there.

Compound 8

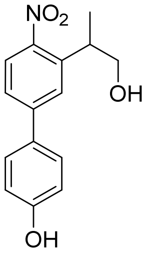

Under an atmosphere of N_2, **6** (307 mg, 1 mmol), **7** (303 mg, 1.19 mmol), toluene (20 mL), saturated Na_2CO_3 solution (10 mL), and water (3 mL) were mixed and degassed. $Pd(PPh_3)_4$ (116 mg, 0.10 mmol) was added and the mixture was stired at 105 °C for 20 min, and 90 °C for 3.5 h. The reaction mixture was allowed to cool down to rt. Water was added and extracted with diethyl ether (3x). The combined organic layers were dried (Na_2SO_4), filtered, and concentrated *in vacuo*.

Under exclusion of light and moisture, the residue (710 mg) was dissolved in THF (8 mL), Tetrabutylammonium fluoride (1 M in THF, 2 mL) was added and the mixture was stirred for 2 h at rt. Afterwards, saturated NH_4Cl solution was added. The organic layer was diluted with diethyl ether, separated and washed with water and brine. Drying (Na_2SO_4), filtration, and concentration afforded the crude product. Column chromatography (silica gel, hexanes/EtOAc 7:4) afforded **8** as a yellow solid (98%, relative to **6**).

*R*f = 0.09 (Hexanes/EtOAc 7:3). IR (KBr) 3469 (s), 2952 (w), 2925 (w), 1635 (m), 1612 (s), 1517 (m), 1349 (m), 823 (s) cm^{-1}. ^{1}H NMR (400 MHz, $CDCl_3$) ∂ 7.84 (d, *J* = 8.5 Hz, 1 H), 7.58 (d, *J* = 1.9 Hz, 1 H), 7.53–7.40 (m, 3 H), 6.91 (d, *J* = 8.6 Hz, 2 H), 5.11 (bs, 1 H), 3.90–3.75 (m, 2 H), 3.72–3.58 (m, 1 H), 1.36 (d, *J* = 7.0 Hz, 3 H). ^{13}C NMR (100 MHz, $CDCl_3$): ∂ 156.3, 149.0, 145.4, 138.9, 131.7, 128.8, 126.3, 125.3, 125.0, 116.0, 68.0, 36.4, 17.6. HRMS m/z calcd. for $C_{15}H_{15}NNaO_4$ ($[M+Na]^+$) 296.08933, found 296.08886.

Compound 9

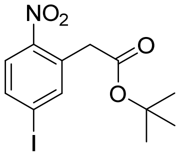

The title compound was synthesized as described by Katayama *et al.*[39] The analytical data matched what was reported there.

Additional analytical data:

*R*f = 0.13 (hexanes/EtOAc 40:1). ^{13}C NMR (100 MHz, $CDCl_3$): ∂ 168.5, 148.5, 142.1, 137.6, 132.1, 126.4, 100.8, 82.2, 40.6, 27.9. HRMS m/z calcd. for $C_{12}H_{14}INNaO_4$ ($[M+Na]^+$) 385.98597, found 385.98598.

Compound 10

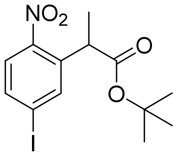

Under an atmosphere of N_2 **9** (1.00 g, 2.75 mmol) was added to a suspension of NaH (60% in oil, 110 mg, 2.75 mmol) in dry THF (10 mL). The purple mixture was cooled to 0 °C and methyl iodide (343 µL, 782 mg, 5.51 mmol) was added dropwise. The mixture was stirred first for 2 h at 0 °C, then for 62 h at rt. The reaction was quenched by adding water and HCl (1 M, 5 mL) at 0 °C. The mixture was extracted with EtOAc (3x). The combined organic layers were washed with brine, dried ($MgSO_4$), filtered, and concentrated *in vacuo*. The crude residue was purified by column chromatography (hexanes/EtOAc 42:1) to yield **10** as a light yellow solid (468 mg, 45%).

R_f = 0.19 (hexanes/EtOAc 38:3). IR (neat) 2975 (w), 1721 (s), 1598 (w), 1556 (w), 1514 (m), 1335 (m), 1243 (s), 1151 (s), 858 (m), 844 (m), 832 (m) cm^{-1}. ^{1}H NMR (400 MHz, CDCl$_3$) ∂ 7.80 (d, *J* = 1.9 Hz, 1 H), 7.74 (dd, *J* = 1.9 Hz, 8.5 Hz, 1 H), 7.62 (d, *J* = 8.5 Hz, 1 H), 4.15 (q, *J* = 7.2 Hz, 1 H), 1.54 (d, *J* = 7.2 Hz, 3 H),1.38 (s, 9 H). ^{13}C NMR (100 MHz, CDCl$_3$): ∂ 171.6, 148.7, 138.4, 137.4, 137.0, 126.1, 100.4, 81.8, 42.1, 27.8, 17.4. ESI-MS m/z 400.00 (100, [M+Na]$^+$) 343.94 (10, [M-^{t}Bu+Na]$^+$). HRMS m/z calcd. for $C_{13}H_{16}INNaO_4$ ([M+Na]$^+$) 400.00162, found 400.00153.

Compound 11

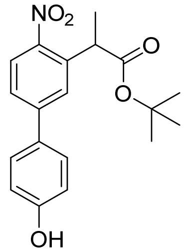

10 (250 mg, 663 µmol) and **7** (201 mg, 694 µmol) were mixed in toluene (10 mL), saturated Na_2CO_3 solution (6.4 mL) and water (2 mL). N_2 was bubbled through the bi-layered solution for 20 min. $Pd(PPh_3)_4$ (76.6 mg, 66.3 µmol) was added and the mixture stirred at 95 °C for 17 h. The solution was allowed to cool to rt. Water and Et_2O were added and the two layers were separated. The aqueous layer was extracted wit Et_2O (3x). The combined organic fractions were dried ($MgSO_4$), filtered, and concentrated.

Tetra-*n*-butylammonium fluoride (1 M in THF, 1.33 mL, 1.33 mmoL) was added to a solution of the crude residue (289 mg) in THF (8 mL). The solution was stirred for 3 h at rt. Saturated NH_4Cl solution and Et_2O were added and the two layers were separated. The aqueous layer was extracted wit Et_2O (3x). The combined organic fractions were dried ($MgSO_4$), filtered, and concentrated. The residue was purified by column chromatography (hexanes/EtOAc 7:3), yielding pure **11** (191 mg, 84% relative to **10**) as a colorless solid.

R_f = 0.65 (hexanes/EtOAc 3:7). IR (neat) 3317 (w), 2989 (w), 1725 (s), 1604 (m), 1579 (m), 1514 (s), 1332 (s), 1304 (m), 1220 (m), 1152 (m), 830 (s) cm^{-1}. ^{1}H NMR (400 MHz, CDCl$_3$) ∂ 8.01 (d, *J* = 8.6 Hz, 1 H), 7.60 (d, *J* = 2.0 Hz, 1 H), 7.54 (dd, *J* = 8.6 Hz, 2.0 Hz, 1 H), 7.48 (d, *J* = 8.6 Hz, 2 H), 6.92 (d, *J* = 8.6 Hz, 2 H), 5.12 (bs, 1 H), 4.32 (q, *J* = 7.2 Hz, 1 H), 1.62 (d, *J* = 7.2 Hz, 3 H), 1.41 (s, 9 H). ^{13}C NMR (125 MHz, CDCl$_3$) ∂ 172.7, 156.5, 147.2, 145.8, 136.3, 131.2, 128.7, 127.6, 125.7, 125.6, 116.0, 81.6, 42.6, 27.9, 17.6. HRMS m/z calcd. for $C_{19}H_{21}NNaO_5$ ([M+Na]$^+$) 366.13119, found 366.13131.

Compound 12

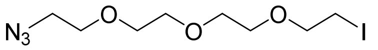

The title compound was prepared as described in the literature. The analytical data matched what was reported before,[40] except for the 13C{1H} NMR spectrum in which 8 instead of 7 signals were observed (see below).

Additional/deviating analytical data:

^{13}C NMR (125 MHz, $CDCl_3$): ∂ 72.0, 70.74, 70.71, 70.3, 70.1, 70.0, 50.7, 2.9. HRMS m/z calcd. for $C_8H_{16}IN_3NaO_3$ ($[M+Na]^+$) 352.01286, found 352.01288.

Compound 13

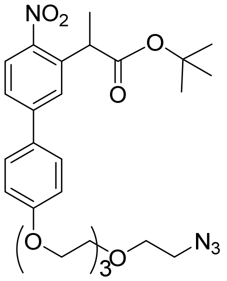

11 (300 mg, 0.874 mmol), **12** (261 mg, 0.794 mmol) and K_2CO_3 (121 mg, 0.874 mmol) were suspended in MeOH (2 mL). The mixture was stirred and heated with a microwave reactor for 12 h at 100 °C. The solvent was removed and the red residue was taken up in saturated NH_4Cl solution and CH_2Cl_2. The two layers were separated. The organic layer was washed with saturated NH_4Cl solution (2x) and water. The combined aqueous layers were extracted with CH_2Cl_2 (3x). The combined organic layers were washed with water, dried ($MgSO_4$), filtered, and concentrated. Purification with column chromatography (hexanes/EtOAc 8:1 → 1:1) gave pure **13** as yellow oil (245 mg, 51%).

R_f = 0.43 (hexanes/EtOAc 3:7). IR (neat) 2880 (w), 2103 (s), 1726 (m), 1605 (s), 1516 (s), 1344 (s), 1248 (s), 1149 (s), 827 (m) cm^{-1}. ^{1}H NMR (400 MHz, $CDCl_3$) ∂ 8.01 (d, *J* = 8.5 Hz, 1 H), 7.61 (d, *J* = 1.9 Hz 1 H), 7.58–7.49 (m, 3 H), 7.04–6.99 (m, 2 H), 4.31 (q, *J* = 7.2 Hz, 1 H), 4.23–4.14 (m, 2 H), 3.94–3.82 (m, 2 H), 3.79–3.63 (m, 10 H), 3.44–3.33 (m, 2 H), 1.61 (d, *J* = 7.2 Hz, 3 H), 1.40 (s, 9 H). ^{13}C NMR (125 MHz, $CDCl_3$) ∂ 172.4, 159.5, 147.3, 145.7, 136.5, 131.3, 128.5, 127.6, 125.6, 125.5, 115.2, 81.4, 70.9, 70.73, 70.72, 70.69, 70.0, 69.7, 67.6, 50.7, 42.5, 27.9, 17.6. HRMS m/z calcd. for $C_{27}H_{36}N_4NaO_8$ ($[M+Na]^+$) 567.24254, found 567.24254.

Targeting Peptide IFLLQR(Pra)RR

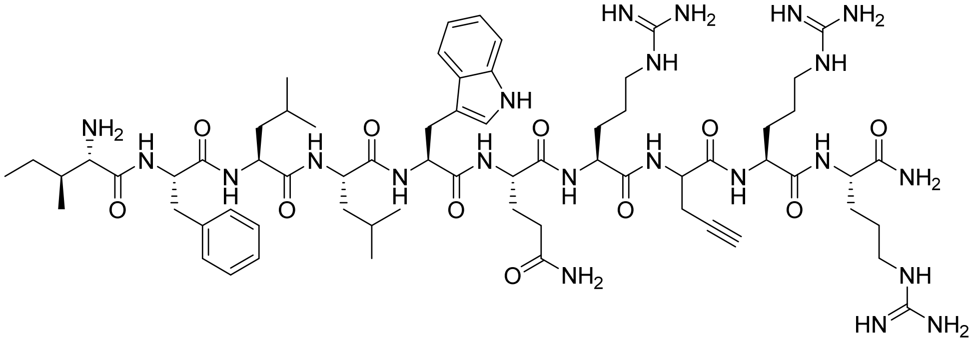

The peptide synthesis was performed according to previously published procedures.[41] In short, solid-phase peptide synthesis was carried out manually in a single-use polypropylene syringe with a filter frit. The syringe was filled with 515 mg Tentagel S Ram (0.24 mmol/g). The resin was swollen in DMF for 1 h before use. All reactions were performed on a mechanical shaker with 600 rpm, soaking approximately 2.5–3.5 mL of freshly prepared solutions into the syringe. Fmoc deprotection steps were performed with piperidine in DMF (2:8, v/v; two runs of 2 min and 10 min, repsectively).Fmoc/Pbf protected amino acids (4 equiv.) were pre-activated in Eppendorf tubes before every coupling step for 5 min with TBTU (3.9 equiv.) and DIPEA (10 equiv.) in DMF under sonication. For each coupling step the resin beads were treated with the activated acid and subsequently washed with DMF (5x) and CH_2Cl_2(5x). The coupling step was monitored with the Kaiser test. The resin beads were then washed again with DMF (5x). The whole procedure (deprotection, coupling, monitoring) was repeated for every monomer until the sequence was completed. The resin was then shrunk with methanol (30 min) and dried under vacuum. Final cleavage of the peptide from the resin and deprotection of the Pbf side chain protecting group were simultaneously performed in TFA/triisopropylsilane (TIS)/H_2O (38:2:1, v/v/v; 3x 2 h). Following the removal of all volatiles under reduced pressure, the crude product was purified by preparative HPLC (20 mL/min, H_2O+0.1% TFA : acetonitrile = 0 min 95:5, 31 min 0:100, 33 min 0:100, 36 min 95:5, 37 min 95:5).

MALDI-MS calcd. for $C_{66}H_{105}N_{22}O_{11}$ ($[M+H]^+$) 1381.8, found 1381.6. HPLC (1 mL/min, acetonitrile: H_2O+0.1%TFA = 0 min 0:100, 30 min 100:0, 35 min 100:0, 36.5 min 0:100): t_R = 12.0 min.

Compound 1

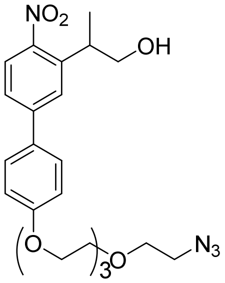

8 (583 mg, 2.14 mmol), **12** (787 mg, 1.95 mmol) and K_2CO_3 (296 mg, 2.14 mmol) were suspended in MeOH (4 mL). The mixture was stirred and heated with a microwave reactor for 10 h at 100 °C. The solvent was removed and the red residue was taken up in NaOH (1 M) and CH_2Cl_2. The two layers were separated. The organic layer was washed with NaOH (1 M). The combined aqueous layers were extracted with CH_2Cl_2 (3x). The combined organic layers were washed with water, dried ($MgSO_4$), filtered, and concentrated. Purification with column chromatography gave pure **1** as yellow oil (726 mg, 78%).

The combined aqueous layers were acidified with conc. HCl and subsequently extracted with CH_2Cl_2 (3x). The combined organic extracts were washed with water, filtered, and concentrated. The residue was pure **8** (119 mg, 20% of what had been used).

R_f = 0.32 (CH_2Cl_2/MeOH 95:5). IR (KBr) 3446 (w), 2873 (w), 2102 (m), 1604 (m), 1583 (w), 1515 (s), 1478 (w), 1348 (w), 1292 (m), 1248 (s), 1116 (m), 1059 (m), 827 (m), 632 (m), 536 (m) cm^{-1}. ^1H NMR (500 MHz, $CDCl_3$): ∂ 7.85 (d, J = 8.5 Hz, 1 H), 7.61 (s, 1 H), 7.55–7.45 (m, 3 H), 7.02 (d, J = 8.8 Hz, 2 H), 4.21–4.16 (m, 2 H), 3.94–3.58 (m, 15 H), 3.37 (t, J = 5.0 Hz, 2 H), 1.81 (bs, 1 H), 1.38 (d, J = 6.9 Hz, 3 H). ^{13}C NMR (125 MHz, $CDCl_3$): ∂ 159.4, 148.8, 145.4, 140.0, 131.6, 128.4, 126.2, 125.2, 125.0, 115.2, 70.8, 70.68, 70.67, 70.6, 70.0, 69.6, 67.9, 67.5, 50.6, 36.4, 17.6. ESI-MS m/z 497.20 (100, $[M+Na]^+$), 513.18 (10, $[M+K]^+$).HRMS m/z calcd. for $C_{23}H_{30}N_4NaO_7$ ($[M+Na]^+$) 497.20067, found 497.20128.

Compound 2

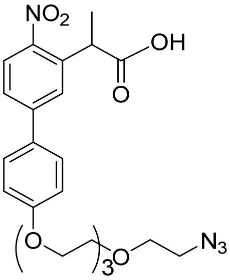

13 (219 mg, 403 µmol) was dissolved in 5% TFA in CH_2Cl_2 (v/v; 38 mL). The mixture was stirred under exclusion of light for 20 h. Water was added and the mixture was extracted with CH_2Cl_2 (3x). The combined organic layers were dried ($MgSO_4$), filtered, and concentrated *in vacuo* to give pure **2** as a highly viscous oil (197 mg, 100%).

IR (neat) 2921 (w), 2877 (w), 2103 (m), 1731 (m), 1604 (s), 1585 (m), 1516 (s), 1343 (s), 1249 (s), 1184 (m), 1121 (m), 943 (w), 827 (m) cm^{-1}. ^1H NMR (500 MHz, $CDCl_3$) ∂ 8.06 (d, *J* = 8.5 Hz, 1 H), 7.62 (d, *J* = 1.9 Hz 1 H), 7.60–7.46 (m, 3 H), 7.06–6.99 (m, 2 H), 4.46 (q, *J* = 7.1 Hz, 1 H), 4.18 (m, 2 H), 3.92–3.86 (m, 2 H), 3.78–3.63 (m, 10 H), 3.40–3.34 (m, 2 H), 1.68 (d, *J* = 7.1 Hz, 3 H). ^{13}C NMR (125 MHz, $CDCl_3$) ∂ 176.9, 159.7, 146.8, 146.2, 135.5, 131.1, 128.6, 128.0, 126.1, 126.0, 115.3, 70.9, 70.72, 70.71, 70.68, 70.0, 69.7, 67.6, 50.7, 41.6, 17.6. HRMS m/z calcd. for $C_{23}H_{28}N_4NaO_8$ ($[M+Na]^+$) 511.17993, found 511.18034.

Caged Lumiracoxib 3

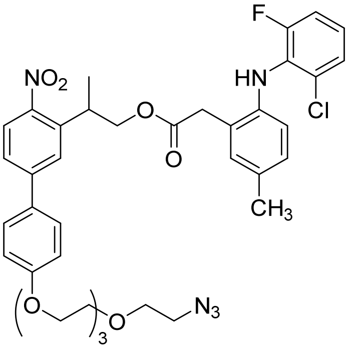

Under an atmosphere of N_2, **1** (52.4 mg, 110 µmol) was dissolved in dry CH_2Cl_2 (10 mL). At 0 °C, *N*,*N'*-dicyclohexylcarbodiimide (34.2 mg, 166 µmol), 4-dimethylaminopyridine (1.3 mg, 11 µmol), and Lumiracoxib (64.9 mg, 0.221 mmol) were added. The resulting suspension was stirred at 0 °C for 10 min and subsequently for 20 h at rt. Saturated $NaHCO_3$ solution was added and the mixture was extracted with CH_2Cl_2 (4x). The combined organic layers were dried ($MgSO_4$), filtered, and concentrated. The crude residue was purified by column chromatography (hexanes/EtOAc 7:3 → 1:1). The product containing fractions were suspended in acetonitrile and filtered with a Pasteur pipette filled with silica to give pure **3** as a slightly yellow solid (66.0 mg, 80%).

R_f = 0.51 (hexanes/EtOAc 3:7). IR (neat) 2883 (w), 2103 (m), 1730 (s), 1604 (m), 1584 (m), 1514 (s), 1479 (m), 1348 (m), 1291 (m), 1245 (s), 1137 (m), 1037 (w), 1046 (w), 906 (m), 827 (m), 764 (m), 715 (m) cm^{-1}. ^1H NMR (500 MHz, $CDCl_3$) ∂ 7.83 (d, *J* = 8.5 Hz, 1 H), 7.52 (d, *J* = 1.9 Hz, 1 H), 7.48–7.41 (m, 3 H), 7.18 (dt, *J* = 8.1 Hz, 1.3 Hz, 1 H), 7.02–6.93 (m, 3 H), 6.91–6.85 (m, 3 H), 6.63 (bs, 1 H), 6.56 (dd, *J* = 8.0 Hz, 3.2 Hz, 1 H), 4.41–4.31 (m, 2 H), 4.20–4.13 (m, 2 H), 3.95–3.85 (m, 3 H), 3.74–3.63 (m, 12 H), 3.38 (t, *J* = 5.0 Hz, 2 H), 2.21 (s, 3 H), 1.38 (d, *J* = 7.0 Hz, 3 H). ^{13}C NMR (125 MHz, $CDCl_3$): ∂ 172.2, 159.4, 155.3 (d, *J* = 248 Hz), 148.5, 145.4, 139.7, 137.8, 131.6, 131.4, 131.2, 129.6 (d, *J* = 13.1 Hz), 128.42, 128.39, 127.2 (d, *J* = 4.36 Hz), 125.9, 125.38 (d, *J* = 3.43 Hz), 125.35, 125.0, 123.9, 121.9 (d, *J* = 8.66 Hz), 118.3 (d, *J* = 3.05 Hz), 115.2, 114.8 (d, *J* = 20.2 Hz), 70.9, 70.71, 70.69, 70.66, 70.0, 69.6, 68.6, 67.6, 50.7, 38.2, 33.2, 20.5, 17.8. ^{19}F NMR (375 MHz, $CDCl_3$): ∂ -118.9. HRMS m/z calcd. for $C_{38}H_{41}ClFN_5NaO_8$ ($[M+Na]^+$) 772.25199, found 772.25115. HPLC (1 mL/min, acetonitrile : H_2O+0.1%TFA = 0 min 10:90, 27 min 100:0, 31 min 100:0, 36 min 1:99, 38 min 1:99, 40 min 10:90, 41 min 10:90): t_R = 22.6 min.

Caged Celecoxib 4

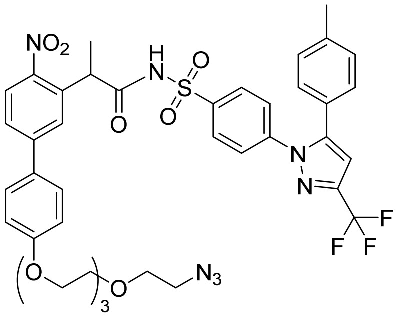

1-(3-Dimethylaminopropyl)-3-ethylcarbodiimide hydrochloride (EDC, 15.5 mg, 81.1 µmol) was added to a stirred solution of **2** (19.8 mg, 40.5 µmol), 4-dimethylaminopyridine (DMAP, 0.5 mg, 4 µmol) and Celecoxib (16.5 mg, 43.3 µmol) in CH_2Cl_2 (1.5 mL) and the resulting reaction mixture was stirred at rt under exclusion of light for 2 h. Saturated NH_4Cl solution and EtOAc were added. The layers were separated and the aqueous layer was extracted with EtOAc (3x). The combined organic layers were washed with brine, dried ($MgSO_4$), filtered, and concentrated. The crude residue was adsorbed to silica and purified by column chromatography (hexanes/EtOAc 5:1 → 1:2) to yield pure **4** (18.5 mg, 54%) as a yellowish solid.

R_f = 0.39 (CH_2Cl_2/MeOH 95:5). IR (neat) 2923 (w), 2103 (s), 1719 (m), 1603 (m), 1516 (m), 1451 (m), 1344 (s), 1237 (s), 1185 (m), 1159 (s), 1127 (s), 1094 (s), 1024 (m), 947 (m), 821 (s) cm^{-1}. ^1H NMR (500 MHz, $CDCl_3$) ∂ 8.72 (bs, 1 H), 7.99–7.91 (m, 3 H), 7.59 (dd, *J* = 8.4 Hz, 1.9 Hz, 1 H), 7.49–7.35 (m, 5 H), 7.16 (d, *J* = 8.0 Hz, 2 H), 7.06 (d, *J* = 8.0 Hz, 2 H), 6.96 (d, *J* = 8.8 Hz, 2 H), 6.73 (s, 1 H), 4.24 (q, *J* = 6.9 Hz, 1 H), 4.15 (t, *J* = 4.8 Hz, 2 H), 3.89 (t, *J* = 4.8 Hz, 2 H), 3.78–3.62 (m, 10 H), 3.38 (t, *J* = 5.0 Hz, 2 H), 2.38 (s, 3 H), 1.51 (d, *J* = 6.9 Hz, 3 H). ^{13}C NMR (125 MHz, $CDCl_3$): 169.8, 159.9, 147.0, 146.8, 145.3, 144.3, 144.0, 143.4, 139.9, 137.4, 134.0, 130.3, 129.8, 129.4, 128.7, 128.5, 127.1, 126.7, 125.9, 125.6, 125.0, 115.3, 106.5, 70.9, 70.8, 70.73, 70.70, 70.1, 69.6, 67.6, 50.7, 41.6, 21.3, 17.3. HRMS m/z calcd. for $C_{40}H_{40}F_3N_7NaO_9S$ ($[M+Na]^+$) 874.24525, found 874.24481. HPLC (1 mL/min, acetonitrile : H_2O+0.1%TFA = 0 min 10:90, 27 min 100:0, 31 min 100:0, 36 min 1:99, 38 min 1:99, 40 min 10:90, 41 min 10:90): t_R = 21.0 min.

Caged Targeted Celecoxib 5

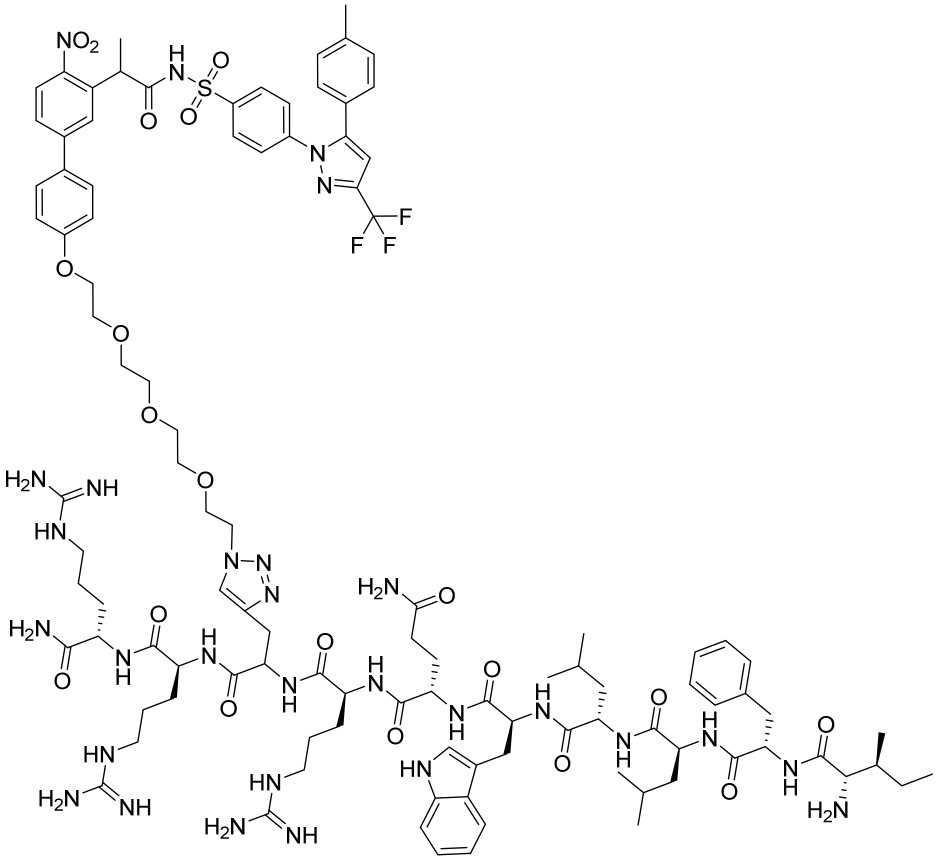

$CuSO_4$ (0.1 M in H_2O, 23.1 µL, 2.31 µmol) and sodium ascorbate (0.1 M in H_2O, 46.3 µL, 4.63 µmol) were mixed and shaken for 10 min. The red slurry was added to a solution of **4** (10.9 mg, 12.7 µmol) and targeting peptide IFLLQR(Pra)RR (16 mg, 11.6 µmol) in a mixture of THF/H_2O (2:1 v/v; 9 mL). The solution was stirred at rt for 23 h. To drive the reaction to completion, $CuSO_4$ (0.1 M in H_2O, 23.1 µL, 2.31 µmol) and sodium ascorbate (0.1 M in H_2O, 46.3 µL, 4.63 µmol) were added, the temperature increased to 60 °C, and stirring continued for 7 h. The solvents were removed by evaporation. The residue was dissolved in acetonitrile in H_2O with 0.1% TFA and purified by preparative HPLC (20 mL/min, H_2O+0.1% TFA : acetonitrile = 0 min 95:5, 31 min 0:100, 33 min 0:100, 36 min 95:5, 37 min 95:5).

MALDI-MS calcd. for $C_{106}H_{145}F_3N_{29}O_{20}S$ ($[M+H]^+$) 2233.1, found 2233.5. HPLC (1 mL/min, acetonitrile : H_2O+0.1%TFA = 0 min 10:90, 12 min 53:47, 18 min 59:41, 27 min 100:0, 31 min 100:0, 36 min 1:99, 38 min 1:99, 40 min 10:90, 41 min 10:90): t_R = 14.9 min.

3.5.4 Spectra

In the following all previously unreported ^1H, ^{13}C and ^{19}F NMR spectra are shown. For the compounds analyzed by HPLC the UV traces at λ=260 nm are shown.

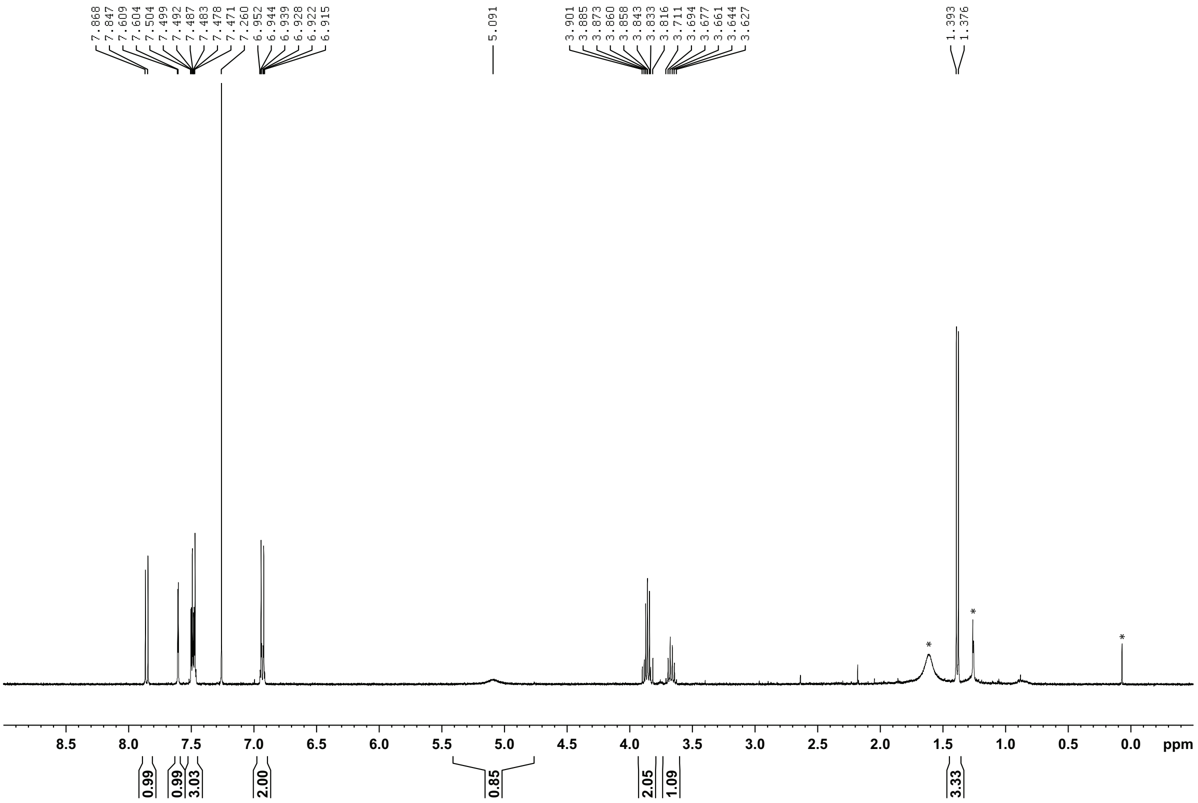

Figure S10. ^{1}H-NMR spectrum of **8** in CDCl$_3$.

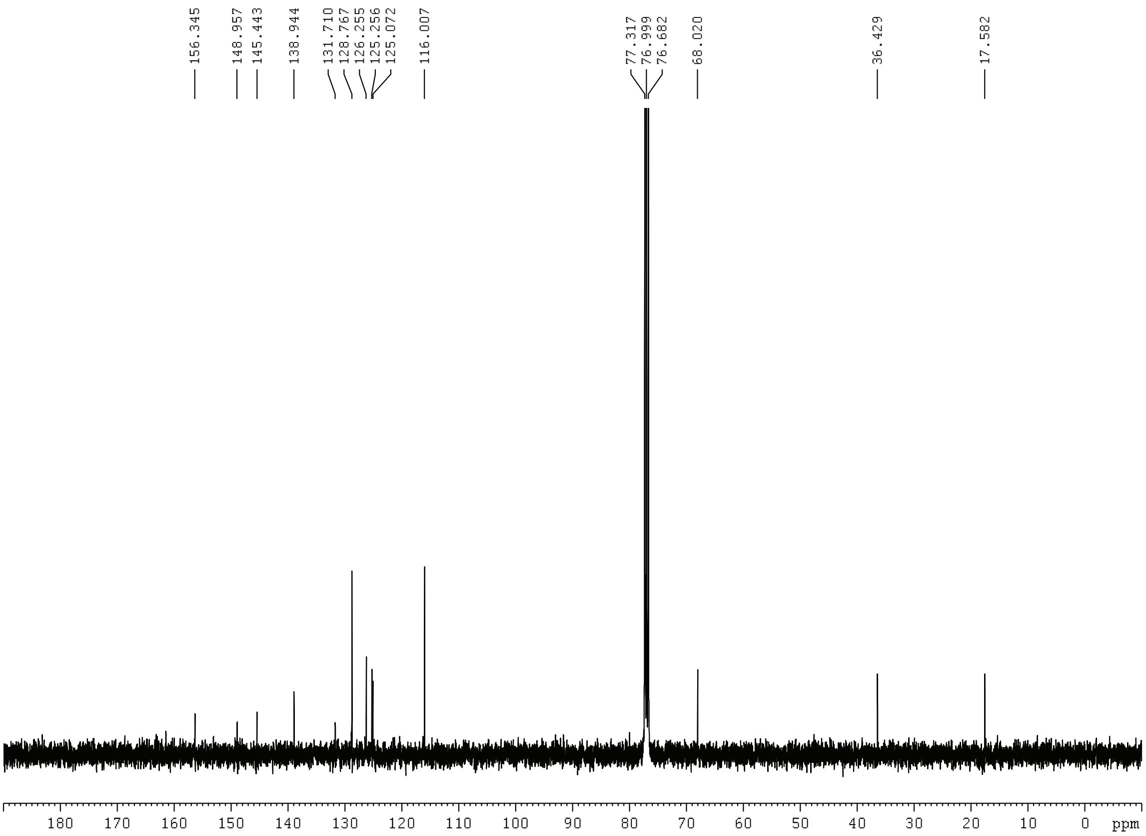

Figure S11. ^{13}C-NMR spectrum of **8** in CDCl$_3$.

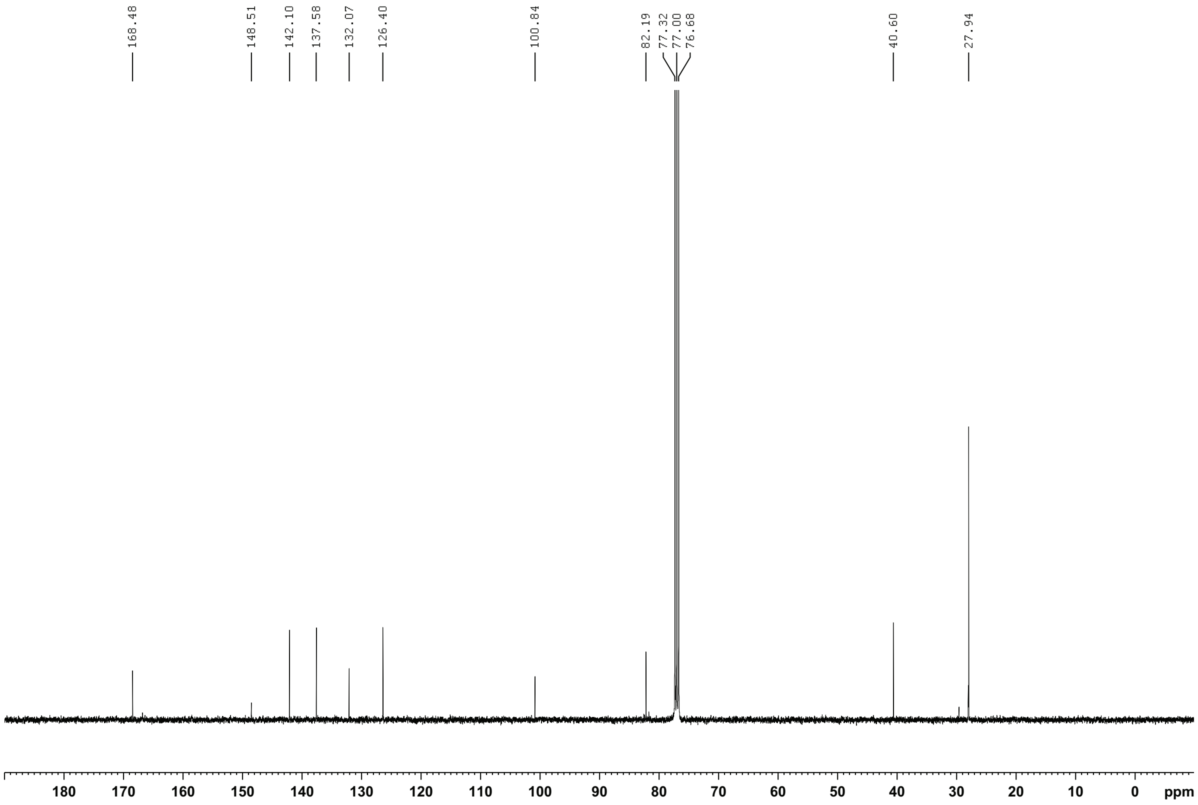

Figure S12. ^{13}C--NMR spectrum of **9** in $CDCl_3$.

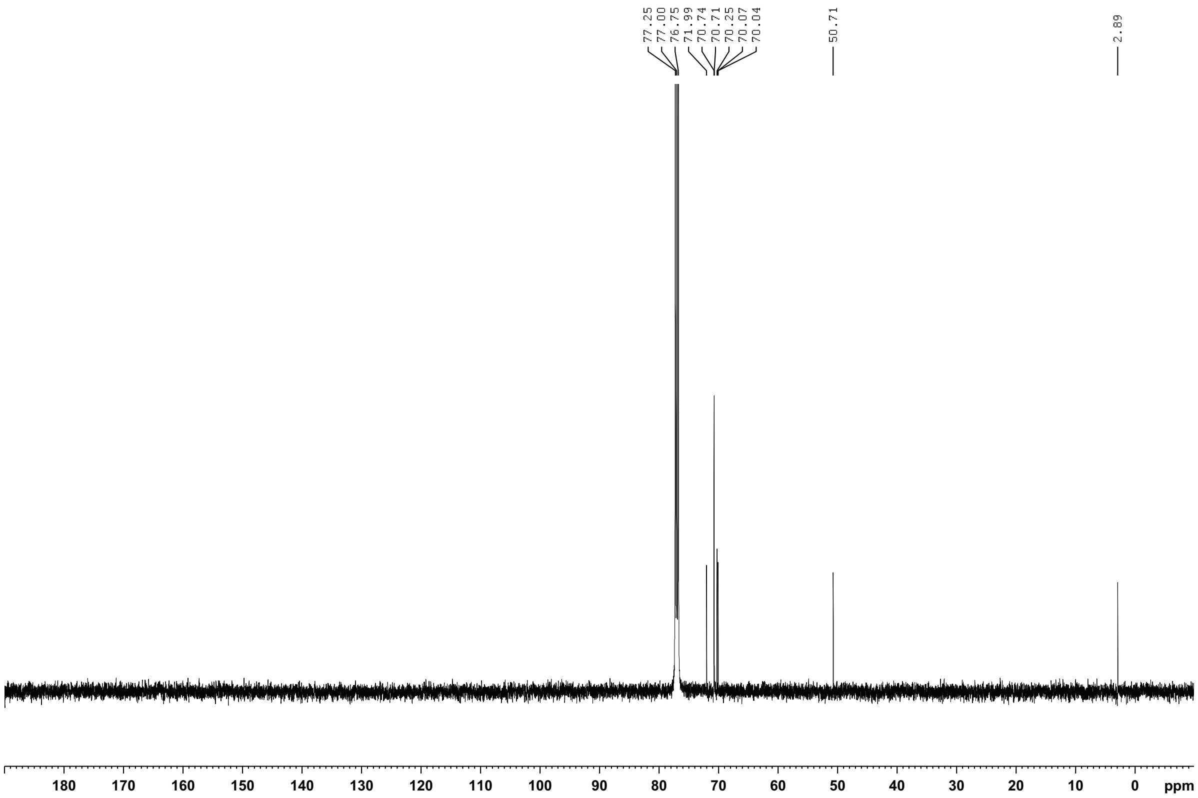

Figure S13. ^{13}C-NMR spectrum of **12** in $CDCl_3$.

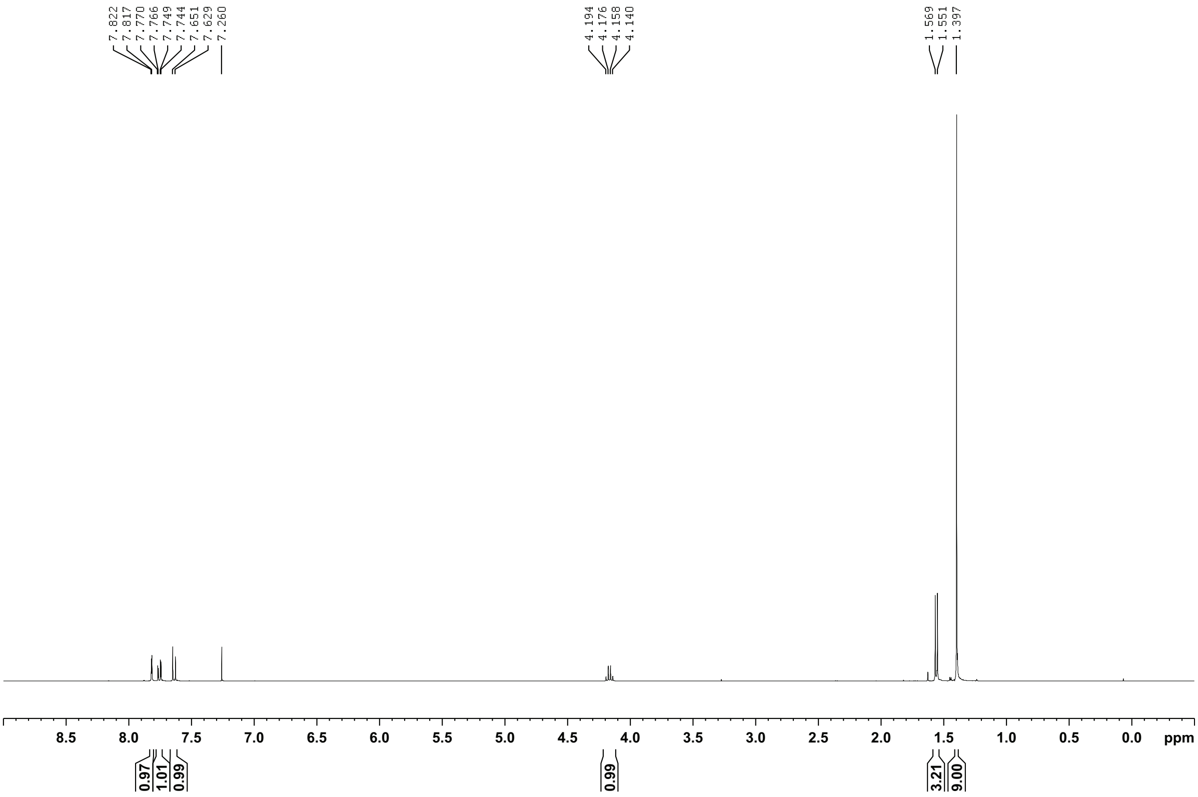

Figure S14. ^{1}H-NMR spectrum of **10** in CDCl$_3$.

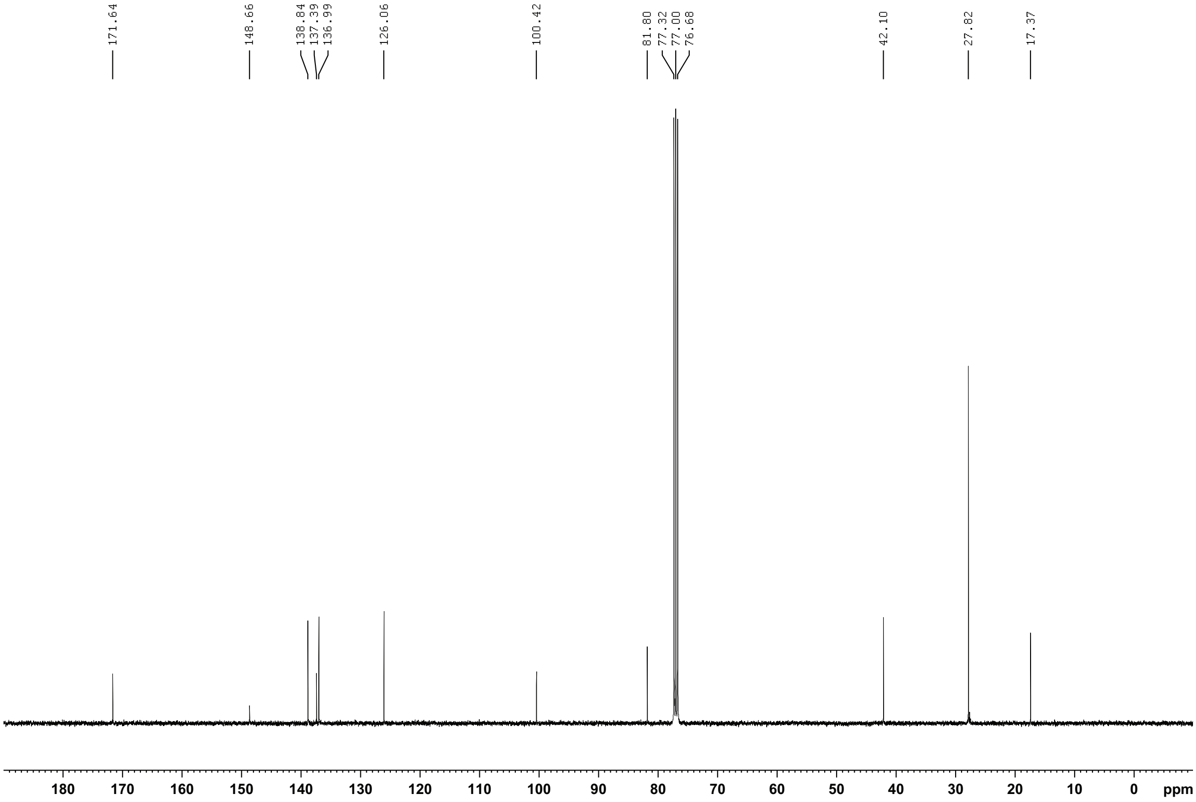

Figure S15. ^{13}C-NMR spectrum of **10** in CDCl$_3$.

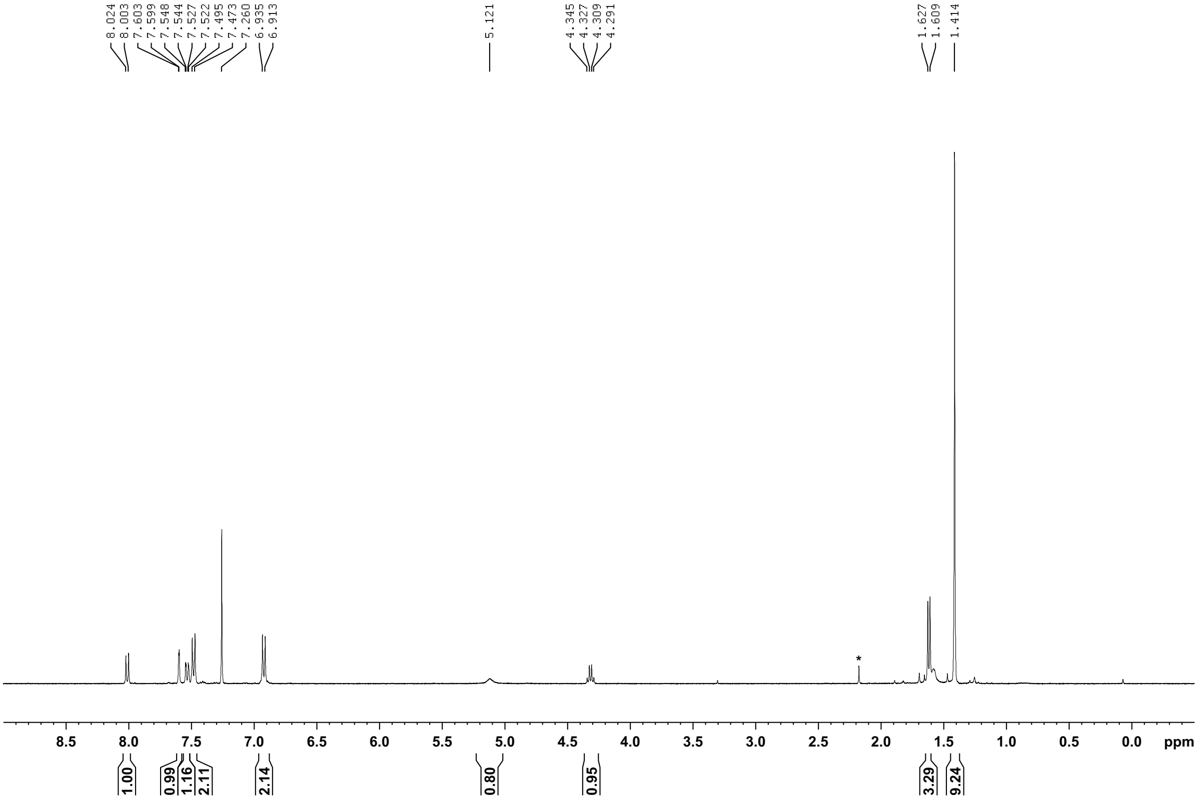

Figure S16. ^{1}H-NMR spectrum of **11** in CDCl$_3$.

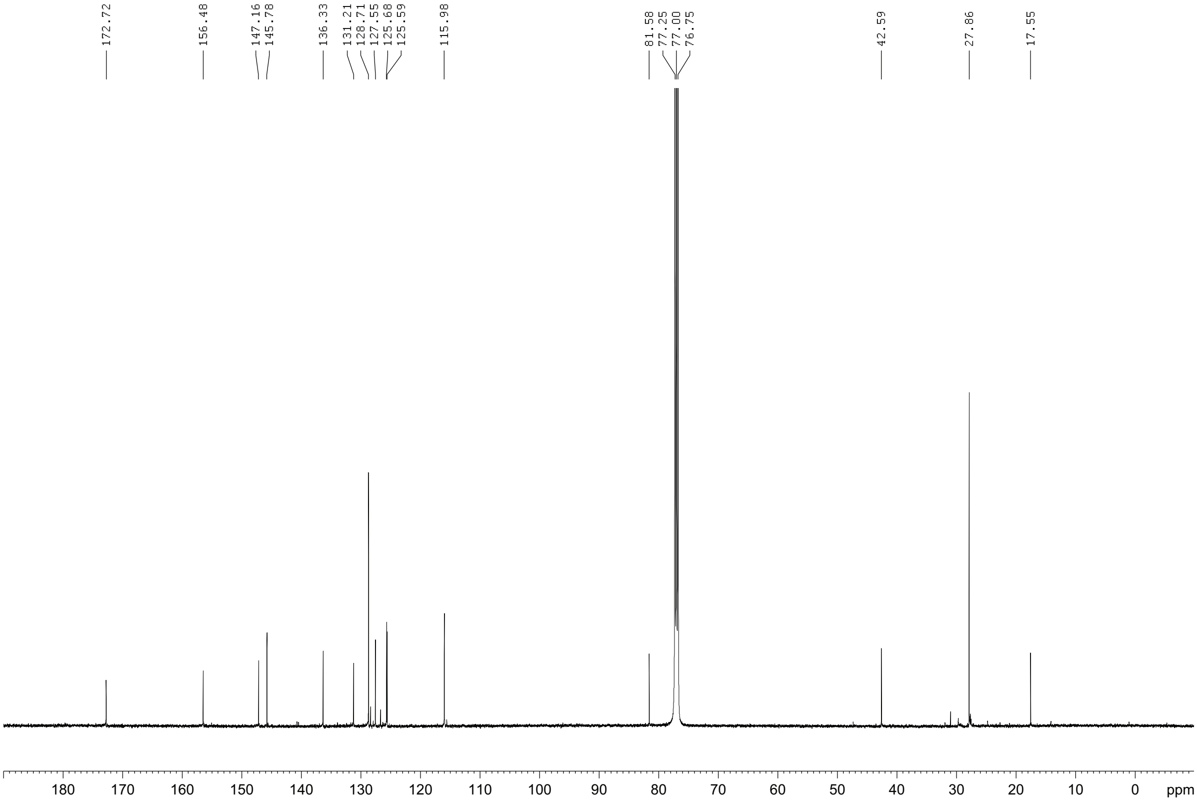

Figure S17. ^{13}C-NMR spectrum of **11** in CDCl$_3$.

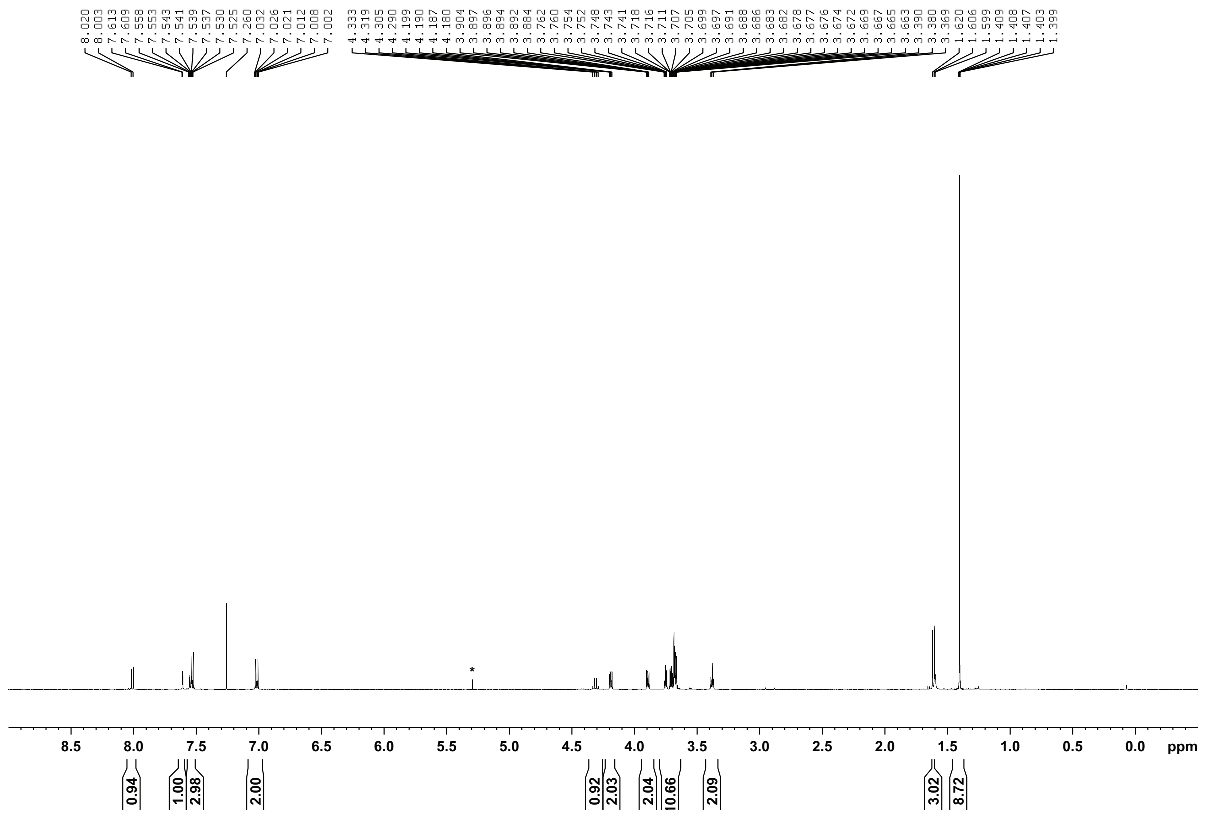

Figure S18. ^{1}H-NMR spectrum of **13** in $CDCl_3$.

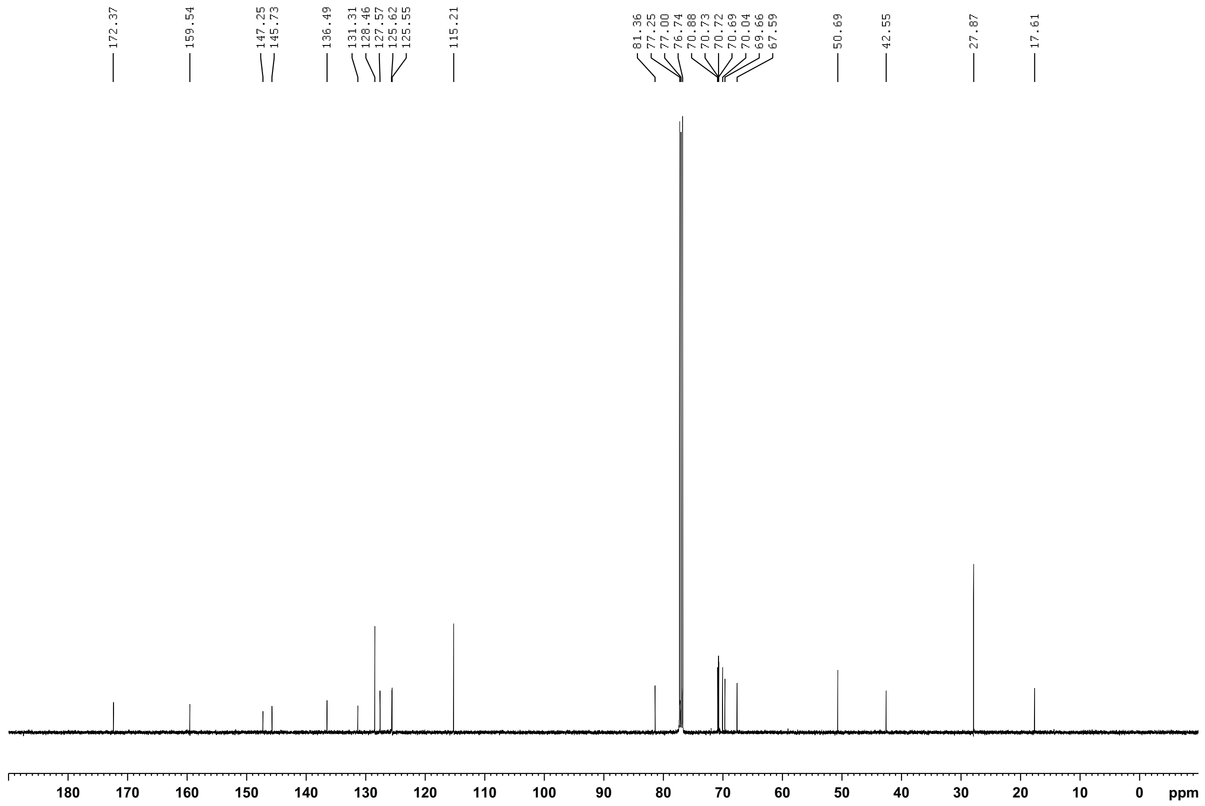

Figure S19. ^{13}C-NMR spectrum of **13** in $CDCl_3$.

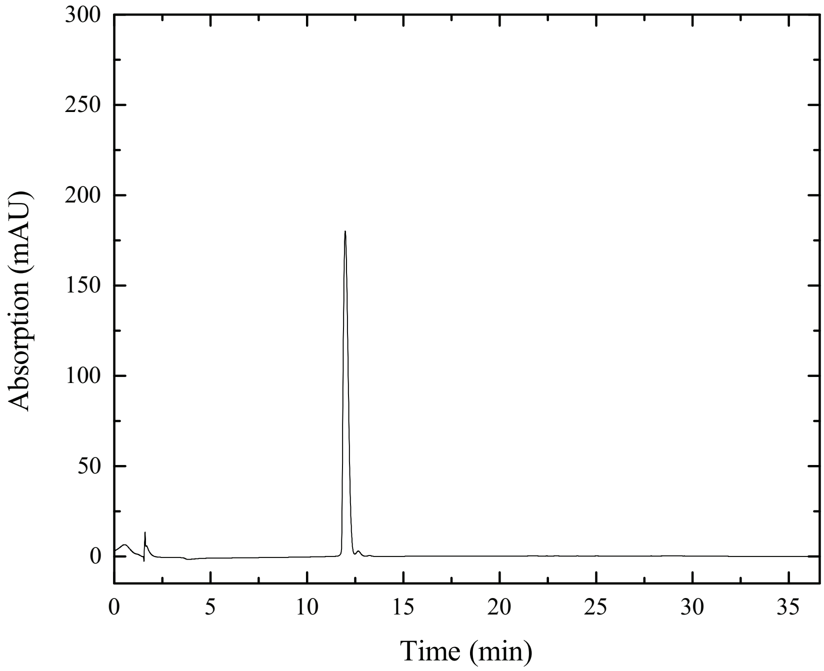

Figure S20. Analytical HPLC trace of the T**argeting Peptide IFLLQR(Pra)RR**.

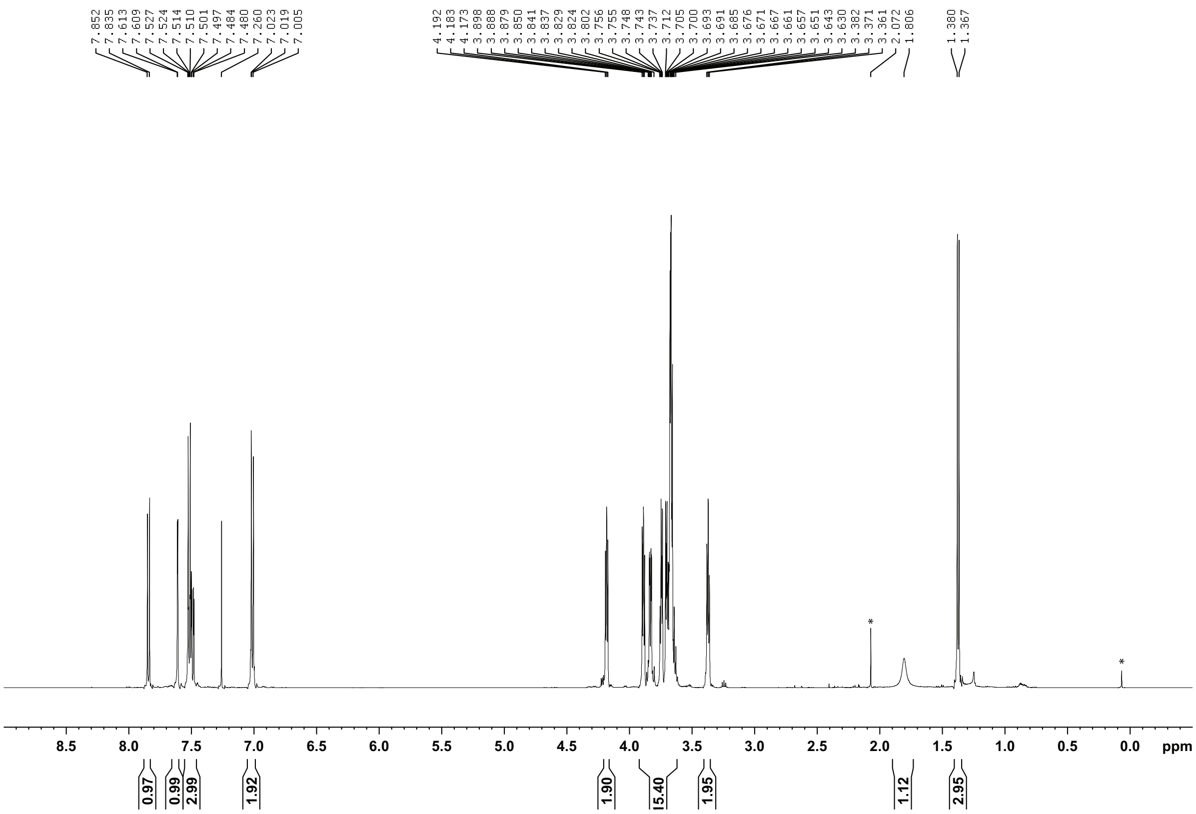

Figure S21. ^{1}H-NMR spectrum of compound **1**in CDCl$_3$.

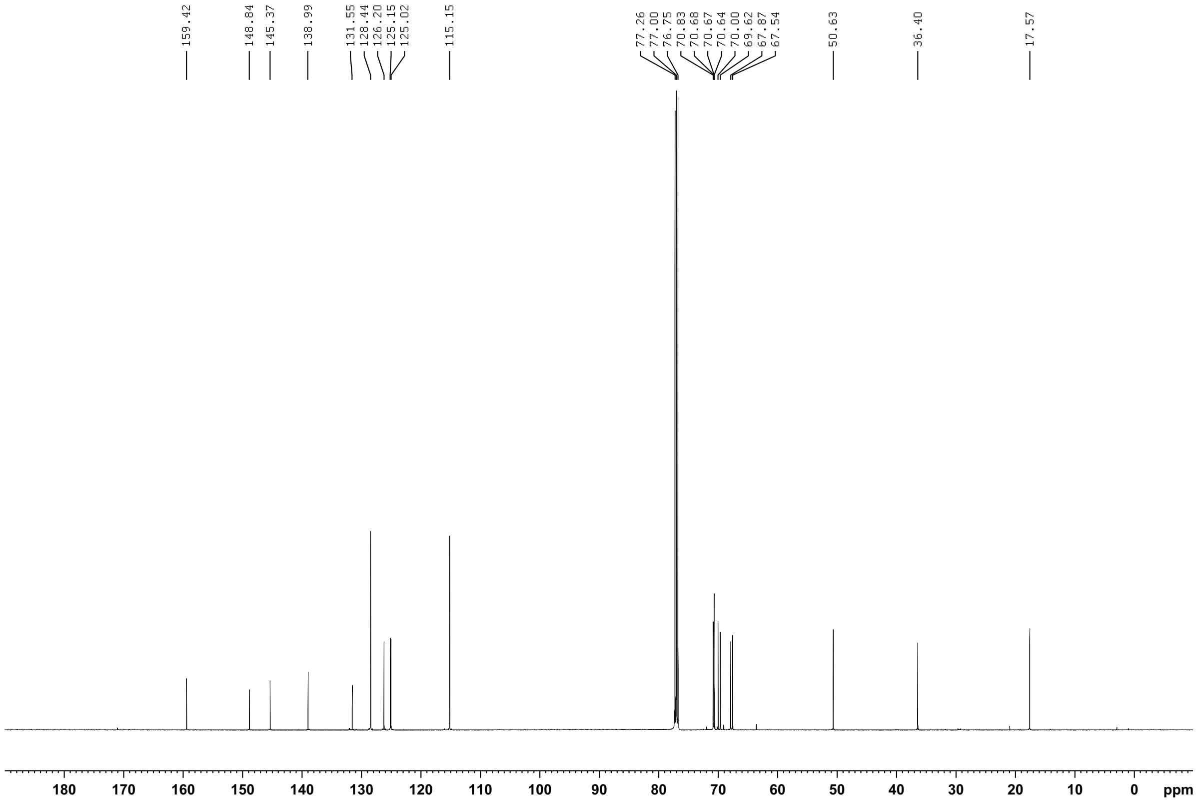

Figure S22. ^{13}C-NMR spectrum of compound **1** in CDCl$_3$.

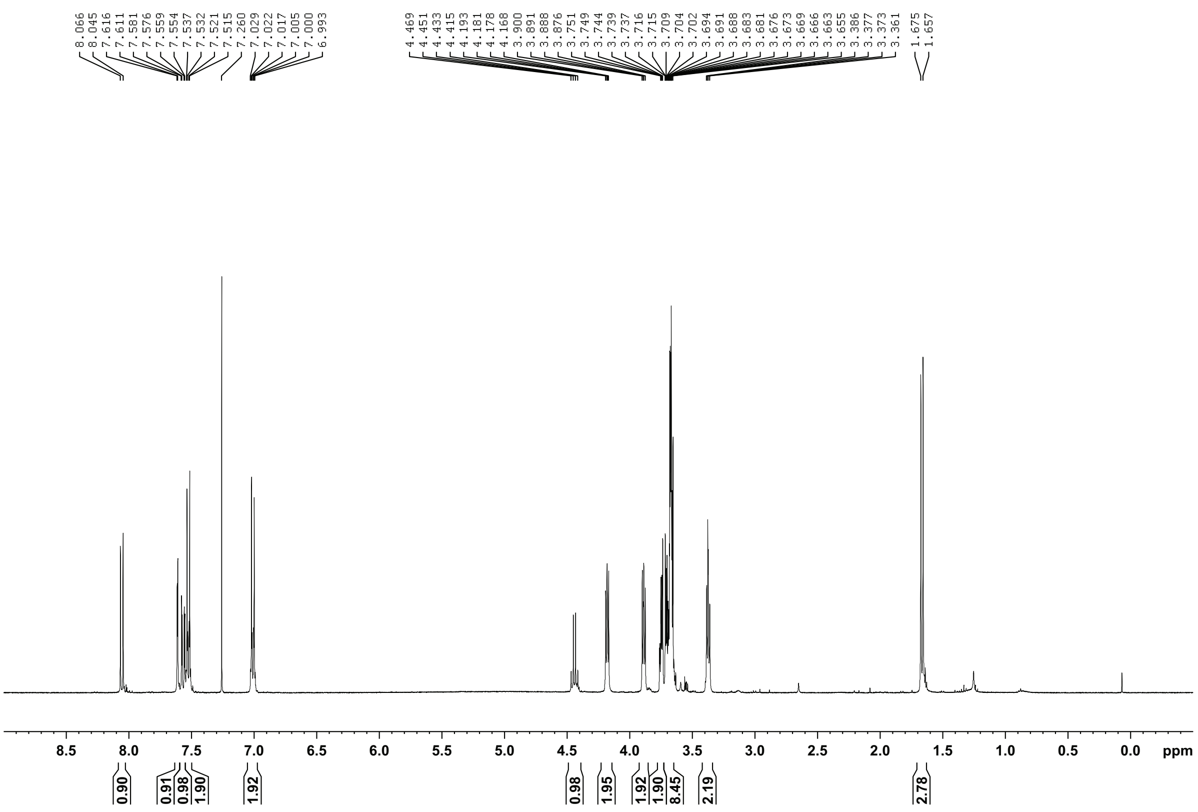

Figure S23. ^{1}H-NMR spectrum of compound **2** in $CDCl_3$.

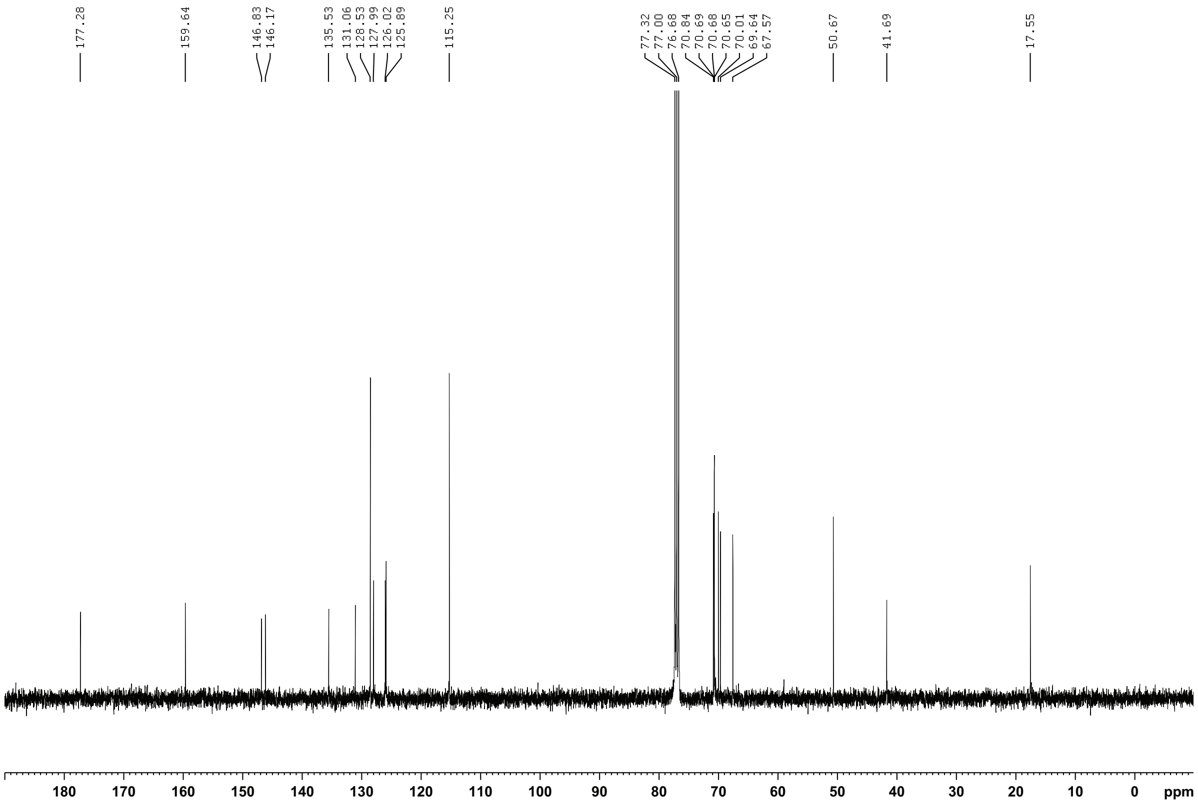

Figure S24. ^{13}C-NMR spectrum of compound **2** in $CDCl_3$.

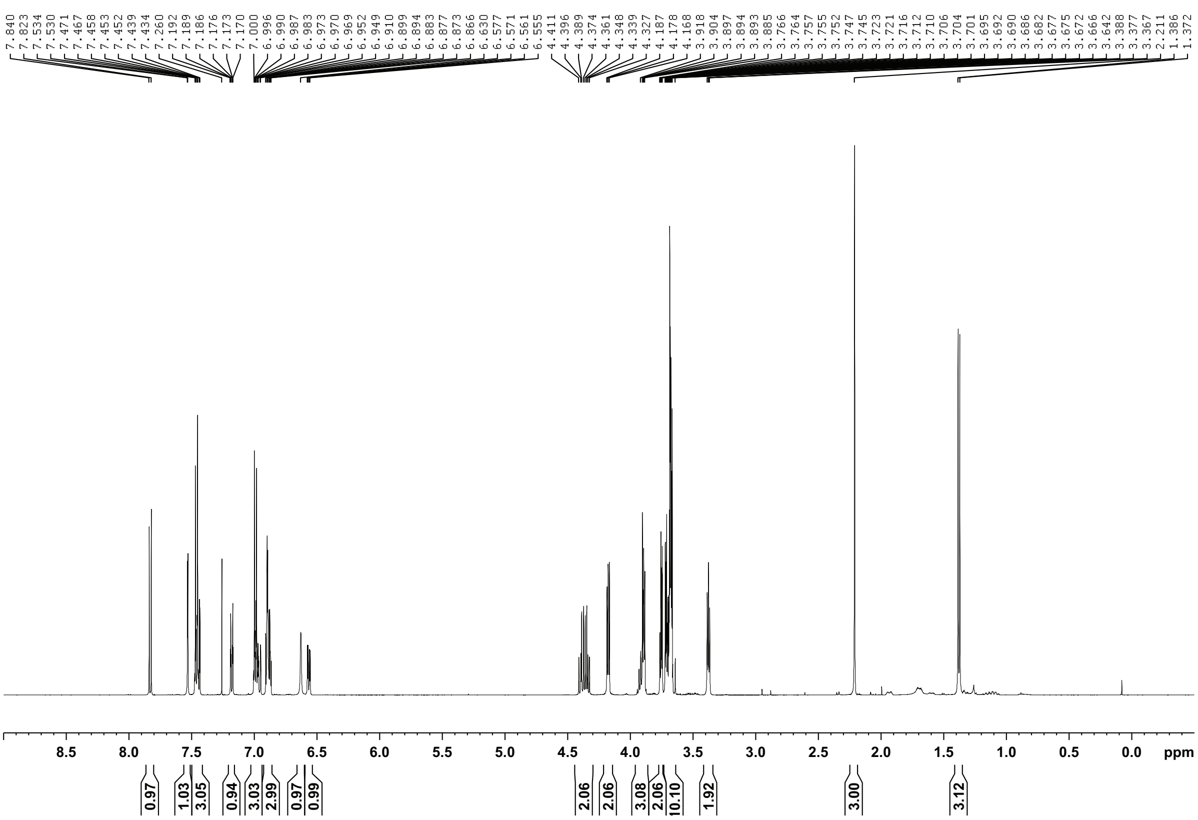

Figure S25. ^{1}H-NMR spectrum of compound **3** in $CDCl_3$.

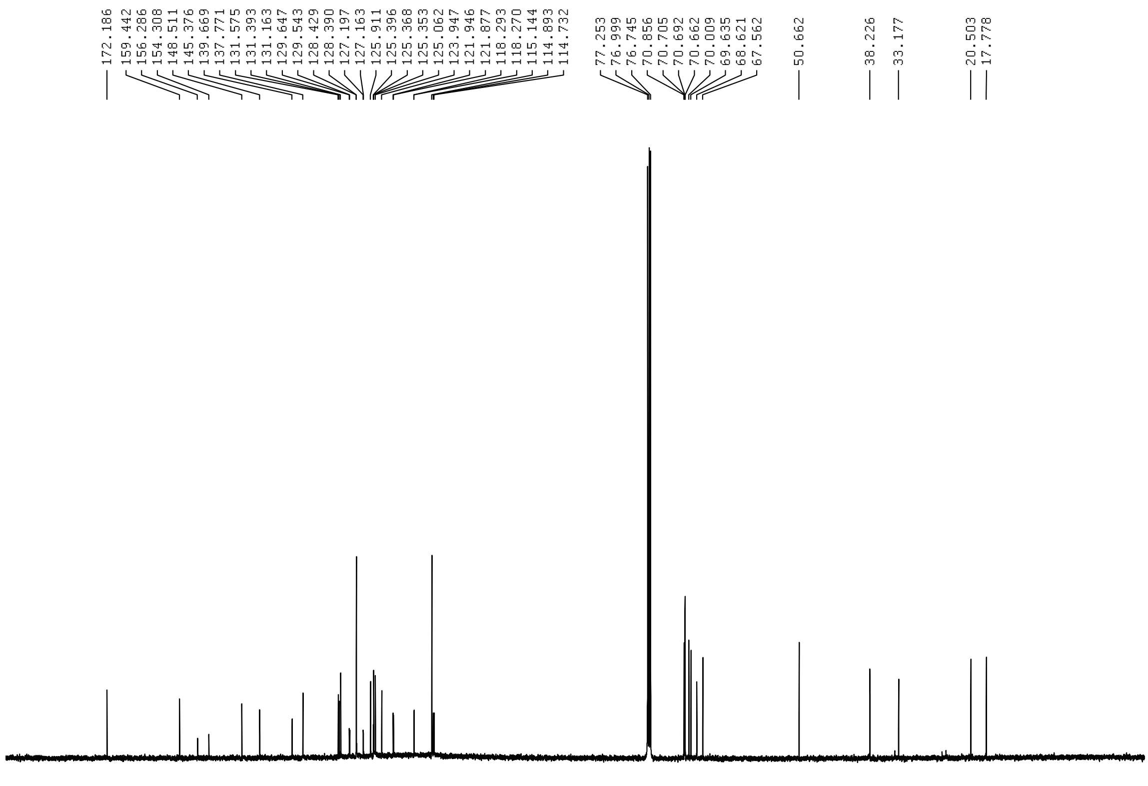

Figure S26. ^{13}C-NMR spectrum of compound **3** in $CDCl_3$.

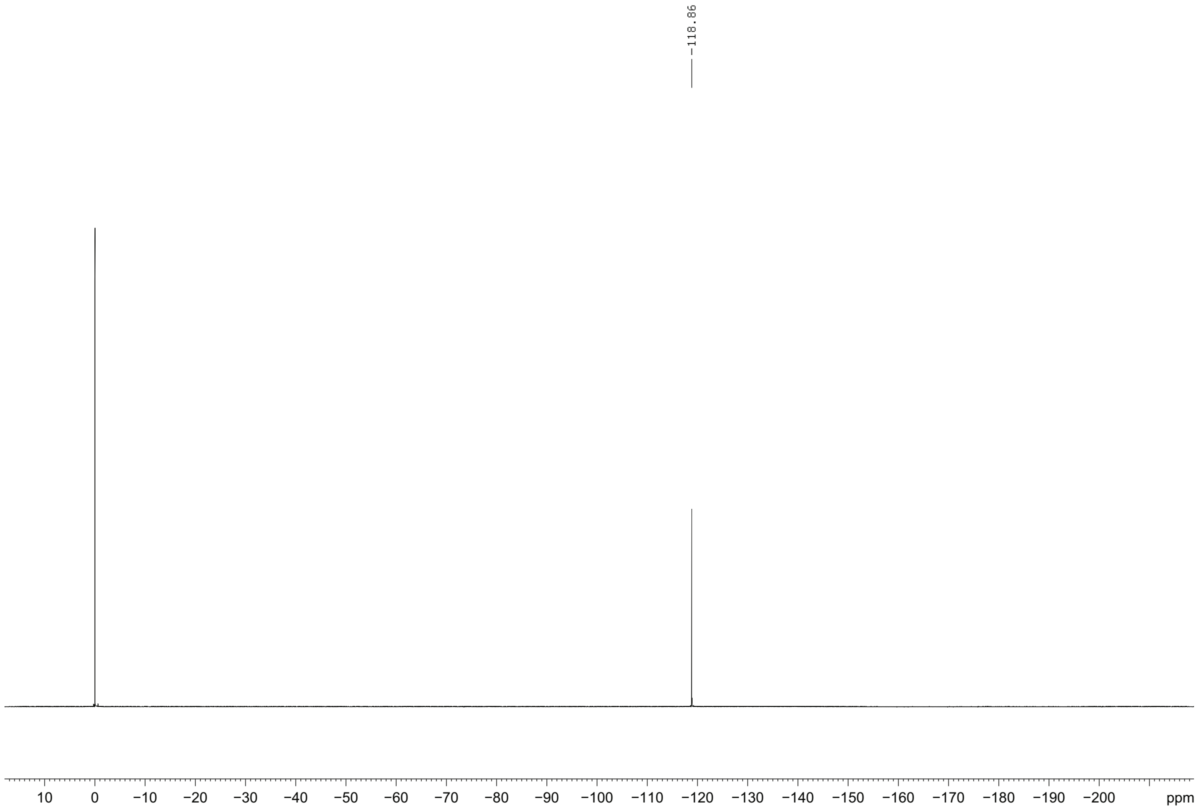

Figure S27. ^{19}F-NMR spectrum of compound **3** in $CDCl_3$ with CCl_3F as standard.

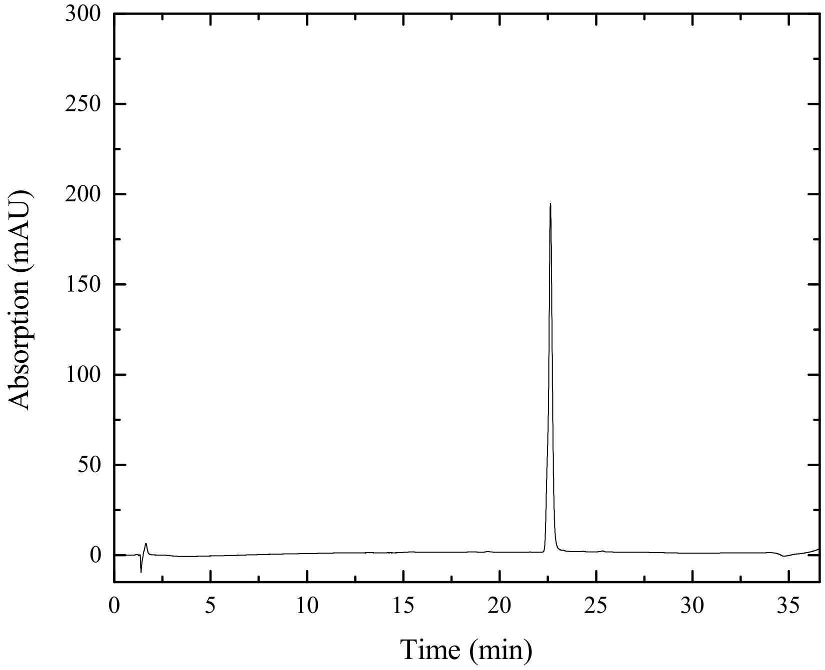

Figure S28. Analytical HPLC trace of compound **3**.

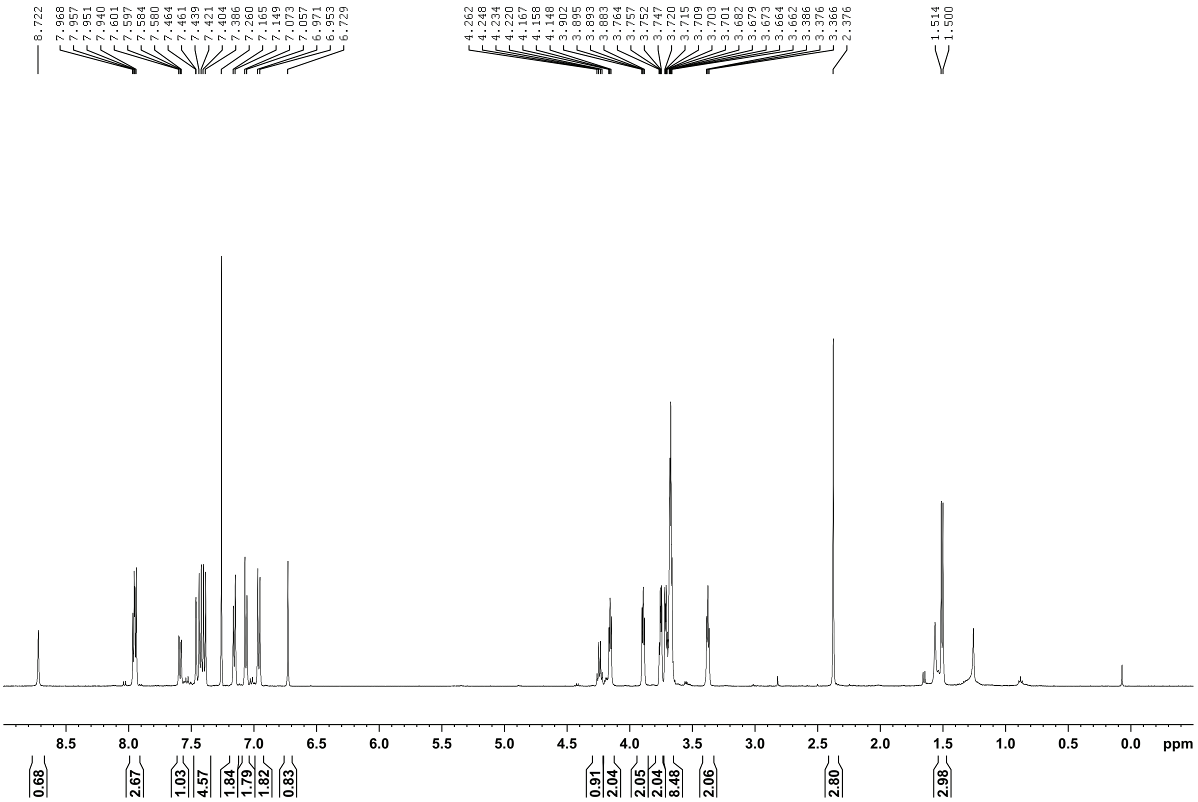

Figure S29. ^{1}H-NMR spectrum of compound **4** in $CDCl_3$.

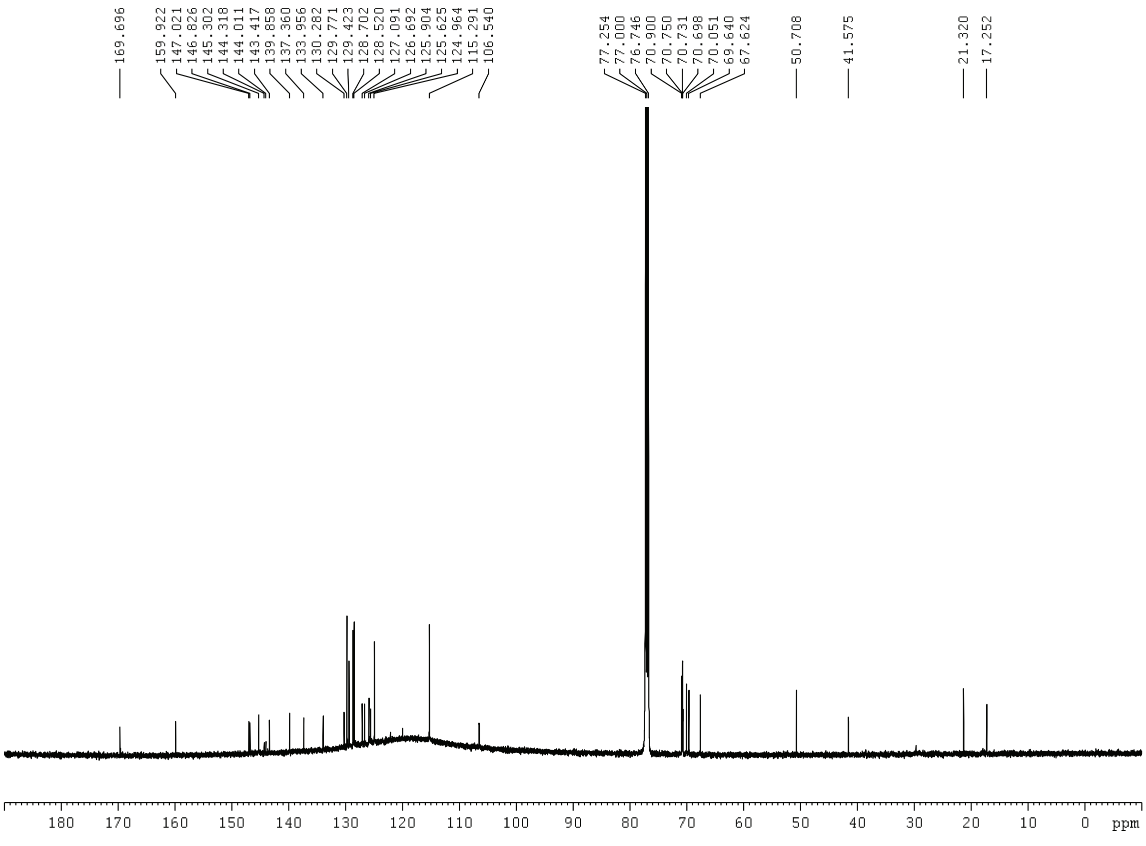

Figure S30. ^{13}C-NMR spectrum of compound **4** in $CDCl_3$.

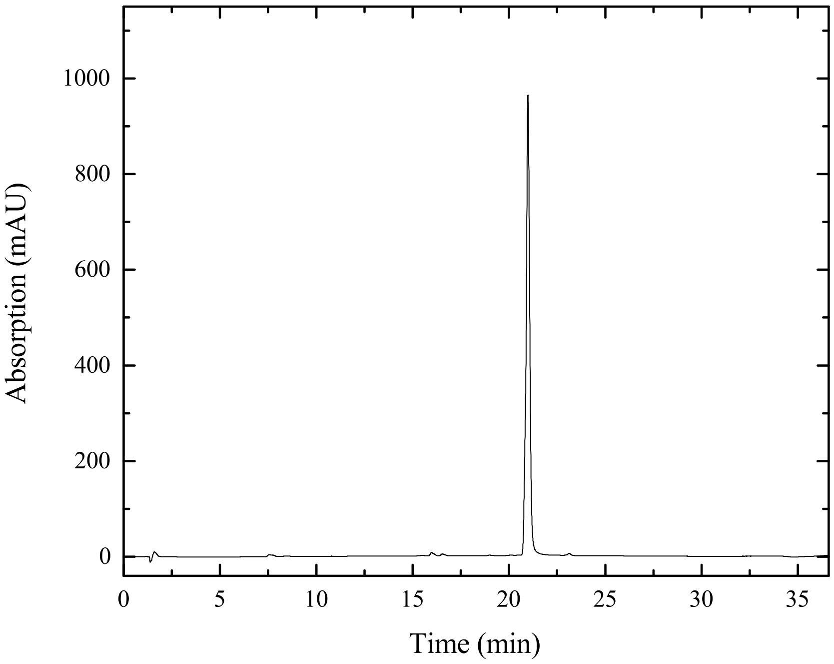

Figure S31. Analytical HPLC trace of compound **4**.

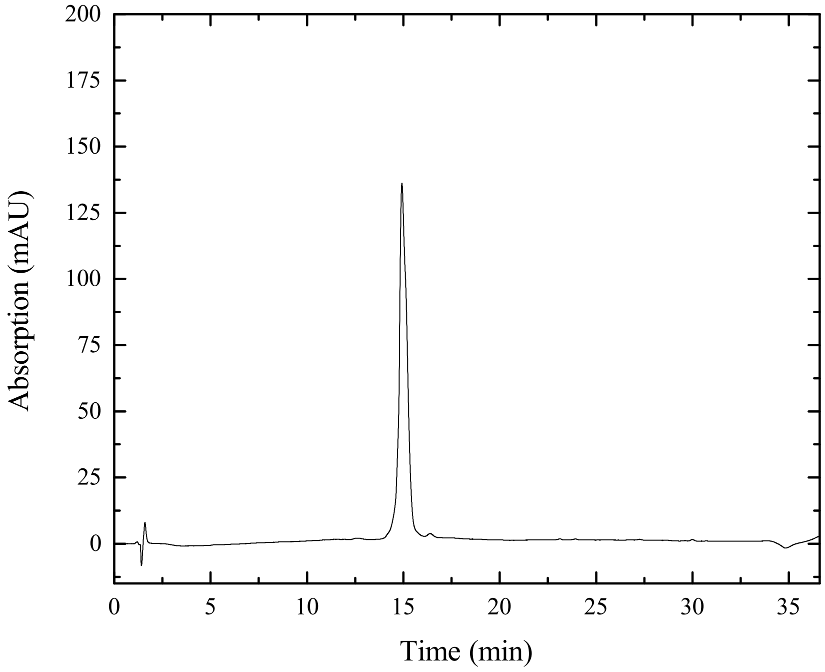

Figure S32. Analytical HPLC trace of compound **5**.

3.6 References and Notes

[1] F. A. Sinicrope, *Mol. Carcinog.* **2006**, *45*, 447–454.

[2] a) H. Nam, N. E. Lewis, J. A. Lerman, D.-H. Lee, R. L. Chang, D. Kim, B. O. Palsson, *Science* **2012**, *337*, 1101–1104; b) X. Chen, D. W. Taylor, C. C. Fowler, J. E. Galan, H.-W. Wang, S. L. Wolin, *Cell* **2013**, *153*, 166–177; c) P. K. Mazur, N. Reynoird, P. Khatri, Jansen, Pascal W. T. C., A. W. Wilkinson, S. Liu, O. Barbash, Van Aller, Glenn S., M. Huddleston, D. Dhanak et al., *Nature* **2014**, *510*, 283–287.

[3] D. Phillips, *Photochem. Photobiol. Sci.* **2010**, *9*, 1589–1596.

[4] C. Brieke, F. Rohrbach, A. Gottschalk, G. Mayer, A. Heckel, *Angew. Chem. Int. Ed.* **2012**, *51*, 8446–8476.

[5] a) J. Broichhagen, I. Jurastow, K. Iwan, W. Kummer, D. Trauner, *Angew. Chem. Int. Ed.* **2014**, DOI: 10.1002/anie.201403666; b) X. Chen, S. Wehle, N. Kuzmanovic, B. Merget, U. Holzgrabe, B. König, C. A. Sotriffer, M. Decker, *ACS Chem. Neurosci.* **2014**, *5*, 377–389.

[6] W. A. Velema, W. Szymanski, B. L. Feringa, *J. Am. Chem. Soc.* **2014**, *136*, 2178–2191.

[7] a) J. Croissant, M. Maynadier, A. Gallud, H. Peindy N'Dongo, J. L. Nyalosaso, G. Derrien, C. Charnay, J.-O. Durand, L. Raehm, F. Serein-Spirau et al., *Angew. Chem. Int. Ed.* **2013**, *52*, 13813–13817; b) Q. Lin, Q. Huang, C. Li, C. Bao, Z. Liu, F. Li, L. Zhu, *J. Am. Chem. Soc.* **2010**, *132*, 10645–10647; c) L. Sun, Y. Yang, C.-M. Dong, Y. Wei, *Small* **2011**, *7*, 401–406; d) S. Diring, D. O. Wang, C. Kim, M. Kondo, Y. Chen, S. Kitagawa, K.-i. Kamei, S. Furukawa, *Nat. Commun.* **2013**, *4*, 2684; e) J. Dong, Z. Xun, Y. Zeng, T. Yu, Y. Han, J. Chen, Y.-Y. Li, G. Yang, Y. Li, *Chem. Eur. J.* **2013**, *19*, 7931–7936.

[8] J. Nicolas, S. Mura, D. Brambilla, N. Mackiewicz, P. Couvreur, *Chem. Soc. Rev.* **2013**, *42*, 1147–1235.

[9] a) G. Mayer, A. Heckel, *Angew. Chem. Int. Ed.* **2006**, *45*, 4900–4921; b) H.-M. Lee, D. R. Larson, D. S. Lawrence, *ACS Chem. Biol.* **2009**, *4*, 409–427; c) G. C. R. Ellis-Davies, *Nat. Meth.* **2007**, *4*, 619–628; d) D. K. Sinha, P. Neveu, N. Gagey, I. Aujard, C. Benbrahim-Bouzidi, T. Le Saux, C. Rampon, C. Gauron, B. Goetz, S. Dubruille et al., *ChemBioChem* **2010**, *11*, 653–663; e) A. A. Kumbhar, A. T. Franks, R. J. Butcher, K. J. Franz, *Chem. Commun.* **2013**, *49*, 2460–2462; f) C. Gwizdala, S. C. Burdette in *Inorganic Chemical Biology: Principles, Techniques and Applications* (Ed.: G. Gasser), John Wiley & Sons, Ltd, **2014**.

[10] a) T. Joshi, V. Pierroz, C. Mari, L. Gemperle, S. Ferrari, G. Gasser, *Angew. Chem. Int. Ed.* **2014**, *53*, 2960–2963; b) A. Leonidova, V. Pierroz, R. Rubbiani, Y. Lan, A. G. Schmitz, A. Kaech, R. K. O. Sigel, S. Ferrari, G. Gasser, *Chem. Sci.* **2014**, 4044–4056.

[11] T. M. Dore in *Dynamic studies in biology. Phototriggers, photoswitches and caged biomolecules* (Eds.: M. Goeldner, R. Givens), Wiley-VCH, Weinheim, **2005**.

[12] E. B. Brown, J. B. Shear, S. R. Adams, R. Y. Tsien, W. W. Webb, *Biophys. J.* **1999**, *76*, 489–499.

[13] a) L. M. Palmer, A. S. Shai, J. E. Reeve, H. L. Anderson, O. Paulsen, M. E. Larkum, *Nat. Neurosci.* **2014**, *17*, 383–390; b) J.-i. Tanaka, Y. Horiike, M. Matsuzaki, T. Miyazaki, G. C. R. Ellis-Davies, H. Kasai, *Science* **2008**, *319*, 1683–1687; c) H. Murakoshi, H. Wang, R. Yasuda, *Nature* **2011**, *472*, 100–104; d) H.-B. Kwon, B. L. Sabatini, *Nature* **2011**, *474*, 100–104.

[14] H. J. Montgomery, B. Perdicakis, D. Fishlock, G. A. Lajoie, E. Jervis, J. Guy Guillemette, *Bioorg. Med. Chem.* **2002**, *10*, 1919–1927.

[15] B. Perdicakis, H. J. Montgomery, G. L. Abbott, D. Fishlock, G. A. Lajoie, J. G. Guillemette, E. Jervis, *Bioorg. Med. Chem.* **2005**, *13*, 47–57.

[16] M. Goard, G. Aakalu, O. D. Fedoryak, C. Quinonez, J. St. Julien, S. J. Poteet, E. M. Schuman, T. M. Dore, *Chem. Biol.* **2005**, *12*, 685–693.

[17] D. Abate-Pella, N. A. Zeliadt, J. D. Ochocki, J. K. Warmka, T. M. Dore, D. A. Blank, E. V. Wattenberg, M. D. Distefano, *ChemBioChem* **2012**, *13*, 1009–1016.

[18] A. S. Baker, A. Deiters, *ACS Chem. Biol.* **2014**, in press.

[19] S. Gug, S. Charon, A. Specht, K. Alarcon, D. Ogden, B. Zietz, J. Léonard, S. Haacke, F. Bolze, J.-F. Nicoud et al., *ChemBioChem* **2008**, *9*, 1303–1307.

[20] D. Warther, F. Bolze, J. Léonard, S. Gug, A. Specht, D. Puliti, X.-H. Sun, P. Kessler, Y. Lutz, J.-L. Vonesch et al., *J. Am. Chem. Soc.* **2010**, *132*, 2585–2590.

[21] N. Gagey, M. Emond, P. Neveu, C. Benbrahim, B. Goetz, I. Aujard, J.-B. Baudin, L. Jullien, *Org. Lett.* **2008**, *10*, 2341–2344.

[22] S. C. Boca, M. Four, A. Bonne, van der Sanden, Boudewijn, S. Astilean, P. L. Baldeck, G. Lemercier, *Chem. Commun.* **2009**, 4590–4592.

[23] a) S. Hatakeyama, K. Sugihara, T. K. Shibata, J. Nakayama, T. O. Akama, N. Tamura, S.-M. Wong, A. A. Bobkov, Y. Takano, C. Ohyama et al., *Proc. Natl. Acad. Sci. USA* **2011**, *108*, 19587–19592; b) P. Kapoor, H. Singh, A. Gautam, K. Chaudhary, R. Kumar, G. P. S. Raghava, *PLoS ONE* **2012**, *7*, e35187 EP -.

[24] G. M. Anstead, S. E. Sen, G. D. Prestwich, *Bioorg. Chem.* **1991**, *19*, 300–313.

[25] P. Anstaett, A. Leonidova, G. Gasser, *ChemPhysChem* **2014**, DOI: 10.1002/cphc.201402547.

[26] J. E. T. Corrie, J. H. Kaplan, B. Forbush, D. C. Ogden, D. R. Trentham, *ChemPhysChem* **2015**, DOI: 10.1002/cphc.201402808.

[27] P. Anstaett, A. Leonidova, E. Janett, C. G. Bochet, G. Gasser, *ChemPhysChem* **2015**, DOI: 10.1002/cphc.201500178.

[28] T. Furuta, S. S.-H. Wang, J. L. Dantzker, T. M. Dore, W. J. Bybee, E. M. Callaway, W. Denk, R. Y. Tsien, *Proc. Natl. Acad. Sci. USA* **1999**, *96*, 1193–1200.

[29] A. Specht, F. Bolze, J. F. Nicoud, M. Goeldner in *Methods in Molecular Biology* (Ed.: M. R. Banghart), Humana Press, **2013**.

[30] R. R. Anderson, J. A. Parrish, *J. Investig. Dermatol.* **1981**, *77*, 13–19.

[31] L. Donato, A. Mourot, C. M. Davenport, C. Herbivo, D. Warther, J. Léonard, F. Bolze, J.-F. Nicoud, R. H. Kramer, M. Goeldner et al., *Angew. Chem. Int. Ed.* **2012**, *51*, 1840–1843.

[32] H. A. Collins, M. Khurana, E. H. Moriyama, A. Mariampillai, E. Dahlstedt, M. Balaz, M. K. Kuimova, M. Drobizhev, YangVictor X. D, D. Phillips et al., *Nat. Photonics* **2008**, *2*, 420–424.

[33] C. Bao, M. Jin, B. Li, Y. Xu, J. Jin, L. Zhu, *Org. Biomol. Chem.* **2012**, *10*, 5238–5244.

[34] M. Triesscheijn, P. Baas, Schellens, Jan H. M., F. A. Stewart, *Oncologist* **2006**, *11*, 1034–1044.

[35] a) M. R. Hamblin, T. Hasan, *Photochem. Photobiol. Sci.* **2004**, *3*, 436–450; b) A. Frei, R. Rubbiani, S. Tubafard, O. Blacque, P. Anstaett, A. Felgentraeger, T. Maisch, L. Spiccia, G. Gasser, *J. Med. Chem.* **2014**, *57*, 7280–7292.

[36] a) J. A. Bertout, S. A. Patel, Simon, M. Celeste, *Nat. Rev. Cancer* **2008**, *8*, 967–975; b) P. Vaupel, A. Mayer, *Cancer Metastasis Rev.* **2007**, *26*, 225-239.

[37] S. Bühler, I. Lagoja, H. Giegrich, K.-P. Stengele, W. Pfleiderer, *Helv. Chim. Acta* **2004**, *87*, 620–659.

[38] P. Jeanjot, F. Bruyneel, A. Arrault, S. Gharbi, J.-F. Cavalier, A. Abels, C. Marchand, R. Touillaux, J.-F. Rees, J. Marchand-Brynaert, *Synthesis* **2003**, *2003*, 513–522.

[39] S. Katayama, N. Ae, T. Kodo, S. Masumoto, S. Hourai, C. Tamamura, H. Tanaka, R. Nagata, *J. Med. Chem.* **2003**, *46*, 691–701.

[40] X.-L. Qiu, G. Li, G. Wu, J. Zhu, L. Zhou, P.-L. Chen, A. R. Chamberlin, W.-H. Lee, *J. Med. Chem.* **2009**, *52*, 1757–1767.

[41] A. Leonidova, V. Pierroz, R. Rubbiani, J. Heier, S. Ferrari, G. Gasser, *Dalton Trans.* **2014**, *43*, 4287–4294.

4 Induction of Cytotoxicity Through Photo-Release of Aminoferrocene

Anna Leonidova,[a,§] *Philipp Anstaett,*[a,§] *Vanessa Pierroz*[a,b] *Bernhard Spingler,*[a] *Stefano Ferrari*[b] *and Gilles Gasser*[a]*

[a] Department of Chemistry, University of Zurich, Winterthurerstrasse 190, CH-8057 Zurich, Switzerland.

[b] Institute of Molecular Cancer Research, University of Zurich, Winterthurerstrasse 190, CH-8057 Zurich, Switzerland.

§ These authors have contributed equally to the work.

* Corresponding author: e-mail: gilles.gasser@chem.uzh.ch; Fax: +41 44 635 46 03;
Tel: +41 44 635 46 30; homepage: http://www.gassergroup.com.

This chapter has been submitted for publication in *Inorganic Chemistry* on 17.07.2014.

4.1 Contributions to the publication

P.A. synthesized and characterized the compounds leading to and derived from **PLPG2**. P.A. acquired the photophysical characterization and iron release assay of **Fc-PLPG2-MLS** and partially of **Fc-NH$_2$** and **Fc-PLPG1-MLS**. Contributions to the writing of the manuscript were made.

4.2 Abstract

Reactive oxygen species (ROS)-activated aminoferrocene-based prodrug candidates successfully take advantage of intrinsically high amounts of ROS in tumor tissues. Interestingly, the ROS-initiated activation of these prodrug candidates leads to formation of unstable aminoferrocene (**Fc-NH$_2$**) derivatives, which decay to iron ions. The latter catalytically increase ROS concentration to a lethal level. In this work, we prepared light-controlled aminoferrocene prodrug candidates (**Fc-PLPG1-MLS** and **Fc-PLPG2-MLS**) by derivatizing **Fc-NH$_2$** with an *o*-nitrophenyl (**PLPG1**) and an *o*-nitrobiphenyl (**PLPG2**) photo-labile protecting group (**PLPG**), respectively, and by further conjugation to a mitochondria localization signal (**MLS**) peptide (Cys-D-Arg-Phe-Lys-NH$_2$). The resulting bioconjugates **Fc-PLPG1-MLS** and **Fc-PLPG2-MLS** were found to be more stable and less cytotoxic, in the dark, towards human promyelocytic leukemia cells (HL-60) compared to **Fc-NH$_2$**. Upon light irradiation at 355 nm, both **Fc-PLPG1-MLS** and **Fc-PLPG2-MLS** released **Fc-NH$_2$**, albeit with very different photolysis quantum yields. The **PLPG2** photo-cage was in fact several orders of magnitude more efficient than **PLPG1** in releasing **Fc-NH$_2$**. This difference was reflected by the light irradiation experiments on HL-60 cell line, in which **Fc-PLPG2-MLS** displayed the highest phototoxicity index (2.5 ± 0.4) of all the compounds tested. The iron release assays confirmed the rise in iron ions concentrations upon light irradiation of **Fc-PLPG1-MLS** and **Fc-PLPG2-MLS**. Together with the absence of phototoxicity on the non-malignant hTERT-immortalized retinal pigment epithelial (hTERT RPE-1) cell line, these results indicate catalytic generation of ROS as possible mode of action.

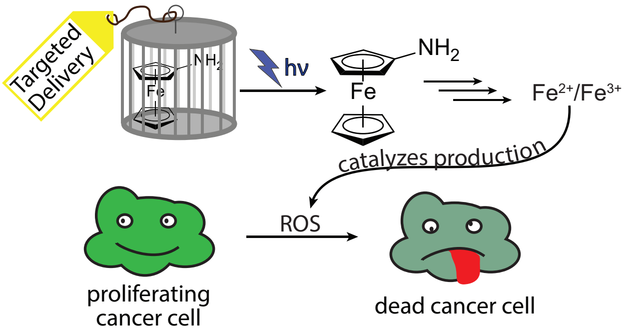

4.3 Introduction

Aminoferrocene-based prodrug candidates recently developed by the Mokhir group have shown considerable selectivity towards cancer cells with IC_{50} values in the lower micromolar range (see Scheme 1 for an example of such a prodrug candidate).[1,2] These prodrug candidates are activated by reactive oxygen species (ROS) such as $^1O_2$, O_2^-, $HO^\bullet$ and H_2O_2, which cleave the B-C bond in an arylboronic acid pinacol ester linked to an aminoferrocene derivative via a carbamate function (see Scheme 1 for mode of action). In water, the resulting phenol is in equilibrium with its phenolate form, which spontaneously fragments into *p*-quinone methide and a carbamated aminoferrocene derivative via 1,6-elimination. The quinone methide is a known toxic compound that readily reacts with nucleophiles and attacks antioxidative defenses cells by alkylating in particular glutathione (Scheme 1, Mechanism 1).[3] Indeed, also hydroxyferrocifen – a very efficient anti-cancer drug candidate developed by the Jaouen group – is being oxidized to quinone methide metabolites.[4] Mokhir's aminoferrocene-based prodrug candidates possess, however, an additional mode of action (Scheme 1, Mechanism 2). The latter is mediated by the carbamated aminoferrocene fragment, which decarboxylates under physiological conditions.[1,2] Most aminoferrocene derivatives are rather unstable since they are easily oxidized to their ferrocenium forms (Fc^+),[5] which in turn can decompose into iron ions and cyclopentadiene ligands.[1] Both Fc^+ and iron ions can catalyze ROS generation elevating cellular levels of ROS to a toxic level.[1,6] Tumors generally function at a higher basal concentration of ROS than normal tissues[7] and are already harmed by relatively small increases in ROS amount. As Mokhir's aminoferrocene-based prodrug candidates are activated by ROS-induced fragmentation, these prodrug candidates are predominantly harming cancer cells.[1,2] As a matter of fact, the most toxic prodrug candidate of the series has shown more than a 10-fold selectivity for human promyelocytic leukemia cell line (HL-60) over normal fibroblasts.[1] Interestingly, the cytotoxicity of the aminoferrocene-based prodrug candidates correlates with their efficiency of ROS production in cells, showing that the aminoferrocene moiety contributes heavily to the observed cytotoxicity.[1,2] A similar concept has also been implemented by the Jacob group using ROS-activated organochalcogen compounds catalyzing ROS generation.[8]

Besides internal triggers such as high ROS levels, external triggers, e.g. light-activation, can be used to control the activity of a compound. Photosensitizers – molecules able to generate toxic singlet oxygen upon light irradiation – are already being applied in the clinic in photodynamic therapy (PDT).[9] A great number of organic photo-active compounds that are activated via cleavage of a light-sensitive bond have been reported.[10,11] When it comes to

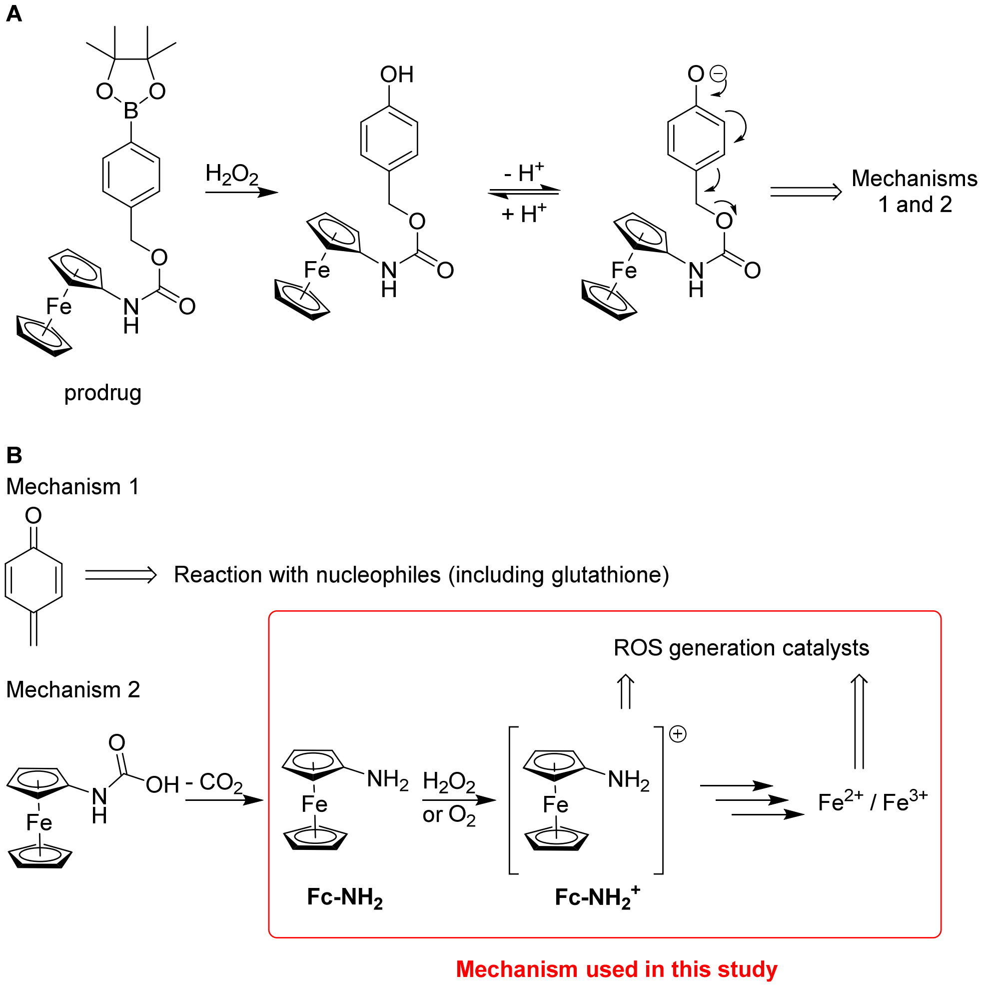

Scheme 1. A) Activation of a previously reported aminoferrocene-based prodrug candidate by ROS. B) Mechanisms of cytotoxicity.[1]

metal complexes, some of them are inherently photo-reactive by themselves via light-induced redox and/or ligand exchange reactions. These changes can be exploited to increase the cytotoxicity of metal compounds[12] or to construct metal-based photo-cages (e.g. for neurotransmitters).[13] Encouraged by the recent use of organic photo-cages in the design of light-activated metal-containing prodrug candidates,[14,15] we envisaged photo-caging a simple cytotoxic ferrocenyl derivative, namely aminoferrocene (**Fc-NH$_2$**) with *o*-nitrophenyl-based and *o*-nitrobiphenyl-based photo-labile protecting groups (PLPG) via a carbamate bond (Scheme 2). The resulting derivatives were expected to be more stable in physiological conditions compared to aminoferrocene itself due to the electron-withdrawing effect of the carbamate. The aminoferrocene would then be liberated upon UV-A light irradiation and oxidized to its ferrocenium form and irons ions, which could act as ROS-generation catalysts in cancer cells. Furthermore, a mitochondrial localization signal (**MLS**) peptide (Cys-D-Arg-Phe-Lys-NH$_2$) was added to the photo-caged aminoferrocene bioconjugate to target mitochondria – organelles where the redox balance plays an especially important role.[16]

4.4 Results and discussion

4.4.1 Synthesis and Characterization

Aminoferrocene (**Fc-NH$_2$**) was caged with an *o*-nitrophenyl-based photo-linker also known as the Dmochowski photo-labile protecting group (**PLPG1**). Interestingly, this PLPG allows for coupling to a further moiety such as a targeting biomolecule. Our group has previously reported the preparation of PLPG-containing bioconjugates of a rhenium(I) complex[17] and the coupling procedure could be successfully applied to the photo-caging and bioconjugation of **Fc-NH$_2$**. Following this synthetic protocol, the primary amino group of **Fc-NH$_2$** was blocked with **PLPG1** via *N*-hydroxysuccinimide ester coupling to give **Fc-PLPG1** (Scheme 2 A). The

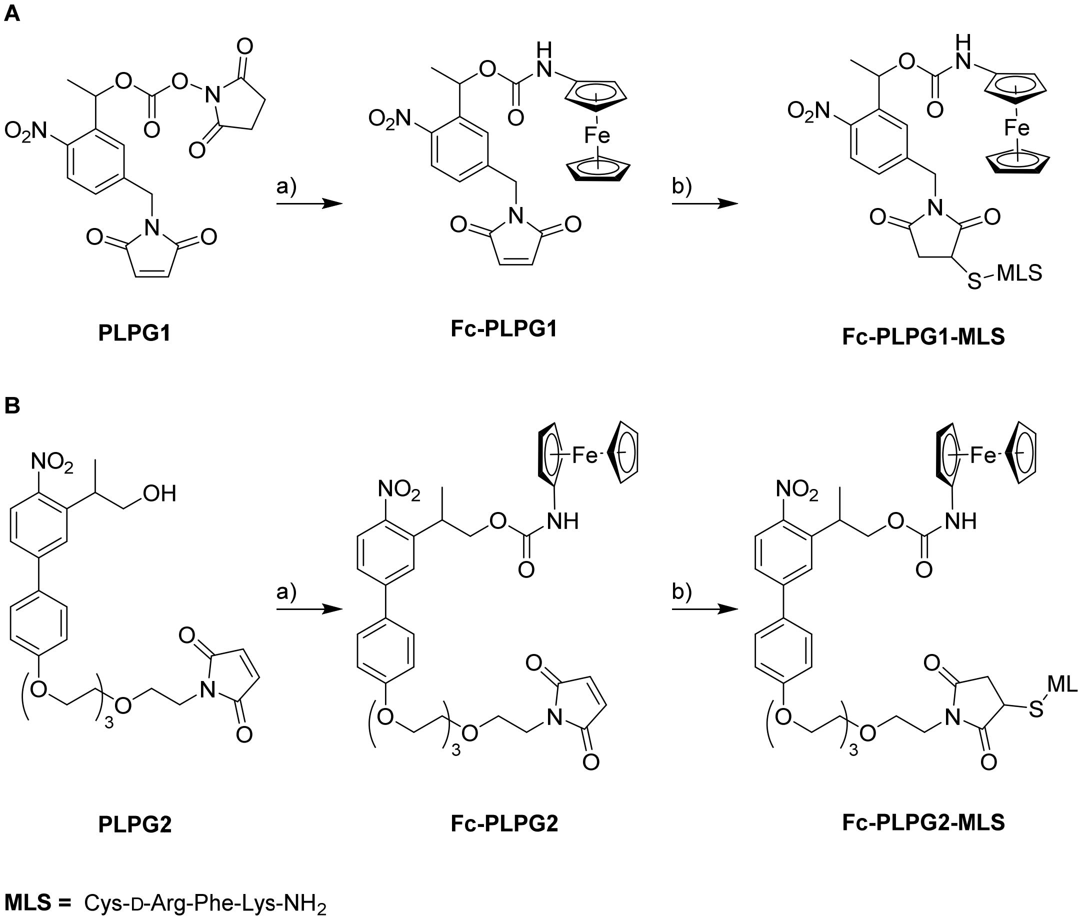

MLS = Cys-D-Arg-Phe-Lys-NH$_2$

Scheme 2. A) Synthesis of **Fc-PLPG1-MLS**: a) **Fc-NH$_2$**, DIPEA, CHCl$_3$, 62%; b) Cys-D-Arg-Phe-Lys-NH$_2$, acetonitrile/water 1:1. B) Synthesis of Fc-PLPG2-MLS: a) i. *N*,*N'*-disuccinimidyl carbonate, triethylamine, acetonitrile; ii. **Fc-NH$_2$**, DIPEA, CH$_2$Cl$_2$, 50% over both steps; b) Cys-D-Arg-Phe-Lys-NH$_2$, acetonitrile/PBS (pH=7.4) 2:1. DIPEA: diisopropylethylamine.

product was fully characterized by ^{1}H- and ^{13}C-NMR, ESI-MS, LC-MS and X-ray crystallography (see X-ray crystallography section). The MS spectrum (Figure S1) showed the expected mass at *m/z* = 503.3 [M$^+$] as well as the isotopic pattern characteristic for iron. In the ^{1}H-NMR of **Fc-PLPG1**, the most notable change in shifts compared to the starting materials **Fc-NH$_2$** and **PLPG1** was observed for the aminoferrocene moiety (Figures S3 and S5). Indeed, both the amino group proton – now part of the carbamate bond – and the substituted cyclopentadienyl (Cp) ring protons shifted significantly downfield of about 3.5 and 0.8 ppm, respectively. The **PLPG1** moiety protons were comparatively less affected (Figures S3 and S6). The protons near the newly formed carbamate bond shifted slightly (0.05-1 ppm) upfield. Interestingly, a slight doubling of peaks of the substituted Cp ring was observed in both ^{1}H- and ^{13}C-NMR spectra.

Likewise, **Fc-NH$_2$** was caged with an *o*-nitrobiphenyl based photo-linker (**PLPG2**) which was previously developed by Goeldner and coworkers (Scheme 2 B).[18] We recently reported a derivative of this cage to which a targeting peptide can be attached via click chemistry.[19] Here, we introduced a maleimide function to allow for coupling of thiol-containing biomolecules. Activation with disuccinimdyl carbonate and subsequent coupling of **Fc-NH$_2$** gave the second caged derivative **Fc-PLPG2**. The product was fully characterized by ^{1}H and ^{13}C NMR, IR spectroscopy, and high resolution mass spectrometry. In the ^{1}H NMR spectrum, possible shifts of the proton signals belonging to the substituted Cp ring are not trackable as in the same region the protons of the tetraethylene glycol linker are observed. However, in analogy with **Fc-PLPG1** and in contrast to **PLPG2**, the multiplet in that region expands down to 4.7 ppm. This indicates that attachment of **Fc-NH$_2$** to **PLPG2** resulted in the same electronic changes due to the carbamate bond formation.

The photo-caged aminoferrocenes **Fc-PLPG1** and **Fc-PLPG2** were then conjugated to a mitochondria localization signal peptide (**MLS**) *via* Michael addition of the cysteine thiol of the peptide to the maleimides of the PLPGs (Scheme 2). After preparative HPLC purification and lyophilisation, **Fc-PLPG1-MLS** and **Fc-PLPG2-MLS** were obtained as light-yellow solids. For **Fc-PLPG1-MLS**, the presence of the desired product was confirmed by ESI-MS where peaks at *m/z* = 352 [M+3H]$^{3+}$, 528.1 [M+2H]$^{2+}$ and 1055.4 [M+H]$^+$ (Figure S10) were observed. As for the photo-caged bioconjugate of rhenium (I) complex, small *m/z* peaks corresponding to products of photo-uncaging (**PLPG-MLS** and **Fc-NH-COOH**) were observed in the LC-MS spectra. This uncaging process happened due to the harsh ionization conditions used for LC-MS as uncaged complex and byproducts eluted at different times (Figures S11 and 27). Successful synthesis of **Fc-PLPG2-MLS** was confirmed by ESI-MS where *m/z* = 436 [M+3H]$^{3+}$, 654 [M+2H]$^{2+}$ and 1307 [M+H]$^+$ (Figure S21) were detected. The purities were checked by analytical HPLC (Figure S20).

4.4.2 X-Ray Crystallography

Single crystals of **Fc-PLPG1** suitable for X-ray analysis were obtained by vapor diffusion recrystallization (see X-ray crystallographic part in the experimental section). Only a few X-ray structures of compounds consisting of 1-(2'-nitrophenyl)ethyl ester unit are known,[20,21,22] but only two of them were actually synthesized as precursors for photolabile substances.[20,21] **Fc-PLPG1** crystallized in the centrosymmetric triclinic space group *P*-1 and is in an overall bent conformation, essentially like a horseshoe, where the two ends, ferrocene and maleimide, almost touch each other (Figure 1). Additionally, **Fc-PLPG1** forms in the solid state a dimer *via* two hydrogen bridges: The amide nitrogen N1 is in close contact with one of the maleimide oxygen atoms O6_$1 (-x+2, -y+2, -z) at a distance of 2.9003(15) Å and the amide of that molecule back binds to the original molecule to build the cyclic dimer (Figure S8).

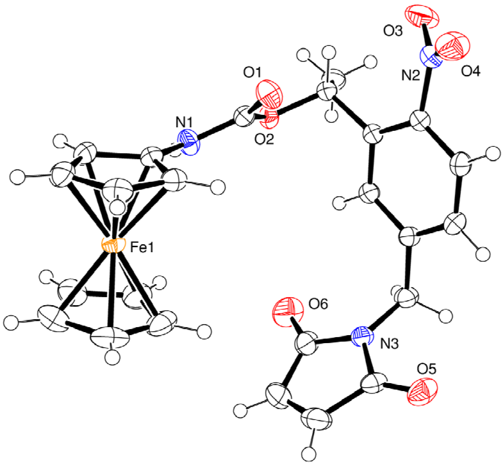

Figure 1. ORTEP representation of the crystal structure of **Fc-PLPG1**. Ellipsoids were drawn at 50% probability.

4.4.3 Photolysis Quantum Yields

With the bioconjugates in hand, the next step in this study was to evaluate the photo-uncaging of **Fc-PLPG1-MLS** and **Fc-PLPG2-MLS** by measuring their laser photolysis quantum yield in PBS (pH=7.4) at 355 nm. The decomposition of **Fc-PLPG1-MLS** and **Fc-PLPG2-MLS** was monitored by LC-MS until 20% of the initial compound was photolysed (Figures S22-24). Calculated relative to the *trans*-to-*cis* photoisomerization quantum yield of azobenzene at this wavelength (15%),[23–25] a yield of 0.07 ± 0.02% for **Fc-PLPG1-MLS** indicates a rather inefficient photo-release process, that runs much slower than the photolysis of the similar Re(I) bioconjugate.[15] The carbamate-based photo-cages for amines first release the amine as a carbamate salt, which then in turn decarboxylates.[11] The rate of decarboxylation depends on the pK_a of the amine group and a more acidic aromatic amine of aminoferrocene is expected to decarboxylate slower than an aliphatic amine of the reported Re(I) complex. However, we monitored the disappearance of **Fc-PLPG1-MLS** rather than the appearance of the released aminoferrocene. Hence, the observed slower decomposition cannot be ascribed to the decarboxylation step. Rapid photo-uncaging of the Re analogue could be ascribed to the high absorptivity of the Re(I) chromophore at the irradiation wavelength, which could enable it to act as an “light-antenna”. Nevertheless, the photolysis quantum yield of **Fc-PLPG1-MLS** at 355 nm is also considerably lower than that of phosphate photo-caged with *o*-nitrophenyl group.[23,25] The exact reasons behind a particularly inefficient photo-release of **Fc-NH$_2$** from **Fc-PLPG1-MLS** remain for the moment unclear. The uncaging quantum yield of **Fc-PLPG2-MLS** was determined in a similar fashion. The quantum yield is with 1.8 ± 0.48% higher than for **Fc-PLPG1-MLS**, and is accompanied by a seven-fold higher absorptivity at 355 nm compared to **Fc-PLPG1-MLS** (Figures S30-31). The propyl-*o*-nitrobiphenyl cage core has previously, to the best of our knowledge, not been used to cage amines via carbamates. A direct comparison regarding the uncaging quantum yield therefore cannot be made in this case.

4.4.4 UV-A Irradiation and Iron Release

Although a monochromatic laser setup allows accurate determination of uncaging quantum yields, it is impractical for cell culture irradiation experiments. To this end, a UV-A reactor (Rayonet) equipped with lamps emitting in the 300-400 nm range (emission centered at 350 nm) was used. To find a suitable UV-A light dose for the cell irradiation experiments, the more slowly uncaging **Fc-PLPG1-MLS** was photolysed under the same experimental setup as for cytotoxicity assays (100 µM in PBS buffer solution (pH=7.4) in a covered 96-well plate, 30 °C). As expected from the quantum yield measurements, the photolysis of **Fc-PLPG1-MLS** proceeded very slowly and required a relatively high light dose to complete (18 J/cm^2) (Figure S25). Such elevated dose of UV-A light would on its own affect cell proliferation, so a maximal UV-A light dose safe for cells (3.3 J/cm^2) was used in cytotoxicity experiments.[15] Using this light dose, neither the light irradiation nor secondary effects, e.g. temperature changes, affected the cells significantly. During irradiation experiments, the formation of aminoferrocene and photo-cage byproducts was detected by LC-MS for **Fc-PLPG1-MLS** only (Figure S27). This is due to the fact that the sample solutions were adjusted to have the same absorbance at the irradiation wavelength. However, **Fc-PLPG1-MLS** has a significantly lower molar absorptivity at 355 nm compared to **Fc-PLPG2-MLS** (Figures S30-31). As a result, **Fc-PLPG1-MLS** was used in a considerably higher concentration and the products of its photolysis were easier to detect. The observation of products corresponding to the typical uncaging reaction are indicative of aminoferrocene being released via this mechanism, as opposed to direct degradation of **Fc-NH$_2$**. Of note, to observe the appearance of aminoferrocene, the samples had to be analyzed immediately after irradiation or kept frozen in liquid nitrogen prior to analysis due to the instability of aminoferrocene. The aminoferrocene peak initially increased with the light dose, but was not observed at higher doses (Figure S26). The irradiation of aminoferrocene alone demonstrated that the compound decomposed faster than the caged **Fc-PLPG1-MLS** released it (Figure S27). The photo-decomposition of aminoferrocene was also followed by UV/Vis spectroscopy (Figure S29). At a lower irradiation dose, the UV absorbance of the sample actually increases in the 250-350 nm range indicating formation of Fc^+, which absorbs stronger than ferrocene in this range.[26] Yet, at higher light doses, the characteristic Fc transitions in the 275-500 nm range decrease and then disappear completely.

Studies on aminoferrocene-based prodrug candidates decomposition have shown that such molecules could decay into iron ions and cyclopentadienyl ligands.[1,2] The release of iron ions played in fact an important role in the cytotoxicity mechanism of Mokhir's complexes as catalysts for ROS generation.[1,2] To verify if the photo-decomposition of **Fc-PLPG1-MLS**, **Fc-PLPG2-MLS** and **Fc-NH$_2$** resulted in the same products, the iron release upon light irradiation was monitored. More specifically, the compounds were irradiated by UV-A (as described above for UV-A dose determination) and the amount of free iron ions was quantified by formation of iron(II) tris(2,2'-bipyridine) complex and monitoring its strong absorption at 509 nm.[1] The assay showed that both **Fc-PLPG1-MLS** and **Fc-PLPG2-MLS** generated iron ions upon light irradiation, but long irradiation times were required to free up all iron (Figures S32-33). The iron release in the dark was also followed for 4 h, but no significant increase in iron ions was detected (Figures S35-36). Aminoferrocene, on the other hand, decomposed rapidly into iron ions even in the dark. Light irradiation only slightly increased the rate of iron release (Figure S34). These results demonstrate that the photo-caging of aminoferrocene succeeds in enhancing its stability at physiological conditions. This effect is most likely due to decreased electron donation from the primary amino group, which is converted to a carbamate in **Fc-PLPG1-MLS** and **Fc-PLPG2-MLS**. The decay into iron ions is clearly a complex multi-step process and the observed rate of **Fc-PLPG1-MLS**, **Fc-PLPG2-MLS** and **Fc-NH$_2$** photolysis is consequently not always proportional to the appearance of iron ions. Indeed, although **Fc-PLPG1-MLS** decomposes considerably slower than **Fc-PLPG2-MLS** (see the quantum yields and absorptivities above), its iron release rate is only about 2-fold slower.

4.4.5 Cytotoxicity

The anti-proliferative effect of **Fc-PLPG1-MLS**, **Fc-PLPG2-MLS** and **Fc-NH$_2$** was investigated on human promyelocytic leukemia (HL-60) and non-cancerous hTERT-immortalized retinal pigment epithelial (hTERT RPE-1) cell lines. To assess the light cytotoxicity, cells were incubated with the compounds for 4 h prior to irradiation and left to recover for 44 h afterwards. Cell viability was quantified using the resazurin assay (6 h incubation). As shown in Table 1, the dark cytotoxicity of **Fc-NH$_2$** towards HL-60 was significantly decreased by photo-caging and peptide conjugation. Only a slight increase in cytotoxicity (1.3-1.5 fold) was observed for **Fc-NH$_2$** and **Fc-PLPG1-MLS** upon light irradiation on HL-60 cells. In the case of **Fc-NH$_2$**, these results can be rationalized in terms of its instability. In fact, most of **Fc-NH$_2$** decomposed before the cells were irradiated (compare Figure S34). The low cytotoxic impact of **Fc-PLPG1-MLS** can be explained by an extremely low uncaging efficiency of this compound. **Fc-PLPG2-MLS** is not as benign in the dark as **Fc-PLPG1-MLS**, but possess an improved phototoxic index of about 2.5. Upon light irradiation, the IC$_{50}$ value of **Fc-PLPG2-MLS** reaches the level of aminoferrocene. All tested compounds are less toxic towards non-cancerous hTERT RPE-1 cells and show no effect of light-irradiation on this cell line. The difference is likely due to the elevated levels of ROS characteristic for tumors. This enhanced ROS generation pushes the ROS scavenging system of cancer cells to the limit and a further increase in ROS can tip the scale towards cellular death. Our data indicate that the cytotoxicity mechanism of **Fc-PLPG1-MLS**, **Fc-PLPG2-MLS** and **Fc-NH$_2$** is likely to involve catalytic ROS generation by the liberated iron ions, as suggested by the Mokhir group for their aminoferrocene-based prodrug candidates.[1,2] Indeed, the IC$_{50}$ values of **Fc-PLPG1-MLS**, **Fc-PLPG2-MLS** and **Fc-NH$_2$** on HL-60 cells are in the same range as those reported by the Mokhir group on the same cell

Table 1. Cytotoxicity (IC$_{50}$) of **PLPG1-MLS**, **Fc-PLPG2-MLS** and **Fc-NH$_2$** towards human cell lines.

	HL-60			**hTERT RPE-1**		
	dark[a] [µM]	**UV-A[b] [µM]**	**Phototoxic Index**	**dark[a] [µM]**	**UV-A[b] [µM]**	**Phototoxic Index**
Fc-NH$_2$	18.4 ± 0.1	12.1 ± 0.7	1.5 ± 0.1	42.4 ± 9.2	38.2 ± 3.1	1.1 ± 0.3
Fc-PLPG1-MLS	72.6 ± 0.8	55.4 ± 3.9	1.3 ± 0.1	>100	>100	-
Fc-PLPG2-MLS	40.0 ± 0.6	15.7 ± 2.8	2.5 ± 0.4	39.0 ± 1.1	37.1 ± 2.9	1.1 ± 0.1

[a] incubated with the compounds for 56 h (including 6 h resazurin assay); [b] incubated with the compounds for 4 h prior to irradiation (10 min, UV-A reactor at 350 nm), then incubated for another 52 h (including 6 h resazurin assay).

line. **Fc-PLPG2-MLS** has in fact the IC_{50} value very close to that of the most toxic compound tested on HL-60 by Mokhir's group (15.7 ± 2.8 *vs* 9 ± 2).[1] All in all, the data demonstrate that the activity of cytotoxic aminoferrocene compounds can be efficiently controlled by a photo-caging strategy.

4.5 Conclusion

In this work, we have successfully prepared and characterized two light-activatable aminoferrocene-based prodrug candidates (**Fc-PLPG1-MLS** and **Fc-PLPG2-MLS**) using two different photo-cages. Upon UV-A light-irradiation, both bioconjugates released aminoferrocene, which rapidly decayed into iron ions under physiological conditions. Despite this decomposition – or most likely due to it – aminoferrocene considerably reduced the proliferation of cancer cells (HL-60) both in dark and upon light irradiation. While both cages improved the stability of aminoferrocene and therefore attenuated its dark cytotoxicity, **Fc-PLPG2-MLS** displayed a higher uncaging efficiency, higher phototoxic index and lower light IC_{50} value compared to **Fc-PLPG1-MLS**. The absence of light effect on healthy cells suggests that **Fc-PLPG1-MLS** and **Fc-PLPG2-MLS** exploit the elevated ROS levels typical of cancer cells. Their mode of action is then likely to be based on the catalysis of ROS generation by released iron ions. In addition to the selectivity derived from this inherent property of the tumors, our photo-caged aminoferrocene prodrug candidates also offer spatial and temporal control of their activity via light irradiation as well as, potentially, selective delivery through a targeting vector. We believe that this potential triple selectivity concept holds great potential, especially when considering the severe side-effects frequently encountered by patients undergoing chemotherapy.

4.6 Experimental Section

4.6.1 Materials and Instruments

Chemicals and solvents were purchased reagent grade or better from commercial suppliers and used without further purification unless otherwise specified. ^{1}H and ^{13}C NMR spectra were recorded with Bruker 400 and 500 spectrometers. UV/Vis spectra were recorded on Varian Cary 50 Scan and Cary 100 spectrophotometers. ESI-MS and LC-MS were obtained with a Bruker Daltonics HCT 6000 mass spectrometer. LC-MS spectra were measured on an Acquity^{TM} from Waters system equipped with a PDA detector and an auto sampler using an Agilent Zorbax 300SB-C18 analytical column (3.5 µm particle size, 300 Å pore size, 150 × 4.6 mm). The LC run (flow rate: 0.3 mL min^{-1}) was performed with a linear gradient of A (distilled water containing 0.1% v/v formic acid) and B (acetonitrile, containing 0.1% v/v formic acid); t = 0 min, 5% B; t = 3 min, 5% B; t = 17 min, 100% B; t = 20 min, 100% B; t = 25 min, 5% B. Analytical HPLC was carried out using a Macherey-Nagel EC 250/3 NUCLEOSIL 100-5 C18 column on a VWR Chromaster system with 5110 pump, 5210 autosampler, 5310 column oven and 5430 diode array detector. Analytical HPLC run (flow rate1 mL/min) were performed with a linear gradient of A (distilled water containing 0.1% v/v TFA) and B (acetonitrile): t = 0 min, B = 5%; t = 18 min, B = 39%; t = 27 min, B = 100%; t = 31 min, B = 100%; t = 36 min, B = 1%; t = 38 min, B = 1%, t = 40 min, B = 5%; t = 41 min, B = 5), unless noted otherwise. HPLC purification was performed on a Merck HITACHI system and a Zorbax XB-300 semi-preparative column (5 µm particle size, 300 Å pore size, 250 mm x 9.4 mm, flow rate: 4 mL min^{-1}), as well as on a Varian ProStar system and an Agilent PrepHT 300SB-C18 preparative column (5 µm particle size, 300 Å pore size, 150 × 21.1 mm. Flow rate: 20 mL min^{-1}). The runs were performed with a linear gradient of A (distilled water containing 0.1% v/v TFA) and B (acetonitrile (Sigma–Aldrich HPLC-grade), containing 0.1% v/v TFA), unless noted otherwise. Semi-preparative runs: t = 0 min, 5% B; t = 12 min, 15% B; t = 32 min, 40% B; t = 50 min, 80% B; t = 51 min, 100% B; t = 56 min, 100% B; t = 61 min, 5% B. Preparative runs: t = 0 min, 5% B; t = 25 min, 100% B; t = 30 min, 100% B; t = 32 min, 5% B. Photolysis quantum yields were measured using an Edinburgh LP-920 setup equipped with a Continuum Surelite laser (355 nm). Cell culture photo-irradiation and iron release assays were conducted using a Rayonet RPR-200 photochemical reactor using 6 bulbs (14 W each) emitting in 300–400 nm range with maximum intensity output at 350 nm. The temperature inside the reactor was 30 °C. The light intensity was 55 W/m^2, as determined with a X1$_1$ optometer (Gigahertz-Optik).

4.6.2 Synthesis and Characterization

Fc-NH$_2$

Aminoferrocene was prepared using a procedure previously published.[27] The analytical data matched what that previously reported.[27]

PLPG1

The photolinker was synthesized following a procedure previously published.[28] The analytical data matched what that previously reported.[28]

Fc-PLPG1

PLPG1 (30 mg, 0.072 mmol) and aminoferrocene (15 mg, 0.072 mmol) were dissolved in dry chloroform (1 mL). Diisopropylethylamine (24 mg, 31 µL, 0.18 mmol) was then added to the mixture, which was stirred for 4 h at 35 °C. The solvent was then removed under vacuum to give a sticky brown solid, which was purified by column chromatography (silica gel, CH_2Cl_2/EtOAc 9:1) to afford **Fc-PLPG1** as an orange-red solid (22 mg, 62%).

R_f = 0.86 (CH_2Cl_2/EtOAc 9:1). ^{1}H NMR (500 MHz, $CDCl_3$) δ 7.92 (d, ^3J = 8.5 Hz, 1H), 7.64 (s, 1H), 7.39 (d, ^3J = 8.5 Hz, 1H), 6.67 (s, 2H), 6.29 (q, ^3J = 6.5 Hz, 1H), 6.02 (s, 1H), 4.71 (s, 2H), 4.49 (m, 1H), 4.46 (m, 1H), 4.15 (s, 5H), 3.98 (m, 1H), 1.63 (d, ^3J = 6.5, 3H). ^{13}C NMR (500 MHz, $CDCl_3$) δ 170.2, 152.6, 147.0, 142.1, 139.4, 134.5, 128.6, 127.5, 125.5, 69.5, 69.0, 64.7, 64.6, 60.9, 60.8, 40.9, 22.3, one signal coincidental or not observed. ESI-MS calcd. for $C_{24}H_{21}FeN_3O_6$ $[M]^+$ 503.3, found 503.1. ESI-HRMS m/z calcd. for $C_{24}H_{21}FeN_3O_6$ ($[M]^+$) 503.0780, found 503.0778; calcd. for $C_{24}H_{21}FeN_3O_6Na$ ($[M+Na]^+$) 526.0677, found 526.0673; calcd. for $C_{24}H_{21}FeN_3O_6K$ ($[M+K]^+$) 542.0417, found 542.0411; calcd. for $C_{19}H_{16}FeN_3O_6$ ($[M-Cp]^+$) 438.0389, found 438.0871; calcd. for $C_{11}H_{11}FeNO_2$ ($[FcNHCOOH]^+$) 245.0139, found 245.0130.

MLS peptide

The peptide was prepared following a previously published general peptide synthesis procedure.[29]

ESI-MS m/z calcd. for $C_{24}H_{41}N_9O_4S$ ($[M+H]^+$) 552.3, found 552.3; calcd. for $C_{24}H_{42}N_9O_4S$ ($[M+2H]^{2+}$) 276.7, found 276.6.

Fc-PLPG1-MLS

Fc-PLPG1 (20 mg, 40 µmol) and **MLS** peptide (35 mg, 40 µmol) were first pre-dissolved in DMSO (30 µL) and then in acetonitrile/water mixture 1:1 (1 mL). The reaction mixture was stirred overnight at room temperature. The solvents were removed by lyophilization and the compound was purified by preparative HPLC to obtain light-yellow solid.

ESI-MS m/z calcd for $C_{48}H_{62}FeN_{12}O_{10}S$ ($[M+H]^+$) 1055.4, found 1055.4; calcd for $C_{48}H_{63}FeN_{12}O_{10}S$ ($[M+2H]^{2+}$) 528.2, found 528.1; calcd for $C_{48}H_{64}FeN_{12}O_{10}S$ ($[M+3H]^{3+}$) 352.3, found 352.2. UV absorption (PBS buffer, pH=7.4): ε_{264} = 13037 ± 173 $M^{-1}cm^{-1}$.

Fc-PLPG2

Under an atmosphere of N_2, *N*,*N'*-disuccinimidyl carbonate (70.3 mg, 0.275 mmol) was added to a solution of **PLPG2** (82.9 mg, 0.157 mmol) in acetonitrile (2 mL). Triethylamine (76.6 µL, 55.6 mg, 0.549 mmol) was added to the stirred suspension, and stirring was continued for 6.5 h. All volatiles were removed on a rotary evaporator. The remaining residue was taken up in EtOAc and washed with 0.1 M $NaHCO_3$. The layers were separated and the aqueous layer was twice extracted with EtOAc. The combined organic layers were washed with brine, dried (Na_2SO_4), filtered and concentrated. Column chromatography (silica gel, CH_2Cl_2/EtOAc 8:2) yielded the intermediate active ester of **PLPG2** as a yellow oil (55 mg, would correspond to 52%), which was directly used in the next reaction step.

The active ester of **PLPG2** (21 mg, would correspond to 31 µmol), aminoferrocene (8.2 mg, 41 µmol) and diisopropylethylamine (6.5 mg, 8.5 µL, 50 µmol) were dissolved in dry CH_2Cl_2 (4 mL) and stirred under exclusion of light for 15 h at rt. Saturated NH_4Cl solution was added and the mixture extracted with CH_2Cl_2 (3x). The combined organic layers were dried ($MgSO_4$), filtered and concentrated. Purification by column chromatography (silica gel, CH_2Cl_2/MeOH 200:1→98:2) gave pure **Fc-PLPG2** as brown viscous oil (23 mg, 96% for 2nd step, 50% over both steps).

R_f = 0.46 (CH_2Cl_2/MeOH 95:5). IR (neat) 3095(w), 2874 (w), 1702 (s), 1604 (m), 1515 (s), 1346 (m), 1232 (m), 1103 (m), 1074 (m), 932 (w), 824 (s), 695 (m) cm^{-1}. ^1H NMR (500 MHz, $CDCl_3$) ∂ 7.85 (d, *J* = 7.9 Hz, 1 H), 7.69–7.42 (m, 4 H), 7.02 (d, *J* = 7.9 Hz, 2 H),6.67 (s, 2 H), 5.72 (bs, 1 H), 4.73–3.30 (m, 28 H), 1.41 (d, *J* = 6.5 Hz, 3 H). ^{13}C NMR (125 MHz, $CDCl_3$): ∂ 170.6, 159.5, 153.2, 149.0, 145.4, 138.0, 134.1, 131.5, 128.5, 125.9, 125.4, 125.0, 115.2, 70.9, 70.7, 70.6, 70.1, 69.6, 69.5, 68.8, 67.8, 67.6, 64.7, 60.6, 37.1, 33.3, 17.4, one signal coincidental or not observed. ESI-MS m/z 778.2 (100, $[M+Na]^+$), 755.2 (49, $[M]^+$), 389.1 (88, $[M+Na]^{2+}$). HRMS m/z calcd. for $C_{38}H_{41}N_3O_{10}$ ($[M]^+$) 755.21358, found 755.20277.

Fc-PLPG2-MLS

Fc-PLPG2 (20 mg, 26 µmol) and **MLS** peptide (15 mg, 26 µmol) were dissolved in a mixture of acetonitrile (2 mL) and PBS buffer (1 mL). The solution was stirred for 7 h at rt. The solvents were removed by lyophilization. Purification by preparative HPLC (20 mL/min, H_2O

+ 0.1% TFA : acetonitrile = 0 min: 95:5, 27 min: 35:65, 31 min: 0:100, 33 min: 0:100, 36 min: 95:5, 37 min: 95:5, t_R = 13 min) gave pure **Fc-PLPG2-MLS** as a brown solid.

ESI-MS m/z 654 (100, $[M+2\,H]^{2+}$), 436 (40, $[M+3\,H]^{3+}$), 1307 (8, $[M+H]^{+}$). t_R = 22.6 min (HPLC analytical gradient).

4.6.3 X-Ray Crystallography

Crystals were grown by vapour diffusion of cyclohexane into a solution of **Fc-PLPG1** in methylene chloride.[30] Crystallographic data were collected at 183(2) K with Mo K_α radiation (λ = 0.7107 Å) that was graphite-monochromated on an Oxford Diffraction CCD Xcalibur system with a Ruby detector. Suitable crystals were covered with oil (Infineum V8512, formerly known as Paratone N), placed on a nylon loop that is mounted in a CrystalCap Magnetic™ (Hampton Research) and immediately transferred to the diffractometer. The program suite CrysAlis^{Pro} was used for data collection, multi-scan absorption correction and data reduction.[31] The structure was solved with direct methods using SIR97[32] and was refined by full-matrix least-squares methods on F^2 with SHELXL-97.[33]

4.6.4 Photophysical Characterization

Photolysis quantum yield

20 mM DMSO stock solutions of **Fc-PLPG1-MLS** and **Fc-PLPG2-MLS** were diluted in phosphate buffer (pH=7.4) to obtain optical density at 355 nm (OD(λ = 355 nm)) of 0.2. Fluorescence cuvette (1 cm x 0.2 cm, Hellma 105.250-QS with 100 µL of solution was irradiated at 355 nm using an Edinburgh LP-920 laser flash photolysis setup equipped with a Continuum Surelite Nd:YAG laser, frequency tripled to generate light with a wavelength of 355 nm. The laser beam was slightly misaligned to obtain a suitable irradiation power. A fresh aliquot of solution was used for each irradiation. After a certain number of laser shots the solutions were transferred to amber HPLC vials with a 200 µL inlet. The vials were then kept frozen in liquid nitrogen and unfrozen 2 min prior to analysis by LC-MS due to the instability of released aminoferrocene. The peak corresponding to **Fc-PLPG1-MLS** or **Fc-PLPG2-MLS** was integrated and the percentage of remaining compound (calculated from the peak area) was plotted against the number of laser shots. The experiment was continued until the number of laser shots that decomposed 20% of **Fc-PLPG1-MLS** or **Fc-PLPG2-MLS** was reached. At less than 20% conversion, the photolysis curve could be fitted by a simple linear regression. The slope of the linear fit m_{sample} was then used to calculate

the photolysis quantum yield by comparing it to the quantum yield of azobenzene photoisomerization. For that, *trans*-azobenzene was dissolved in methanol to obtain OD(λ = 355 nm) = 0.2 and irradiated in the same conditions as **Fc-PLPG1-MLS** and **Fc-PLPG2-MLS**. The conversion of azobenzene was monitored by following the UV/Vis absorbance at 355 nm. The irradiation was continued until 20% of azobenzene had isomerized. The percentage of remaining amount of *trans*-azobenzene was then plotted versus the irradiation dose (measured in number of laser shots) and fitted by a linear curve as for **Fc-PLPG1-MLS** and **Fc-PLPG2-MLS** (see above). The slope of azobenzene curve $m_{reference}$ was used to calculate the photolysis quantum yield of **Fc-PLPG1-MLS** or **Fc-PLPG2-MLS** (ϕ_{sample}) using the following equation:

$$\phi_{sample} = \phi_{reference} \times \frac{n_{sample,0} \times m_{sample}}{n_{reference,0} \times m_{reference}}$$

where $\phi_{reference}$ is the quantum yield of azobenzene *trans*-*cis* isomerization at 355 nm (15%), and n_0 are the amounts (in mol) of the respective compounds before irradiation. At least three independent sets of experiments were averaged to obtain the single-photon uncaging quantum yields.

Photolysis in UV reactor

To estimate the UV-A dose needed for **Fc-PLPG1-MLS** uncaging in cells, 20 mM DMSO stock solution of it was diluted with PBS buffer (pH=7.4) to obtain a final concentration of 100 µM (highest concentration used in cytotoxicity experiments). The solution was pipetted in 100 µL portions on a 96-well plate (used for cytotoxicity experiments) and irradiated in the UV reactor with different light doses. The solution composition was analyzed by LC-MS. The relative concentration of the photolysed compound was calculated from the area of the corresponding LC-MS peak. Percentage of remaining compound *vs.* the irradiation dose could be fitted by a single exponential (first order kinetics law):

$$C(x) = C_0 \times e^{-kx}$$

where C_0 is the initial concentration, k is the rate constant and x is the irradiation dose. The same procedure was applied for aminoferrocene to monitor its decomposition during UV-A irradiation.

Iron release

Release of iron ions from aminoferrocene, **Fc-PLPG1-MLS** and **Fc-PLPG2-MLS** was monitored using a procedure adapted from Mokhir's work.[1] More specifically, the compound of interest (5 µL, 4 mM DMSO stock solution) was diluted in PBS (pH=7.4, 175 µL). The concentration of iron ions was then detected by addition of $Na_2S_2O_4$ (10 µL, 0.8 M in water) and 2,2'-bipyridine (10 µL, 12 mM in DMF:water 1:1), which forms iron(II) tris(2,2'-bipyridine) complex. The amount of formed complex was quantified by observing its strong absorbance at 509 nm. The experiments were conducted in a 96-well plate using a Spectramax M2^e microplate reader (Molecular Devices).

4.6.5 Cell Culture

The human promyelocytic leukemia cells (HL-60) were cultured in RPMI (Gibco) supplemented with 20% heat inactivated fetal calf serum (Gibco), 100 U/mL penicillin, 100 µg/mL streptomycin at 37 °C and 5% CO_2. The hTERT-immortalized retinal pigment epithelial cell line (hTERT RPE-1) was maintained in DMEM (Gibco) supplemented with 10% FCS (Gibco), 100 U/mL penicillin, 100 µg/mL streptomycin at 37 °C and 5% CO_2.

Photo-toxicity studies

Photo-toxicity studies were performed on two different cell lines, namely, HL-60 and hTERT RPE-1, by a fluorometric cell viability assay using resazurin (Promocell GmbH). Briefly, one day before treatment, cells were plated in triplicates in 96-well plates at a density of 4×10^3 cells/well in 100 µL. Cells were then treated with increasing concentrations of the complexes for either 48 h in the dark or 4 h in the dark followed by 10 min irradiation at 350 nm (3.3 J/cm^2) and then placed back in the incubator in the dark for the remaining 44 h. After treatment, resazurin (0.2 mg/mL final concentration) was added to the 200 µL. After 6 h of incubation at 37 °C, the fluorescence of the highly red fluorescent resorufin product was quantified at 590 nm emission with 540 nm excitation wavelength in a SpectraMax M5 microplate reader.

4.7 Acknowledgments

This work was supported by the Swiss National Science Foundation (Professorship N° PP00P2_133568 and Research Grants N° 200021_129910 and N° 200020_146776 to G.G.), the University of Zurich (G.G. and S.F.), the Stiftung für Wissenschaftliche Forschung of the University of Zurich (G.G. and S.F.), the Novartis Jubilee Foundation (G.G.), the Stiftung zur Krebsbekämpfung (S.F.), the Huggenberger-Bischoff Stiftung (S.F.), the COST Action CM1105 (G.G.) and the University of Zurich Priority Program (S.F.). The authors would also like to thank Yanjun Lan for her help with the scaled-up synthesis of **PLPG1**.

4.8 Supporting Information

4.8.1 Synthesis of PLPG2 precursors

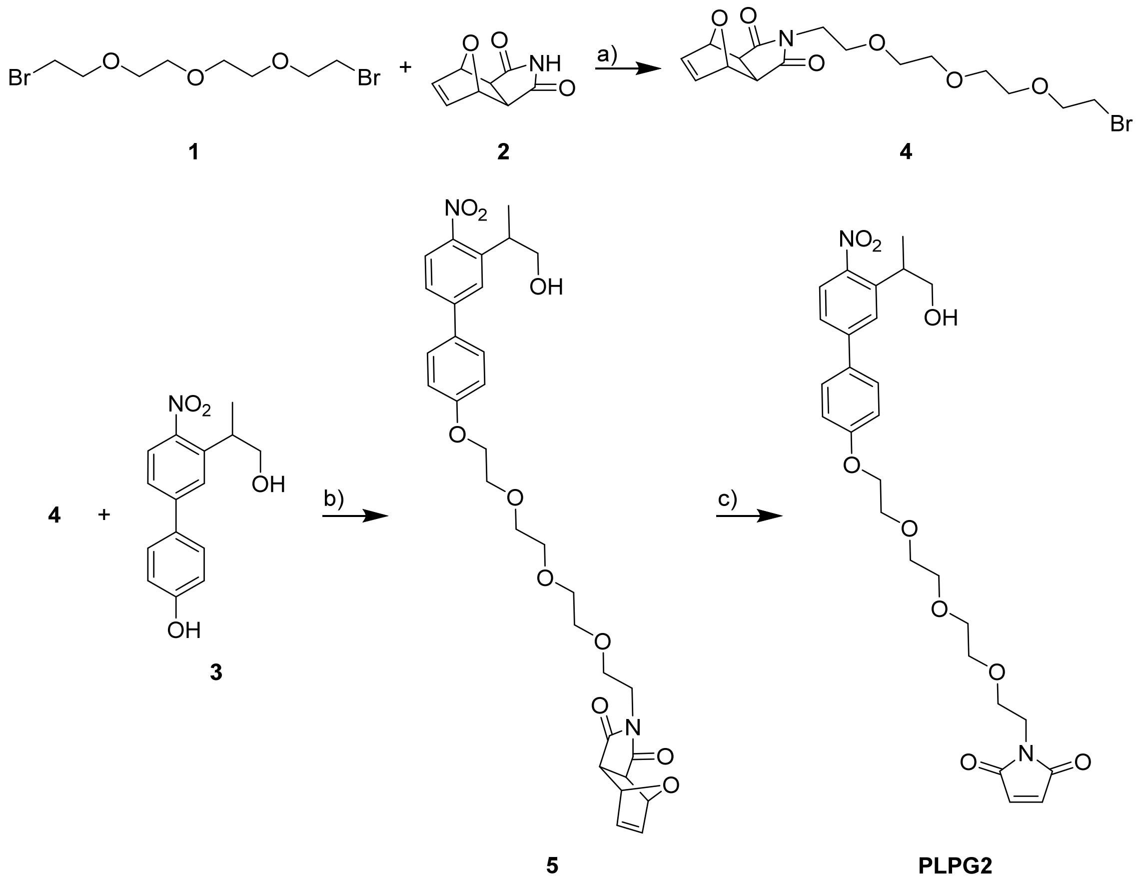

Scheme S1. Synthesis of **6**. a) K_2CO_3, acetone, rt, 28 h, 93%; b) K_2CO_3, butanone, reflux for 14 h, then rt for 4 d, 50%; c) anisole, 155 °C, 1.5 h, 100%.

Compound 1

The title compound was prepared as described by Bordi *et al.*[34] The analytical data matched what was reported there.

Compound 2

The title compound[35] was prepared as described by Tang *et al.*[28] The analytical data matched what was reported there.

Compound 3

The synthesis of the title compound was recently reported by us.[19] The analytical data matched what was reported there.

Compound 4

2 (500 mg, 3.03 mmol) was added to a stirred solution of **1** (2.91 g, 9.08 mmol) in acetone (20 mL). The solution was treated with K_2CO_3 (2.09 g, 15.1 mmol) and the resulting suspension was stirred for 28 h at rt. The solvent was removed and the residue was taken up in diethyl ether and water. The layers were separated and the aqueous layer was extracted with CH_2Cl_2 (2x). The combined organic layers were dried (Na_2SO_4), filtered, and concentrated *in vacuo*. The crude brown oil (3.22 g) was subjected to column chromatography (silica gel, CH_2Cl_2/MeOH 99:1 → CH_2Cl_2/MeOH 33:1) to give **4** as colorless oil (1.14 g, 93%). **1** could partially be recovered (1.14 g, 3.56 mmol).

R_f = 0.28 (DCM/MeOH 98:2). IR (neat) 2866 (w), 1775 (w), 1693 (s), 1396 (m), 1096 (m), 1022 (m), 879 (m) cm^{-1}. ^1H NMR (400 MHz, $CDCl_3$) ∂ 6.51 (t, J = 0.89 Hz 2 H), 5.24 (t, J = 0.89 Hz, 2 H), 3.82–3.44 (m, 16 H), 2.84 (s, 2 H). ^{13}C NMR (100 MHz, $CDCl_3$): ∂ 176.1, 136.6, 80.9, 72.5, 70.7, 70.5, 70.4, 70.1, 67.1, 61.8, 47.5, 38.2. ESI-MS m/z 428.1 (100, $[M+Na]^+$), 279.0 (16, $[M-C_8H_5NO_2+Na]^+$), 358.0 (8, $[M-C_4H_4O+Na]^+$). HRMS m/z calcd. for $C_{16}H_{22}BrNNaO_6$ ($[M+Na]^+$) 426.05227, found 426.05194.

Compound 5

3 (128 mg, 0.468 mmol) was added to a stirred suspension of **4** (192 mg, 0.475 mmol) and K_2CO_3 (323 mg, 2.34 mmol) in butanone (15 mL). The mixture was stirred at 65 °C for 22 h. Silica (5 g) was added and all volatiles were removed. Purification by column chromatography (silica gel, CH_2Cl_2/MeOH 99:1 → 98:2) afforded **5** as a yellow oil (184 mg, 66%).

R_f = 0.34 (CH_2Cl_2/MeOH 97:3). IR (neat) 3459 (w), 2873 (m), 1772 (w) 1695 (s), 1604 (m), 1514 (s), 1347 (m), 1248 (m), 825 (m), 878 (w), 825 (m). ^1H NMR (400 MHz, $CDCl_3$) ∂ 7.86 (d, J = 8.5 Hz, 1 H), 7.62 (d, J = 1.9 Hz, 1 H), 7.55–7.47 (m, 3 H), 7.06–6.98 (m, 2 H), 6.48 (t, J = 0.9 Hz, 2 H), 5.25 (t, J = 0.9 Hz, 2 H), 4.20–4.16 (m, 2 H), 3.91–3.57 (m, 16 H), 2.83 (s, 2 H), 1.64 (t, J = 5.8 Hz, 1 H), 1.39 (d, J = 6.9 Hz, 3 H). ^{13}C NMR (100 MHz, $CDCl_3$): ∂ 176.1, 159.5, 148.9, 145.2, 139.0, 136.6, 131.6, 128.5, 126.3, 125.2, 125.1, 115.3, 80.9, 70.8, 70.7, 70.62, 70.55, 70.1, 69.7, 67.9, 67.6, 67.1, 47.5, 38.2, 17.6. HRMS m/z calcd. for $C_{31}H_{36}N_2NaO_{10}$ ($[M+Na]^+$) 619.22622, found 619.22544.

PLPG2

5 (98.8 mg, 0.166 mmol) were dissolved in anisole (1.9 mL). The solution was stirred for 1.5 h under an atmosphere of nitrogen at 155 °C, followed by removal of anisole by distillation. Clean **PLPG2** (87.7 mg, 100%) remained as a brownish oil.

R_f = 0.25 (CH_2Cl_2/MeOH 95:5). IR (neat) 3463 (w), 2874 (m), 1702 (s), 1604 (m), 1516 (s), 1405 (m), 1350 (m), 1248 (m), 825 (s), 695 (s) cm^{-1}. ^1H NMR (500 MHz, $CDCl_3$) ∂ 7.85 (d, J = 8.5 Hz, 1 H), 7.62 (d, J = 1.7 Hz, 1 H), 7.57–7.47 (m, 3 H), 7.02 (d, J = 8.7 Hz, 2 H), 6.71–6.66 (m, 2 H), 4.22–4.14 (m, 2 H), 3.91–3.81 (m, 4 H), 3.74–3.53 (m, 14 H) 1.38 (d, J = 6.9 Hz, 3 H). ^{13}C NMR (125 MHz, $CDCl_3$): ∂ 170.6, 159.4, 148.9, 145.4, 139.0, 134.1, 131.6, 128.5, 126.2, 125.2, 125.0, 115.2, 70.9, 70.7, 70.6, 70.1, 69.7, 67.9, 67.8, 67.6, 37.1, 36.4, 17.6. HRMS m/z calcd. for $C_{27}H_{32}N_2NaO_9$ ($[M+Na]^+$) 551.20000, found 551.19946.

4.8.2 Spectra

In the following, analytical spectra of the newly synthesized and previously not characterized compounds are shown.

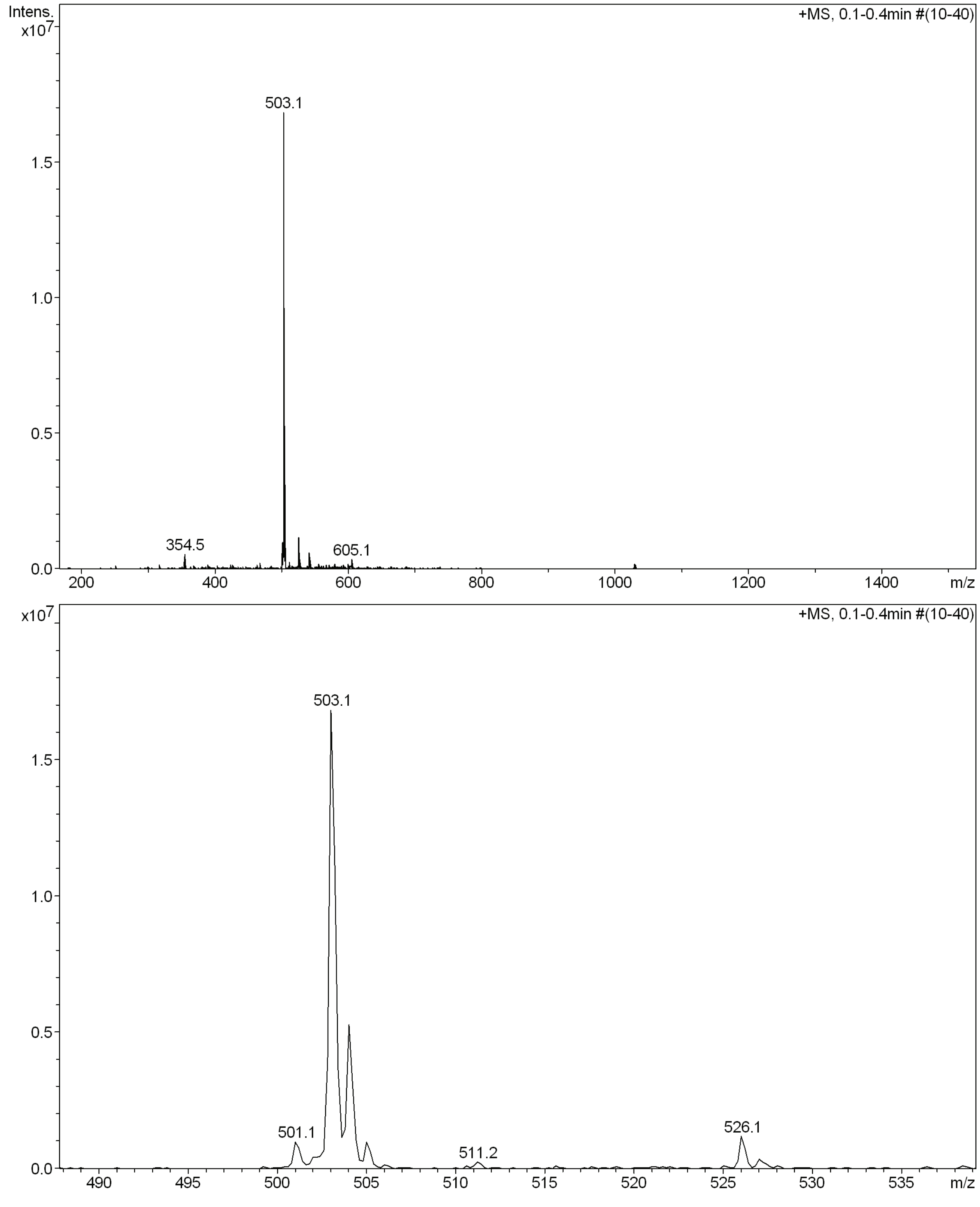

Figure S1. ESI-MS spectrum of **Fc-PLPG1**, showing the full scan range (top) and a magnification of the most relevant range (bottom).

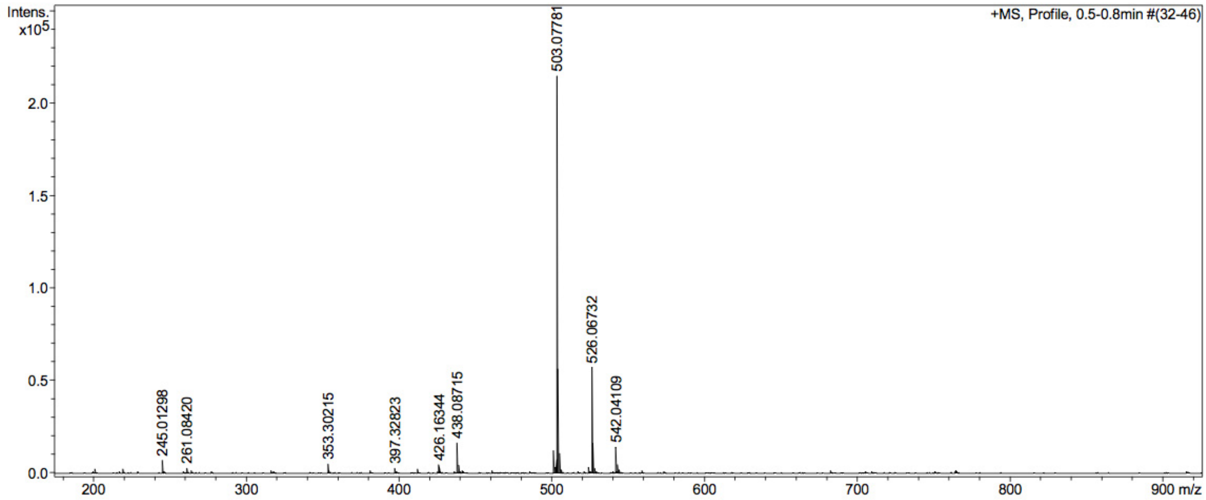

Figure S2. HR ESI-MS spectrum of **Fc-PLPG1**.

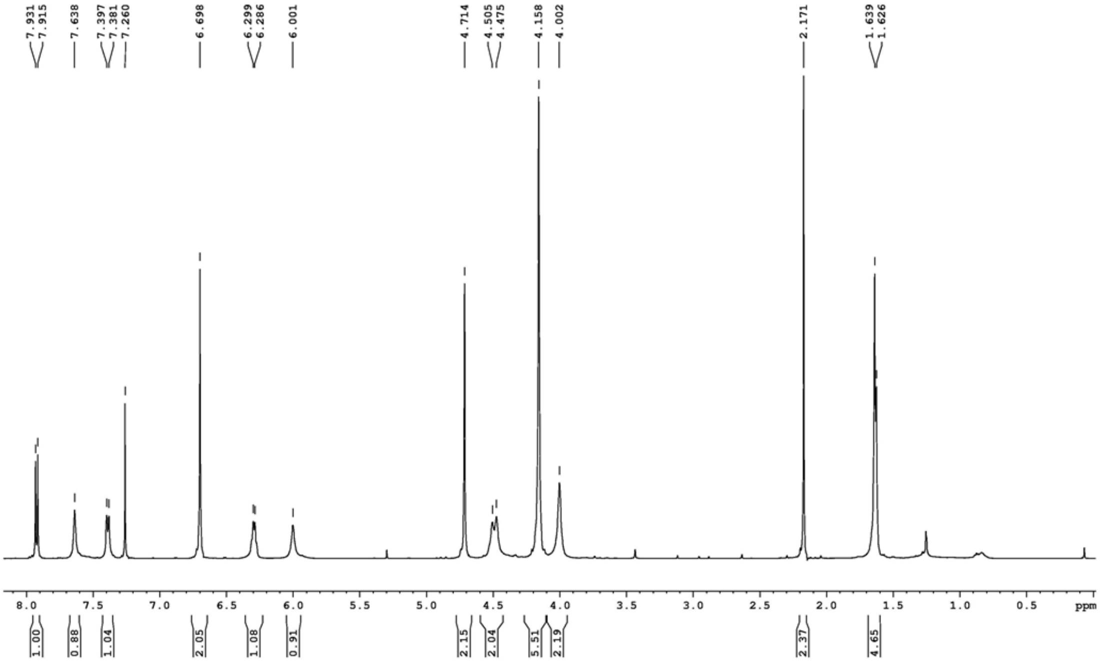

Figure S3. ^{1}H-NMR spectrum of **Fc-PLPG1** in $CDCl_3$.

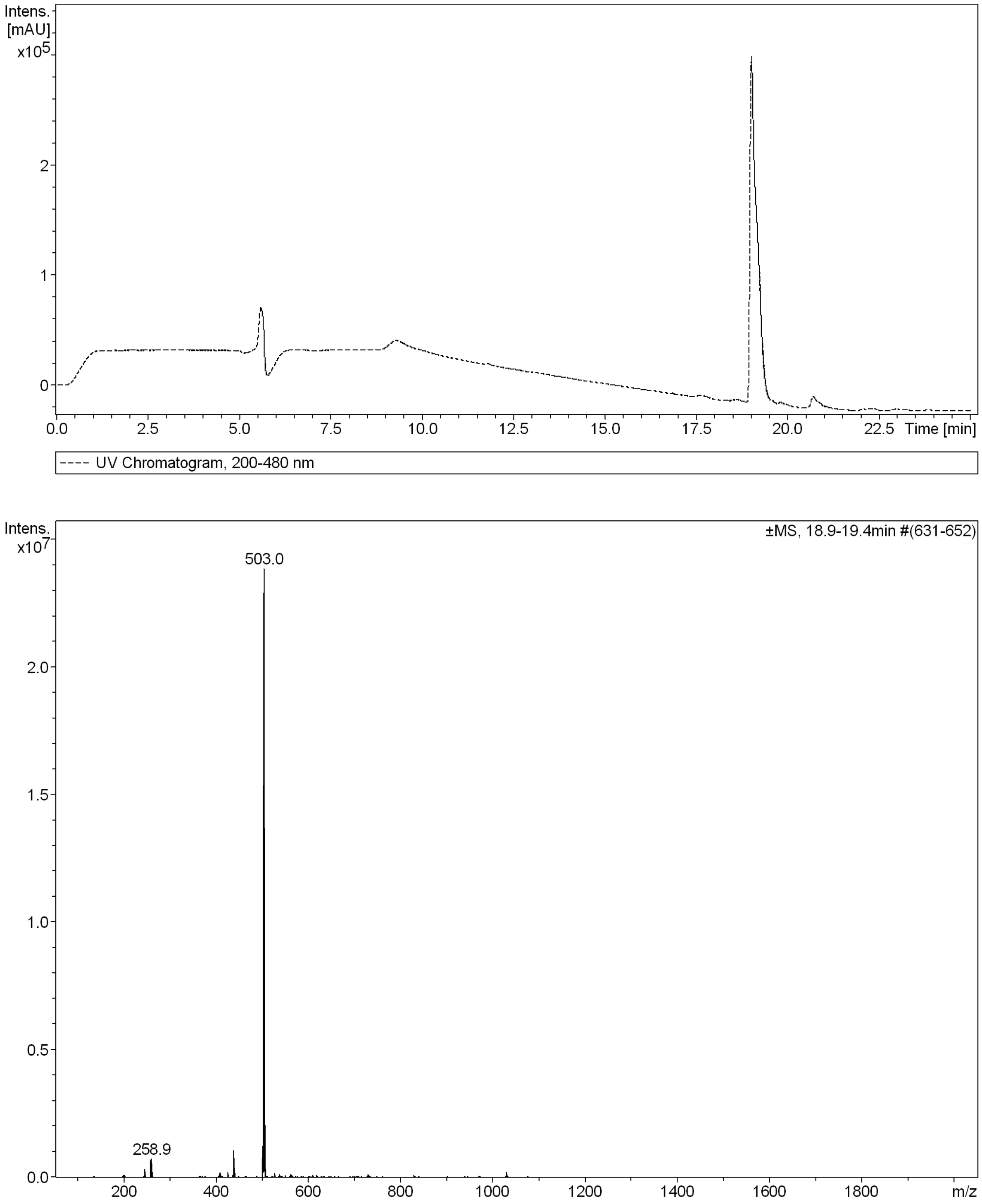

Figure S4. LC-MS spectrum of **Fc-PLPG1**.

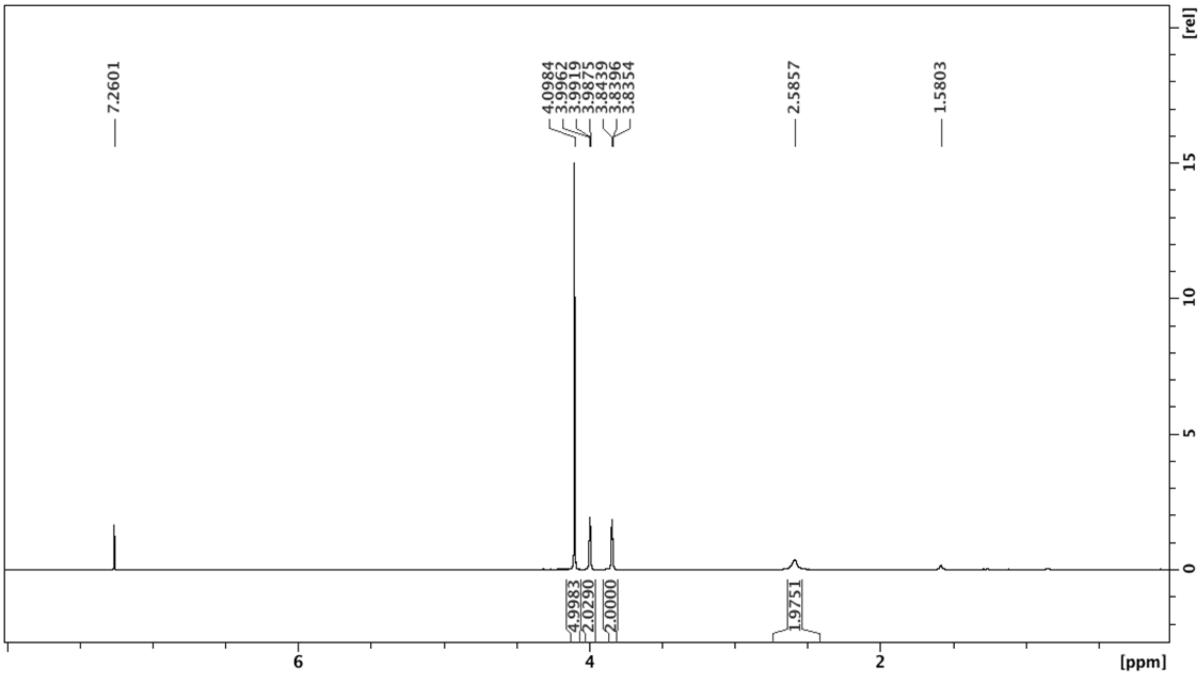

Figure S5. ^{1}H-NMR spectrum of **Fc-NH$_2$** in CDCl$_3$.

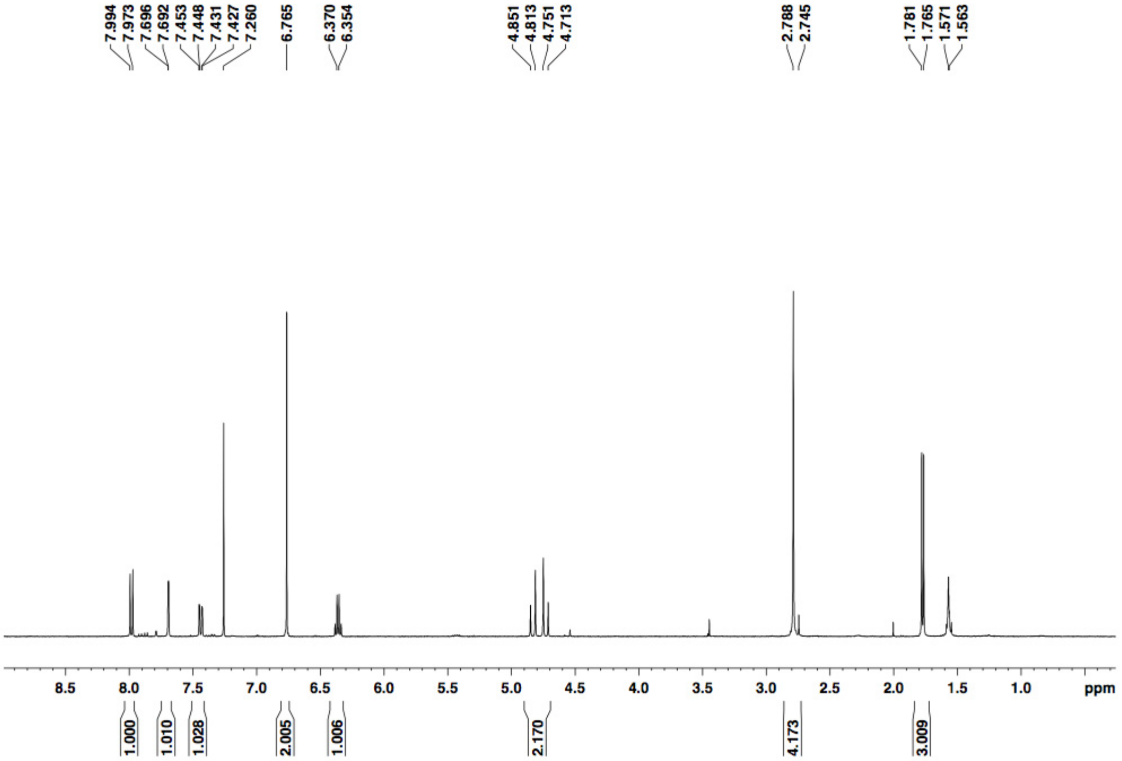

Figure S6. ^{1}H-NMR spectrum of **PLPG1** in CDCl$_3$.

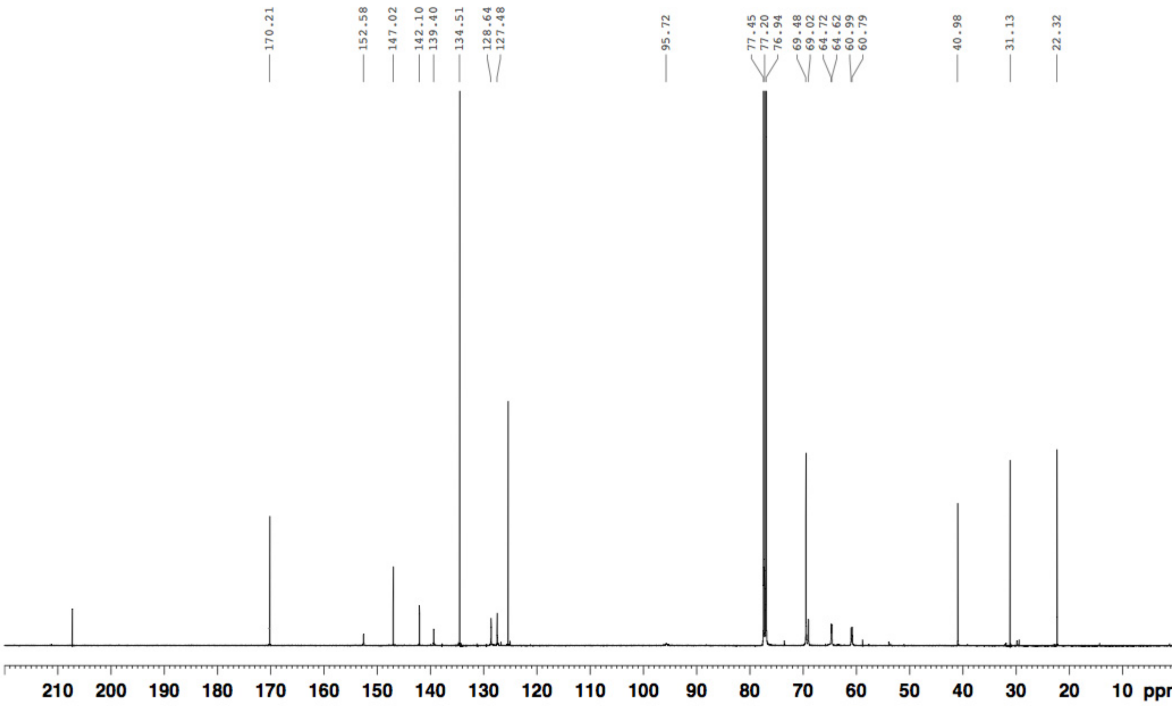

Figure S7. ^{13}C-NMR spectrum of **Fc-PLPG1** in $CDCl_3$.

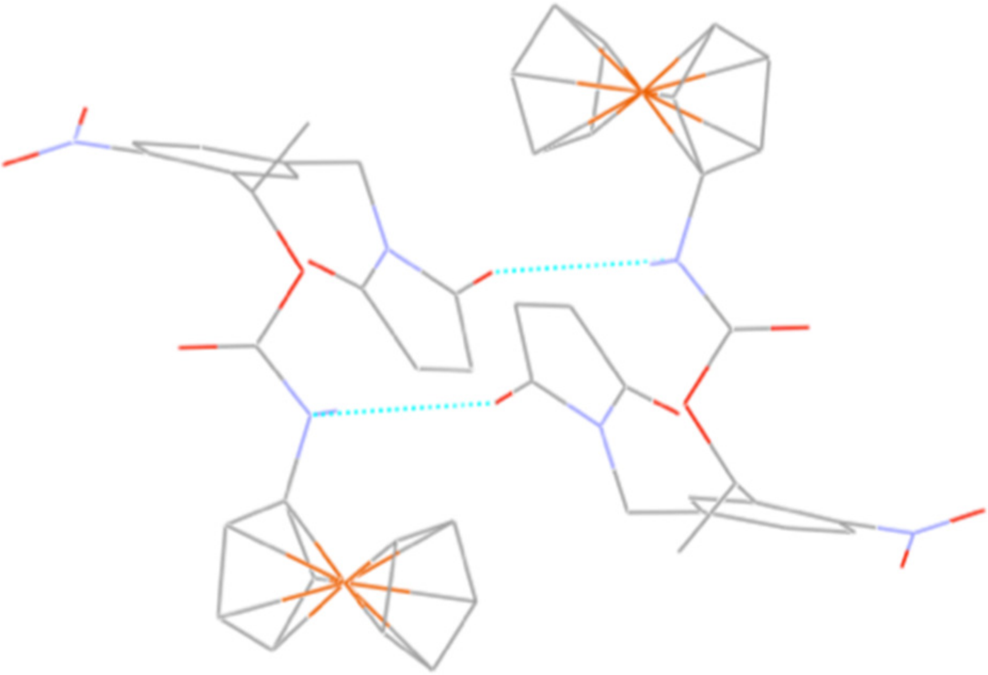

Figure S8. X-ray structure of **Fc-PLPG1**.

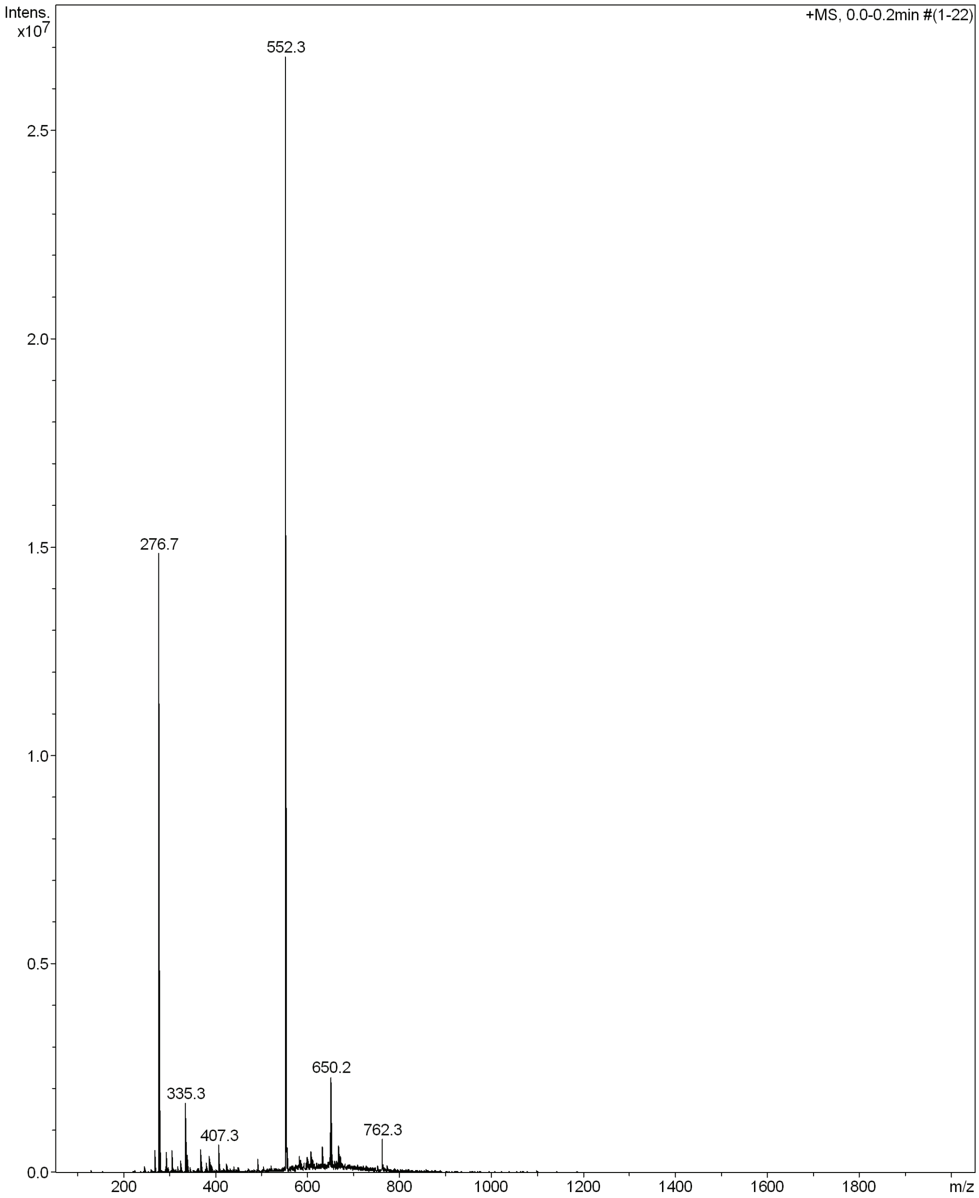

Figure S9. ESI-MS spectrum of **MLS** peptide.

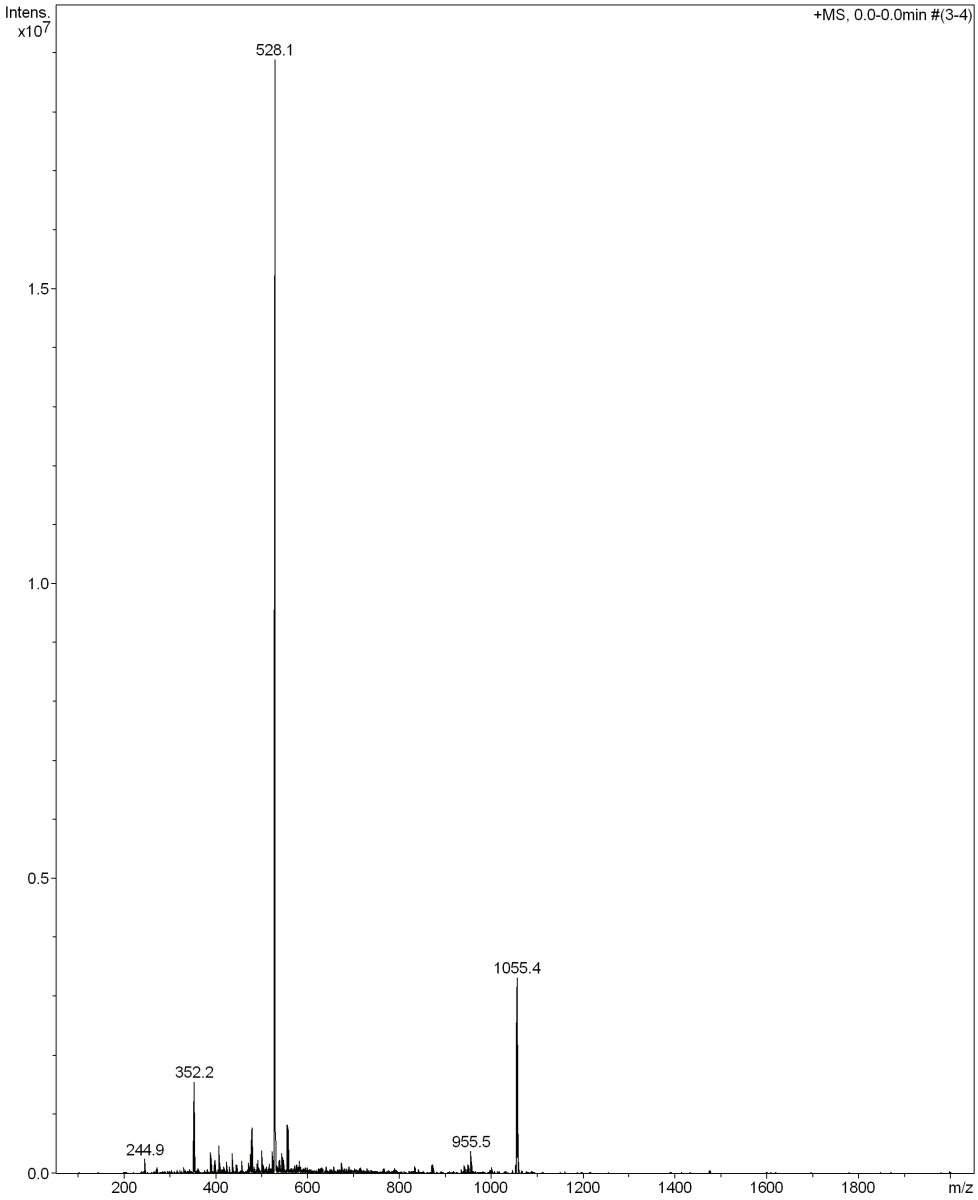

Figure S10. ESI-MS spectrum of **Fc-PLPG1-MLS.**

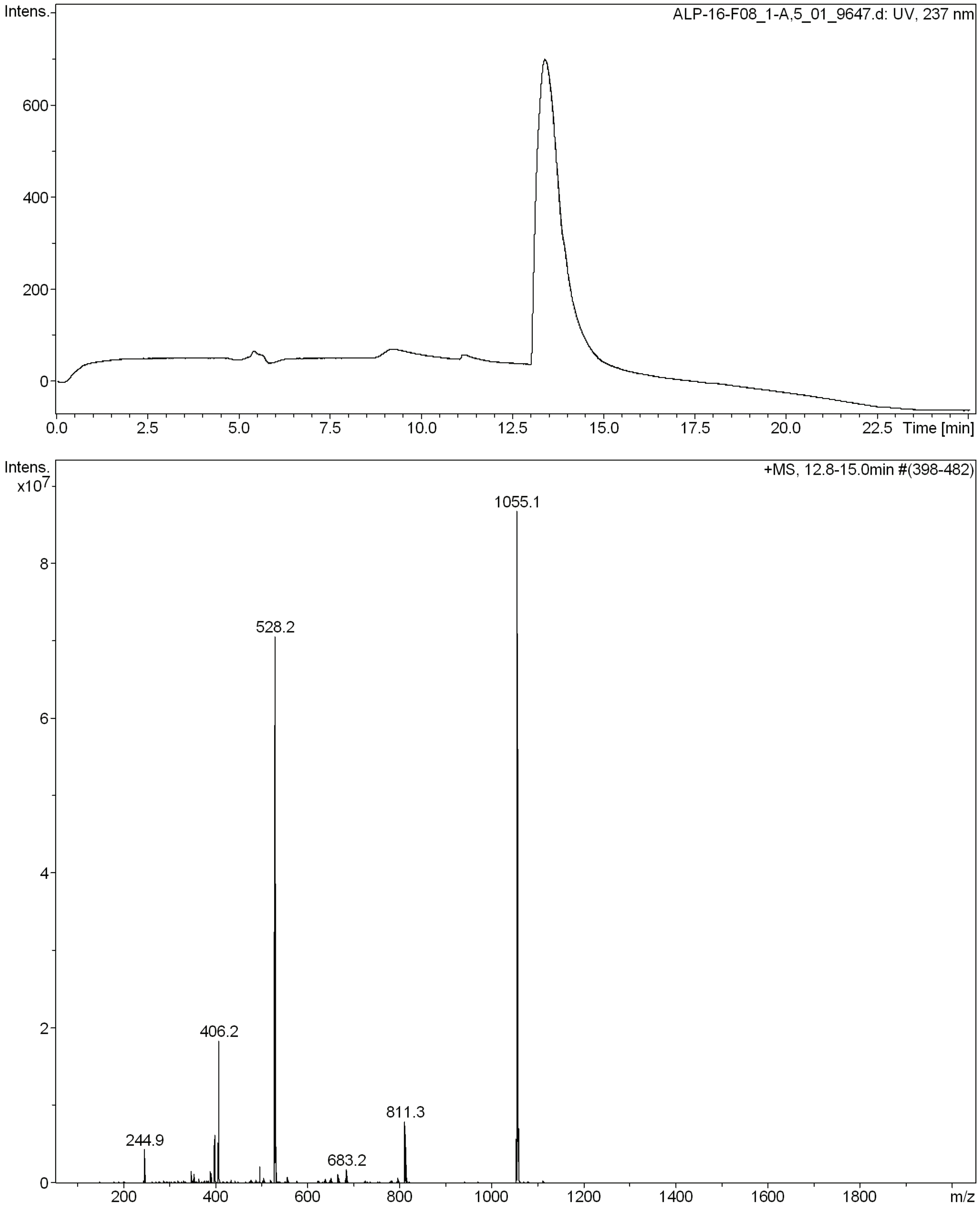

Figure S11. LC-MS spectrum of **Fc-PLPG-MLS1**.

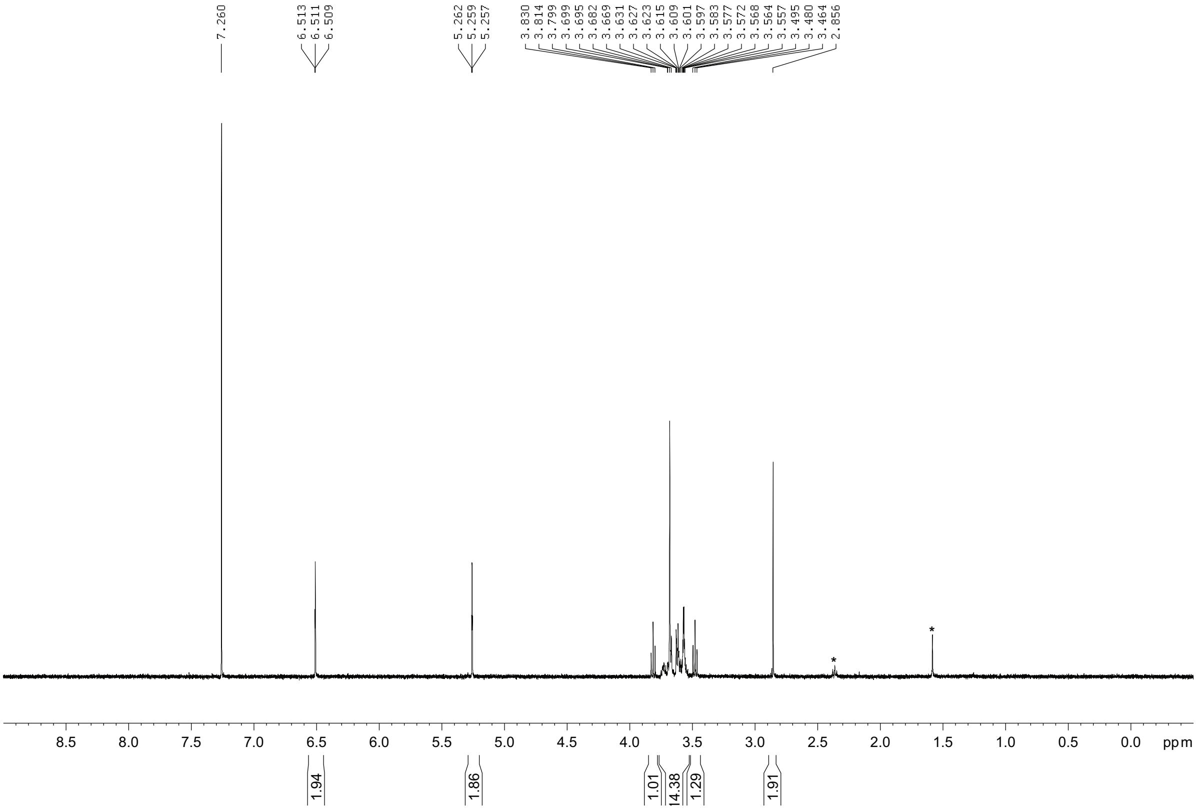

Figure S12. ^{1}H-NMR spectrum of compound **4** in CDCl3.

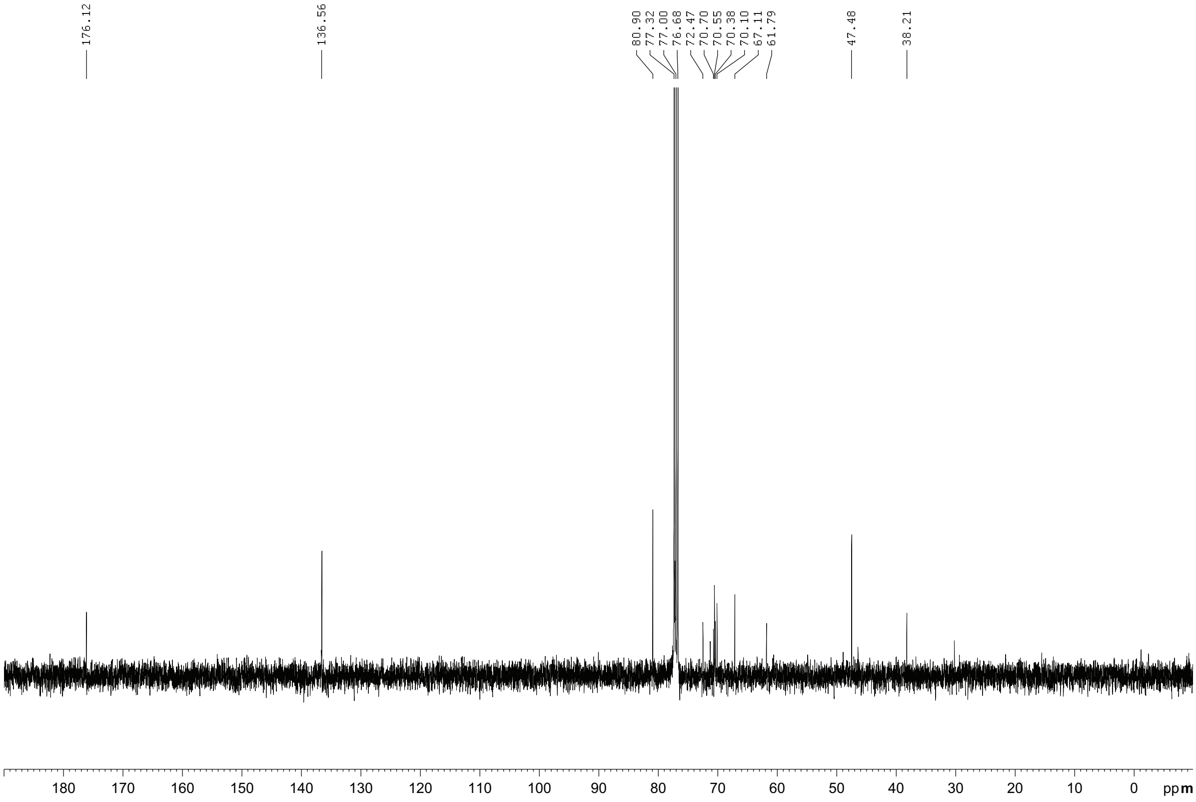

Figure S13. ^{13}C-NMR spectrum of compound **4** in $CDCl_3$.

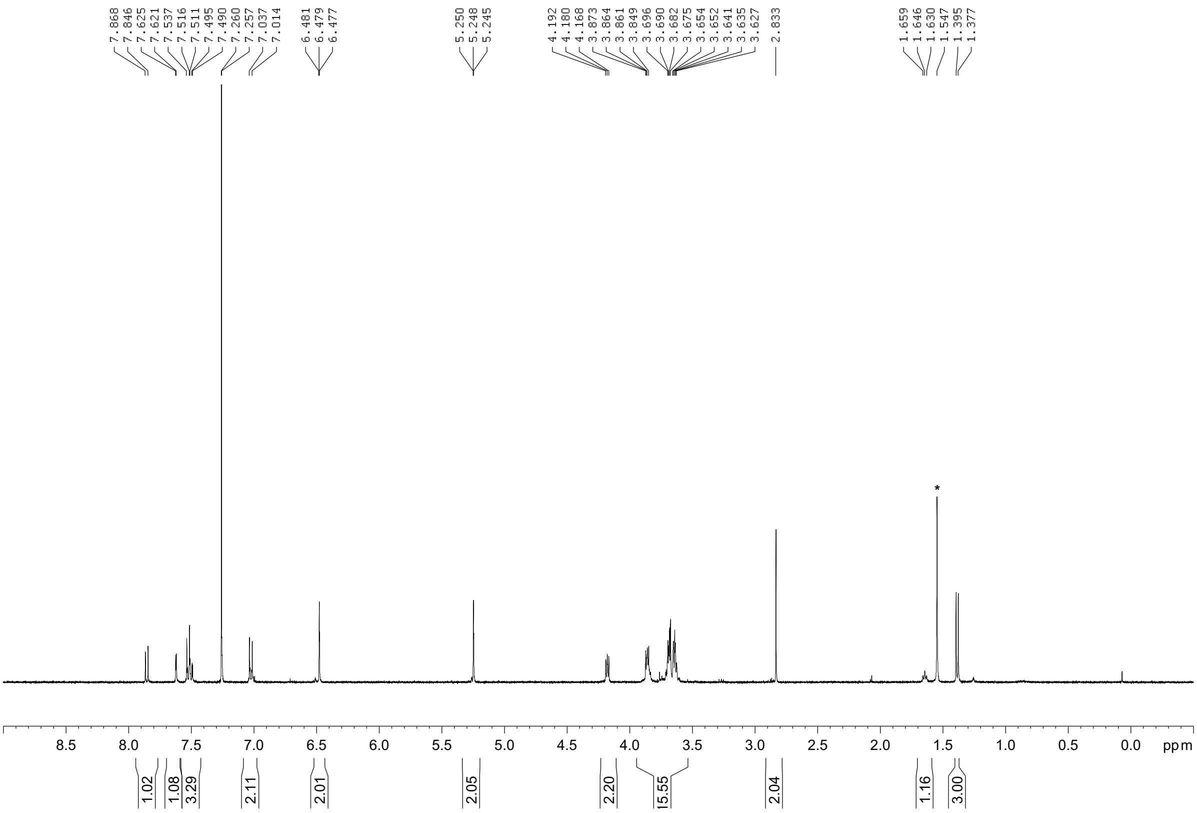

Figure S14. ^{1}H-NMR spectrum of compound **5** in $CDCl_3$.

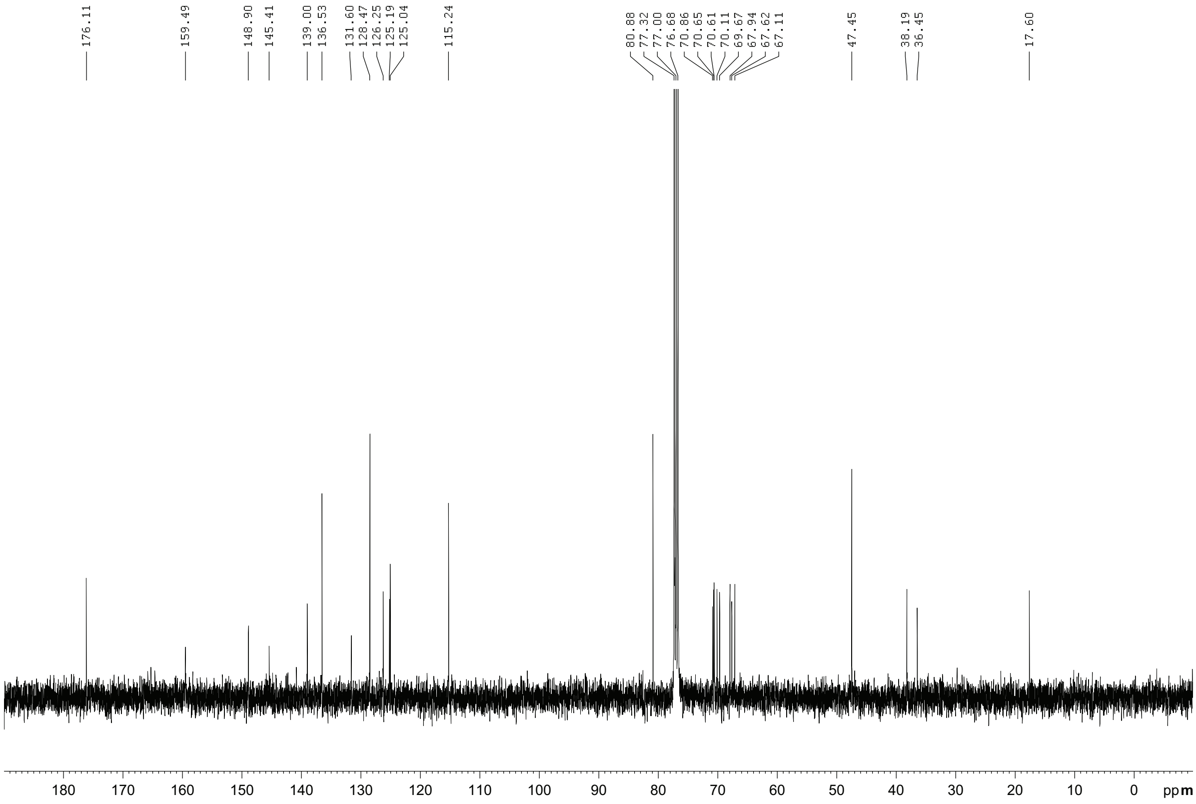

Figure S15. ^{13}C-NMR spectrum of compound **5** in $CDCl_3$.

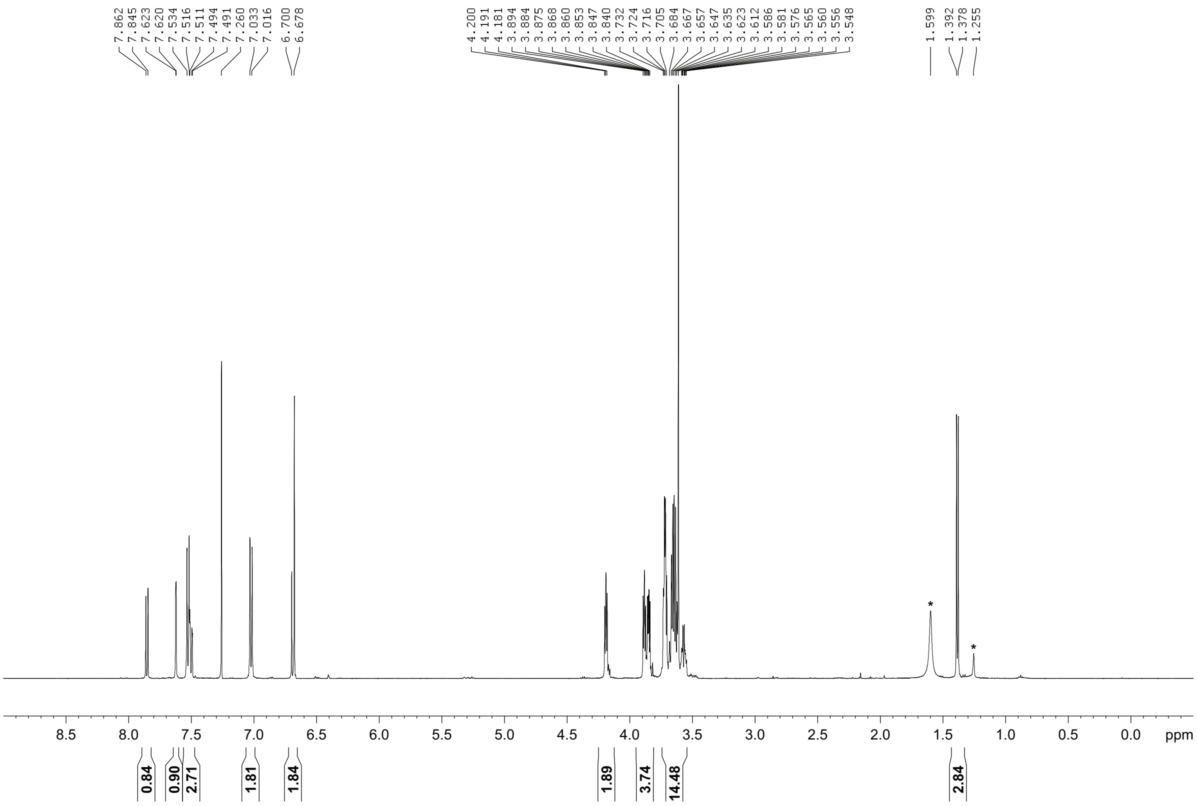

Figure S16. ^{1}H-NMR spectrum of compound **PLPG2** in $CDCl_3$.

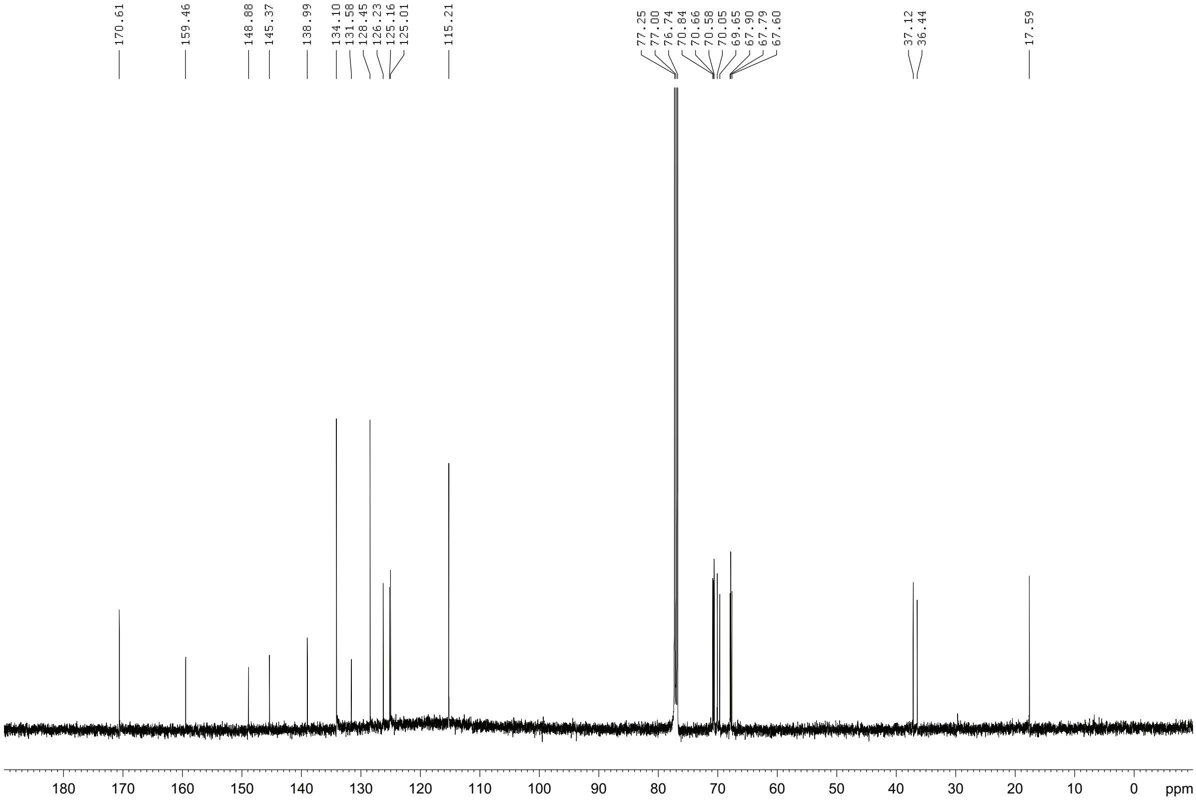

Figure S17. ^{13}C-NMR spectrum of compound **PLPG2** in $CDCl_3$.

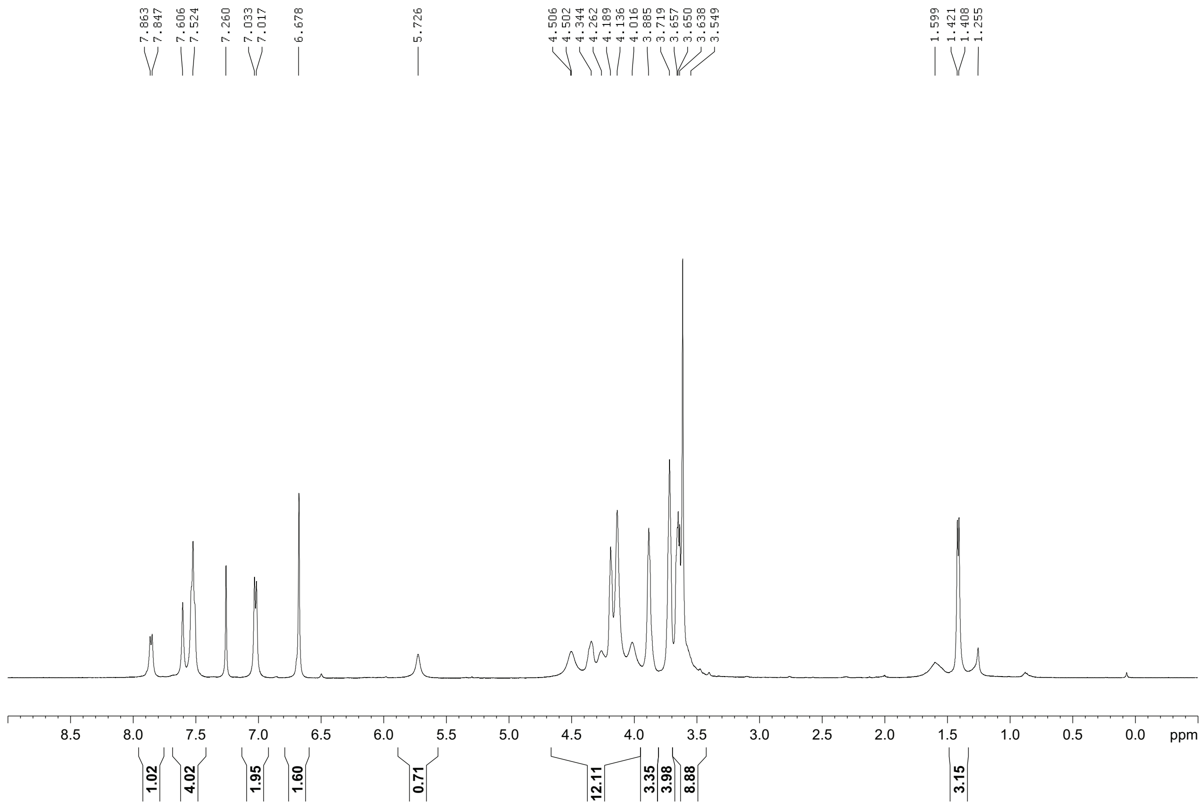

Figure S18. ^{1}H-NMR spectrum of **Fc-PLPG2** in $CDCl_3$.

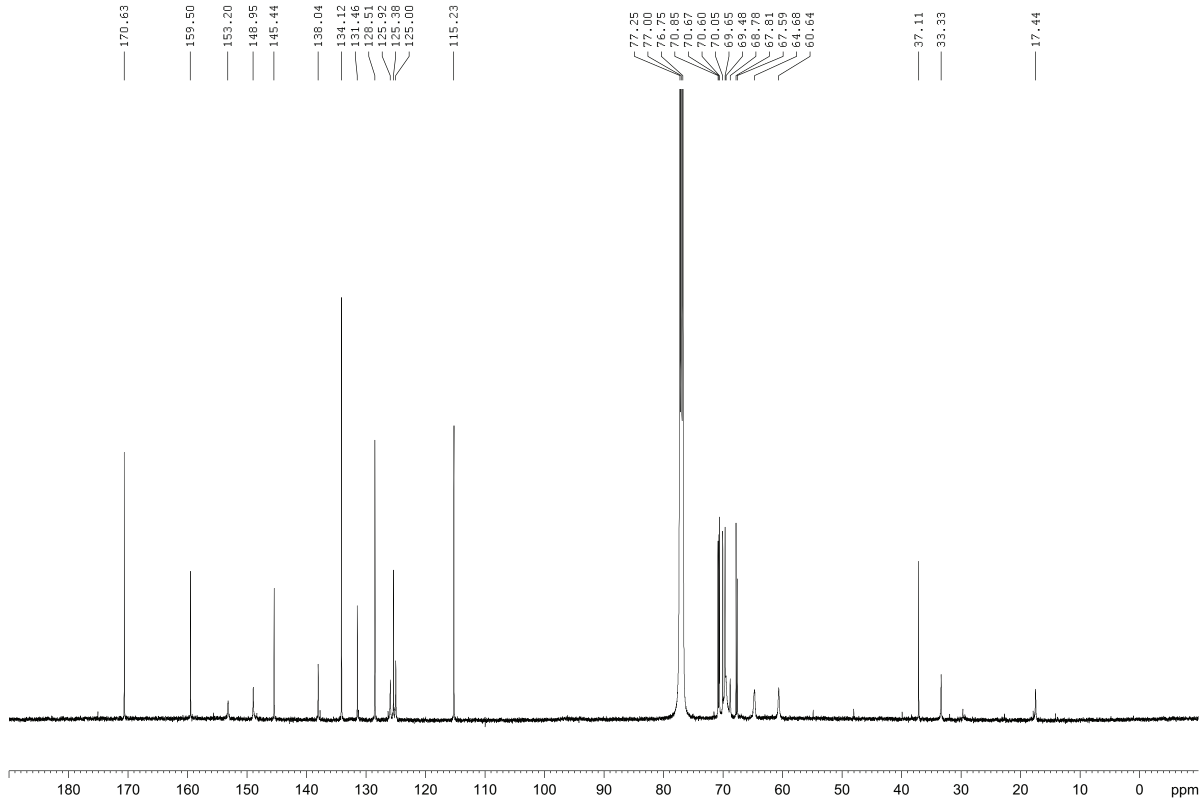

Figure S19. ^{13}C-NMR spectrum of **Fc-PLPG2** in $CDCl_3$.

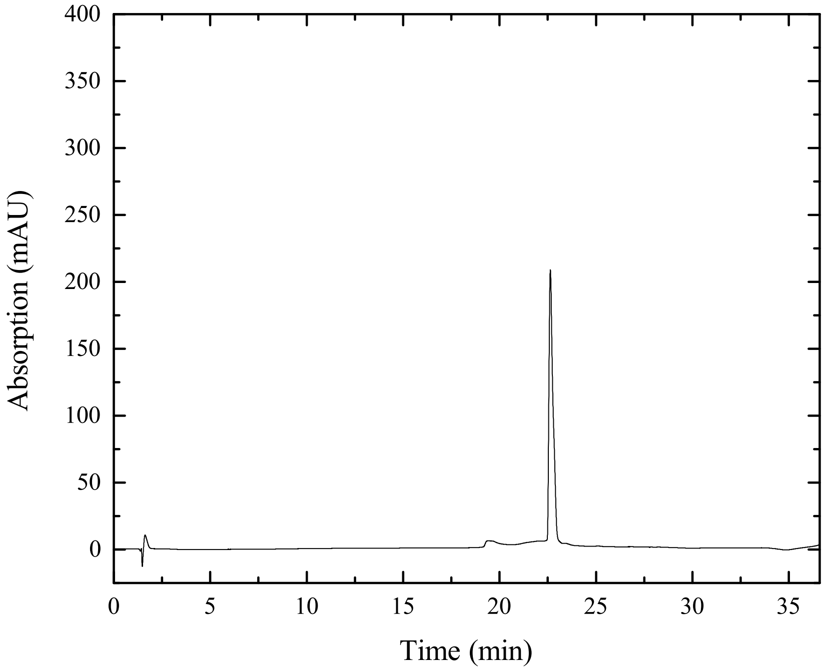

Figure S20. Analytical HPLC trace of **Fc-PLPG2-MLS**.

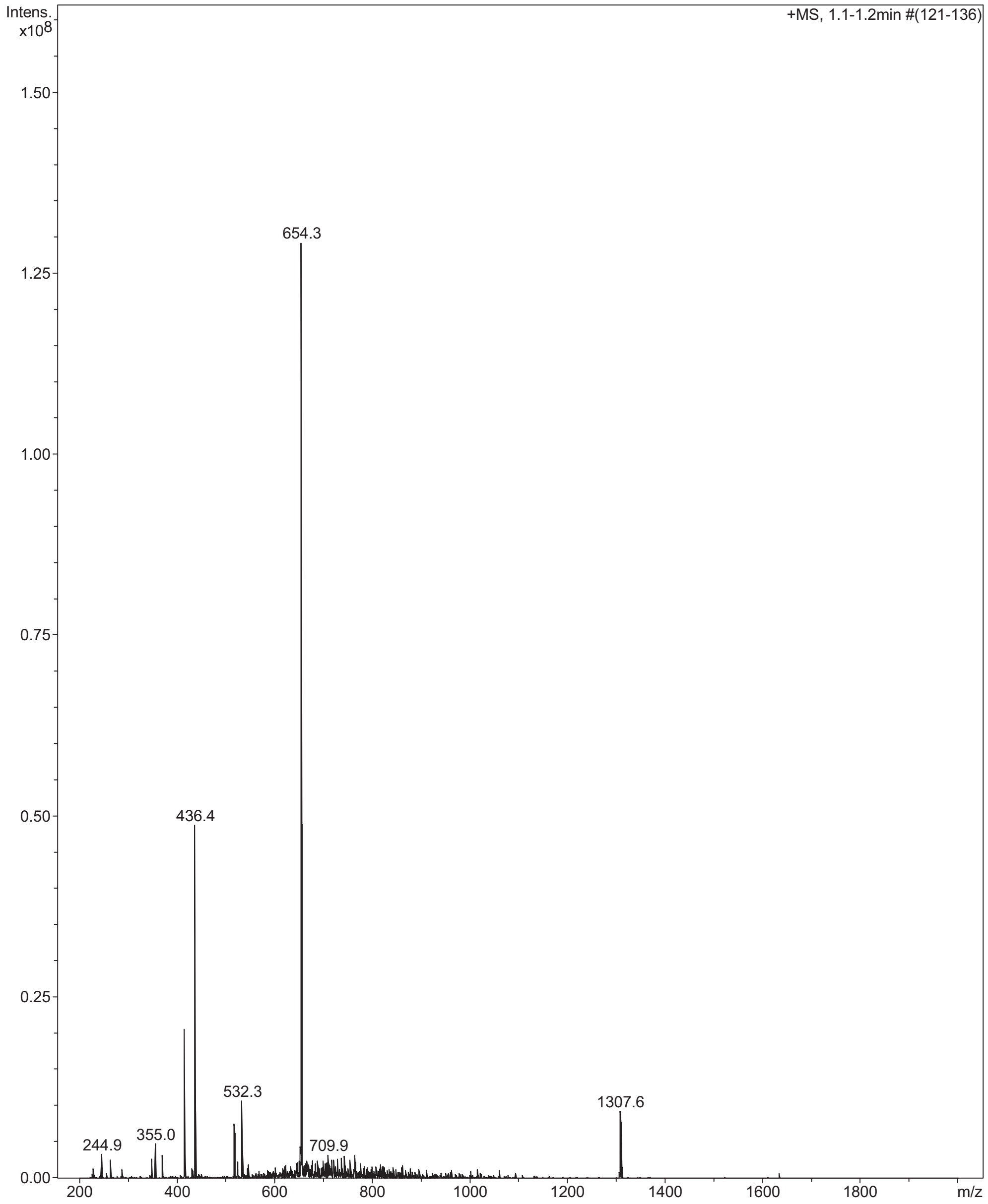

Figure S21. ESI-MS of **Fc-PLPG2-MLS**.

4.8.3 Laser Photolysis Quantum Yield Determination

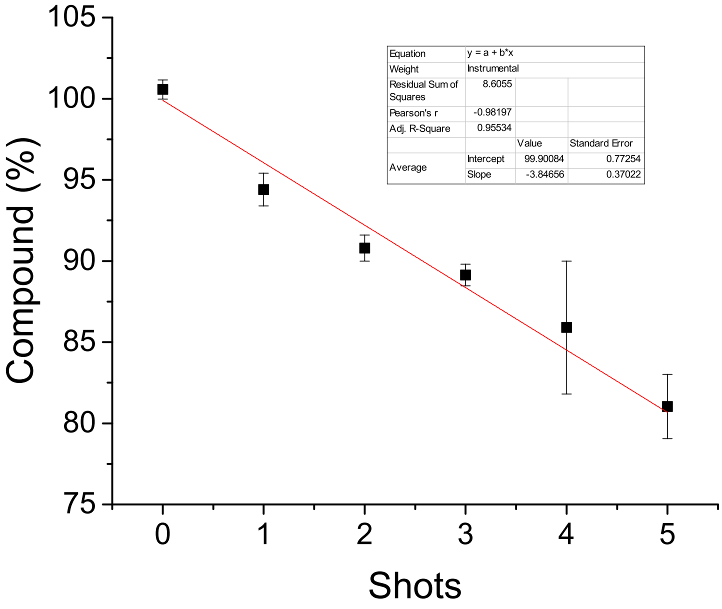

Equation	y = a + b*x		
Weight	Instrumental		
Residual Sum of Squares	8.6055		
Pearson's r	-0.98197		
Adj. R-Square	0.95534		
		Value	Standard Error
Average	Intercept	99.90084	0.77254
	Slope	-3.84656	0.37022

Figure S22. Determination of photolysis quantum yield: conversion of *trans*-azobenzene upon laser irradiation at 355 nm in MeOH, quantified by UV/Vis spectroscopy.

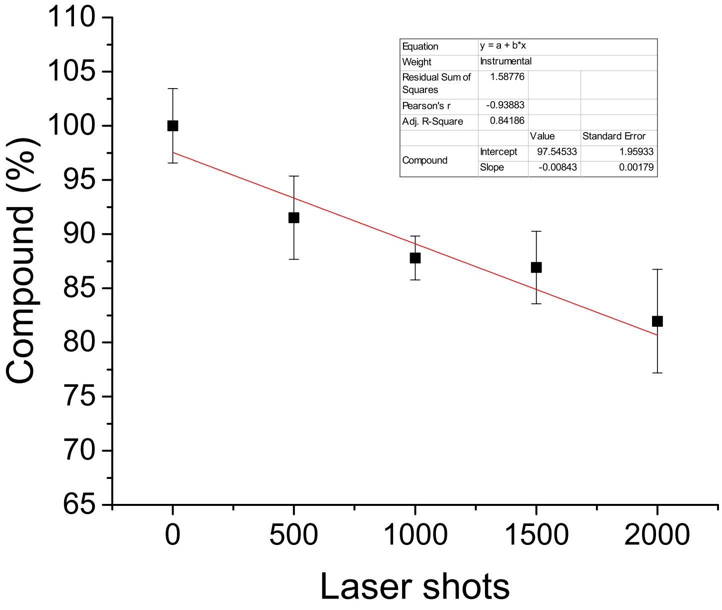

Equation	y = a + b*x		
Weight	Instrumental		
Residual Sum of Squares	1.58776		
Pearson's r	-0.93883		
Adj. R-Square	0.84186		
		Value	Standard Error
Compound	Intercept	97.54533	1.95933
	Slope	-0.00843	0.00179

Figure S23. Determination of photolysis quantum yield: decomposition of **Fc-PLPG1-MLS** in PBS (pH=7.4) upon laser irradiation at 355 nm, quantified by UPLC.

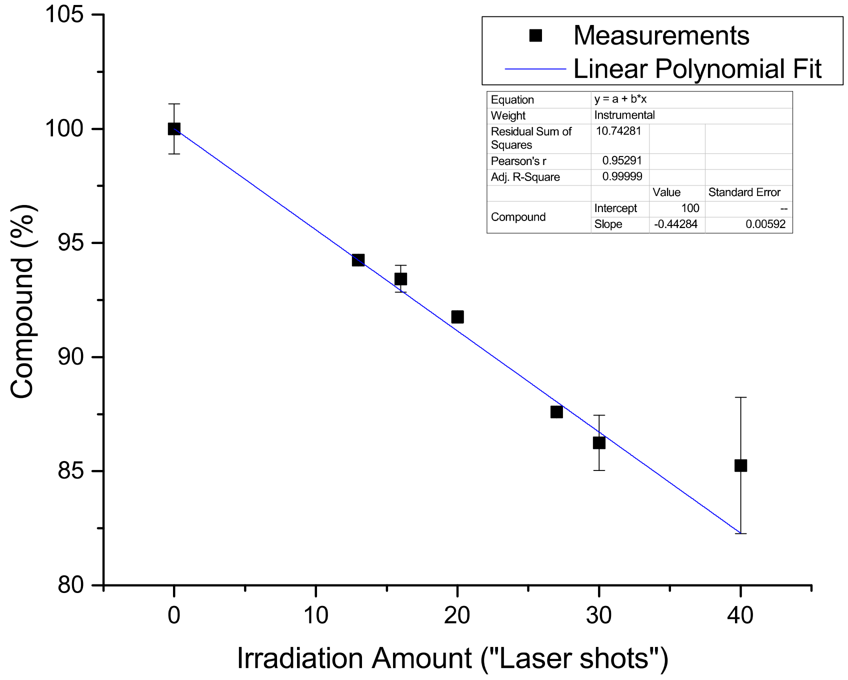

Figure S24. Determination of photolysis quantum yield: decomposition of **Fc-PLPG2-MLS** in PBS (pH=7.4) upon laser irradiation at 355 nm, quantified by UPLC.

4.8.4 UV-A Photoreactor Photolysis

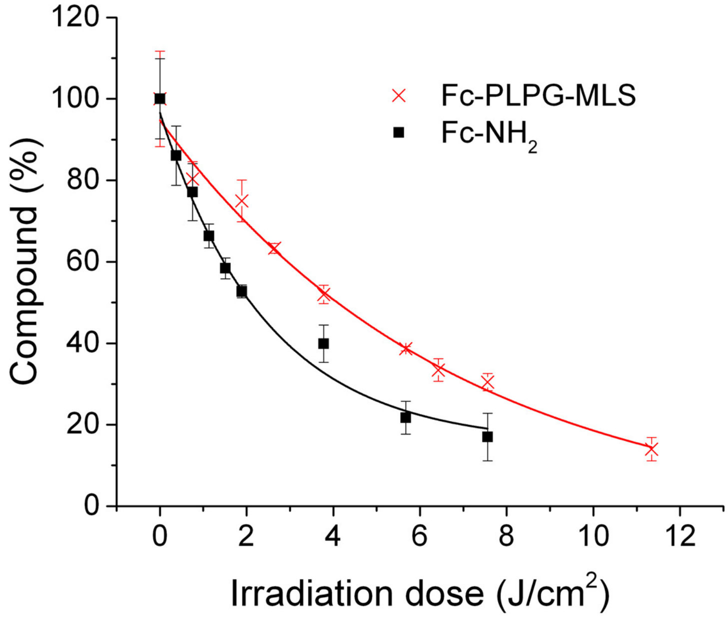

Figure S25. Decomposition of **Fc-PLPG1-MLS** and **Fc-NH$_2$** in PBS (pH=7.4) upon UV-A irradiation (Rayonet reactor) quantified by LC-MS.

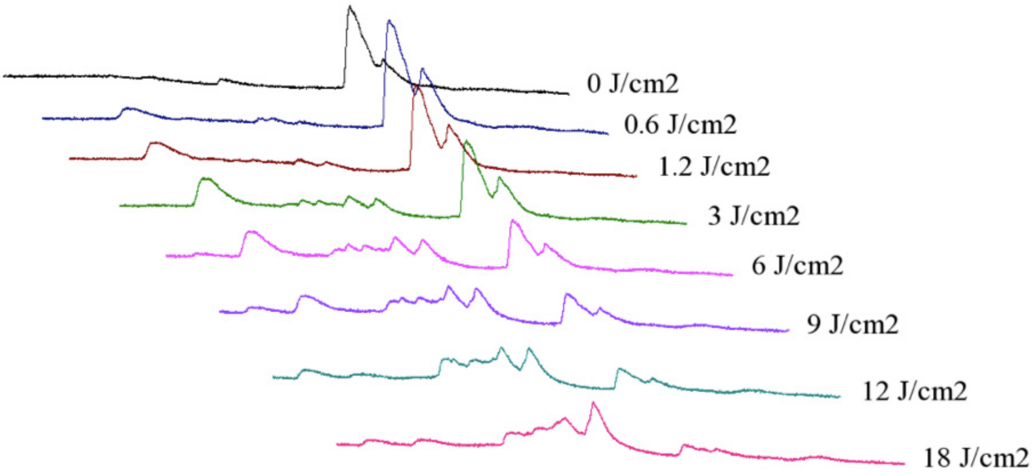

Figure S26. LC spectra of the decomposition of **Fc-PLPG1-MLS** in PBS (pH=7.4) upon UV-A irradiation (Rayonet reactor).

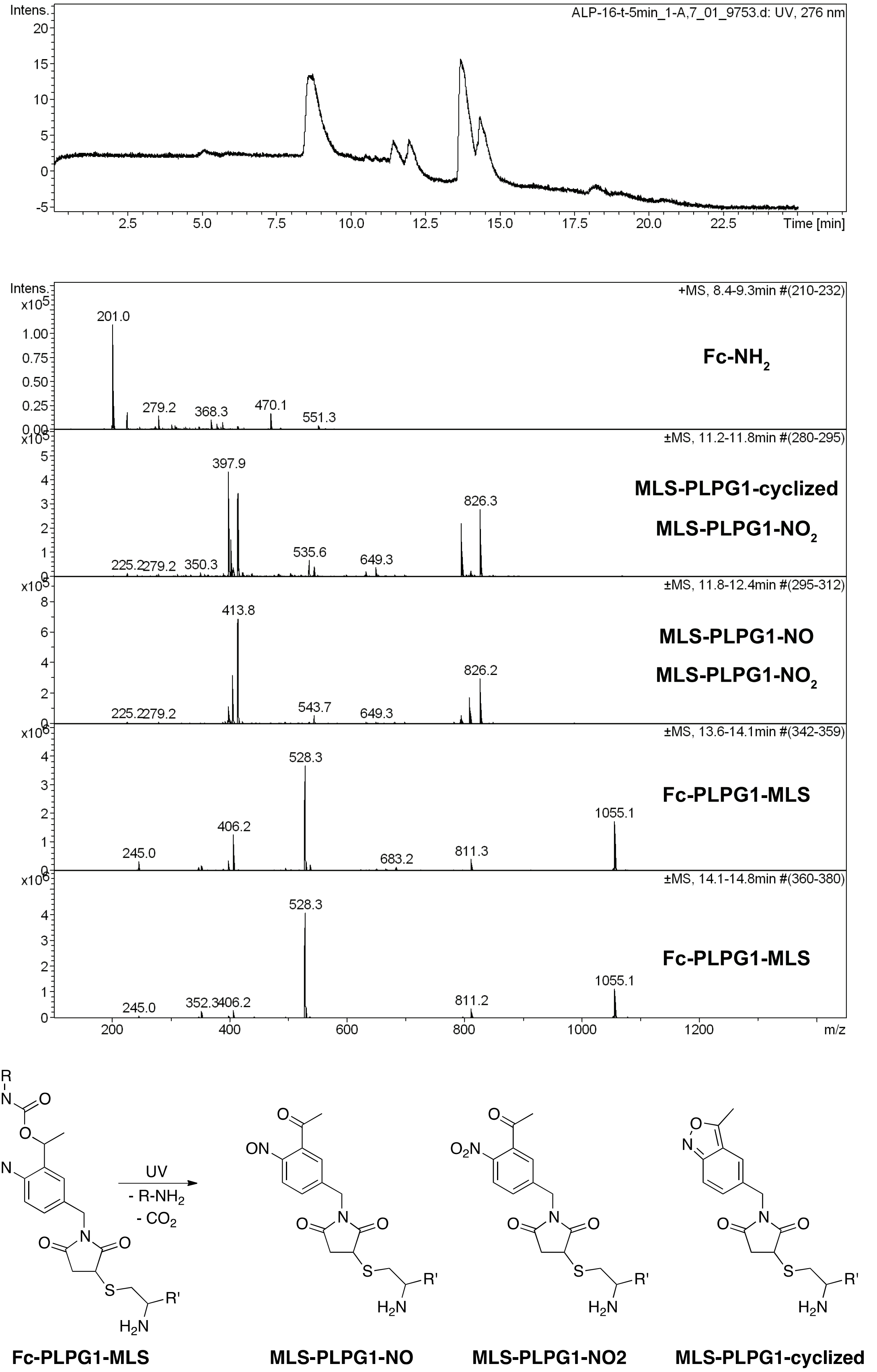

Figure S27. LC-MS spectra of the decomposition of **Fc-PLPG1-MLS** after UV-A irradiation (3 J/cm^2 dose, Rayonet reactor) in PBS (pH=7.4) quantified by LC-MS (top) and the possible byproducts of **PLPG1** (below).

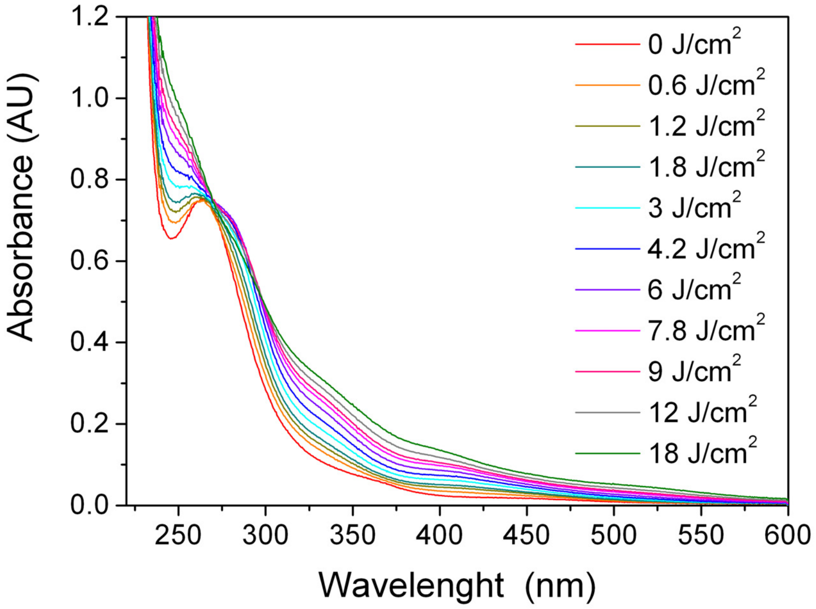

Figure S28. Variation of the UV/Vis spectrum of **Fc-PLPG1-MLS** during UV-A irradiation (Rayonet reactor) in PBS (pH=7.4).

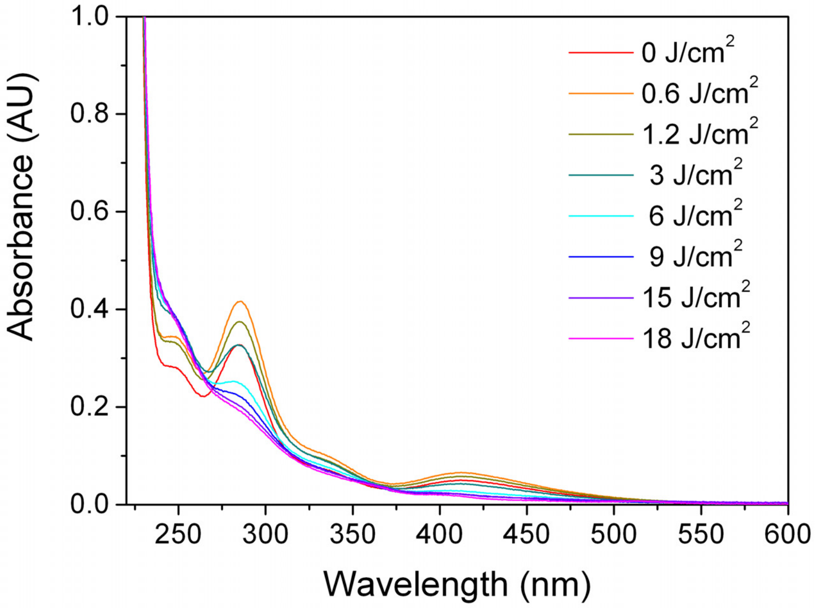

Figure S29. Variation of the UV/Vis spectrum of **Fc-NH$_2$** during UV-A irradiation (Rayonet reactor) in PBS (pH=7.4).

4.8.5 UV/Vis Spectra

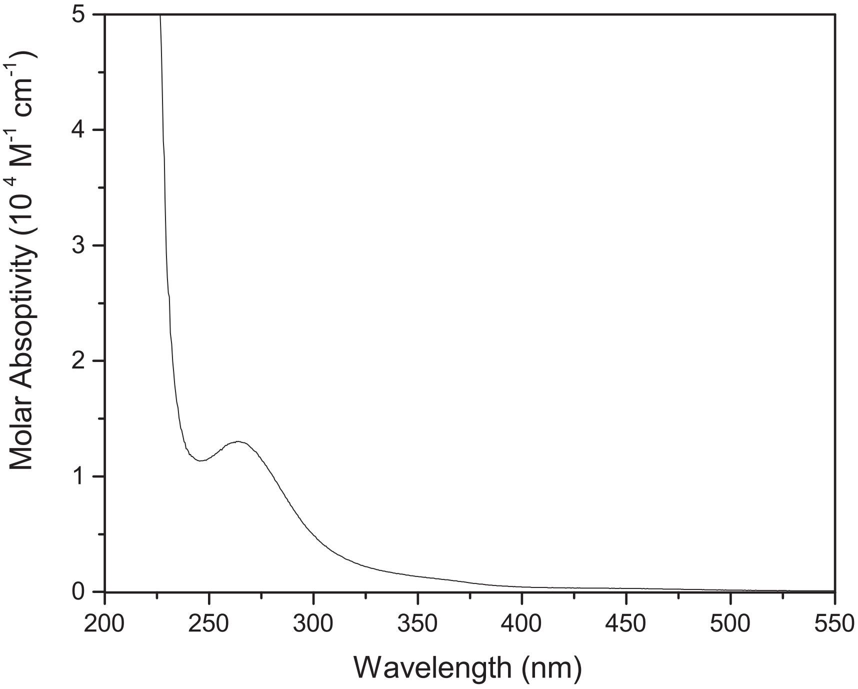

Figure S30. UV/Vis spectrum of **Fc-PLPG1-MLS** in PBS (pH=7.4).

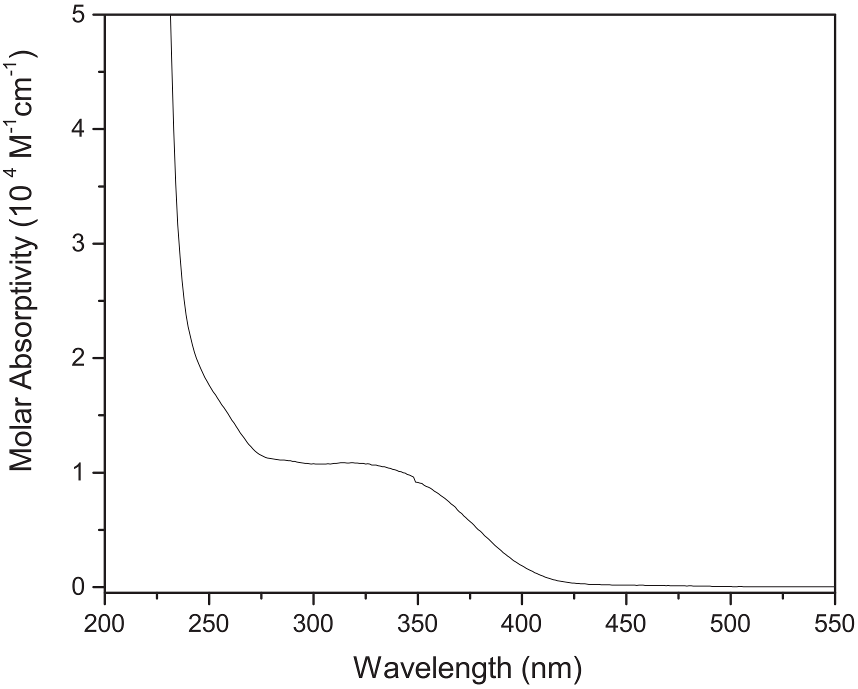

Figure S31. UV/Vis spectrum of **Fc-PLPG2-MLS** in PBS (pH=7.4).

4.8.6 Iron Release upon UV-A Irradiation

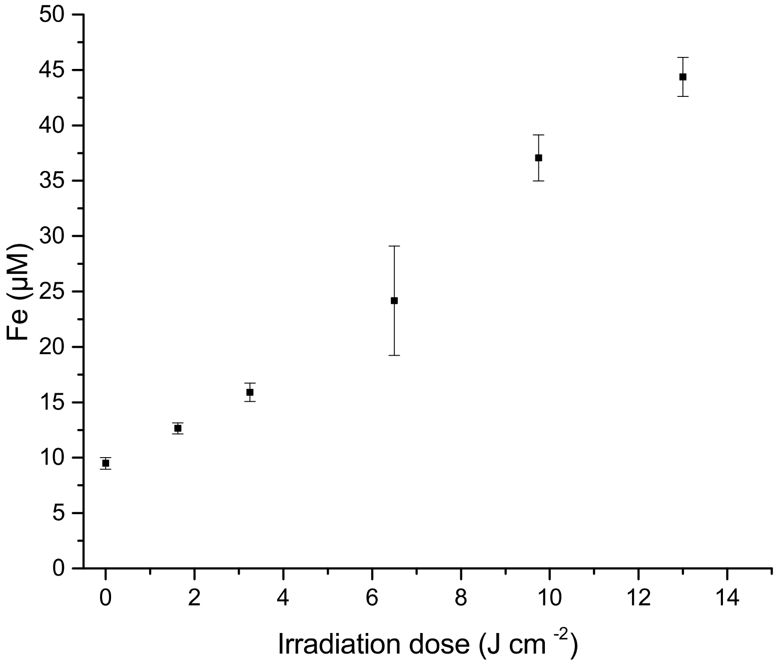

Figure S32. Iron release from **Fc-PLPG1-MLS** in PBS (pH=7.4) during light irradiation (Rayonet reactor).

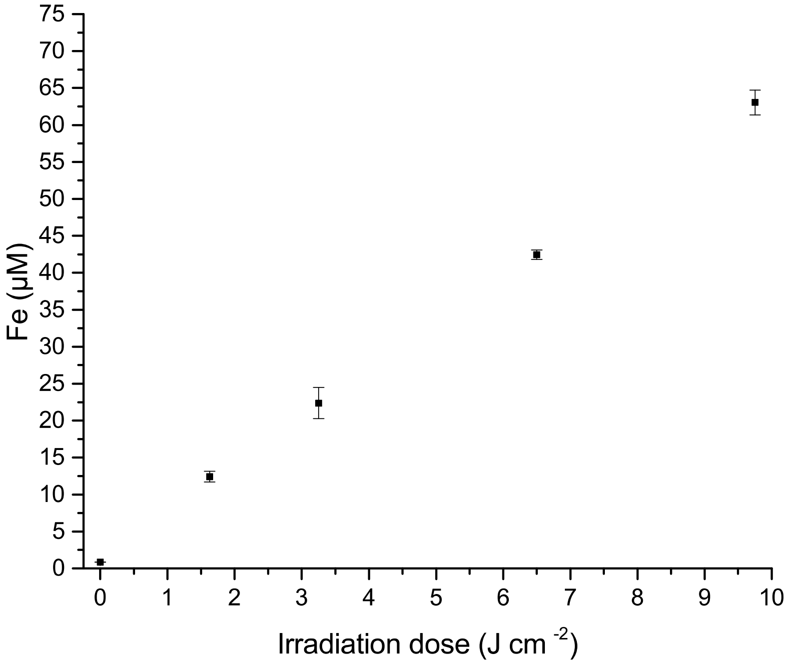

Figure S33. Iron release from **Fc-PLPG2-MLS** in PBS (pH=7.4) during light irradiation (Rayonet reactor).

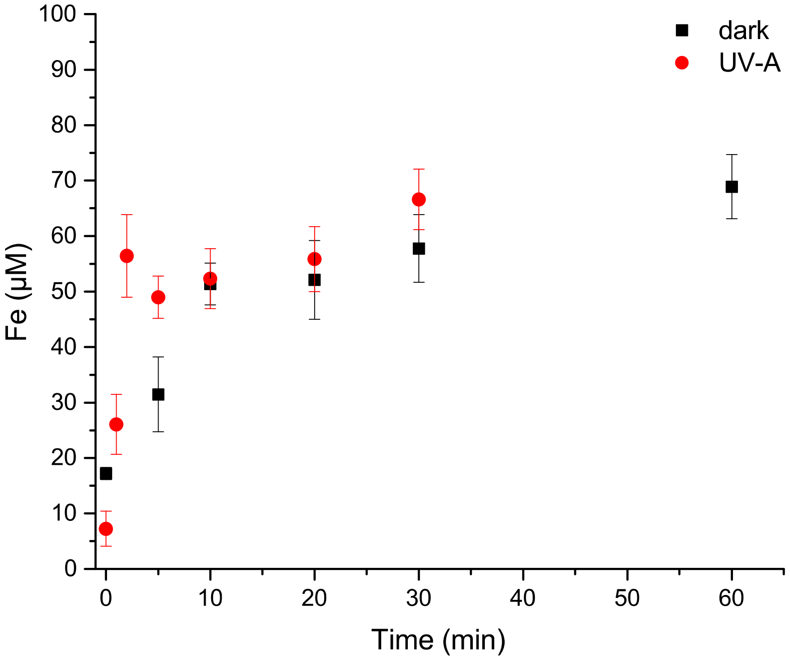

Figure S34. Iron release from **Fc-NH$_2$** in PBS (pH=7.4) in the dark and during light irradiation (Rayonet reactor).

4.8.7 Iron Release in the Dark

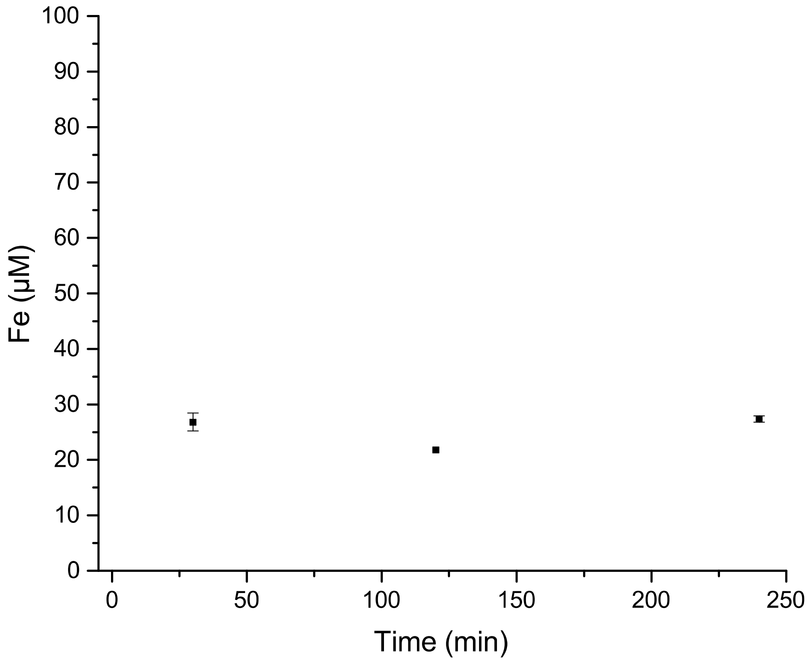

Figure S35. Iron release from **Fc-PLPG1-MLS** in PBS (pH=7.4) in the dark at room temperature.

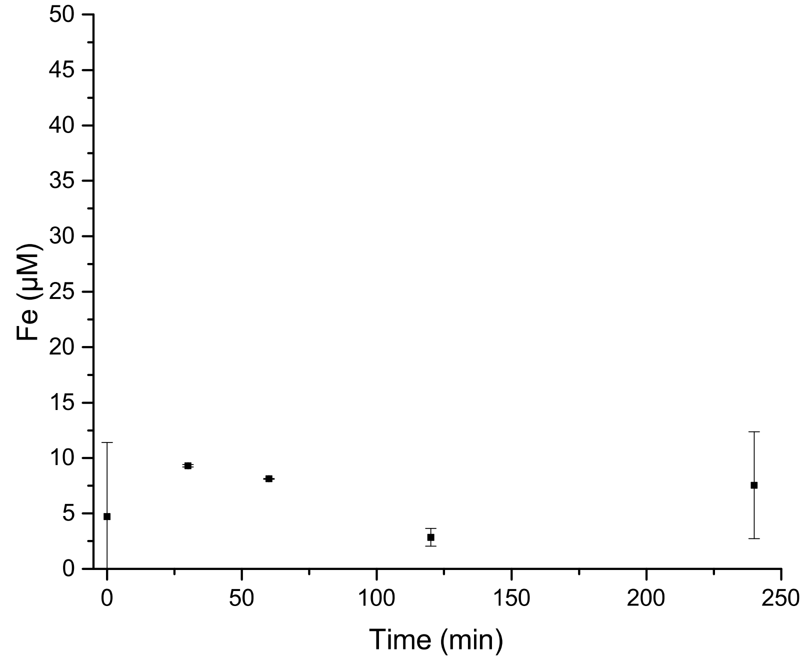

Figure S36. Iron release from **Fc-PLPG2-MLS** in PBS (pH 7.4) in the dark at room temperature.

4.9 References and Notes

[1] H. Hagen, P. Marzenell, E. Jentzsch, F. Wenz, M. R. Veldwijk, A. Mokhir, *J. Med. Chem.* **2012**, *55*, 924–934.

[2] P. Marzenell, H. Hagen, L. Sellner, T. Zenz, R. Grinyte, V. Pavlov, S. Daum, A. Mokhir, *J. Med. Chem.* **2013**, *56*, 6935–6944.

[3] a) K. Kashfi, B. Rigas, *Biochem. Biophys. Res. Commun.* **2007**, *358*, 1096–1101; b) N. Hulsman, J. P. Medema, C. Bos, A. Jongejan, R. Leurs, M. J. Smit, de Esch, Iwan J. P., D. Richel, M. Wijtmans, *J. Med. Chem.* **2007**, *50*, 2424–2431.

[4] a) D. Hamels, P. M. Dansette, E. A. Hillard, S. Top, A. Vessières, P. Herson, G. Jaouen, D. Mansuy, *Angew. Chem. Int. Ed.* **2009**, *48*, 9124–9126; b) E. Hillard, A. Vessières, L. Thouin, G. Jaouen, C. Amatore, *Angew. Chem. Int. Ed.* **2006**, *45*, 285–290.

[5] a) G. R. Knox, P. L. Pauson, *J. Chem. Soc.* **1961**, 4615–4618; b) W. E. Britton, R. Kashyap, M. El-Hashash, M. El-Kady, M. Herberhold, *Organometallics* **1986**, *5*, 1029–1031.

[6] a) P. Köpf-Maier, H. Köpf, E. W. Neuse, *J. Cancer Res. Clin. Oncol.* **1984**, *108*, 336-340; b) P. Köpf-Maier, H. Köpf, *Chem. Rev.* **1987**, *87*, 1137–1152; c) D. R. van Staveren, N. Metzler-Nolte, *Chem. Rev.* **2004**, *104*, 5931–5986; d) S. Goldstein, D. Meyerstein, G. Czapski, *Free Radicals Biol. Med.* **1993**, *15*, 435–445.

[7] a) B. Halliwell, *Biochem. J.* **2007**, *401*, 1–11; b) R. H. Engel, A. W. Evens, *Front. Biosci.* **2006**, *11*, 300–312; c) T. Finkel, *Curr. Opin. Cell Biol.* **2003**, *15*, 247–254; d) P. T. Schumacker, *Cancer Cell* **2006**, *10*, 175–176; e) J. O'Donnell-Tormey, C. J. DeBoer, C. F. Nathan, *J. Clin. Invest.* **1985**, *76*, 80–86; f) T. P. Szatrowski, C. F. Nathan, *Cancer Res.* **1991**, *51*, 794–798; g) J. R. Stone, *Arch. Biochem. Biophys.* **2004**, *422*, 119–124; h) F. Antunes, E. Cadenas, *FEBS Lett.* **2000**, *475*, 121–126.

[8] a) N. Lilienthal, C. Prinz, A. A. Peer-Zada, M. Doering, L. A. Ba, M. Hallek, C. Jacob, M. Herling, *Leuk. Lymphoma* **2011**, *52*, 1407–1411; b) M. Doering, L. A. Ba, N. Lilienthal, C. Nicco, C. Scherer, M. Abbas, Zada, Abdul Ali Peer, R. Coriat, T. Burkholz, L. Wessjohann et al., *J. Med. Chem.* **2010**, *53*, 6954–6963.

[9] a) D. E. J. G. J. Dolmans, D. Fukumura, R. K. Jain, *Nat. Rev. Cancer* **2003**, *3*, 380–387; b) A. F. Taub, *Dermantol. Clin.* **2007**, *25*, 101–109; c) D. M. A. Vera, M. H. Haynes, A. R. Ball, T. Dai, C. Astrakas, M. J. Kelso, M. R. Hamblin, G. P. Tegos, *Photochem. Photobiol.* **2012**, *88*, 499–511.

[10] a) G. Mayer, A. Heckel, *Angew. Chem. Int. Ed.* **2006**, *45*, 4900–4921; b) C. P. McCoy, C. Rooney, C. R. Edwards, D. S. Jones, S. P. Gorman, *J. Am. Chem. Soc.* **2007**, *129*, 9572–9573; c) Y. Wei, Y. Yan, D. Pei, B. Gong, *Bioorg. Med. Chem. Lett.* **1998**, *8*, 2419–2422; d) S. Ibsen, E. Zahavy, W. Wrasdilo, M. Berns, M. Chan, S. Esener, *Pharm. Res.* **2010**, *27*, 1848-1860; e) P. D. Kehayova, C. D. Woodrell, P. J. Dostal, P. P. Chandra, A. Jain, *Photochem. Photobiol. Sci.* **2002**, *1*, 774–779; f) M. Noguchi, M. Skwarczynski, H. Prakash, S. Hirota, T. Kimura, Y. Hayashi, Y. Kiso, *Bioorg. Med. Chem.* **2008**, *16*, 5389–5397; g) W. Lin, D. Peng, B. Wang, L. Long, C. Guo, J. Yuan, *Eur. J. Org. Chem.* **2008**, *2008*, 793–796; h) N. Ueberschaar, H.-M. Dahse, T. Bretschneider, C. Hertweck, *Angew. Chem. Int. Ed.* **2013**, *52*, 6185–6189.

[11] M. Goeldner, R. Givens (Eds.) *Dynamic studies in biology*. *Phototriggers, photoswitches and caged biomolecules*, Wiley-VCH, Weinheim, **2005**.

[12] a) M. Roy, S. Saha, A. K. Patra, M. Nethaji, A. R. Chakravarty, *Inorg. Chem.* **2007**, *46*, 4368–4370; b) N. J. Farrer, J. A. Woods, L. Salassa, Y. Zhao, K. S. Robinson, G. Clarkson, F. S. Mackay, P. J. Sadler, *Angew. Chem. Int. Ed.* **2010**, *49*, 8905–8908; c) D. Maeda, H. Shimakoshi, M. Abe, Y. Hisaeda, *Dalton Trans.* **2009**, 140–145; d) A. F. Westendorf, J. A. Woods, K. Korpis, N. J. Farrer, L. Salassa, K. Robinson, V. Appleyard, K. Murray, R. Grünert, A. M. Thompson et al., *Mol. Cancer Ther.* **2012**, *11*, 1894–1904; e) C. R. Maldonado, N. Gomez-Blanco, M. Jauregui-Osoro, V. G. Brunton, L. Yate, J. C. Mareque-Rivas, *Chem. Commun.* **2013**, *49*, 3985–3987; f) J. S. Butler, P. J. Sadler, *Curr. Opin. Chem. Biol.* **2013**, *17*, 175–188; g) J. Mlcouskova, J. Stepankova, V. Brabec, *J. Biol. Inorg. Chem.* **2012**, *17*, 891-898; h) Y. Zhao, G. M. Roberts, S. E. Greenough, N. J. Farrer, M. J. Paterson, W. H. Powell, V. G. Stavros, P. J. Sadler, *Angew. Chem. Int. Ed.* **2012**, n/a; i) J. Talib, D. G. Harman, C. T. Dillon, J. Aldrich-Wright, J. L. Beck, S. F. Ralph, *Dalton Trans.* **2009**, 504–513; j) A. K. Patra, T. Bhowmick, S. Roy, S. Ramakumar, A. R. Chakravarty, *Inorg. Chem.* **2009**, *48*, 2932–2943; k) T. K. Goswami, M. Roy, M. Nethaji, A. R. Chakravarty, *Organometallics* **2009**, *28*, 1992–1994; l) F. Barragán, P. López-Senín, L. Salassa, S. Betanzos-Lara, A. Habtemariam, V. Moreno, P. J. Sadler, V. Marchán, *J. Am. Chem. Soc.* **2011**, *133*, 14098–14108; m) B. S. Howerton, D. K. Heidary, E. C. Glazer, *J. Am. Chem. Soc.* **2012**, *134*, 8324–8327; n) E. Wachter, D. K. Heidary, B. S. Howerton, S. Parkin, E. C. Glazer, *Chem. Commun.* **2012**, *48*, 9649–9651; o) M. Frasconi, Z. Liu, J. Lei, Y. Wu, E. Strekalova, D. Malin, M. W. Ambrogio, X. Chen, Y. Y. Botros, V. L. Cryns et al., *J. Am. Chem. Soc.* **2013**, *135*, 11603–11613; p) A. Hussain, S. Gadadhar, T. K. Goswami, A. A. Karande, A. R. Chakravarty, *Dalton Trans.* **2012**, *41*, 885–895; q) A. Kastl, A. Wilbuer, A. L. Merkel, L. Feng, P. Di Fazio, M. Ocker, E. Meggers, *Chem. Commun.* **2012**, *48*, 1863–1865; r) Q.-X. Zhou, W.-H. Lei, Y.-J. Hou, Y.-J. Chen, C. Li, B.-W. Zhang, X.-S. Wang, *Dalton Trans.* **2013**, *42*, 2786–2791; s) J. S. Butler, J. A. Woods, N. J. Farrer, M. E. Newton, P. J. Sadler, *J. Am. Chem. Soc.* **2012**, *134*, 16508–16511.

[13] a) L. Zayat, C. Calero, P. Alborés, L. Baraldo, R. Etchenique, *J. Am. Chem. Soc.* **2003**, *125*, 882–883; b) L. Zayat, M. Salierno, R. Etchenique, *Inorg. Chem.* **2006**, *45*, 1728–1731; c) L. Zayat, M. G. Noval, J. Campi, C. I. Calero, D. J. Calvo, R. Etchenique, *ChemBioChem* **2007**, *8*, 2035–2038; d) M. Salierno, C. Fameli, R. Etchenique, *Eur. J. Inorg. Chem.* **2008**, *2008*, 1125–1128; e) T. Respondek, R. N. Garner, M. K. Herroon, I. Podgorski, C. Turro, J. J. Kodanko, *J. Am. Chem. Soc.* **2011**, *133*, 17164–17167.

[14] a) K. L. Ciesienski, K. L. Haas, M. G. Dickens, Y. T. Tesema, K. J. Franz, *J. Am. Chem. Soc.* **2008**, *130*, 12246–12247; b) K. L. Ciesienski, L. M. Hyman, D. T. Yang, K. L. Haas, M. G. Dickens, R. J. Holbrook, K. J. Franz, *Eur. J. Inorg. Chem.* **2010**, 2224–2228; c) A. A. Kumbhar, A. T. Franks, R. J. Butcher, K. J. Franz, *Chem. Commun.* **2013**, *49*, 2460–2462; d) T. Joshi, V. Pierroz, C. Mari, L. Gemperle, S. Ferrari, G. Gasser, *Angew. Chem. Int. Ed.* **2014**, *53*, 2960–2963.

[15] A. Leonidova, V. Pierroz, R. Rubbiani, Y. Lan, A. G. Schmitz, A. Kaech, R. K. O. Sigel, S. Ferrari, G. Gasser, *Chem. Sci.* **2014**, 4044–4056.

[16] T. R. Figueira, M. H. Barros, A. A. Camargo, R. F. Castilho, Ferreira, Julio C B, A. J. Kowaltowski, F. E. Sluse, N. C. Souza-Pinto, A. E. Vercesi, *Antioxid. Redox Signaling* **2013**, *18*, 2029–2074.

[17] A. Leonidova, V. Pierroz, L. A. Adams, N. Barlow, S. Ferrari, B. Graham, G. Gasser, *ACS Med. Chem. Lett.* **2014**, *5*, 809–814.

[18] S. Gug, S. Charon, A. Specht, K. Alarcon, D. Ogden, B. Zietz, J. Léonard, S. Haacke, F. Bolze, J.-F. Nicoud et al., *ChemBioChem* **2008**, *9*, 1303–1307.
[19] P. Anstaett, G. Gasser **2014**, submitted.
[20] J. E. T. Corrie, G. P. Reid, D. R. Trentham, M. B. Hursthouse, M. A. Mazid, *J. Chem. Soc., Perkin Trans. 1* **1992**, 1015–1019.
[21] S. Martina, S. A. MacDonald, V. Enkelmann, *J. Org. Chem.* **1994**, *59*, 3281–3283.
[22] a) J. J. Marugan, K. Leonard, P. Raboisson, J. M. Gushue, R. Calvo, H. K. Koblish, J. Lattanze, S. Zhao, M. D. Cummings, M. R. Player et al., *Bioorg. Med. Chem. Lett.* **2006**, *16*, 3115–3120; b) B. P. Stupi, H. Li, J. Wang, W. Wu, S. E. Morris, V. A. Litosh, J. Muniz, M. N. Hersh, M. L. Metzker, *Angew. Chem. Int. Ed.* **2012**, *51*, 1724–1727.
[23] P. Anstaett, A. Leonidova, E. Janett, C. G. Bochet, G. Gasser, *ChemPhysChem* **2015**, DOI: 10.1002/cphc.201500178.
[24] J. E. T. Corrie, J. H. Kaplan, B. Forbush, D. C. Ogden, D. R. Trentham, *ChemPhysChem* **2015**, DOI: 10.1002/cphc.201402808.
[25] P. Anstaett, A. Leonidova, G. Gasser, *ChemPhysChem* **2014**, DOI: 10.1002/cphc.201402547.
[26] H. B. Gray, Sohn, Y. S., N. Hendrickson, *J. Am. Chem. Soc.* **1971**, *93*, 3603–3612.
[27] A. Leonidova, T. Joshi, D. Nipkow, A. Frei, J.-E. Penner, S. Konatschnig, M. Patra, G. Gasser, *Organometallics* **2013**, *32*, 2037–2040.
[28] X. Tang, I. J. Dmochowski, *Nat. Protocols* **2007**, *1*, 3041–3048.
[29] A. Leonidova, V. Pierroz, R. Rubbiani, J. Heier, S. Ferrari, G. Gasser, *Dalton Trans.* **2014**, *43*, 4287–4294.
[30] B. Spingler, S. Schnidrig, T. Todorova, F. Wild, *CrystEngComm* **2012**, *14*, 751.
[31] *CrysAlis^{Pro} Software System*, Oxford Diffraction Ldt., Oxford, UK, **2007**.
[32] A. Altomare, M. C. Burla, M. Camalli, G. L. Cascarano, C. Giacovazzo, A. Guagliardi, Moliterni, Anna Grazia Giuseppina, G. Polidori, R. Spagna, *J. Appl. Cryst.* **1999**, *32*, 115–119.
[33] G. Sheldrick, *Acta Cryst.* **2008**, *A64*, 112–122.
[34] F. Bordi, G. Cerichelli, N. de Berardinis, M. Diociaiuti, L. Giansanti, G. Mancini, S. Sennato, *Langmuir* **2010**, *26*, 6177–6183.
[35] H. Kwart, I. Burchuk, *J. Am. Chem. Soc.* **1952**, *74*, 3094–3097.

5 Outlook

The photo-caging of bio-active compounds has two main fields of application, namely chemical biology and medicinal therapy. In chemical biology, as discussed in chapter 3, especially the two-photon technique is of interest since it offers subcellular resolution.[1] This is already being exploited, but almost exclusively for studying brain function upon release of neurotransmitters such as γ-aminobutyric acid (GABA) or glutamate.[2] However, other research areas could profit from a more locally controlled release. A look at the COX inhibitors in chapter 3 gives a good example for this. Although Celecoxib and Lumiracoxib were both thought to selectively act as COX-2 inhibitors, they have rather different effects on cancer cells. Celecoxib is cytotoxic, while Lumiracoxib is not. Recent research results suggest that these effects could be due to COX-2 independent interactions, which greatly differ between the non-steroidal anti-inflammatory drugs.[3] Notably, aspirin does not only inhibit COX, but also alters gene expression.[4] Finding and evaluating such off-target effects could be greatly facilitated by subcellular targeting and uncaging.

The second application of the photo-caging of bioactive molecules is undoubtedly in the field of therapy. Currently, Photodynamic therapy (PDT) is the most important therapy which is based on the modulation of the activity of molecules with light.[5,6] It is in use for the treatment of cancer,[6] and its potential against infective diseases is currently being explored.[7] PDT relies on the photo-physical excitation of a drug dye to its excited singlet state and subsequent formation of reactive species, mainly $^1O_2$. Classical PDT suffers from several shortcomings, including the nature of the therapeutically used light as well as the phototoxic side-effects of the photosensitizers. Solutions for many of these problems are currently under investigation.[5,8] However, despite the clinical success and on-going research in the field of PDT, a fundamental limitation of this technique is not solvable: The mechanism of action is based upon the production of $^1O_2$, while most tumors are hypoxic. This constitutes an important selectivity problem. Furthermore, PDT is restricted to diseases where cells need to be killed. Other localized diseases, such as arthritis, cannot benefit from the advantages of light-triggered curing with PDT. As discussed in the previous chapters, the potential of photochemistry goes well beyond the production of $^1O_2$. A much more universal and selective approach would be to use the concept of caging.

Although (two-photon) uncaging has mostly been applied to answer questions in chemical biology (*vide supra*), therapeutic agents have also been caged.[10] Nevertheless, to date,

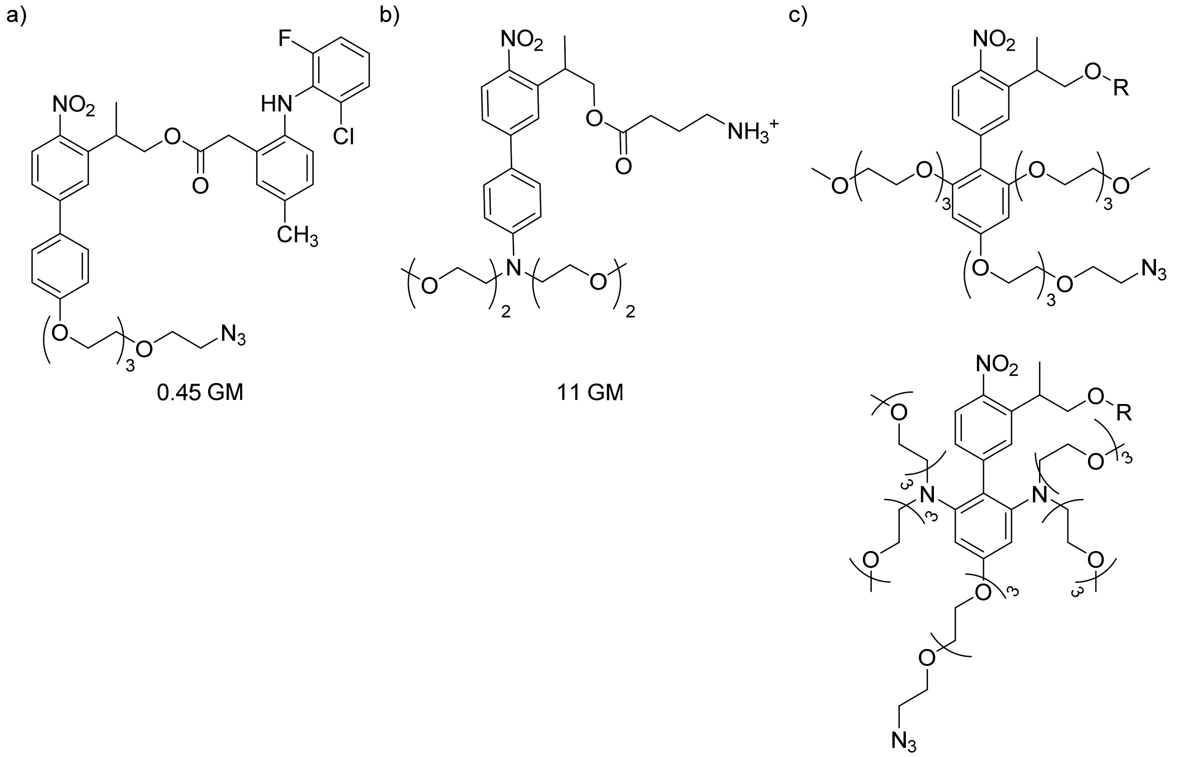

Figure 1. Two-photon cages and their uncaging action cross-sections at 800 nm; a) caged Lumiracoxib, as described in chapter 3 of this thesis; b) a recently developed new generation cage by Goeldner, Specht and coworkers;[9] c) proposed new cage structures.

caging has remained a tool for research only. The implementation of the concept for therapeutic use is very intriguing, because it provides the opportunity to utilize known chemical entities with already known biological properties. It even might allow to “recover” compounds, which previously failed clinical trials[11] or have been withdrawn from the market due to adverse drug effects,[12] as side effects could be circumvented by activating the compounds only where and when they are needed. This could potentially lower the immense costs of developing completely new drug candidates. Given the imminent increased appearance of cancer, especially in developing countries,[13] approaches which decrease the therapeutic costs are of great importance. The most foreseeable (chemical) problems on the way will be the solubility of the caged compounds in aqueous media, and the effectiveness of uncaging. Scattering in discrete biological tissues might become a significant problem.[14] Both difficulties could be tackled by modifying the cage core (see Figure 1). Although it is not possible to date to predict the two-photon uncaging cross-section for a given compound, it seems that push-pull systems are favorable.[15] Consequently, the introduction of electron-donating groups at the donor system could improve the effectiveness of the uncaging process. Goeldner, Specht and coworkers have recently reported a cage with improved two-photon uncaging cross-section following this principle (Figure 1 b).[9] Additional substituents at the lower phenyl ring could therefore further increase the uncaging efficiency, while at the same time improving the solubility in aqueous systems (Figure 1 c). Alternative approaches, which try to separate the two-photon absorption from uncaging process are currently under investigation by other groups.[16] Greatly increased two-photon absorbances can be expected, but with the trade-off of needing even bigger molecular systems with even lower solubility in water.

In conclusion, the further development of two-photon uncaging as mean to deliver photo-activatable bio-active components is of high interest. Moving towards more complex biological methodologies based on the research presented in this thesis, will show if further improvements on the chemical, or maybe even physical/instrumental side, are needed. On both levels further improvements are possible, casting the chances for further successful advances in a positive light.

5.1 References and Notes

[1] J. M. Amatrudo, J. P. Olson, G. Lur, C. Q. Chiu, M. J. Higley, G. C. R. Ellis-Davies, *ACS Chem. Neurosci.* **2014**, *5*, 64–70.

[2] a) C. Q. Chiu, G. Lur, T. M. Morse, N. T. Carnevale, G. C. R. Ellis-Davies, M. J. Higley, *Science* **2013**, *340*, 759–762; b) H.-B. Kwon, B. L. Sabatini, *Nature* **2011**, *474*, 100–104.

[3] a) E. Niederberger, C. Manderscheid, G. Geisslinger, *Biochem. Biophys. Res. Commun.* **2006**, *342*, 940–948; b) S. T. Palayoor, M. J-Aryankalayil, A. Y. Makinde, D. Cerna, M. T. Falduto, S. R. Magnuson, C. N. Coleman, *J. Cardiovasc. Pharmacol.* **2012**, *59*, 487-499 10.1097/FJC.0b013e31824ba6b5.

[4] M. Iizaka, Y. Furukawa, T. Tsunoda, H. Akashi, M. Ogawa, Y. Nakamura, *Biochem. Biophys. Res. Commun.* **2002**, *292*, 498–512.

[5] D. Phillips, *Photochem. Photobiol. Sci.* **2010**, *9*, 1589–1596.

[6] M. Triesscheijn, P. Baas, Schellens, Jan H. M., F. A. Stewart, *Oncologist* **2006**, *11*, 1034–1044.

[7] a) M. R. Hamblin, T. Hasan, *Photochem. Photobiol. Sci.* **2004**, *3*, 436–450; b) A. Frei, R. Rubbiani, S. Tubafard, O. Blacque, P. Anstaett, A. Felgentraeger, T. Maisch, L. Spiccia, G. Gasser, *J. Med. Chem.* **2014**, submitted.

[8] a) S. C. Boca, M. Four, A. Bonne, van der Sanden, Boudewijn, S. Astilean, P. L. Baldeck, G. Lemercier, *Chem. Commun.* **2009**, 4590–4592; b) E. Dahlstedt, H. A. Collins, M. Balaz, M. K. Kuimova, M. Khurana, B. C. Wilson, D. Phillips, H. L. Anderson, *Org. Biomol. Chem.* **2009**, *7*, 897–904; c) M. K. Kuimova, H. A. Collins, M. Balaz, E. Dahlstedt, J. A. Levitt, N. Sergent, K. Suhling, M. Drobizhev, N. S. Makarov, A. Rebane et al., *Org. Biomol. Chem.* **2009**, *7*, 889–896; d) N. Shirasu, S. O. Nam, M. Kuroki, *Anticancer Res.* **2013**, *33*, 2823–2831.

[9] L. Donato, A. Mourot, C. M. Davenport, C. Herbivo, D. Warther, J. Léonard, F. Bolze, J.-F. Nicoud, R. H. Kramer, M. Goeldner et al., *Angew. Chem. Int. Ed.* **2012**, *51*, 1840–1843.

[10] a) G. Mayer, A. Heckel, *Angew. Chem. Int. Ed.* **2006**, *45*, 4900–4921; b) C. Brieke, F. Rohrbach, A. Gottschalk, G. Mayer, A. Heckel, *Angew. Chem. Int. Ed.* **2012**, *51*, 8446–8476; c) H.-M. Lee, D. R. Larson, D. S. Lawrence, *ACS Chem. Biol.* **2009**, *4*, 409–427; d) G. C. R. Ellis-Davies, *Nat. Meth.* **2007**, *4*, 619–628.

[11] J. A. DiMasi, L. Feldman, A. Seckler, A. Wilson, *Clin. Pharmacol. Ther.* **2010**, *87*, 272–277.

[12] I. R. Edwards, J. K. Aronson, *Lancet* **2000**, *356*, 1255–1259.

[13] B. Steward, C. P. Wild (Eds.) *World Cancer Report 2014*, World Health Organization, **2014**.

[14] E. Chaigneau, A. J. Wright, S. P. Poland, J. M. Girkin, Silver, R. Angus, *Opt. Express* **2011**, *19*, 22755–22774.

[15] G. Bort, T. Gallavardin, D. Ogden, P. I. Dalko, *Angew. Chem. Int. Ed.* **2013**, *52*, 4526–4537.

[16] L. Flamigni, *Functional Arrays for Light Energy Capture and Charge Separation*, 25th IUPAC Conference on Photochemistry, Bordeaux, France, **2014**.

Part II

Peptide Nucleic Acid for Nanotechnology

6 Peptide Nucleic Acid – An Opportunity for Bio-Nanotechnology

Philipp Anstaett[a,§] *and Gilles Gasser*[a*]

[a] Department of Chemistry, University of Zurich, Winterthurerstrasse 190, CH-8057 Zurich, Switzerland.

[§] SCS-Metrohm Foundation Award for best oral presentation.

[*] Corresponding author: e-mail: gilles.gasser@chem.uzh.ch; Fax: +41 44 635 46 03; Tel: +41 44 635 46 30; homepage: http://www.gassergroup.com.

This chapter has been published in *Chimia* **2014**, *68*, 264–268. Copyright © Swiss Chemical Society: CHIMIA, 68, 264–268, 2014, DOI: 10.2533/chimia.2014.264.

6.1 Contributions to the publication

P.A. wrote the first draft of the manuscript.

6.2 Abstract

DNA is a major player in the field of bio-nanotechnology and many interesting applications have been realized using this oligonucleotide. In contrast, the use of peptide nucleic acid (PNA), which is a non-natural, neutral analogue of DNA with superior hybridization strengths compared to DNA, is still in its infancy in bio-nanotechnology. However, as demonstrated in this short review using selected studies, promising examples demonstrating the tremendous opportunities that PNA can offer for bio-nanotechnology were recently described.

Keywords: Biotechnology • Nanoparticle • Nanotechnology • Peptide nucleic acid (PNA) • Sensing.

6.3 Article

DNA bio-nanotechnology has over the last decade become an important and quite diverse field of research, including studies about the assembly of DNA strands by themselves (DNA origami),[1] DNA modified nanoparticles,[2] and the combination of all sorts of other nanomaterials with DNA, e.g. nanotubes.[3] For applications of DNA, peptide nucleic acid (PNA), which is a non-natural analogue of DNA, has become an interesting alternative (see Figure 1 for the comparison of the structures of PNA and DNA).[4,5] To understand if and how PNA can impact bio-nanotechnology, the differences and consequential potential advantages of PNA over its naturally occurring analogues DNA and RNA have to be considered (see Figure 1). The nucleobases as well as their spatial arrangement are identical and complementary to each other in PNA, DNA and RNA. Complementary strands of the different nucleic acid oligomers can therefore bind to one another. Consequently, combinations of existing DNA bio-nanotechnology with PNA are possible. What distinguishes the different oligonucleotides is the backbone. While DNA and RNA possess a backbone consisting of (desoxy-)ribose sugars connected by phosphodiesters, PNA relies on a *N*-(2-aminoethyl)glycine based framework, which links the subunits like in a peptide with amide bonds. This change results in a number of important differences between PNA and its natural analogues, and has sparked great interest in various fields of research.[5] Although *N*-(2-aminoethyl)glycine has recently been found to be produced by cyanobacteria,[6] the PNA backbone is still regarded as unnatural and as such cannot be degraded enzymatically. Most importantly, the backbone is uncharged, making PNA highly interesting for use in electronic devices. Moreover, it eliminates the intrinsic electrostatic repulsion between individual nucleotide strands contributing to greater hybridization strengths. Partially due to this and for entropic reasons the binding strength of PNA oligomers to both complementary PNA and DNA strands is higher than of DNA strands. Finally, the single base mismatch sensitivity is usually greater for PNA than for DNA.

In the past, our group has mainly been engaged in combining PNA with metal complexes,[7] and we were wondering why PNA has only scarcely been applied in bio-nanotechnology. In this short review we highlight, on basis of selected literature examples, how the above mentioned properties of PNA can indeed be exploited to advance bio-nanotechnology.

Relatively much work has been done with PNA-functionalized silicon nanowires (SiNWs).[8–11] The main reason for this is probably due to the uncharged nature of PNA, which is a significant advantage for SiNW based semiconductors, as they rely on charge differences on the SiNW surface for sensing (*vide infra*). Additionally, procedures for modification of SiNWs

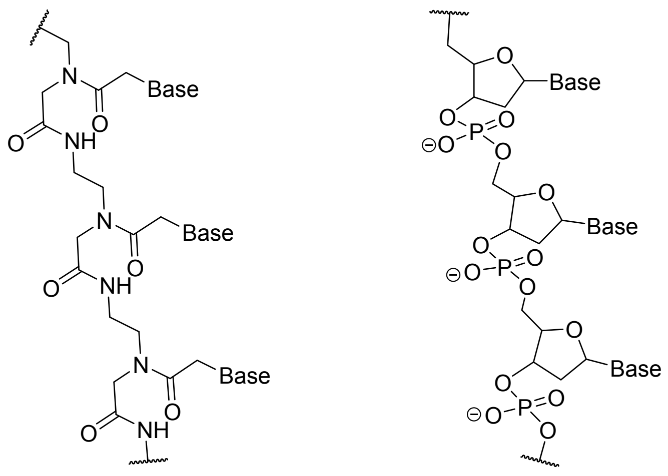

PNA DNA

Figure 1. Chemical structures of PNA and DNA.

with PNA are straight-forward and known for more than ten years.[12] For example, PNA-functionalized SiNWs were used for label-free detection of a specific DNA sequence (Figure 2).[12] The SiNWs were modified with PNA as “receptors” with the well-established biotin-avidin immobilization methodology. The SiNWs were used as semiconducting element between two electrodes and were, at the same time, inside a microfluidic channel. Upon addition of the complementary DNA sequence binding between the DNA and the PNA occurred, leading to a fast increase of conductance due to the electrostatic gating effect. Addition of non-complementary DNA did not substantially alter the conductance. A detection limit of 10 fM for a deletion of three bases in the gene encoding for cystic fibrosis transmembrane receptor, which leads to the corresponding disease, could be achieved due to the superior binding properties of the PNA. The sensor design and manufacturing process has since been improved, allowing for preparation of highly uniform SiNW arrays.[9] The potential advantages of using PNA compared to DNA for SiNW sensors have been pointed out by Gao and coworkers:[9] 1) increased hybridization efficiency due to stronger binding of DNA/PNA hybrids than of DNA/DNA hybrids; 2) lower basal conductance due to the uncharged nature of PNA allowing for the use of a regime of low ionic strength, which minimizes the appearance of strong electric fields and thereby background signal; 3) the greater mismatch sensitivity of PNA compared to DNA.[13] Indeed, PNA improved the performance of the sensor, showing greater conductance differences upon binding of the complementary DNA strand than the corresponding DNA-based SiNW sensors (see Figure 3 for comparison between DNA- and PNA-based SiNW sensors).[9] In another direct comparison, a SiNW sensor with PNA capture probe was four times more sensitive than the equivalent sensor with DNA-functionalization.[8]

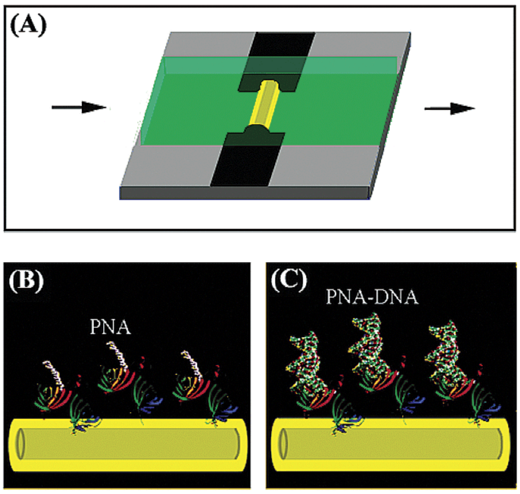

Figure 2. (A) Schematic representation of the PNA and SiNW based sensor for DNA detection. The SiNW (yellow) connects two electrodes (black) and spans a microfluidic channel (green). The arrows indicate the direction of the flow. (B) PNA-modified SiNW before addition of complementary DNA. (C) PNA-modified SiNW after addition of complementary DNA which leads to PNA-DNA hybridization. Reprinted with permission from [12]. Copyright 2004 American Chemical Society.

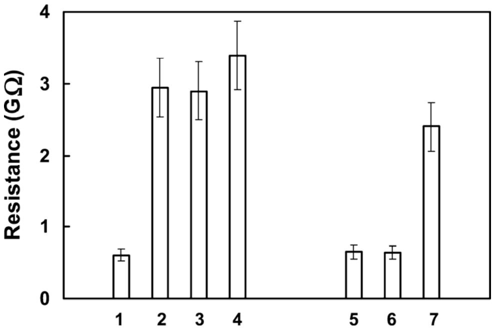

Figure 3. “Resistance of the SiNW after different treatments. (1) A blank SiNW, (2) (1)+DNA capture probes, (3) (2) after hybridized with 1.0 nM complementary PNA, (4) (2) after hybridized with 1.0 nM complementary DNA, (5) a blank SiNW, (6) (5)+PNA capture probes, and (7) (6) after hybridized with 1.0 nM complementary DNA. Same capture probe and sample sequences were used, respectively.”[9] Reprinted with permission from [9]. Copyright 2007 American Chemical Society.

Apart from the sensing of DNA, PNA functionalized SiNWs have been employed for investigating an important physical property of SiNW sensors, namely the distance dependence of their field effect.[10] The response depends on the distance between the SiNW and the charge layer, i.e. the charged DNA. A neutral linker between the DNA and the SiNW had therefore to be employed, and PNA fulfilled this task. The report has general implications for the future design of SiNW sensors, e.g. for the detection of DNA and RNA.

Also single-walled carbon nanotubes (SWNTs) have been functionalized with PNA. The attachment can be achieved covalently *via* NHS active ester chemistry[14] or non-covalently *via* π-π-stacking between the PNA bases and the SWNT and electrostatic interactions between the amino groups of the PNA and the SWNT.[15] These conjugates were capable of binding complementary DNA or RNA strands, respectively, presumably with greater strength than it would have been possible with DNA functionalized SWNTs. The absence of charges in PNA reduces non-specific electrostatic interactions with electrodes and surfaces, making them especially interesting for self-assembled nano-electronics applications.[14] First studies into this direction have been undertaken.[16] Interestingly, non-covalently bound DNA and PNA wrap very differently around SWNTs.[17] This observation has, to the best of our knowledge, not been put to any use yet.

In analogy to the non-covalent binding to SWNTs, single stranded oligonucleotides can also bind to graphene oxide, a water-soluble derivative of graphene. This interaction relies again on π-π-stacking. Because of its great π-π-stacking ability, graphene oxide is known to quench the fluorescence of dyes in close proximity.[18] Small fluorophore-labeled PNA oligomers can be used to detect complementary DNA and RNA, as the formation of oligonucleotide duplexes can lead to their detachment from the graphene oxide. This has been applied for monitoring the function of RNA polymerase. As soon as complementary RNA has been synthesized, the labeled PNA strands quantitatively bind the RNA, leading to desorption of the PNA from the graphene oxide and lighting up of the fluorophore. The advantage of PNA probes for this system lies in the stronger binding to even low concentrations of RNA, rendering the assay independent from buffer concentrations and external influences such as temperature.[19]

Recently, the same concept for sensing RNA with a fluorophore-labeled PNA and, in this case, nano graphene oxide (NGO) has even been applied for monitoring microRNA (miRNA) expression levels in living cells (Figure 4).[20] Notably, previous methods were not able to achieve this goal.[21] NGO is negatively charged at physiological pH, and therefore uncharged PNA was expected to lead to less unspecific desorption than negatively charged DNA. Indeed, it was shown that PNA-NGO adducts are stable when treated with cell lysate, while DNA-NGO adducts disassembled leading to non-specific fluorescence. Moreover, the PNA based system has a very low detection limit (~1 pM) due to the superior binding strength of PNA to miRNAs. The system could even be used to detect multiple miRNAs simultaneously by employing multiple complementary PNA strands with different dye labels.

Another area of interest for PNA application is surface-enhanced Raman spectroscopy (SERS). This technique relies on the strong amplification of Raman signals by metallic nanostructures.[22] PNAs have already been used in this context.[23,24,25] For example, Bazan and coworkers have developed a SERS sensor for single stranded DNA (Scheme 1). Interestingly, this sensor would not work with DNA instead of PNA.[24] More specifically, in

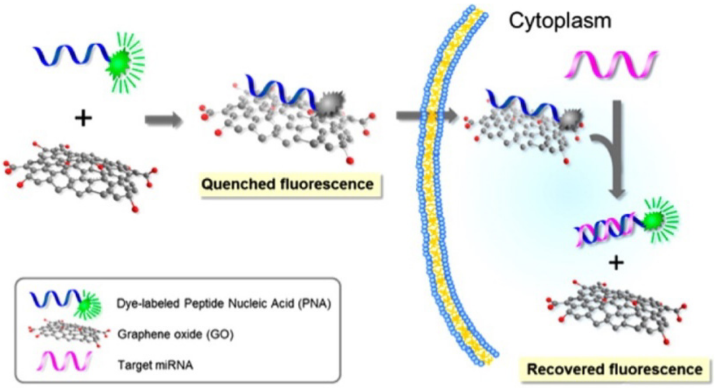

Figure 4. Schematic representation of the working principle of intracellular miRNA sensing using NGO and PNA. Extracelullarly, fluorophore labeled PNA binds to NGO, leading to quenching of the fluorophore. After crossing of the cellular membrane, the PNA-NGO complex stays intact until a complementary miRNA strand is in proximity. A PNA-RNA duplex is then formed leading to desorption of the construct from NGO. Thereby, the fluorophore is not quenched anymore and can be detected. Adapted with permission from [20]. Copyright 2013 American Chemical Society.

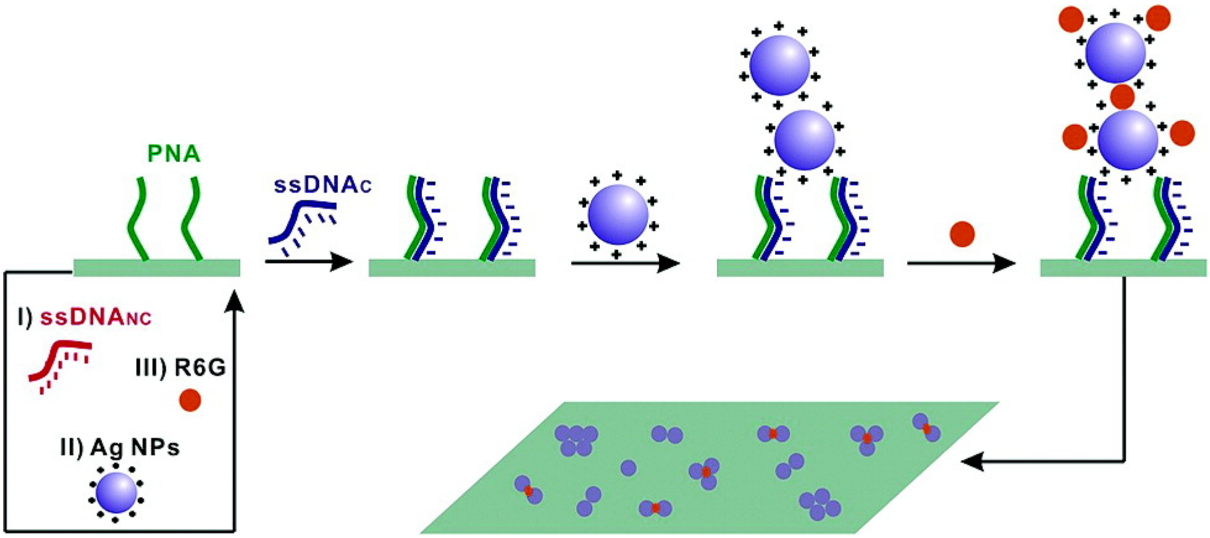

Scheme 1. PNA is deposited on a glass slide. Addition of non-complementary DNA with AgNPs and a SERS reporter (Rhodamine 6 G, R6G) leads to no assemblies. Complementary DNA strands bind to the PNA, thereby immobilizing negative charges. Positively charged AgNPs are electrostatically bound to the hybrids, R6G can bind to the AgNPs, and finally SERS can be observed. Reprinted with permission from [24]. Copyright 2007 American Chemical Society.

this study, PNA was immobilized on a glass slide. Subsequently, complementary DNA was hybridized to the PNA, while non-complementary DNA was washed away. The negative charges on the backbone of the complementary DNA then lead to electrostatic attraction of positively charged silver nanoparticles (AgNPs). After addition of a SERS reporter dye, which binds to AgNPs, strongly enhanced Raman signals could be observed. If, in contrast, only non-complementary DNA was added, no enhancement was observed, as no AgNPs were deposited. The use of DNA instead of PNA would have led to non-specific deposition of the AgNPs due to the inherent negative charge of DNA.

As can be seen with the previous example, the interplay of nanoparticles with PNA is very intriguing due to the unique physico-chemical properties of nanoparticles and PNA. Indeed, PNA has also been used to functionalize nanoparticles such as silica-coated magnetic nanoparticles (γ-Fe_2O_3), which were immobilized on a silver substrate,[23] gelatin nanoparticles,[26] and others.[27] Gold nanoparticles (AuNPs) still represent the arguably most prominent class of nanoparticles. Recently, DNA modified AuNPs were shown to be quickly and efficiently hybridized with PNAs carrying different functionalities, ranging from small molecules like fluorophores and drugs, to differently sized biomolecules like siRNA, aptamers and antibodies.[28] Their *in vitro* use as imaging agent has been demonstrated.

However, there are, generally, only very few reports about PNA modified AuNPs, especially about directly PNA-modified AuNPs, i.e. with attachment of the PNA to the gold surface of the NP.[29,30,31] There is a straight-forward explanation: Addition of PNAs to unmodified AuNPs lead to their agglomeration and subsequent precipitation from solution (Figure 5). This effect is thought to be mainly due to the adsorption of PNA bases to gold surfaces, which is stronger than for negatively charged DNA.[32] Thus, the initial stabilization of the AuNPs is lost and the general tendency of the NPs to aggregate induces the destabilization. The precipitation is permanent, and the non-specific binding of PNA to AuNPs is therefore not reversible, in contrast to its binding to graphene oxide (*vide supra*). It has been shown that this aggregation tendency is even strong enough to be used for sequence-selective quantification of DNA[33] and RNA.[34]

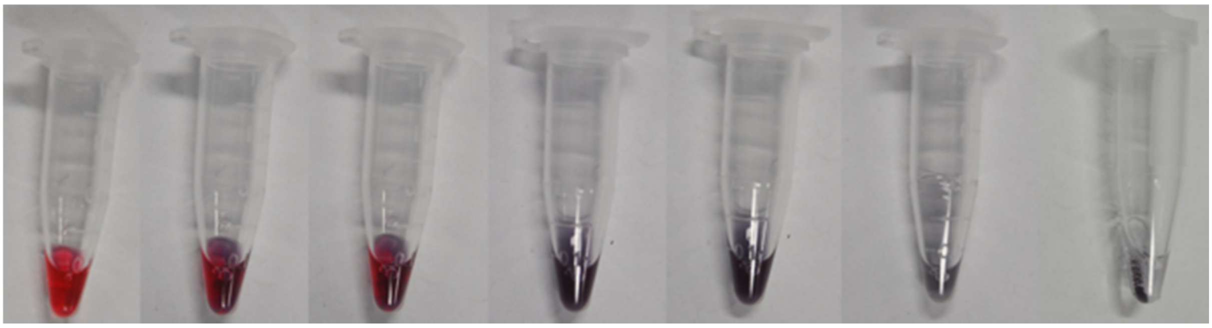

Figure 5. Evolution of aggregation and precipitation of AuNPs upon addition of PNA. Time frame from first to last picture: less than one minute.

The problem can be circumvented by immobilizing the AuNPs e.g. on an Au(1,1,1) surface *via* thiol/amine linkers before modification with thiol-linked PNA.[35] The pre-disposition of the AuNPs obviously prevents aggregation upon addition of PNA. It was found that the single-mismatch sensitivity of PNA/DNA hybrids is already improved on unmodified Au(1,1,1) surfaces, compared to PNA/DNA hybrids in solution.[31] Immobilization of AuNPs on the

Au(1,1,1) surfaces further increased the mismatch discrimination, mainly due to the greater melting temperatures (T_m) of the fully complementary hybrids.[35] This effect was greater for PNA than for DNA probes. The study therefore shows the potential of combining AuNPs with PNA. Notably, the T_m of the PNA/DNA hybrid was depending on the size of the AuNPs, leading to higher T_m with smaller NP diameter. This was attributed to the greater PNA probe density on smaller particles. This last point shows that the "nanoscopic" environment has a noticeable impact on the molecular level. Consequently, it can be expected that particles which are not immobilized on a surface have distinct properties. Apart from that, having the particles in solution allows for additional applications, e.g. they can be added to setups with differently functionalized surfaces.

Recently, in collaboration with the Bach group at Monash University (Australia), we have reported a new method for generating such directly PNA modified AuNPs in solution.[29] To overcome the abovementioned stability issues, we proposed a two-step process for the synthesis (Scheme 2). First, the AuNPs were modified with a thiolated surfactant which provides steric and electrostatic stabilization. In a second step, the particles can be treated with thiol-linked PNA without inducing agglomeration of the AuNPs. The PNA-modified AuNPs were tested in comparison to analogous DNA-modified AuNPs by assaying the self-assembly properties towards PNA modified gold surfaces. The test was carried out in the absence of ions, where DNA-DNA assembly would not be possible due to electrostatic repulsion between the charged oligonucleotide backbones. The PNA modified AuNPs showed superior binding affinity towards the complementary PNA strands on the surface. Notably, the nature of the thiol linker (short, long, monothiol, trithiol) did not have an influence on the outcome of the self-assembly experiment. The methodology therefore seems to be flexible and the linker of the PNA can, in future studies, be chosen to best fit the application, without running into problems with nanoparticle stability again. These new PNA modified AuNPs will likely entail new innovations, as many of the great applications of DNA-modified AuNPs can potentially be improved by using PNA-modified AuNPs instead.

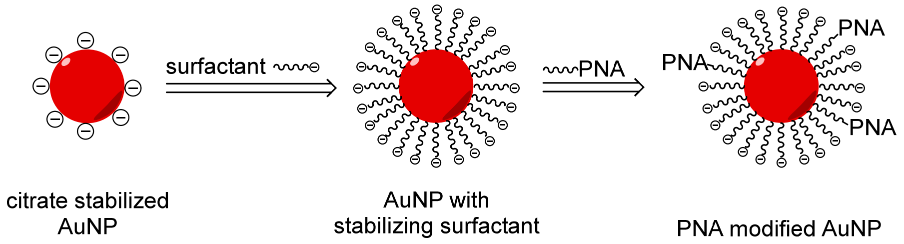

Scheme 2. Overview of the two-step process for functionalization of AuNPs with a stabilizing surfactant and thiol-linked PNA. Adapted with permission from [29]. Copyright 2013 WILEY-VCH Verlag GmbH & Co. KGaA, Weinheim.

In summary, DNA-based bio-nanotechnology can be greatly advanced by the use of PNA. Worthy of note, there are many more examples than the ones described above, e.g. miRNA sensing with PNA in nanogaps[36] or self-assembled PNA/DNA nanostructures.[37] Nevertheless, it has to be pointed out that the field is still in its infancy, and studying PNA for bio-nanotechnology will still hold many obstacles. There are, for example, also reports where the use of PNA instead of DNA brings basically no advantages.[38] Incompatibility issues like the ones of “naked” AuNPs towards PNA could be encountered for other systems as well. Nevertheless, the promises this technology holds are great and further investigations are likely to lead to innovative discoveries.

6.4 Acknowledgments

This work was supported by the Swiss National Science Foundation (Professorship N° PP00P2_133568 to G.G.), the University of Zurich (G.G.) and the Stiftung für Wissenschaftliche Forschung of the University of Zurich (G.G.). The authors thank their Australian collaborators from Monash University, namely Prof. Dr. Udo Bach, Dr. Alison M. Funston, Dr. Yuanhui Zheng and Dr. Thibaut Thai , for their help towards this project. P.A. thanks the Swiss Chemical Society (SCS) and Metrohm for this award.

6.5 References and Notes

[1] a) T. Torring, N. V. Voigt, J. Nangreave, H. Yan, K. V. Gothelf, *Chem. Soc. Rev.* **2011**, *40*, 5636–5646; b) F. C. Simmel, *Front. Life Sci.* **2012**, *6*, 3–9.
[2] A. Kumar, J.-H. Hwang, S. Kumar, J.-M. Nam, *Chem. Commun.* **2013**, *49*, 2597–2609.
[3] a) S. Song, Y. Qin, Y. He, Q. Huang, C. Fan, H.-Y. Chen, *Chem. Soc. Rev.* **2010**, *39*, 4234–4243; b) Z. Wang, Y. Lu, *J. Mater. Chem.* **2009**, *19*, 1788–1798; c) C.-H. Lu, B. Willner, I. Willner, *ACS Nano* **2013**, *7*, 8320–8332.
[4] P. E. Nielsen, M. Egholm, R. H. Berg, O. Buchardt, *Science* **1991**, *254*, 1497–1500.
[5] P. E. Nielsen, D. H. Appella (Eds.) *Methods in Molecular Biology*, Humana Press, **2014**.
[6] S. A. Banack, J. S. Metcalf, L. Jiang, D. Craighead, L. L. Ilag, P. A. Cox, *PLoS ONE* **2012**, *7*, e49043.
[7] a) G. Gasser, A. M. Sosniak, N. Metzler-Nolte, *Dalton Trans.* **2011**, *40*, 7061–7076; b) G. Gasser, K. Jäger, M. Zenker, R. Bergmann, J. Steinbach, H. Stephan, N. Metzler-Nolte, *J. Inorg. Biochem.* **2010**, *104*, 1133–1140; c) G. Gasser, S. Neumann, I. Ott, M. Seitz, R. Heumann, N. Metzler-Nolte, *Eur. J. Inorg. Chem.* **2011**, *2011*, 5471–5478; d) G. Gasser, A. Pinto, S. Neumann, A. M. Sosniak, M. Seitz, K. Merz, R. Heumann, N. Metzler-Nolte, *Dalton Trans.* **2012**, *41*, 2304–2313; e) G. Gasser, A. M. Sosniak, A. Leonidova, H. Braband, N. Metzler-Nolte, *Aust. J. Chem.* **2011**, *64*, 265–272; f) T. Joshi, M. Patra, L. Spiccia, G. Gasser, *Artif. DNA PNA XNA* **2013**, *4*, 11–18.
[8] Z. Li, B. Rajendran, T. I. Kamins, X. Li, Y. Chen, R. S. Williams, *Appl. Phys. A* **2005**, *80*, 1257–1263.
[9] Z. Gao, A. Agarwal, A. D. Trigg, N. Singh, C. Fang, C.-H. Tung, Y. Fan, K. D. Buddharaju, J. Kong, *Anal. Chem.* **2007**, *79*, 3291–3297.
[10] G.-J. Zhang, G. Zhang, J. H. Chua, R.-E. Chee, E. H. Wong, A. Agarwal, K. D. Buddharaju, N. Singh, Z. Gao, N. Balasubramanian, *Nano Lett.* **2008**, *8*, 1066–1070.
[11] G.-J. Zhang, L. Zhang, M. J. Huang, Z. H. H. Luo, G. K. I. Tay, E.-J. A. Lim, T. G. Kang, Y. Chen, *Sens. Actuators, B* **2010**, *146*, 138–144.
[12] J.-i. Hahm, C. M. Lieber, *Nano Lett.* **2003**, *4*, 51–54.
[13] a) T. Ratilainen, A. Holmén, E. Tuite, P. E. Nielsen, B. Nordén, *Biochemistry* **2000**, *39*, 7781–7791; b) M. Egholm, O. Buchardt, L. Christensen, C. Behrens, S. M. Freier, D. A. Driver, R. H. Berg, S. K. Kim, B. Norden, P. E. Nielsen, *Nature* **1993**, *365*, 566–568.
[14] K. A. Williams, P. T. M. Veenhuizen, B. G. de la Torre, R. Eritja, C. Dekker, *Nature* **2002**, *420*, 761.
[15] T. Dastagir, E. S. Forzani, R. Zhang, I. Amlani, L. A. Nagahara, R. Tsui, N. Tao, *Analyst* **2007**, *132*, 738–740.
[16] K. V. Singh, R. R. Pandey, X. Wang, R. Lake, C. S. Ozkan, K. Wang, M. Ozkan, *Carbon* **2006**, *44*, 1730–1739.
[17] J. Rajendra, A. Rodger, *Chem. Eur. J.* **2005**, *11*, 4841–4847.
[18] a) S. He, B. Song, Di Li, C. Zhu, W. Qi, Y. Wen, L. Wang, S. Song, H. Fang, C. Fan, *Adv. Funct. Mater.* **2010**, *20*, 453–459; b) C.-H. Lu, H.-H. Yang, C.-L. Zhu, X. Chen, G.-N. Chen, *Angew. Chem.* **2009**, *121*, 4879–4881.
[19] J. S. Park, A. Baek, I.-S. Park, B.-H. Jun, D.-E. Kim, *Chem. Commun.* **2013**, *49*, 9203–9205.
[20] S.-R. Ryoo, J. Lee, J. Yeo, H.-K. Na, Y.-K. Kim, H. Jang, J. H. Lee, S. W. Han, Y. Lee, V. N. Kim et al., *ACS Nano* **2013**, *7*, 5882–5891.

[21] a) C. Chen, D. A. Ridzon, A. J. Broomer, Z. Zhou, D. H. Lee, J. T. Nguyen, M. Barbisin, N. L. Xu, V. R. Mahuvakar, M. R. Andersen et al., *Nucleic Acids Res.* **2005**, *33*, e179; b) J. Q. Yin, R. C. Zhao, K. V. Morris, *Trends Biotechnol.* **2008**, *26*, 70–76; c) S. W. Kim, Z. Li, P. S. Moore, A. P. Monaghan, Y. Chang, M. Nichols, B. John, *Nucleic Acids Res.* **2010**, *38*, e98.

[22] R. Aroca, *Surface-Enhanced Vibrational Spectroscopy*, John Wiley & Sons, Ltd, **2007**.

[23] F. Wang, H. Shen, J. Feng, H. Yang, *Microchim. Acta* **2006**, *153*, 15–20.

[24] L. Fabris, M. Dante, G. Braun, S. J. Lee, N. O. Reich, M. Moskovits, T.-Q. Nguyen, G. C. Bazan, *J. Am. Chem. Soc.* **2007**, *129*, 6086–6087.

[25] a) C. Fang, A. Agarwal, K. D. Buddharaju, N. M. Khalid, S. M. Salim, E. Widjaja, M. V. Garland, N. Balasubramanian, D.-L. Kwong, *Biosens. Bioelectron.* **2008**, *24*, 216–221; b) F. Gao, J. Lei, H. Ju, *Anal. Chem.* **2013**, *85*, 11788–11793.

[26] C. Coester, J. Kreuter, H. von Briesen, K. Langer, *Int. J. Pharm.* **2000**, *196*, 147–149.

[27] a) R. Jayakumar, K. P. Chennazhi, Muzzarelli, R. A. A., H. Tamura, S. V. Nair, N. Selvamurugan, *Carbohydr. Polym.* **2010**, *79*, 1–8; b) G. Eidelshtein, S. Halamish, I. Lubitz, M. Anzola, C. Giannini, A. Kotlyar, *J. Self-Assem. Mol. Electron.* **2013**, *1*, 69–84; c) K. Langer, C. Coester, C. Weber, H. von Briesen, J. Kreuter, *Eur. J. Pharm. Biopharm.* **2000**, *49*, 303–307; d) J. L. Turner, M. L. Becker, X. Li, J.-S. A. Taylor, K. L. Wooley, *Soft Matter* **2005**, *1*, 69–78; e) H. Fang, K. Zhang, G. Shen, K. L. Wooley, J.-S. A. Taylor, *Mol. Pharmaceutics* **2009**, *6*, 615–626.

[28] Z. Zhang, Y. Liu, C. Jarreau, M. J. Welch, J.-S. A. Taylor, *Biomater. Sci.* **2013**, *1*, 1055–1064.

[29] P. Anstaett, Y. Zheng, T. Thai, A. M. Funston, U. Bach, G. Gasser, *Angew. Chem. Int. Ed.* **2013**, *52*, 4217–4220.

[30] a) R. Chakrabarti, A. M. Klibanov, *J. Am. Chem. Soc.* **2003**, *125*, 12531–12540; b) J. Duy, L. Connell, W. Eck, S. Collins, R. Smith, *J. Nanopart. Res.* **2010**, *12*, 2363–2369.

[31] S. Ghosh, S. Mishra, T. Banerjee, R. Mukhopadhyay, *Langmuir* **2013**, *29*, 3370–3379.

[32] A. Gourishankar, S. Shukla, K. N. Ganesh, M. Sastry, *J. Am. Chem. Soc.* **2004**, *126*, 13186–13187.

[33] R. Kanjanawarut, X. Su, *Anal. Chem.* **2009**, *81*, 6122–6129.

[34] V. G. Joshi, K. Chindera, A. K. Singh, A. P. Sahoo, V. D. Dighe, D. Thakuria, A. K. Tiwari, S. Kumar, *Anal. Chim. Acta* **2013**, *795*, 1–7.

[35] S. Ghosh, S. Mishra, R. Mukhopadhyay, *Langmuir* **2013**, *29*, 11982–11990.

[36] Y. Fan, X. Chen, A. D. Trigg, C.-H. Tung, J. Kong, Z. Gao, *J. Am. Chem. Soc.* **2007**, *129*, 5437–5443.

[37] M. O. Guler, J. K. Pokorski, D. H. Appella, S. I. Stupp, *Bioconjugate Chem.* **2005**, *16*, 501–503.

[38] T. Endo, K. Kerman, N. Nagatani, Y. Takamura, E. Tamiya, *Anal. Chem.* **2005**, *77*, 6976–6984.

7 Synthesis of Stable Peptide Nucleic Acid-Modified Gold Nanoparticles and their Assembly onto Gold Surfaces

Philipp Anstaett,[a] Yuanhui Zheng,[b,c] Thibaut Thai,[b,d] Alison M. Funston,[e] Udo Bach[b,c,d] and Gilles Gasser[a]**

[a] Institute of Inorganic Chemistry, University of Zurich, Winterthurerstrasse 190, CH-8057 Zurich, Switzerland.

[b] The Melbourne Centre for Nanofabrication, 151 Wellington Road, Clayton 3168, Victoria, Australia.

[c] Commonwealth Scientific and Industrial Research Organization, Materials Science and Engineering, Clayton South, Victoria 3169, Australia.

[d] Department of Materials Engineering, Faculty of Engineering, Monash University, Clayton 3800, Victoria, Australia.

[e] School of Chemistry, Monash University, Clayton, Victoria 3800, Australia.

* Corresponding authors:
G.G.: e-mail: gilles.gasser@aci.uzh.ch, homepage: http://www.gassergroup.com;
U.B.: e-mail: udo.bach@monash.edu, homepage: http://www.udobach.com.

This chapter has been published in *Angewandte Chemie International Edition* **2013**, *52*, 4217-4220 and *Angewandte Chemie* **2013**,*125*, 4311-4314. Copyright © 2013 WILEY-VCH Verlag GmbH & Co. KGaA, Weinheim. Reproduced with permission.

7.1 Contributions to the publication

P.A. performed all experiments and wrote the first draft of the manuscript.

7.2 Abstract

PNA does it better: Peptide nucleic acid (PNA) oligomers were attached to gold nanoparticles (AuNPs) through a variety of mono- and trithiol linkers. These functionalized particles had sufficient stability for sequence-specific self-assembly onto gold surfaces (see figure) in the absence of ions or surfactants. The nanoparticle surface densities obtained were superior to comparable DNA-modified AuNPs.

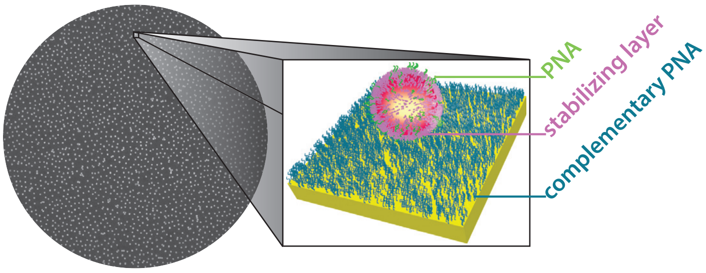

Keywords: Gold nanoparticles • Nanoparticles • Peptide nucleic acids • Self-Assembly • Solid-phase synthesis.

7.3 Article

DNA-based gold-nanoparticle (AuNP) systems are currently employed in a growing range of applications,[1] which include gene regulation,[2] nanofabrication,[3] sensing,[4–6] and plasmonic rulers.[7,8] However, a disadvantage of the assembly of DNA-modified NPs is the need for salt to keep their assemblies stable. Halogens are known to damage silver nanoparticles (AgNPs),[9] while the addition of salt in general destabilizes colloidal particles. Additionally, the presence of substantial amounts of ions is problematic for the study and use of physical phenomena that rely on electrostatics.[10,11] Thus, the functionalization of nanoparticles with the non-natural DNA analogue peptide nucleic acid (PNA), instead of DNA, is extremely attractive. PNA has many advantages over DNA including a higher stability against biodegradation, greater mismatch sensitivity, and higher binding efficiency to PNA, DNA, and RNA.[12] Hence, shorter oligonucleotide strands could potentially be used for the assembly of PNA-functionalized AuNPs compared to those required for stable DNA-based assembly. An increase in the resolution control of close-packed gold nanoparticles could therefore be observed. Additionally, the stability of PNA-DNA and PNA-PNA hybrids is independent of the ionic strength of the medium.[13] In comparison, DNA alone is not able to form assemblies under ion-free conditions as the electrostatic repulsion between the negatively charged strands is too high. Therefore, AuNP assemblies relying on PNA hybridization could be formed without the addition of salt, unlike DNA-AuNP hybrids. Despite the huge potential of PNA-based AuNPs, there are only a few articles reporting the direct attachment of PNA onto AuNPs.[14,15] Part of the reason for this is the strength of the interaction between gold and the neutral PNA, which is much stronger than with the negatively charged DNA.[16] The stronger tendency of PNA to adsorb flat onto the gold particle through direct interaction of the bases with the gold surface, rather than the preferred covalent linkage through a thiol–gold bond, results in a significantly thinner PNA layer and a strongly reduced PNA loading, leading to poor colloidal stabilization. This, combined with the lack of surface charge, results in inherently poor colloidal stability of PNA-modified metal nanoparticles.[17] This problem has not been sufficiently overcome with the PNA-functionalized AuNPs reported so far (see below). Herein, we use a conjugation technique that allows, for the first time, the synthesis of highly stable PNA-functionalized metal nanoparticles. We first functionalized the AuNPs with a stabilizing surfactant commonly used for DNA functionalization[18,19] and, in a second step, covalently attached the PNA to the AuNP surface. A variety of linkers were used, showing the wide applicability of the described method. Furthermore, we demonstrated the binding specificity of the PNA-functionalized nanoparticles to complementary oligomers, and the accessibility of the PNA strands, by directed assembly of PNA-AuNP conjugates to PNA-functionalized gold substrates. Scanning electron microscopy (SEM) imaging was used to show the sequence-specific binding to unstructured and micropatterned surfaces.

Functionalization of gold nanoparticles or surfaces with PNAs requires the modification of the oligomers with a terminal thiol group. Usually, either a cysteine or a similar monothiol-containing linker is inserted at the amino end of a PNA strand (Table 1, entry 1). Trithiol-capped DNA oligomers have been shown to bind more efficiently to AuNP surfaces and are displaced more slowly by other thiols compared to mono- and cyclic dithiol-capped derivatives.[20] As this stability towards subsequent ligand-exchange manipulation is of interest, for example, for sensing applications, we wanted to link the PNA strand in an analogous manner. However, to the best of our knowledge, trithiol ligands have not previously been used with solid-phase peptide/PNA synthesis (SPPS).[21] To fill this gap, we designed a novel and easy-to-prepare trithiol linker (**1**, Scheme 1). More specifically, the tribromide **2**[22] was converted into the trithioether **1** by reaction with triphenylmethanethiol in the presence of NaH. **1** could then be attached directly to different PNA sequences using standard SPPS procedures (Table 1, entry 2).[23] To assess the impact of the distance between the PNA and the AuNPs, PNA sequences containing ethylene glycol spacers between the PNA and the tripodal ligand were also synthesized (Table 1, entry 4). Importantly, the final step of SPPS, which necessitates trifluoroacetic acid (TFA) to cleave the PNA sequence from the solid support, also removes the trityl protecting groups of the thiols. An excess of a reducing agent such as tris(2-carboxyethyl)phosphine (TCEP) is required in this step to prevent formation of a disulfide bridge network.

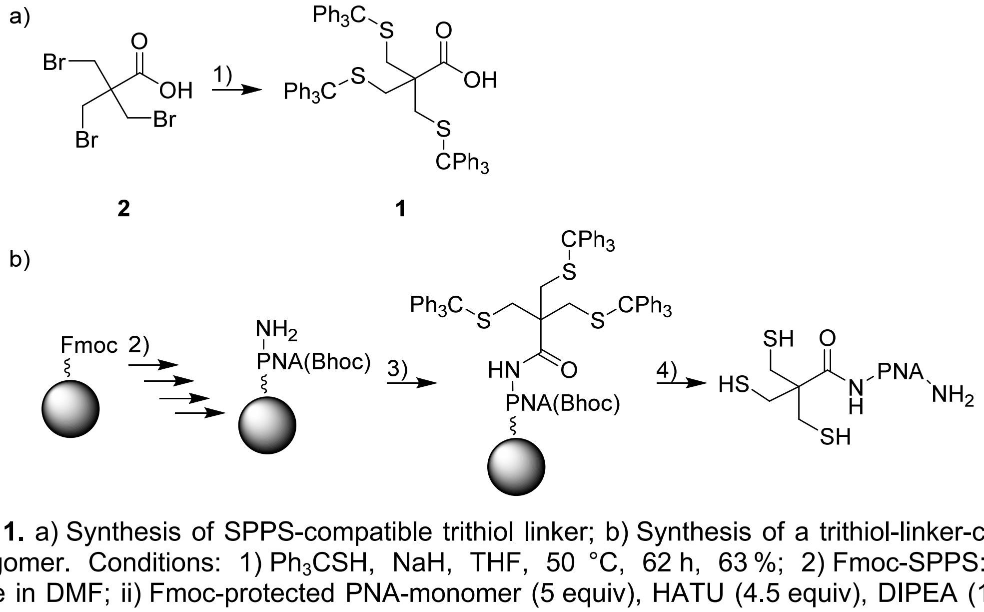

Scheme 1. a) Synthesis of SPPS-compatible trithiol linker; b) Synthesis of a trithiol-linker-containing PNA oligomer. Conditions: 1) Ph_3CSH, NaH, THF, 50 °C, 62 h, 63 %; 2) Fmoc-SPPS: i) 20 % piperidine in DMF; ii) Fmoc-protected PNA-monomer (5 equiv), HATU (4.5 equiv), DIPEA (10 equiv), 2,6-lutidine (10 equiv), DMF; 3) **1** (3 equiv), HATU (2.75 equiv), DIPEA (13 equiv), 2,6-lutidine (13 equiv), procedure repeated again; 4) TFA:phenol:triisopropylsilane 38:2:1 (*v*/*v*/*v*), TCEP (1000 equiv). Fmoc=fluorenylmethoxycarbonyl; Bhoc=benzhydryloxycarbonyl; HATU=*O*-(7-azobenzotriazol-1-yl)-1,1,3,3-tetramethyluronium hexafluorophosphate; DIPEA=*N*,*N*-diisopropylethylamine.

Table 1. Overview over the PNA and DNA conjugates (see “Type” for differentiation) with thiol linkers.

Entry	Linker Structure	Sequence[a]		Type	Corresponding NP[b]
		a	a'		
1	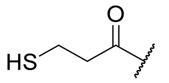	**4**	**9**	PNA	**AuNP-4**
2	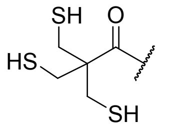	**5**	**10**	PNA	**AuNP-5**
3	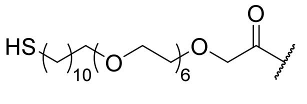	**6**	**11**	PNA	**AuNP-6**
4	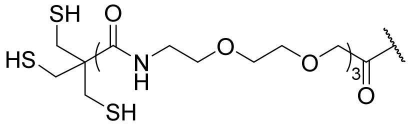	**7**	**12**	PNA	**AuNP-7**
5	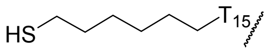	**8**	**13**	DNA	**AuNP-8**

[a] The sequences, denoted N→C terminus (PNA), or 5′→3′ (DNA), respectively, are as follows: a: TCTCAGTATT; a′: AATACTGAGA; [b] 40 nm AuNPs, functionalized with **3** and the respective oligonucleotide.

With the thiol-containing PNA sequences made, we then investigated their ability to form stable PNA-functionalized AuNPs. Duy et al. reported the synthesis of PNA-modified particles in highly concentrated Tween 20 solutions.[15] However, we found that the particles prepared using this method were not sufficiently stable for self-assembly purposes and therefore, did not provide the anticipated advantages of PNA on AuNPs. In the presence of Tween 20, we observed only non-selective aggregation. If the Tween 20 concentration was lowered, the PNA-functionalized NPs aggregated, even in the absence of ions. For DNA-modified particles, it was demonstrated that the additional attachment of 1-mercapto-6-hexyl-tri(ethylene glycol) improves salt stability through steric shielding without decreasing the hybridization efficiency.[24] Because PNA, in contrast to DNA, lacks negative charges, 32-mercapto-3,6,9,12,15,18,21-heptaoxadotriacontan-1-oic acid **3** was chosen for pre-functionalization of the AuNPs, because **3** incorporates steric shielding as well as additional electrostatic stabilization (Scheme 2).[18] The final particles were, therefore, envisioned to remain stable in the presence of ions as well as under a wide range of pH values.[25]

Additionally, **3** was used as a linker molecule for PNA (Table 1, entry 3). After in situ trityl protection of the thiol group of **3**, the carboxylate was coupled to the PNAs on the solid

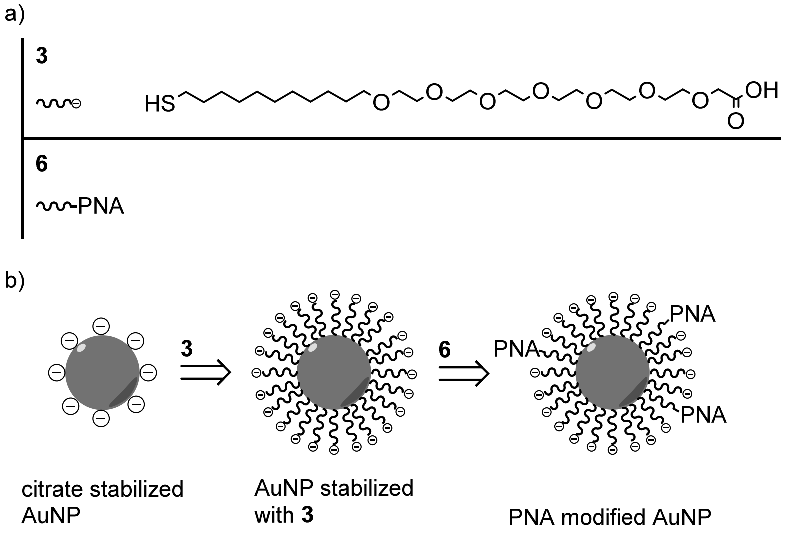

Scheme 2. a) Illustrations of **3** and **6** and chemical formula of **3**; b) Overview of the two functionalization steps in the synthesis of PNA-modified AuNPs with stabilizing **3** and a representative PNA.

support (see Supporting Information for more details). This reaction did not proceed in the commonly used solvent for such coupling reactions, namely dimethylformamide (DMF). By switching to tetrahydrofuran (THF), which has a significantly lower dielectric constant, the desired product could be obtained.[26] We believe that the critical micelle concentration (CMC) of the PEG-derivative **3** and/or its activated ester is too low in DMF, rendering the carboxylate and/or active ester site of the respective molecules inaccessible. For comparison, DNA-modified AuNPs were prepared using a linker with a 15-mer thymine spacer. Such linkers are often used for DNA-modified AuNPs because thymine has a very low affinity towards gold.[27]

The thermal stability of the PNA-PNA, PNA-DNA, and DNA-DNA hybrids in the absence of AuNPs was measured using UV/Vis spectroscopy (see Supporting Information). Consistent with previous reports,[28] the melting temperatures of the PNA-PNA duplexes were significantly higher than for the corresponding DNA-PNA or DNA-DNA duplexes, indicative of their greater stability. This highlights a major advantage of using PNA (as compared to DNA), because the PNA-modified particles have the potential to create assemblies with either shorter inter-particle distances or stronger hybridization than DNA-based systems, as fewer bases are required to achieve sufficient binding. Moreover, the PNA is not responsible for the stabilization of the particles and therefore the colloidal stability is largely independent of the oligomer length, unlike in the case of the common DNA-functionalized particles.

The preparation of PNA-modified AuNPs is described in detail in the Supporting Information. In brief, Tween 20,[29] phosphate buffer (pH 7.4), and **3** were successively added to a solution of AuNPs (40 nm diameter). After incubation for 12 hours, a sufficiently dense layer of **3** formed, protecting the AuNPs. The thiolated PNA was then added, and the incubation continued for another eight hours. Using this procedure, similar surface charges were predicted for all AuNPs, including the DNA modified **AuNP-8**.

The stability of particles functionalized with the different PNAs was investigated using UV/Vis spectroscopy. Partial aggregation results in a decrease of the extinction coefficient and/or red shifting/broadening of the localized surface plasmon resonance and can therefore easily be detected. In 1 mM phosphate buffer solutions, no changes in the UV/Vis spectra could be observed after 20 hours for any of the AuNPs (see Supporting Information for spectra). Similarly, in 10 mM buffer solutions, only minor decreases of λ_{max} were observed. At a phosphate buffer concentration of 0.1 M, aggregation and precipitation were visible within seconds for **AuNP-6** while the λ_{max} decreased less than 20 % over the course of 15 hours for all other PNA-functionalized AuNPs.

Self-assembly experiments were carried out in the absence of additional ions or surfactants. Gold-coated substrates were modified with complementary PNA **7** or with non-complementary PNA **12**, as a negative control. After incubating 5 µL of NP solution on the PNA-modified substrates for four hours in a humidification chamber, the substrates were washed four times with water. After drying, SEM measurements were performed to determine the coverage densities of AuNPs on the substrate surface (see Figure 1 and Table 2). To the best of our knowledge, these are the first images proving the sequence-specific self-assembly of PNA modified nanoparticles.

All PNA- and DNA-functionalized nanoparticles selectively bound to the surfaces modified with complementary **7**. The PNA-modified AuNPs showed almost identical particle densities of about 40 μm^{-2} (i.e. 40 particles per μm^2). These observations along with the even distribution of particles on the surface suggest that the average distance between NPs adsorbed to the surface is dictated by the electrostatic repulsion forces between the negatively charged NPs. Also the trithiol-substituted AuNPs **AuNP-5** and **AuNP-7** reached

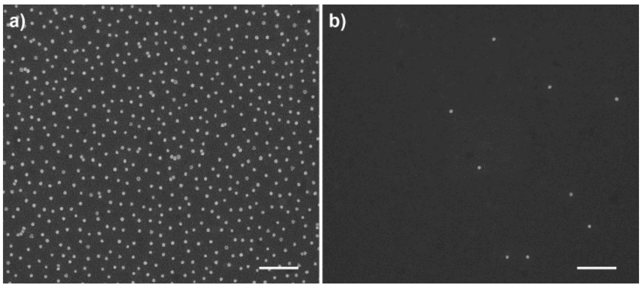

Figure 1. SEM images of surfaces modified with a) complementary PNA **7** and b) non-complementary PNA **12** after incubation with **AuNP-6**. Scale bars=500 nm.

Table 2. Number of bound nanoparticles per µm^2.[a]

Nanoparticle	Complementary 7 [µm^{-2}]	Non-Complementary 12 [µm^{-2}]
AuNP-4	38	3.6
AuNP-5	39	5.1
AuNP-6	39	2.8
AuNP-7	43	5.5
AuNP-8	26	1.1

[a] As determined by particle counting in the SEM images.

this threshold and are expected to withstand oxidation or replacement by analytes if used, for example, for sensing applications in future studies.[20] Moreover, the similar surface coverage density of **AuNP-5** with **AuNP-6** demonstrates effective PNA hybridization, despite the use of a linker that is significantly shorter than the stabilizing surfactant **3**. Notably, the coverage density of the DNA-modified **AuNP-8** is lower compared to the PNA-modified AuNPs. This is in line with the results of the thermal denaturation experiments; different charge densities of the particles could also be a reason for this result, but this is unlikely because of the identical preparation conditions. Some non-complementary binding occurs in all cases, although slightly less in case of **AuNP-8**.

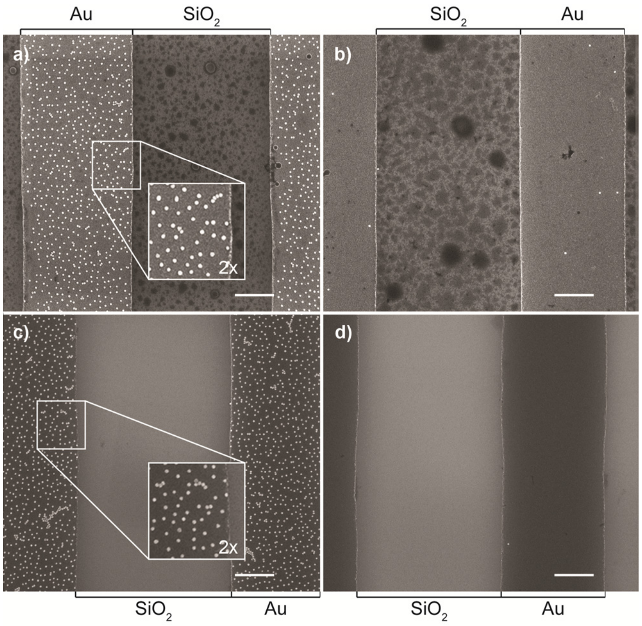

Figure 2. SEM images of micropatterned surfaces with a) complementary PNA **7** and PEG-modified silica, b) non-complementary PNA **12** and PEG-modified silica, c) complementary PNA **7** and fluoroalkyl-modified silica, d) non-complementary PNA **12** and fluoroalkyl-modified silica, after incubation with **AuNP-6**. Scale bars=1 µm. The magnification of the insets is double that of the parent image.

DNA-based systems have been shown to be usable for specific deposition of AuNPs onto patterned substrates, a feature especially of interest in the context of nanoelectronics.[30] To test if our PNA-modified AuNPs were capable of fulfilling this task as well, we incubated **AuNP-6** on micropatterned substrates with lines of Au and silica. The substrates were first modified with hydrophilic PEGylated silanes or hydrophobic fluoroalkyl silanes and then with PNAs **7** or **12**, as described above for gold-coated substrates. **AuNP-6** assembles exclusively onto the areas with complementary PNA (Figure 2). Hence, the nanoparticles stick to neither hydrophilic nor hydrophobic surfaces but rather only to complementary oligonucleotide sequences. This further demonstrates the rigidity and practicality of our PNA-based system.

In summary, we have demonstrated the preparation of stable PNA-modified particles through a novel approach involving the use of a thiolated alkyl PEG carboxylate surfactant. Standard, as well as novel, mono- and trithiol linkers were found to be compatible with this approach. The potential of these PNA-nanoparticles as new building blocks for self-assembling systems was confirmed by synthesizing particles that were able to self-assemble under additive-free conditions, an endeavor which has, to the best of our knowledge, not been directly shown with any other DNA/PNA-based systems. The superior properties of PNA compared to DNA make these particles highly interesting for future studies. Ion-free conditions are needed for investigation of electrostatic phenomena[10,11] and are not compatible with DNA hybridization. Sensing applications[4–6] could also benefit from the increased binding strength of PNA hybrids. This strength also allows for the investigation of optical phenomena at unprecedentedly small inter-particle distances.[7,8]

7.4 Acknowledgments

This work was supported by the Swiss National Science Foundation (Professorship No. PP00P2_133568 to G.G.), the University of Zurich (G.G.), the Australian Research Council (Australian Research Fellowship to U.B. and Future Fellowship to A.M.F. (FT110100545)) and the Commonwealth Scientific and Industrial Research Organization (OCE Science Leader position to U.B.). This work was performed in part at the Melbourne Centre for Nanofabrication, an initiative partly funded by the Commonwealth of Australia and the Victorian Government.

7.5 Supporting Information

7.5.1 Instrumentation and Materials

PNA monomers and [2-(2-(Fmoc-amino)ethoxy)ethoxy]acetic acid (Fmoc-AEEA-OH spacer) were purchased from Link Technologies Ltd. (Lanarkshire, Scotland), TentaGel S RAM resin beads from Rapp Polymers GmbH (Germany), citrate stabilized AuNP solutions from Ted Pella, Inc. (USA), triphenylmethanethiol from Sigma-Aldrich (USA), thiol-modified DNA oligomers from Fidelity Systems (USA), TCEP from TCI Europe and Apollo Scientific (UK), 32-mercapto-3,6,9,12,15,18,21-heptaoxadotriacontan-1-oic acid **3** was obtained from ProChimia Surfaces (Poland). Water used for AuNP modification and self-assembly was deionized with a Millipore Milli-Q Advantage (conductivity: 18.2 MΩ/cm at rt). ^{1}H and^{13}C NMR spectra were recorded on Bruker Avance (400 and 500) spectrometers. ^{13}C NMR measurements were carried out as ^{13}C {H}. NMR spectra were referenced to the residual solvent signal. IR spectra were acquired on a Perkin-Elmer Spectrum 2 FT-IR instrument. High resolution ESI-MS spectra were measured with a Bruker ESQUIRE-LC quadrupole ion trap instrument and MALDI-MS spectra on a Bruker Autoflex I. UV-ozone cleaning was performed with a Sumaco Inc. UV-1. AuNP stability measurements were performed on an Agilent Cary 60 UV/Vis. Temperature dependent UV/Vis experiments were performed on Varian UV Cary 100 Bio and Varian UV Cary 500 Scan instruments. SEM images were acquired with a FEI Nova NanoSEM 430.

7.5.2 Synthetic Procedures

General Procedure for solid phase peptide synthesis (SPPS)

SPPS was performed manually in 5 mL polypropylene one-way syringes as reaction vessels, which were equipped with a frit at the bottom. They were filled with 98 mg of polystyrene resin beads TentaGel S RAM (0.24 mmol/g). The resin was swollen in DMF before use for 1 h. All reactions were performed on a mechanical shaker with 600 rpm, soaking approximately 2.5–3.5 mL of freshly prepared solutions into the syringe. Fmoc/Bhoc protected PNA monomers (5 equiv.) were pre-activated in Eppendorf tubes before every coupling step for 5 min with HATU (4.5 equiv.) in DMF, adding DIPEA and 2,6-lutidine (10 equiv. each) under sonication. For each coupling step the resin beads were treated with the activated acid and subsequently washed with DMF. The coupling step was monitored with the Kaiser test. Substances other than the usual PNA monomers were coupled in the same way, unless noted otherwise. Double Fmoc deprotection was performed with piperidine in DMF (2:8, v/v; 2 min, 10 min). The resin beads were then washed successively with DMF, DCM and DMF. The whole procedure (deprotection, coupling, monitoring) was repeated for every monomer until the sequence was completed. The resin was then shrunk with methanol (30 min) and dried under vacuum. Final cleavage of the PNA oligomer from the resin and the deprotection of all Bhoc and Boc side chain protecting groups were simultaneously performed in TFA/triisopropylsilane (TIS)/H_2O (38:2:1, v/v/v; 3x 2 h). Following the removal of TFA under reduced pressure, the crude product was purified by HPLC with a gradient of 0.1% TFA in water and acetonitrile (Agilent Zorbax SB300-C18, 4 mL/min, 0 min 95:5, 8 min 85:15, 28 min 60:40, 50 min 20:80, 51 min 0:100, 56 min 0:100, 61 min 95:5). MALDI-MS spectra, LC/MS, and analytical HPLC traces (Macherey-Nagel EC 250/3 NUCLEOSIL 100-5 C18, 1 mL/min, 0.1% TFA in water : acetonitrile 95:5 → 0:100 over 30 min) were recorded. The purities were determined from the HPLC UV traces at 260 nm.

3-(tritylthio)-2,2-bis((tritylthio)methyl)propanoic acid 1

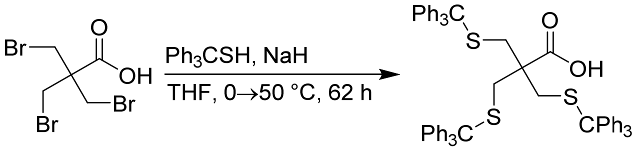

63%

2 **1**

Triphenylmethanethiol (1.63 g, 5.89 mmol) was slowly added to a cooled (0 °C) suspension of NaH (177 mg, 7.36 mmol) in dry THF (20 mL). After 15 min, **2** (499 mg, 1.47 mmol) was added. The mixture was heated to 50 °C and stirred at that temperature for 62 h. The reaction was quenched with H_2O. CH_2Cl_2 and HCl (1 M, 8 mL) were added. The layers were separated and the aqueous layer was extracted with CH_2Cl_2 (3x). The combined organic layers were washed with brine, dried ($MgSO_4$), filtered, and concentrated. The crude product was purified by column chromatography (hexanes/EtOAc 170:1 → 8:2) giving pure **1** (860 mg, 63%) as a colorless solid.

R_f = 0.10 (hexanes/EtOAc 8:2). IR (KBr) 3056 (m), 3030 (m), 2923 (w), 1706 (m), 1594 (w), 1489 (m), 1443 (m), 741 (s), 699 (s). ^{1}H NMR (400 MHz, $CDCl_3$) ∂ 7.40–7.30 (m, 18 H), 7.20–7.07 (m, 27 H), 2.29 (s, 6 H). ^{13}C NMR (100 MHz, $CDCl_3$): ∂ 177.0, 144.6, 129.8, 128.0, 126.8, 66.5, 49.6, 36.8. HRMS m/z calcd. for $C_{62}H_{51}O_2S_3$ ($[M-H]^-$) 923.30567, found 923.30487.

Precursor sequence a' PAN087

SPPS was performed according to the general procedure (vide supra), until the last coupling was completed.

Precursor sequence a PAN088

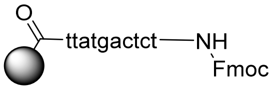

SPPS was performed according to the general procedure (vide supra), until the last coupling was completed.

Compound 4

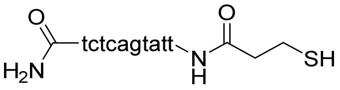

4 was synthesized according to the general procedure for SPPS (vide supra). In the last coupling step 3-(tritylthio)propionic acid (5 equiv) was used instead of a PNA monomer.

MALDI-MS calcd. for $C_{111}H_{142}N_{52}NaO_{34}S$ ($[M+Na]^+$) 2802.1, found 2802.2. ESI-MS m/z 927.5 (65, $[M+3\,H]^{3+}$), 696.0 (100, $[M+4\,H]^{4+}$), 557.0 (15, $[M+5\,H]^{5+}$). HPLC: t_R = 7.13 min, 92% purity

Compound 5

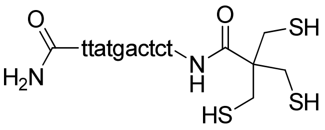

5 was synthesized according to the general procedure for SPPS (vide supra), with the following modifications: **1** (3 equiv.) was pre-activated in a Eppendorf tube before each coupling step for 15 min with HATU (2.75 equiv.) in DMF, adding DIPEA and 2,6-lutidine (13 equiv. each). The activated acid was then coupled for 4 h to ¼ of **PAN088**. The coupling was repeated to ensure completion. Before adding TFA to cleave the PNA from the resin, approximately 3 mg of TCEP were added.

MALDI-MS calcd. for $C_{113}H_{147}N_{52}O_{34}S_3$ ($[M+H]^+$) 2872.1, found 2872.0. ESI-MS m/z 1436.4 (2, $[M+2\,H]^{2+}$), 958.2 (100, $[M+3\,H]^{3+}$), 719.0 (47, $[M+4\,H]^{4+}$), 575.5 (4, $[M+5\,H]^{5+}$). HPLC: t_R = 8.34 min, 99% purity.

Precursor PAN100

Carboxylic acid **3** (45 mg, 86 µmol) was dissolved in dry THF (400 µL). Triphenylchloromethane (27 mg, 96 µmol) and DIPEA (16 µL, 12 mg, 96 µmol) were added and the resulting solution was stirred at rt for 40 h. Appropriate aliquots were taken and treated with *N*,*N'*-diisopropylcarbodiimide (1 equiv.), hydroxybenzotriazole (1 equiv.), and DIPEA (2 equiv.). The solution was shaken for 30 min before employing it as activated acid in SPPS (see **11**, **6**).

Compound 6

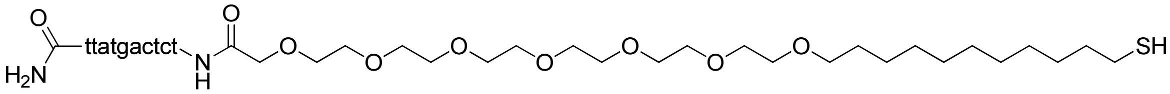

6 was synthesized according to the general procedure for SPPS (vide supra), with the following modifications: ½ of **PAN088** was deprotected and washed with THF (2x). The resin was then soaked with the solution **PAN100** (24 µmol acid, 2 equiv.). The coupling procedure was repeated to increase the amount of coupled linker. Before adding TFA to cleave the PNA from the resin, approximately 3 mg of TCEP were added.

MALDI-MS calcd. for $C_{133}H_{187}N_{52}O_{41}S$ ($[M+H]^+$) 3200.4, found 3200.4. ESI-MS m/z 1067.6 (7, $[M+3\,H]^{3+}$), 801.1 (100, $[M+4\,H]^{4+}$), 641.1 (24, $[M+5\,H]^{5+}$). HPLC: t_R = 15.1 min, 95% purity.

Compound 7

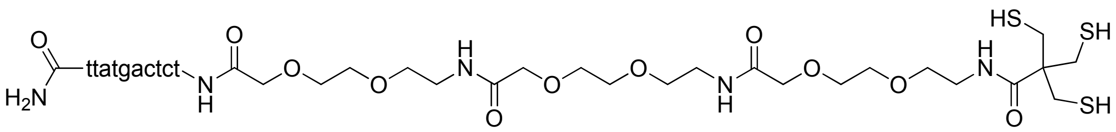

Fmoc-AEEA-OH spacer (5 equiv.) was coupled to ¼ of **PAN088** according to the general SPPS procedure. The procedure was repeated twice to attach a total of three spacers. **1** (3 equiv.) was pre-activated in a Eppendorf tube before each coupling step for 15 min with HATU (2.75 equiv.) in DMF, adding DIPEA and 2,6-lutidine (13 equiv. each). The coupling was repeated to ensure completion.

MALDI-MS calcd. for $C_{131}H_{179}N_{55}NaO_{43}S_3$ ($[M+Na]^+$) 3329.3, found 3329.4. ESI-MS m/z 1103.3 (13, $[M+3\,H]^{3+}$), 827.9 (100, $[M+4\,H]^{4+}$), 662.5 (16, $[M+5\,H]^{5+}$). HPLC: t_R = 9.15 min, 92% purity.

Compound 9

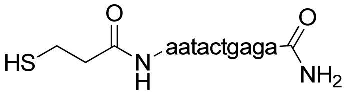

9 was synthesized according to the general procedure for SPPS (vide supra). In the last coupling step 3-(tritylthio)propionic acid (5 equiv) was used instead of a PNA monomer.

MALDI-MS calcd. for $C_{112}H_{140}N_{63}O_{28}S$ ($[M+H]^+$) 2847.1, found 2847.0. ESI-MS m/z 949.8 (56, $[M+3\,H]^{3+}$), 712.7 (100, $[M+4\,H]^{4+}$), 570.4 (78, $[M+5\,H]^{5+}$), 475.6 (13, $[M+6H]^{6+}$). HPLC: t_R = 6.71 min, 92% purity.

Compound 10

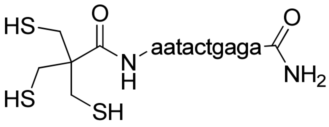

10 was synthesized according to the general procedure for SPPS (vide supra), with the following modifications: **1** (3 equiv.) was pre-activated in an Eppendorf tube before each coupling step for 15 min with HATU (2.75 equiv.) in DMF, adding DIPEA and 2,6-lutidine (13 equiv. each). The activated acid was then coupled for 4 h to ¼ of **PAN087**. The coupling was repeated to ensure completion (without intermediate deprotection). Before adding TFA to cleave the PNA from the resin, approximately 3 mg of TCEP were added.

MALDI-MS calcd. for $C_{114}H_{144}N_{63}O_{28}S_3$ ($[M+H]^+$) 2939.1, found 2938.8. ESI-MS m/z 980.5 (8, $[M+3\,H]^{3+}$), 735.7 (46, $[M+4\,H]^{4+}$), 588.8 (100, $[M+5\,H]^{5+}$), 490.9 (13, $[M+6\,H]^{6+}$). HPLC: t_R = 7.80 min, 98% purity.

Compound 11

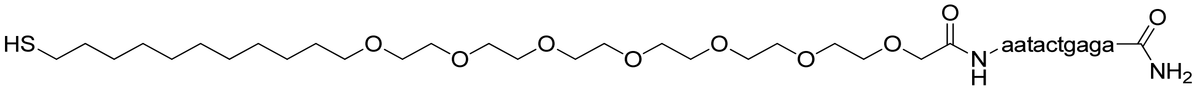

11 was synthesized according to the general procedure for SPPS (vide supra), with the following modifications: ½ of **PAN087** was deprotected and washed with THF (2x). The resin was then soaked with the solution **PAN100** (24 µmol acid, 2 equiv.). The coupling procedure was repeated to increase the amount of coupled linker. Before adding TFA to cleave the PNA from the resin, approximately 3 mg of TCEP were added.

MALDI-MS calcd. for $C_{134}H_{184}N_{63}O_{35}S$ ($[M+H]^+$) 3267.4, found 3267.3. ESI-MS m/z 817.8 (28, $[M+3\,H]^{3+}$), 654.5 (100, $[M+4\,H]^{4+}$), 546.6 (20, $[M+5\,H]^{5+}$). HPLC: t_R = 14.5 min, 99% purity.

Compound 12

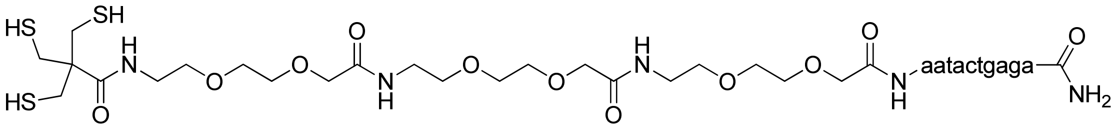

Fmoc-AEEA-OH spacer (5 equiv.) was coupled to ¼ of **PAN087** according to general SPPS procedure. The procedure was repeated twice to attach a total of three spacers. **1** (3 equiv.) was pre-activated in a Eppendorf tube before each coupling step for 15 min with HATU (2.75 equiv.) in DMF, adding DIPEA and 2,6-lutidine (13 equiv. each). The coupling was repeated to ensure completion.

MALDI-MS calcd. for $C_{132}H_{176}N_{66}NaO_{37}S_3$ ($[M+H]^+$) 3396.4, found 3396.3. ESI-MS m/z 1125.5 (9, $[M+3\,H]^{3+}$), 844.6 (100, $[M+4\,H]^{4+}$), 675.9 (71, $[M+5\,H]^{5+}$), 563.5 (11, $[M+6\,H]^{6+}$). HPLC: t_R = 8.70 min, 94% purity.

General Procedure for Preparation of PNA modified AuNP

A citrate stabilized AuNP (40 nm diameter) solution with an OD=1 was concentrated from 0.5 mL to 50 µL by centrifugation (3800 rpm, 45 min). Tween20 (2.5% v/v in water, 2 µL), phosphate buffer (0.1 M, pH=7.4, 30 µL), thiol **3** (1.66 mM in water, 3 µL), and bis(p-sulfonatophenyl)phenylphosphine dihydrate dipotassium salt (BSPP, 0.1 M, 2.5 µL) were subsequently added. The solution was incubated on a shaker overnight (12 h). PNA (100 µM, 4 µL) was added, and incubation continued for 8 h. The nanoparticles were washed by adding 0.5 mL water, centrifuging (3800 rpm, 45 min), and removing the supernatant. The washing procedure was repeated another three times. The particles were dispersed in water (25µL).

General Procedure for Preparation of DNA modified AuNP

A citrate stabilized AuNP (40 nm diameter) solution with an OD=1 was concentrated from 0.5 mL to 50 µL by centrifugation (3800 rpm, 45 min). Tween20 (2.5% v/v in water, 2 µL), phosphate buffer (0.1 M, pH=7.4, 30 µL), thiol **3** (1.66 mM in water, 3 µL), DNA (100 µM, 4 µL), and BSPP (0.1 M, 2.5 µL) were subsequently added. The solution was incubated on a shaker for 20 h. The nanoparticles were washed by adding 0.5 mL water, centrifuging (3800 rpm, 45 min), and removing the supernatant. The washing procedure was repeated another three times. The particles were dispersed in water (25µL).

General Procedure for Gold-coated Silicon Substrates

Au coated substrates were fabricated on a 4-inch silica-coated silicon wafer (Universitywafers.com). The wafer was cleaned by immersing it in an acetone bath at 70 °C for 3 min followed by rinsing with *iso*-propanol and was dried under a stream of N_2. 3 nm of Ti and 30 nm of Au were deposited with an electron-beam evaporator. The substrate was treated with an UV-ozone cleaner (0.5 L/min, 3 min). The substrate was then immersed into a solution of PNA (100 µM, 35 µL) and BSPP (0.1 M, 5.25 µL) in EtOH (138 µL) for 24 h. After this surface treatment, the substrate was washed by rinsing it with ethanol, acetonitrile:water 1:1, water, ethanol, and dried under N_2.

Micropatterned Substrates

Micropatterned substrates were fabricated on a 4-inch silica-coated silicon wafer (Universitywafers.com). The wafer is patterned with 2 µm lines on a 4 µm period covering 12 mm^2. The wafer was cleaned by immersing it in an acetone bath at 70 °C for 3 min followed by rinsing with *iso*-propanol and finally dried under a stream of N_2. A positive photoresist (AZ 1512HS: AZ Electronics Materials) was spin-coated at 3,000 rpm for 30 seconds on the wafer, which was softbaked at 90 °C for 1 min, exposed to UV light (45 mJ/cm^2) through a chromium mask (MiniFAB Pty. Ltd., Scoresby, VIC, Australia) and finally developed for 50 s in a 3:2 mixture of AZ 726 MIF developer (AZ Electronics Materials) and ultrapure water. The exposed areas of the wafer were then etched 65 nm with reactive ion etching with a mixture of SF_6 (7 sccm) and CHF_3 (50 sccm), a gas pressure of 7 mT, an ICP power of 2500 W, a RIE power of 50 W and a He back pressure of 10 mT. 3 nm of Ti and 12 nm of Au were deposited with an electron-beam evaporator. The photoresist was removed by sonicating the substrate in acetone for 10 min followed by 10 min of UV-ozone cleaning (0.5 L/min, 3 min). The substrate was then immersed into a mixture of 2.5 µl of 2-[methoxy(polyethyleneoxy)propyl]trimethoxy-silane (PEG-silane, Gelest), 1.25 mL of toluene and 1 µL of concentrated HCl (Sigma Aldrich) for 50 min. After this surface treatment, the substrate was washed by rinsing it with toluene, ethanol, ultrapure water and dried under N_2. The substrate was then immersed into a solution of PNA (100 µM, 35 µL) and BSPP (0.1 M, 5.25 µL) in EtOH (138 µL) for 24 h. After this surface treatment, the substrate was washed by rinsing it with ethanol, acetonitrile:water 1:1, water, ethanol, and dried under N_2.

General Procedure for Self-Assembly of AuNPs onto Substrates

PNA modified (micropatterened) substrates were placed in a humidity chamber with droplets of phosphate buffer (0.1 mM, pH=7.4) in the humidification wells. PNA or DNA modified AuNPs (5 µL) were put on top of the substrates. After 4 h incubation in the closed chamber, the substrates were washed with water (4x) and partially dried with a tissue (Kimwipe), by putting it on the edge of the substrate and making use of the capillary force. The substrate was allowed to completely dry under ambient conditions.

7.5.3 Spectra

In the following analytical spectra of the newly synthesized and previously not characterized compounds are shown.

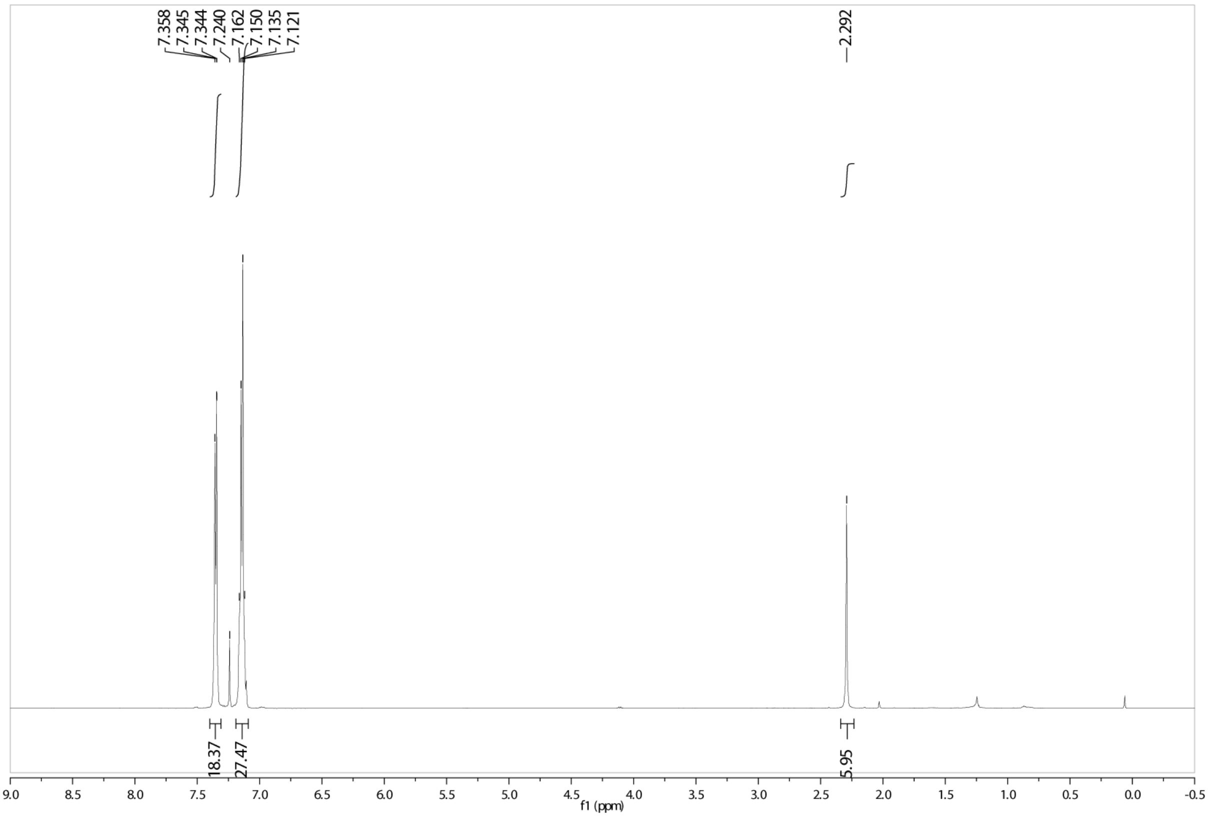

Figure S1. ^{1}H spectrum of compound **1** in $CDCl_3$.

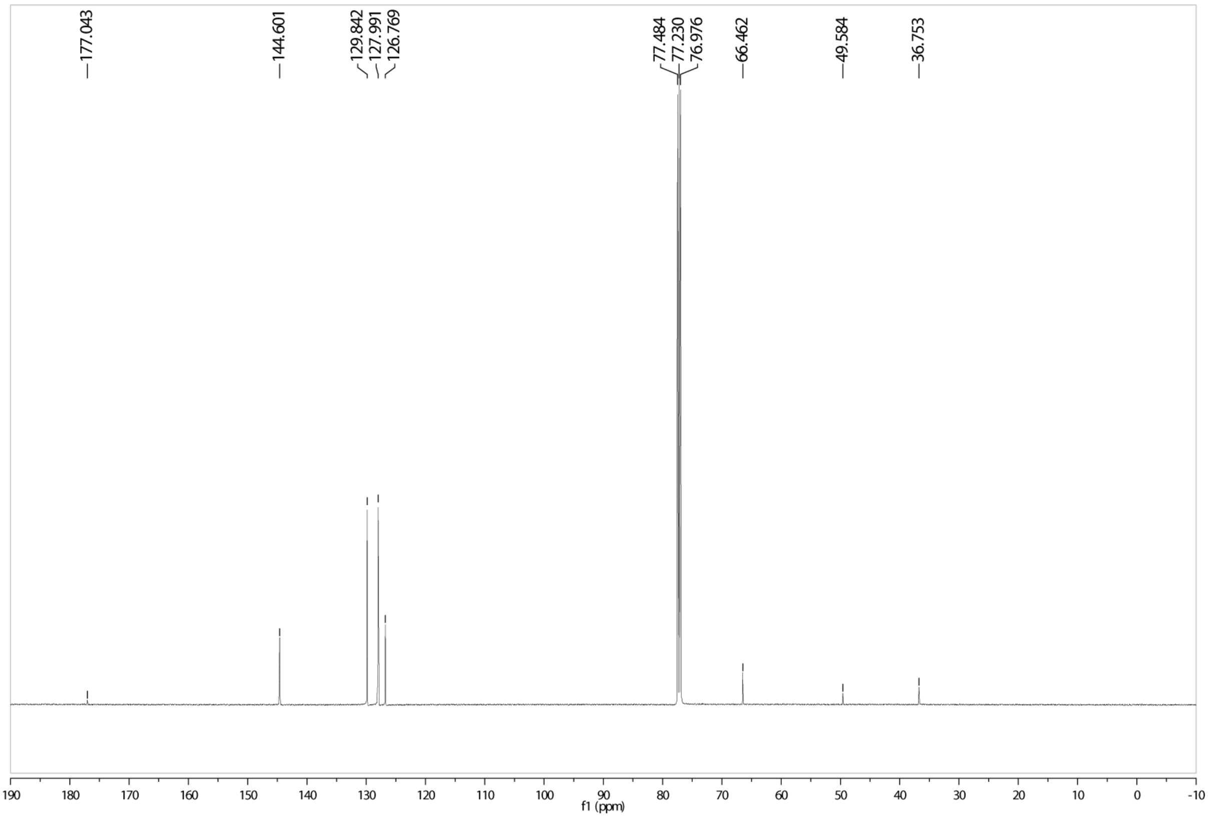

Figure S2. ^{13}C spectrum of compound **1** in $CDCl_3$.

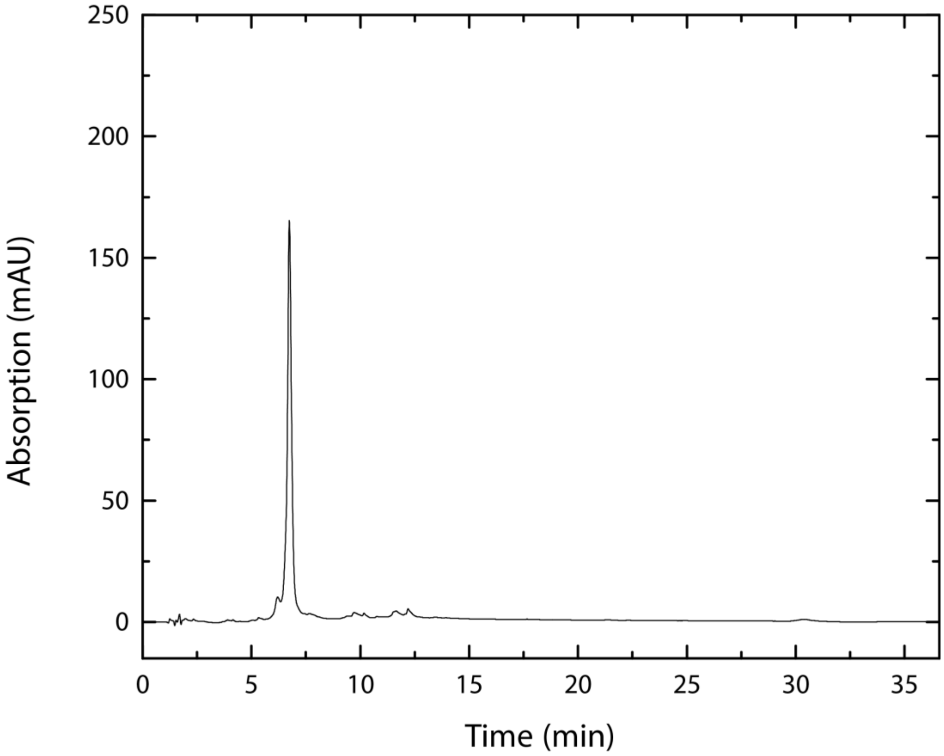

Figure S3. Analytical HPLC trace of compound **4**.

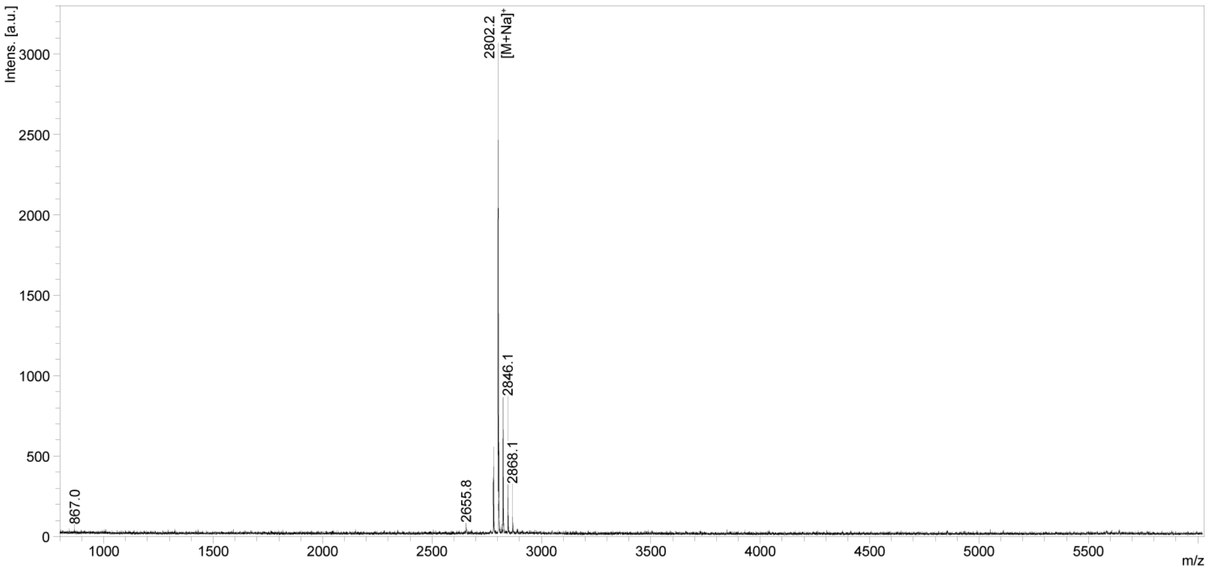

Figure S4. MALDI-MS spectrum of compound **4**.

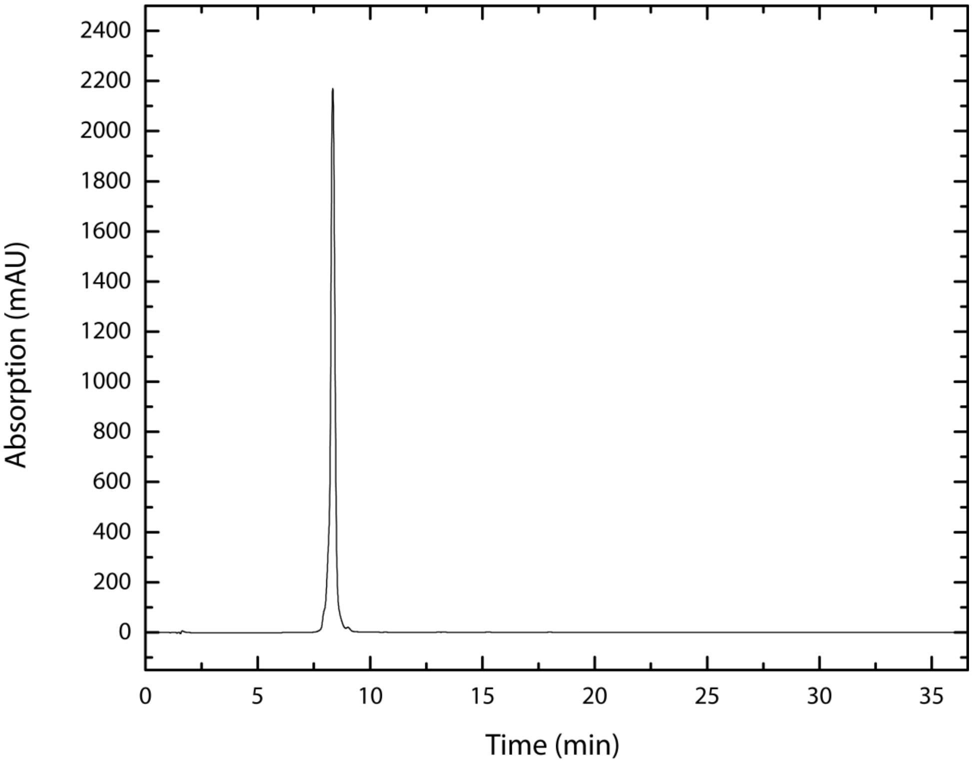

Figure S5. Analytical HPLC trace of compound **5**.

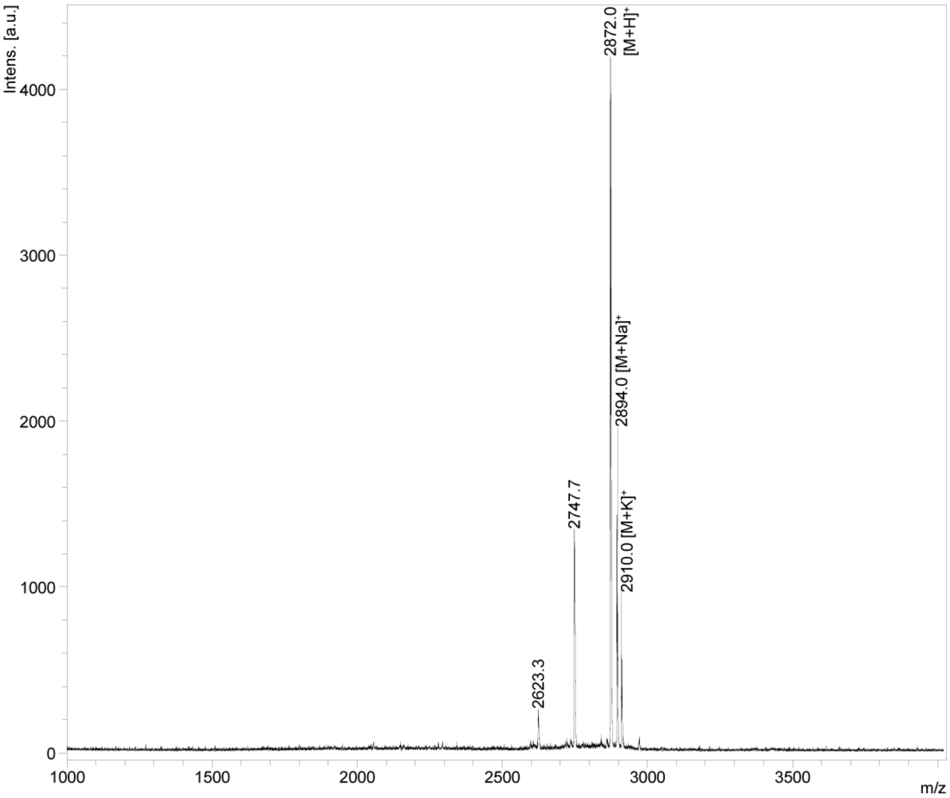

Figure S6. MALDI-MS spectrum of compound **5**.

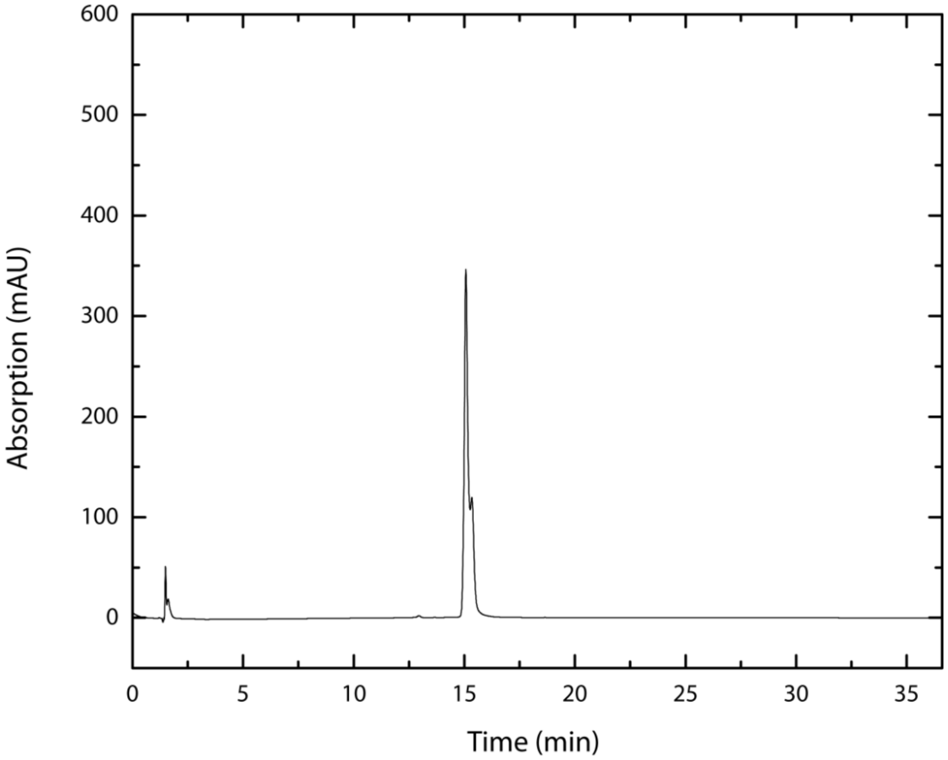

Figure S7. Analytical HPLC trace of compound **6**.

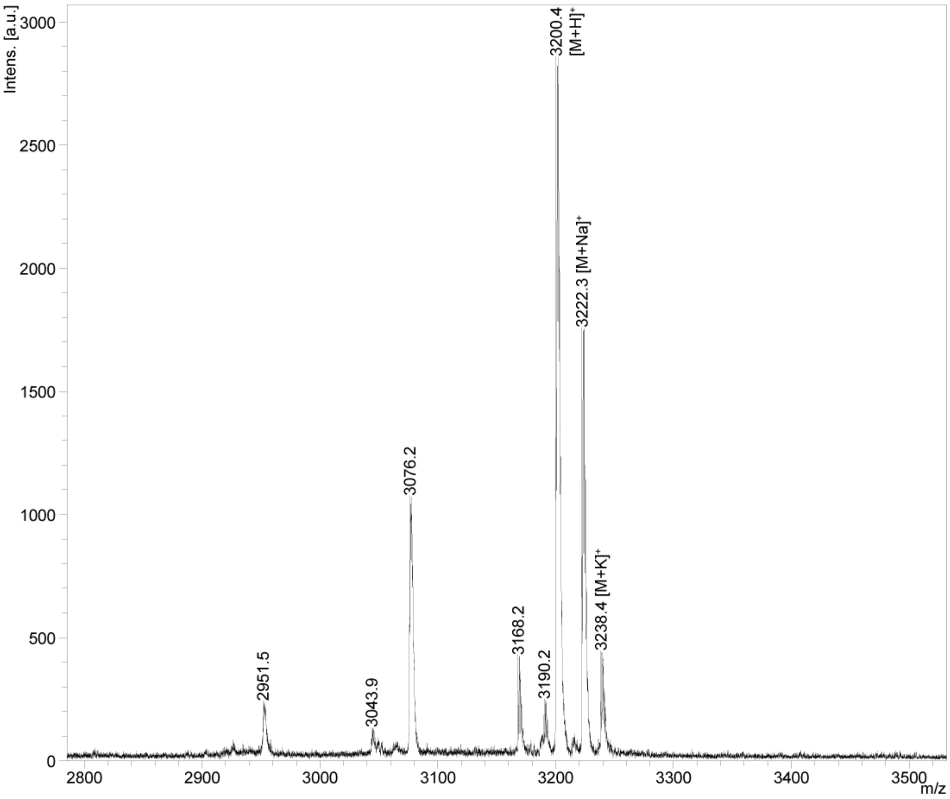

Figure S8. MALDI-MS spectrum of compound **6**.

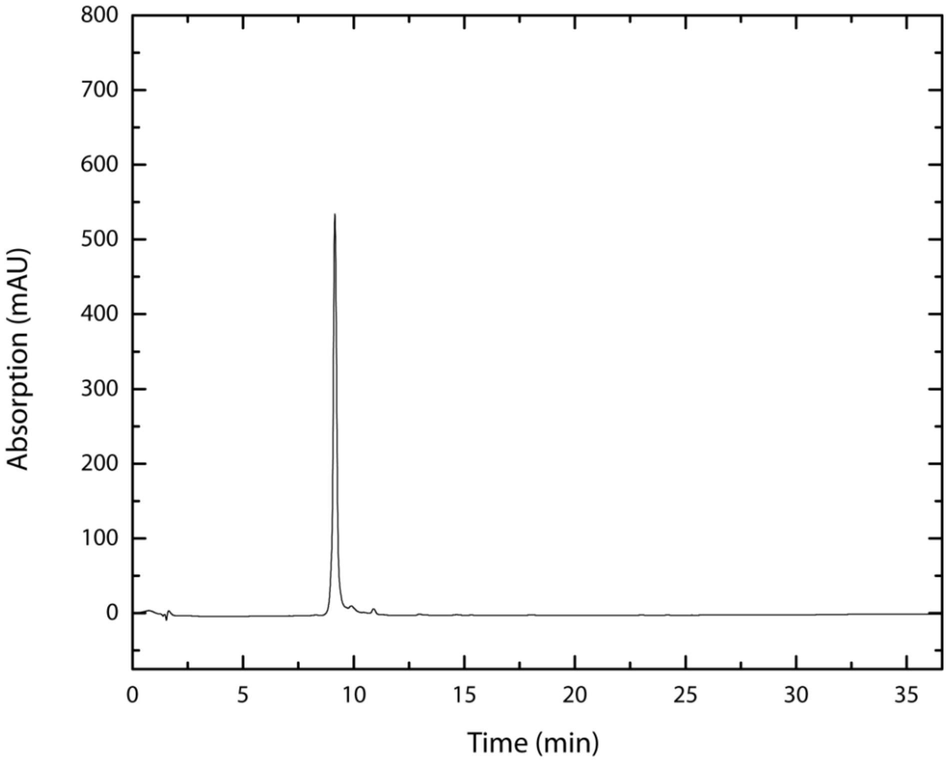

Figure S9. Analytical HPLC trace of compound **7**.

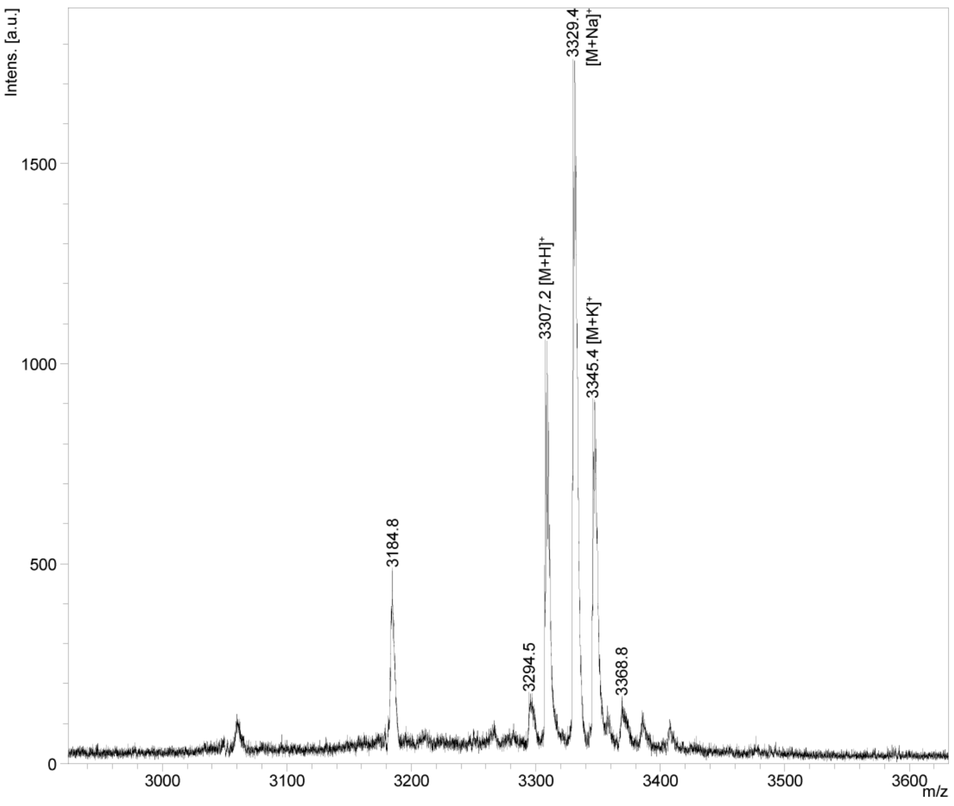

Figure S10. MALDI-MS spectrum of compound **7**.

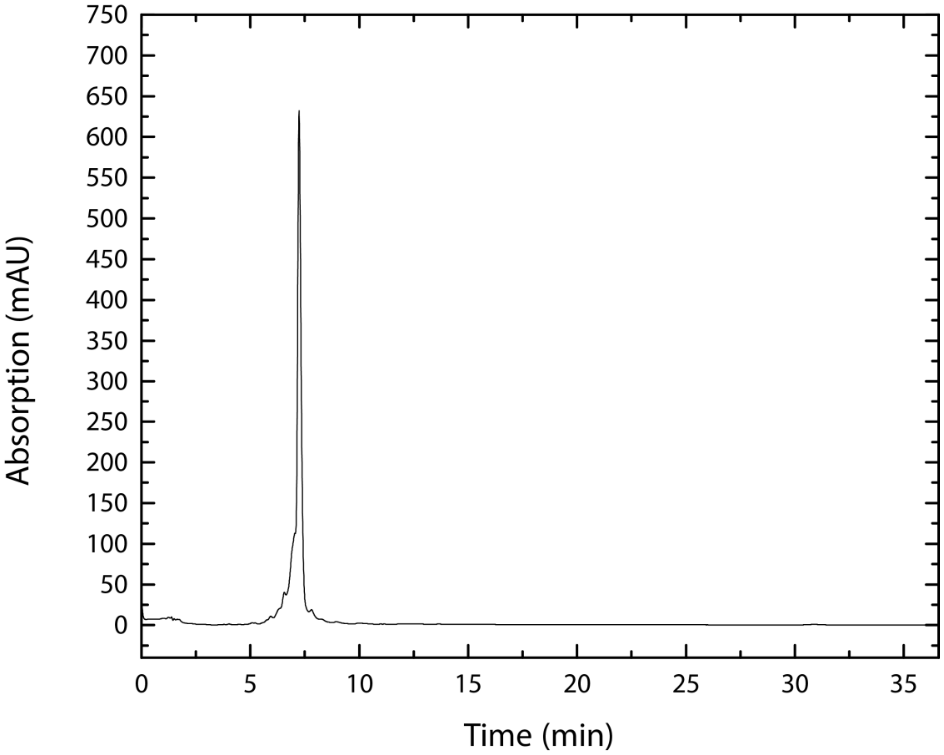

Figure S11. Analytical HPLC trace of compound **9**.

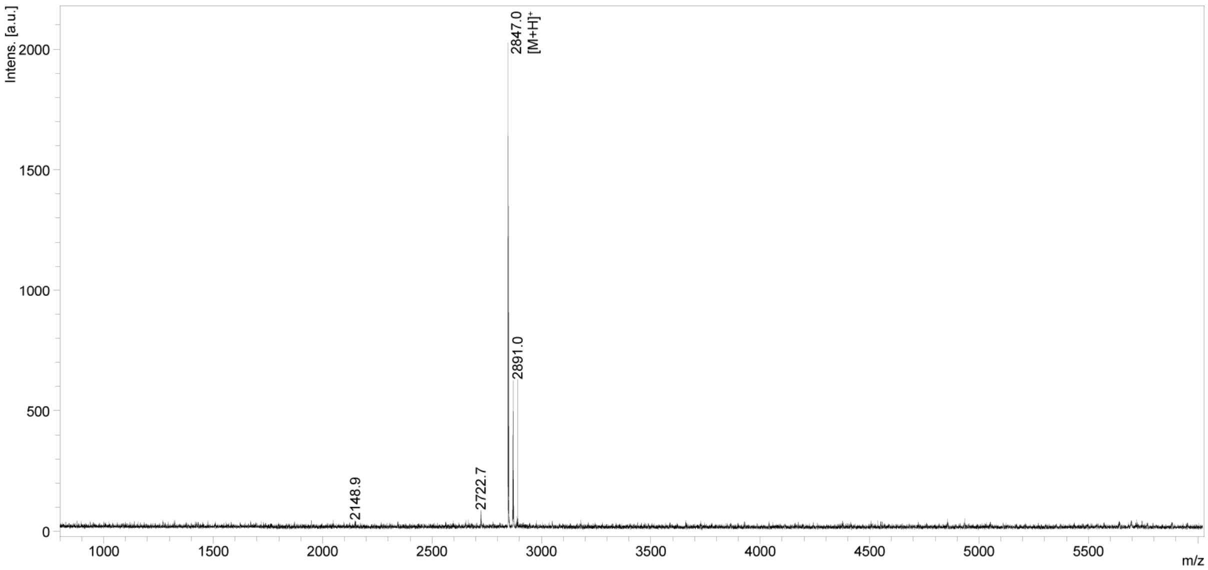

Figure S12. MALDI-MS spectrum of compound **9**.

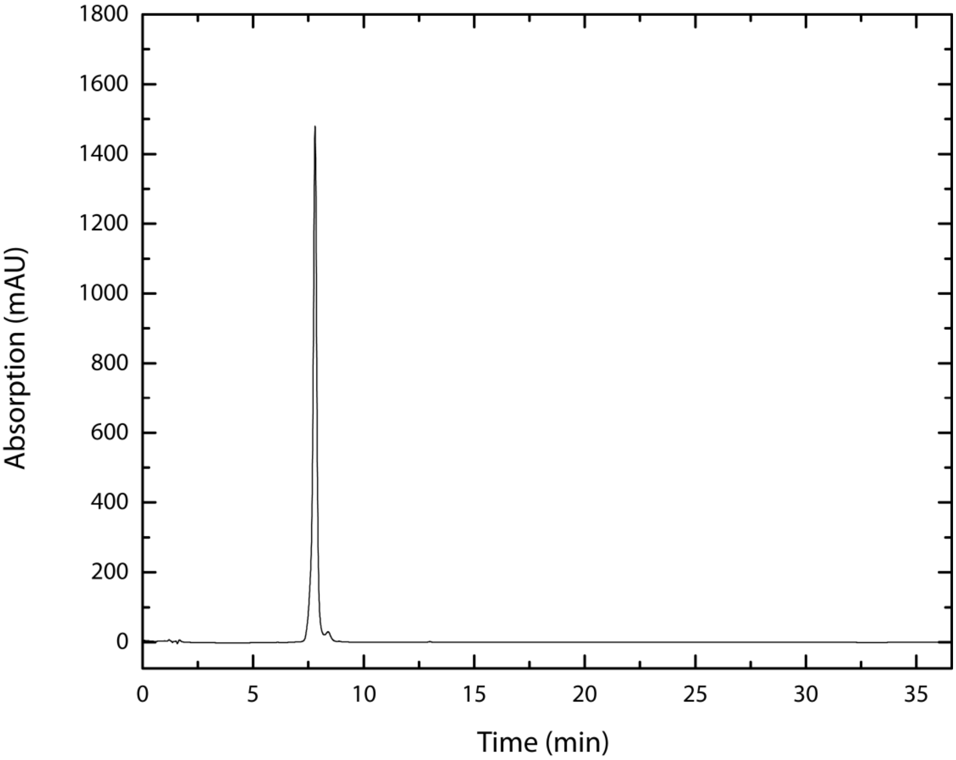

Figure S13. Analytical HPLC trace of compound **10**.

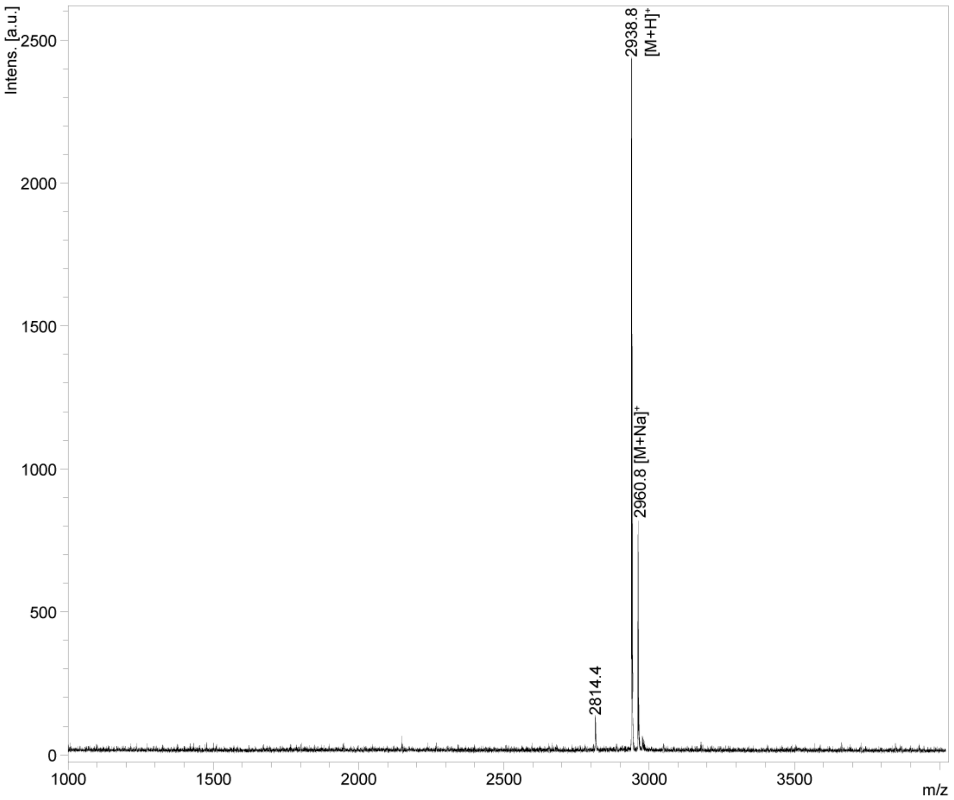

Figure S14. MALDI-MS spectrum of compound **10**.

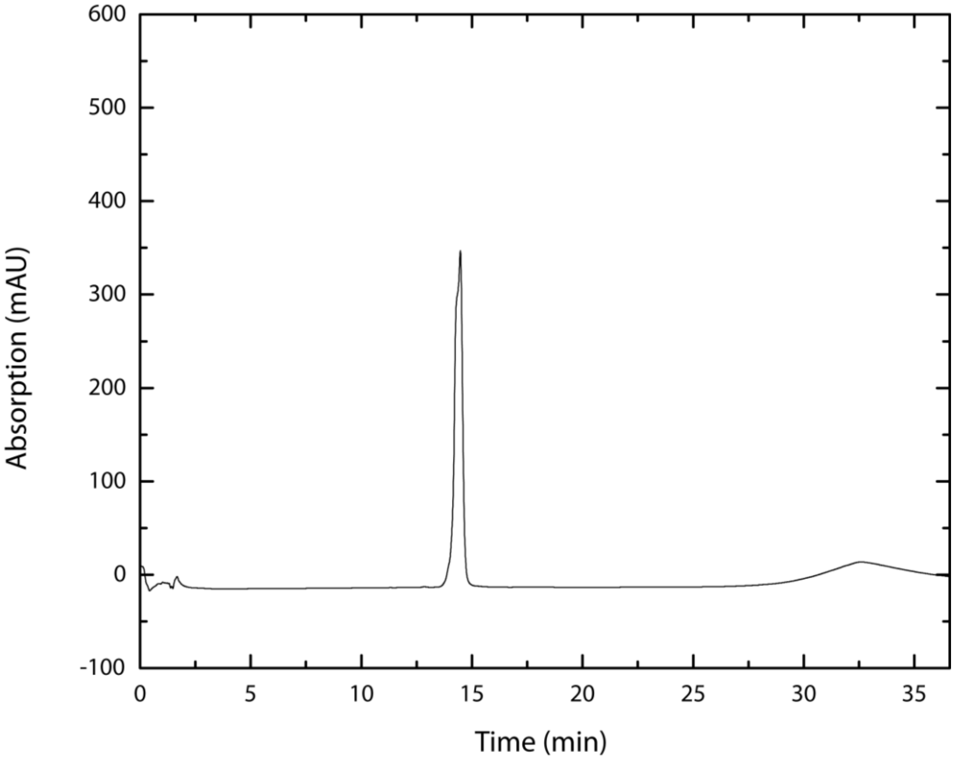

Figure S15. Analytical HPLC trace of compound **11**.

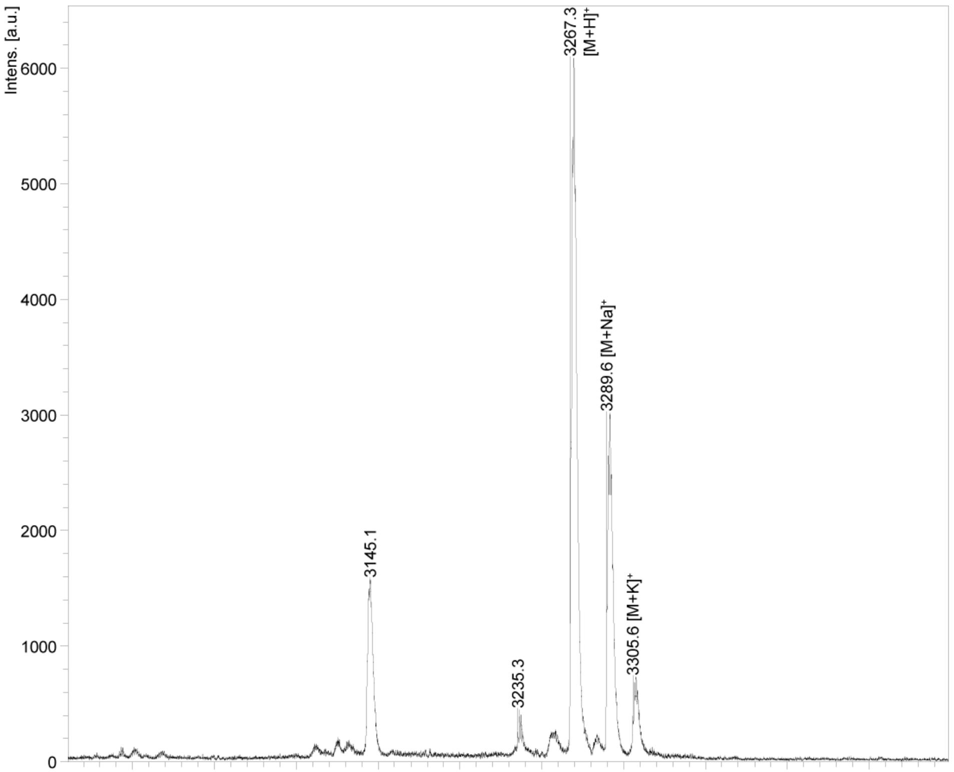

Figure S16. MALDI-MS spectrum of compound **11**.

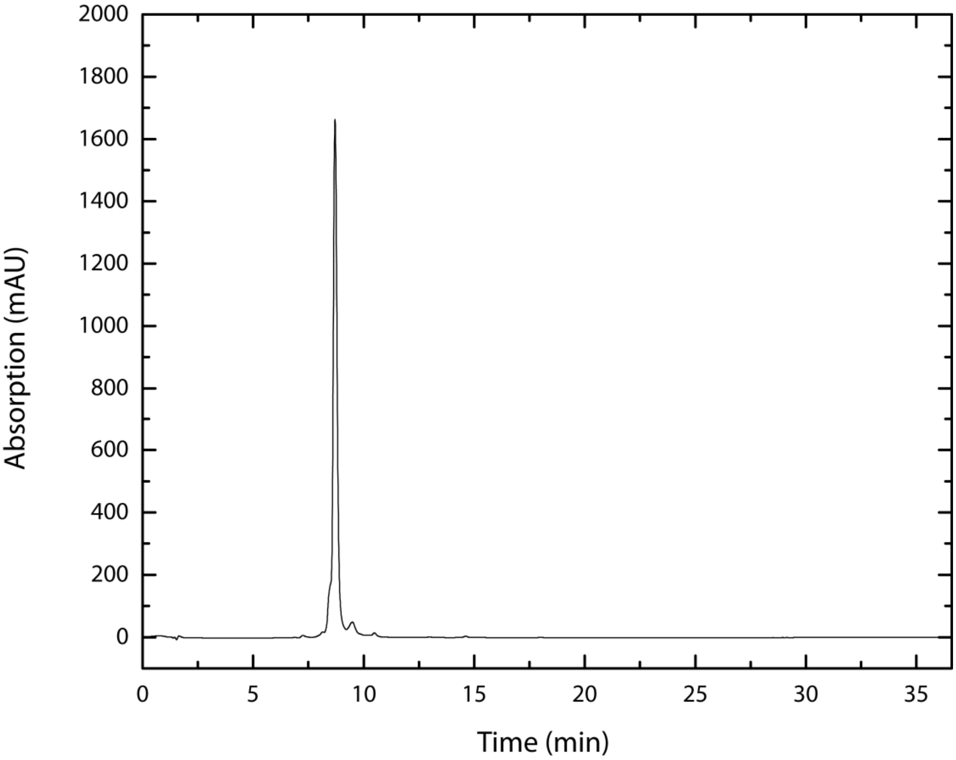

Figure S17. Analytical HPLC trace of compound **12**.

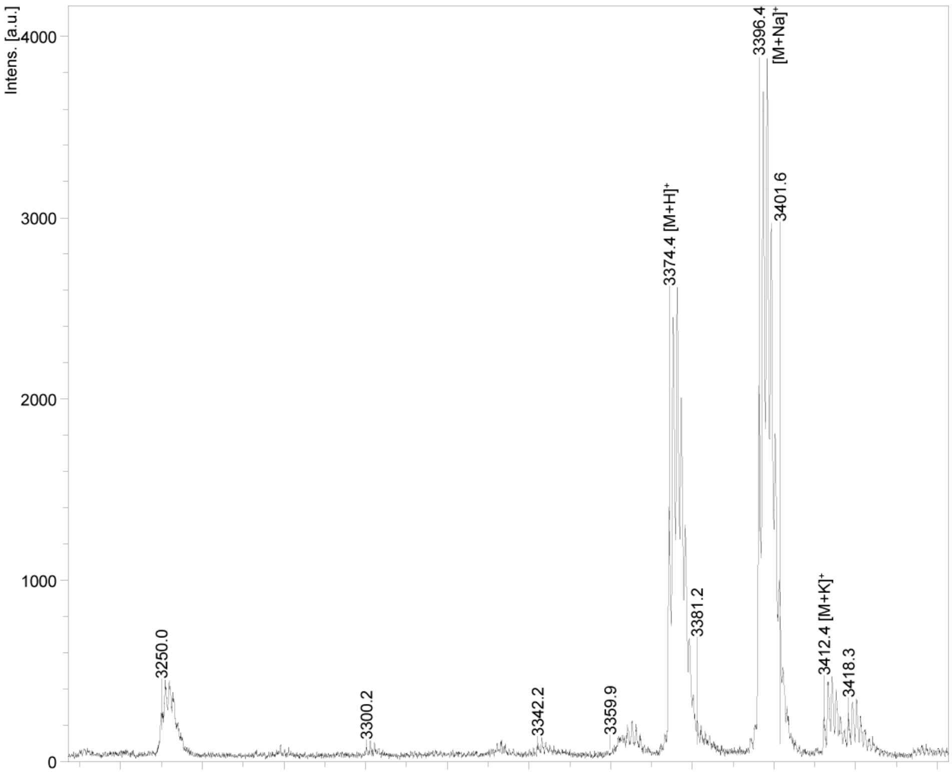

Figure S18. MALDI-MS spectrum of compound **12**.

7.5.4 UV/Vis Melting Curve Experiments

The melting experiments were carried out as described by Metzler-Nolte and coworkers.[1] The oligonucleotide, buffer, and TCEP concentrations are described in Table S1.

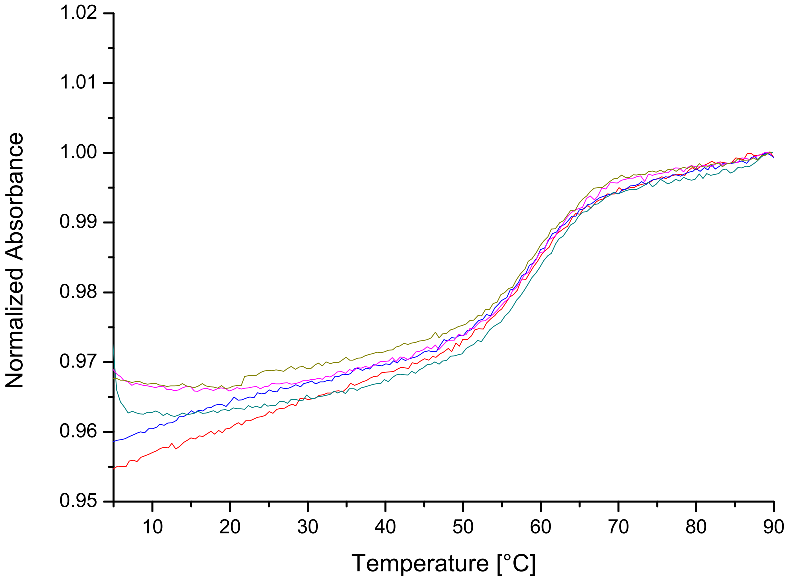

Figure S19. Temperature dependent UV/Vis Absorbance at λ=260 nm of a solution of **4** and **9** under conditions **I** (see Table S1). The individual lines represent different heating or cooling runs.

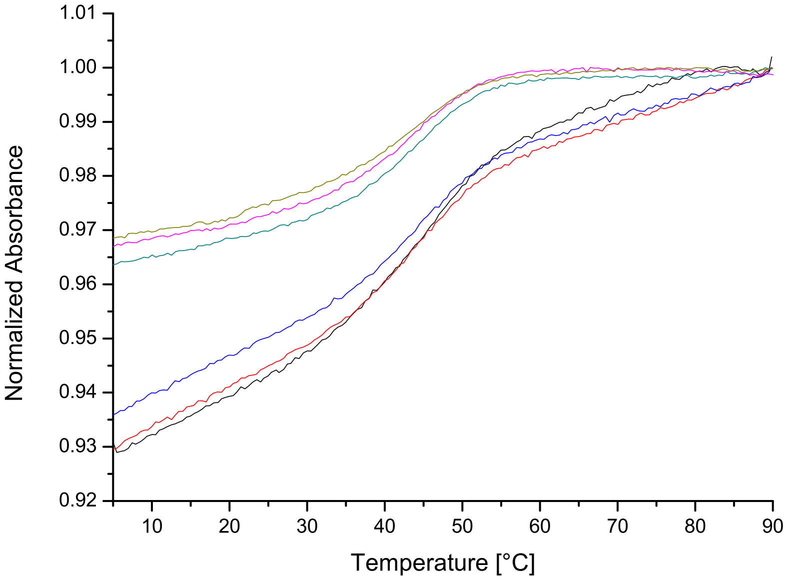

Figure S20. Temperature dependent UV/Vis Absorbance at λ=260 nm of a solution of **8** and **9** under conditions **I** (see Table S1). The individual lines represent different heating or cooling runs.

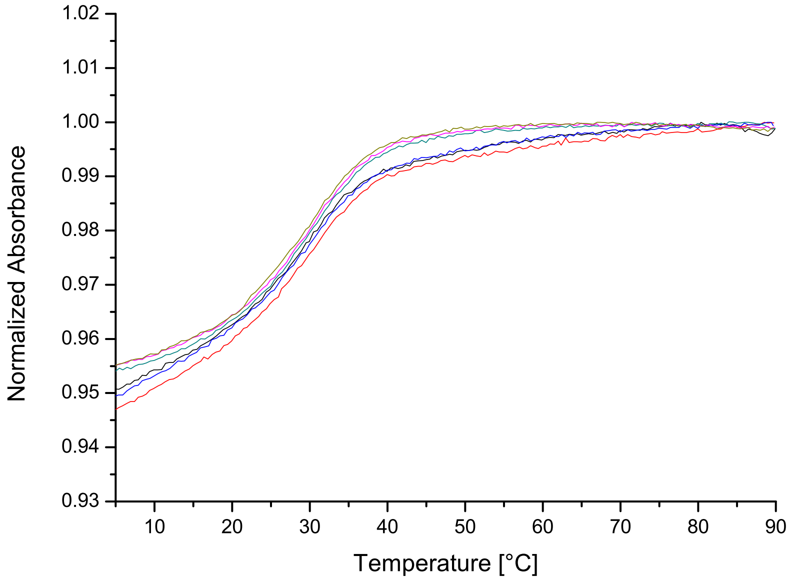

Figure S21. Temperature dependent UV/Vis Absorbance at λ=260 nm of a solution of **8** and **13** under conditions **I** (see Table S1). The individual lines represent different heating or cooling runs.

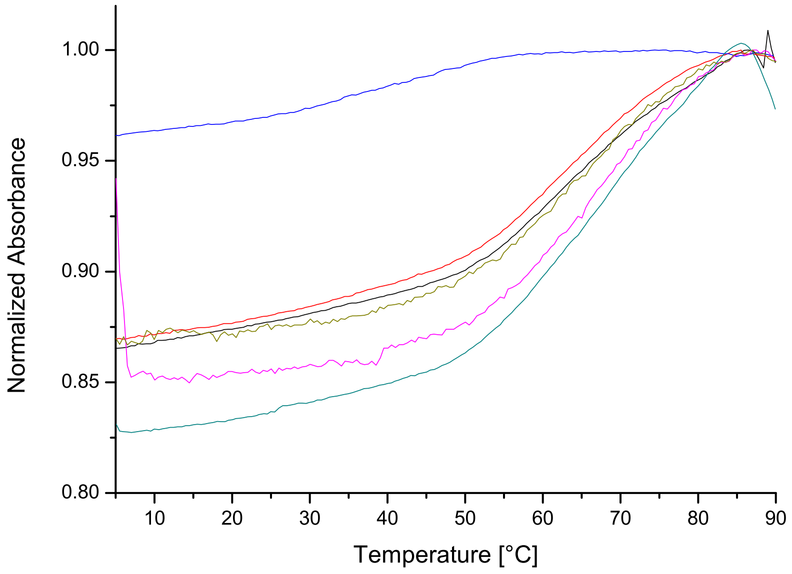

Figure S22. Temperature dependent UV/Vis Absorbance at λ=260 nm of a solution of **4** and **9** under conditions **II** (see Table S1). The individual lines represent different heating or cooling runs.

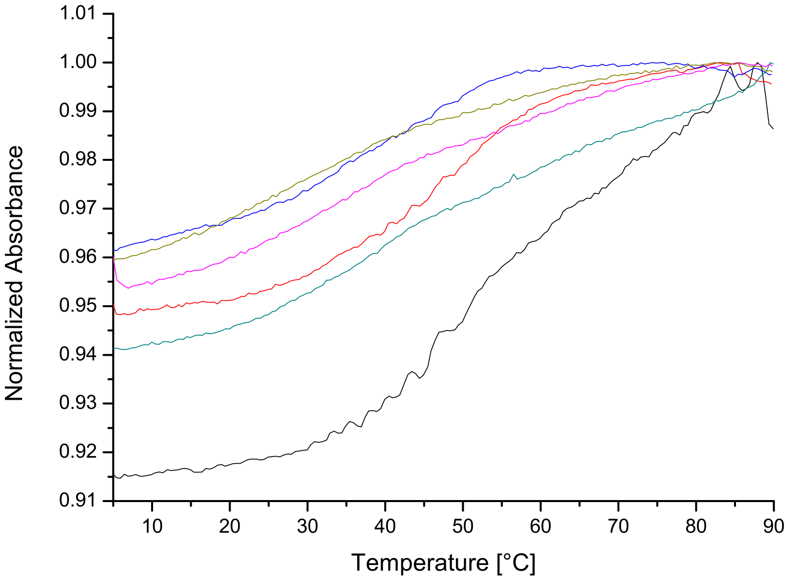

Figure S23. Temperature dependent UV/Vis Absorbance at λ=260 nm of a solution of **8** and **9** under conditions II (see Table S1). The individual lines represent different heating or cooling runs.

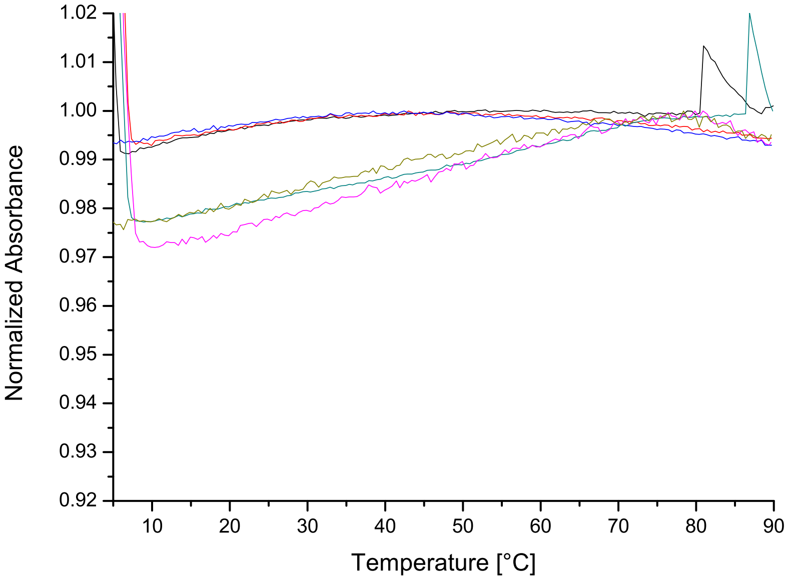

Figure S24. Temperature dependent UV/Vis Absorbance at λ=260 nm of a solution of **8** and **13** under conditions II (see Table S1). The individual lines represent different heating or cooling runs.

Table S1. Melting temperatures (Tm) of oligonucleotide hybrids as obtained by UV/Vis experiments between 5 °C and 90 °C. At least 5 runs were averaged.

Sequence a	Sequence a'	Conditions[a]	T_m [° C]
4	**9**	I	60
4	**13**	I	45
8	**13**	I	31
4	**9**	II	66
4	**13**	II	42
8	**13**	II	Not observed

[a] I: 0.1 M PBS buffer, 1 mM TCEP, 1 µM of each oligonucleotide; II: 1 µM of each oligonucleotide.

7.5.5 UV/Vis Stability Experiments

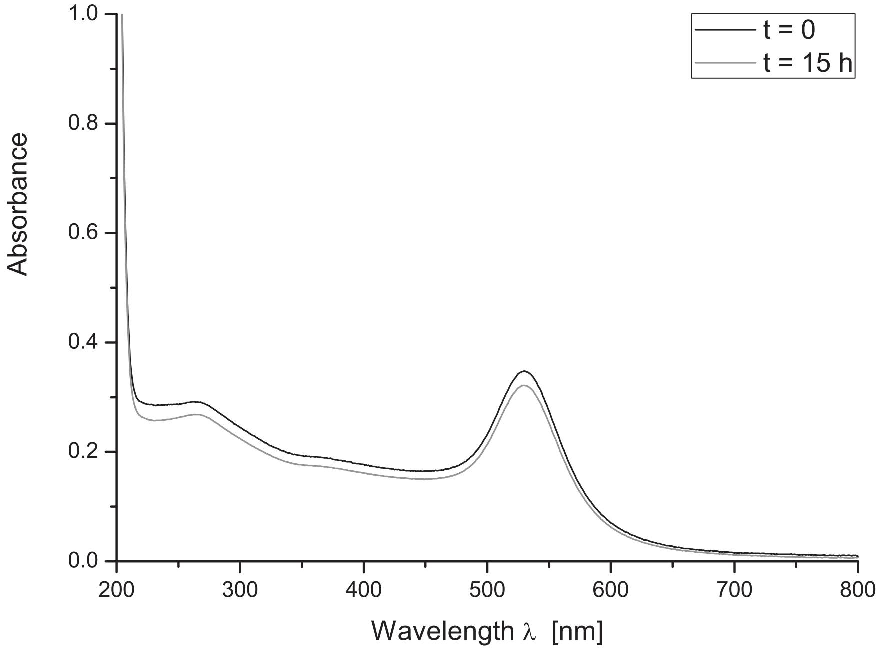

Figure S25. AuNP-4 in 100 mM phosphate buffer (pH=7.4).

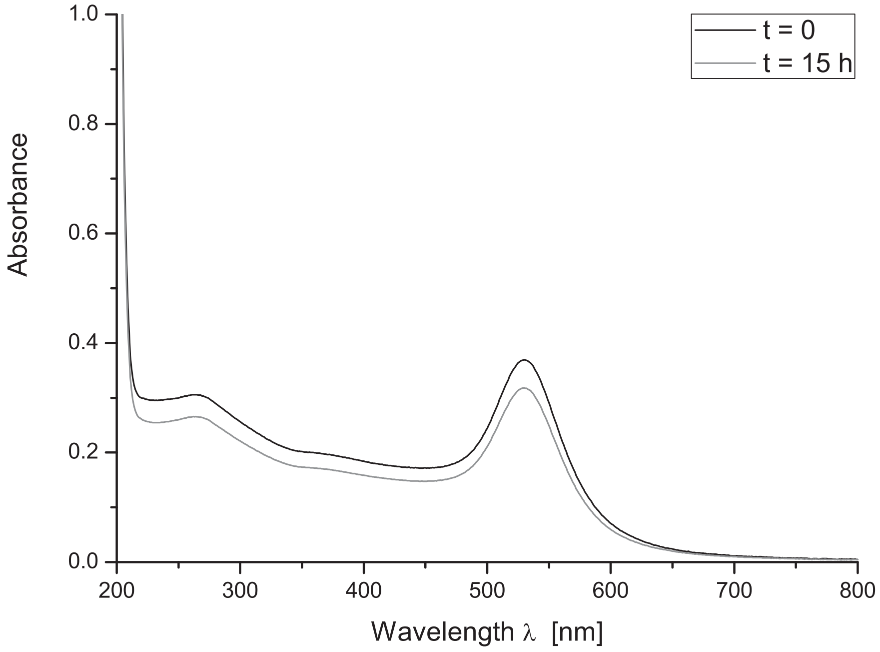

Figure S26. AuNP-5 in 100 mM phosphate buffer (pH=7.4).

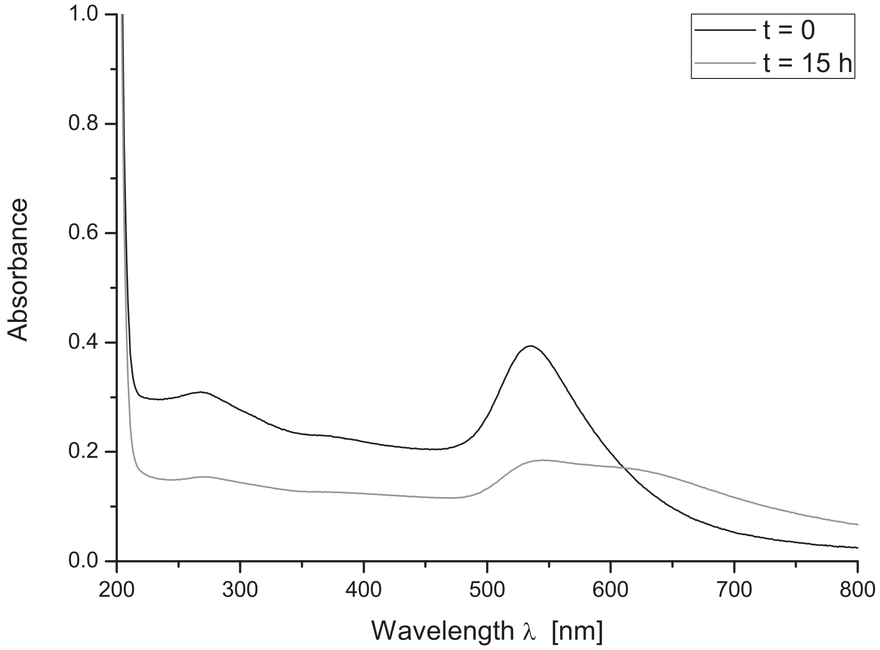

Figure S27. AuNP-6 in 100 mM phosphate buffer (pH=7.4).

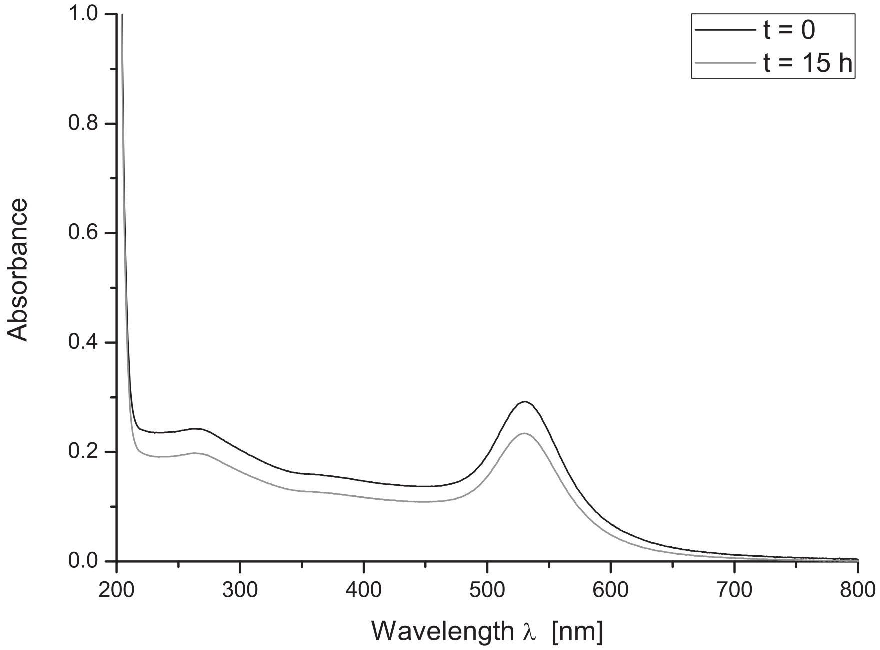

Figure S28. AuNP-7 in 100 mM phosphate buffer (pH=7.4).

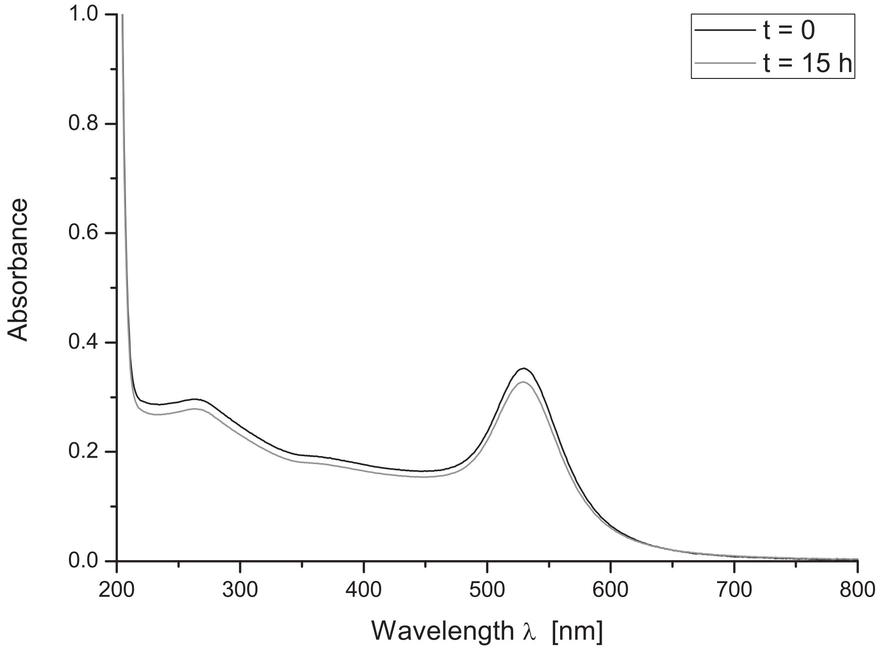

Figure S29. AuNP-8 in 100 mM phosphate buffer (pH=7.4).

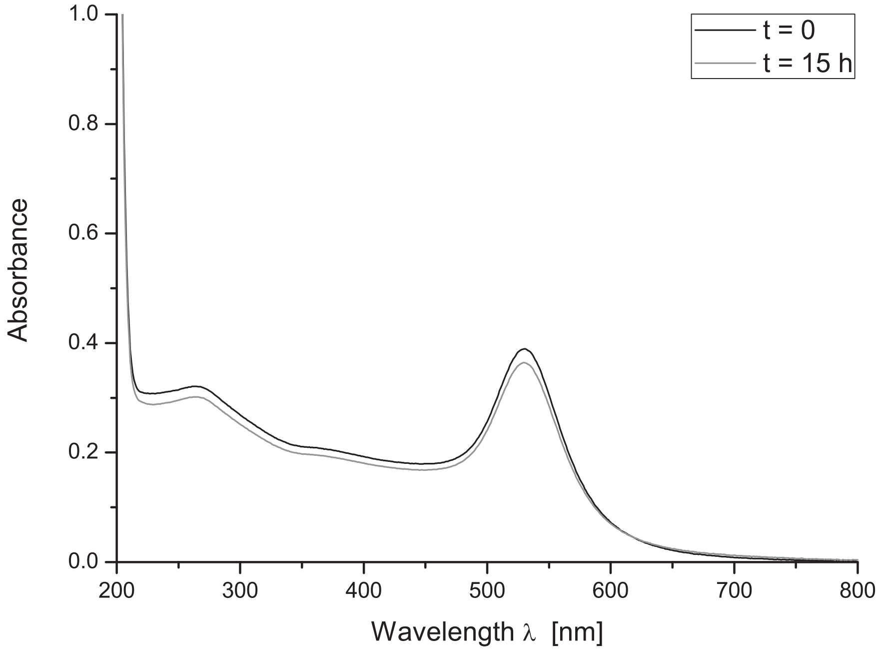

Figure S30. AuNPs synthesized following the general procedure, but without addition of oligonucleotide, in 100 mM phosphate buffer (pH=7.4).

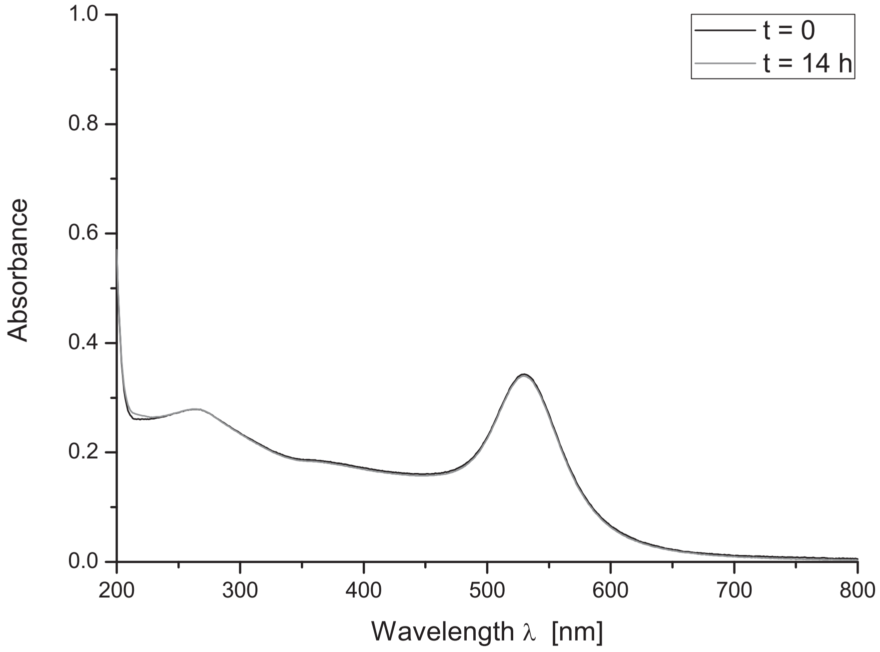

Figure S31. AuNP-4 in 10 mM phosphate buffer (pH=7.4).

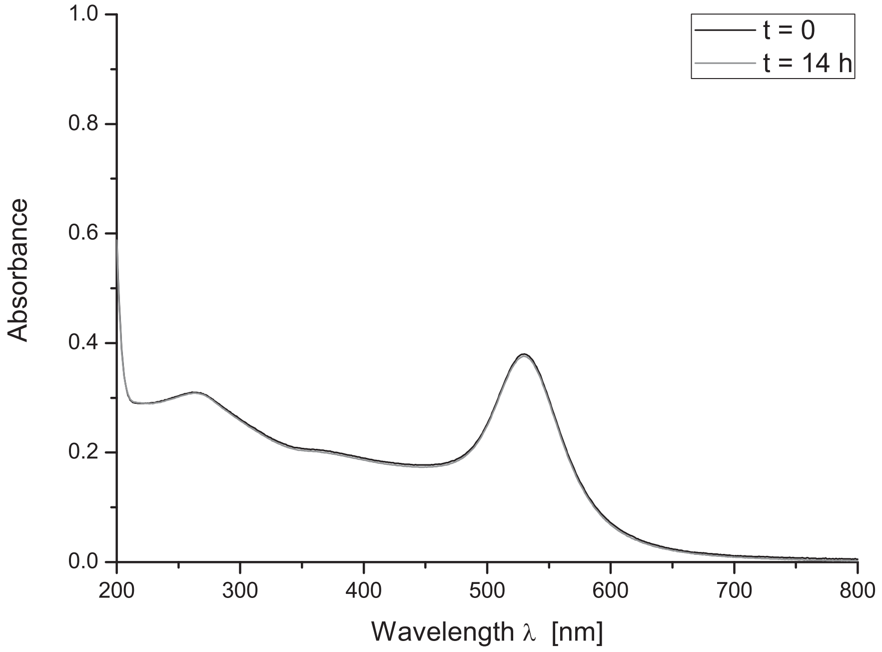

Figure S32. AuNP-5 in 10 mM phosphate buffer (pH=7.4).

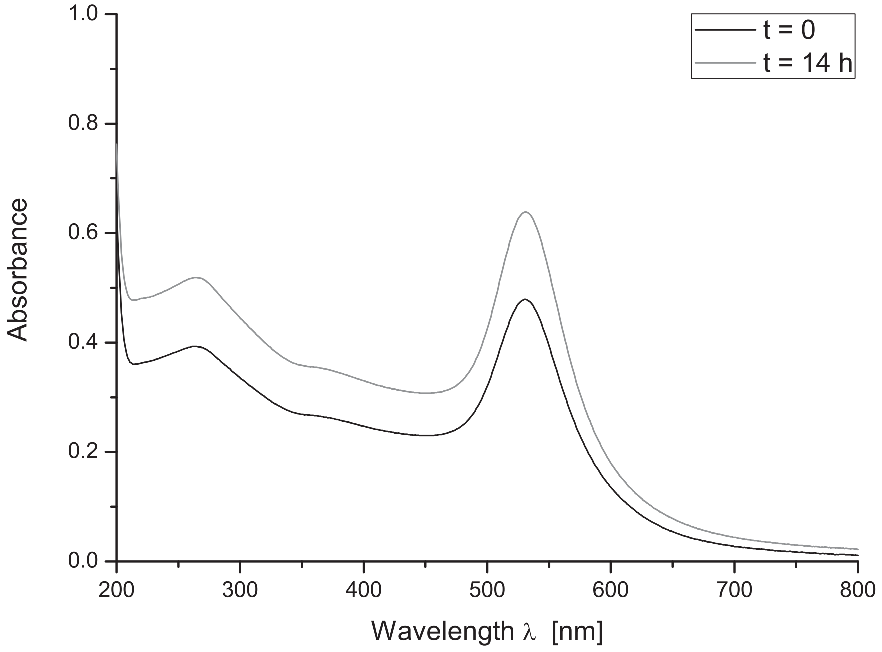

Figure S33. AuNP-6 in 10 mM phosphate buffer (pH=7.4).

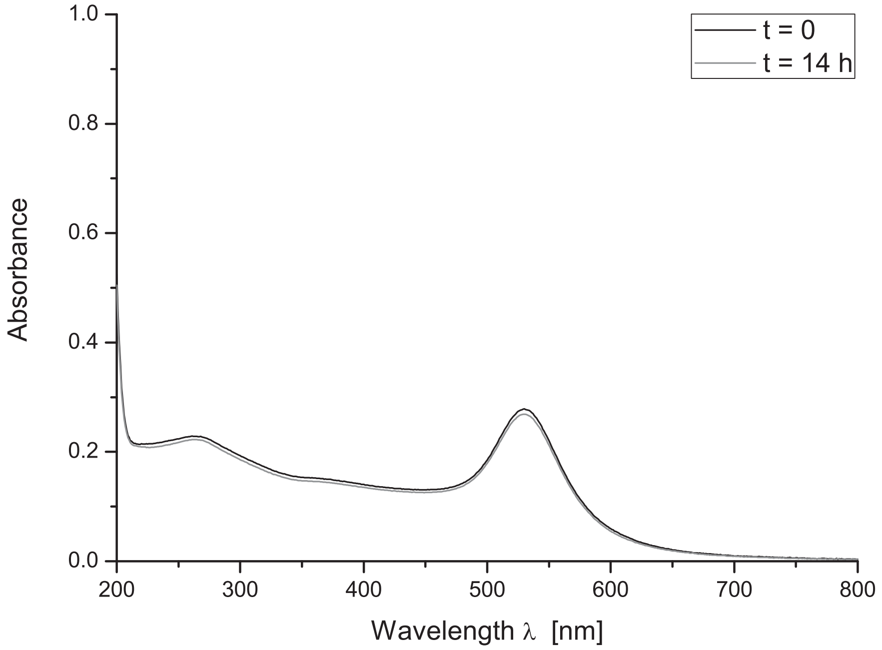

Figure S34. AuNP-7 in 10 mM phosphate buffer (pH=7.4).

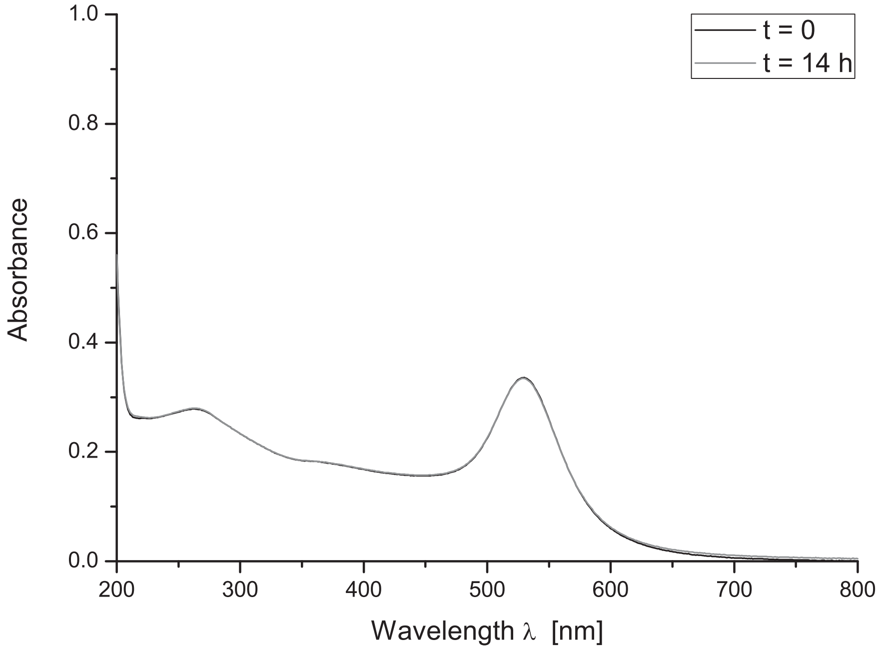

Figure S35. AuNP-8 in 10 mM phosphate buffer (pH=7.4).

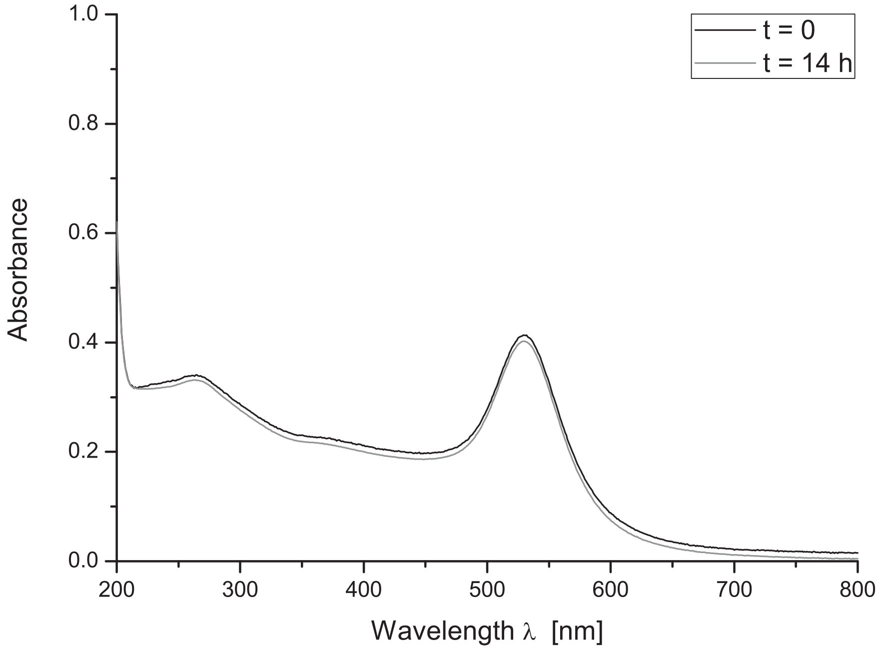

Figure S36. AuNPs synthesized following the general procedure, but without addition of oligonucleotide, in 10 mM phosphate buffer (pH=7.4).

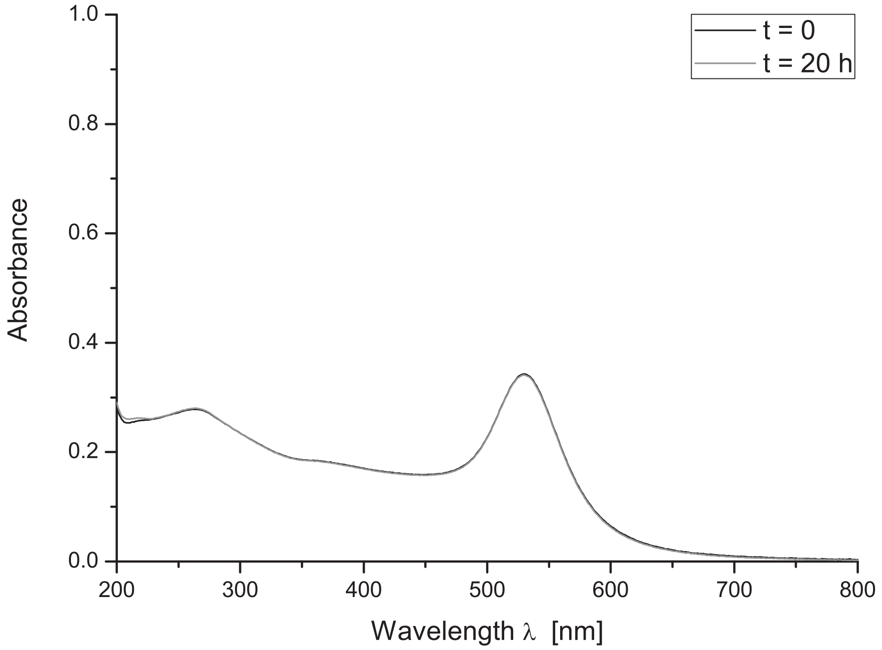

Figure S37. AuNP-4 in 1 mM phosphate buffer (pH=7.4).

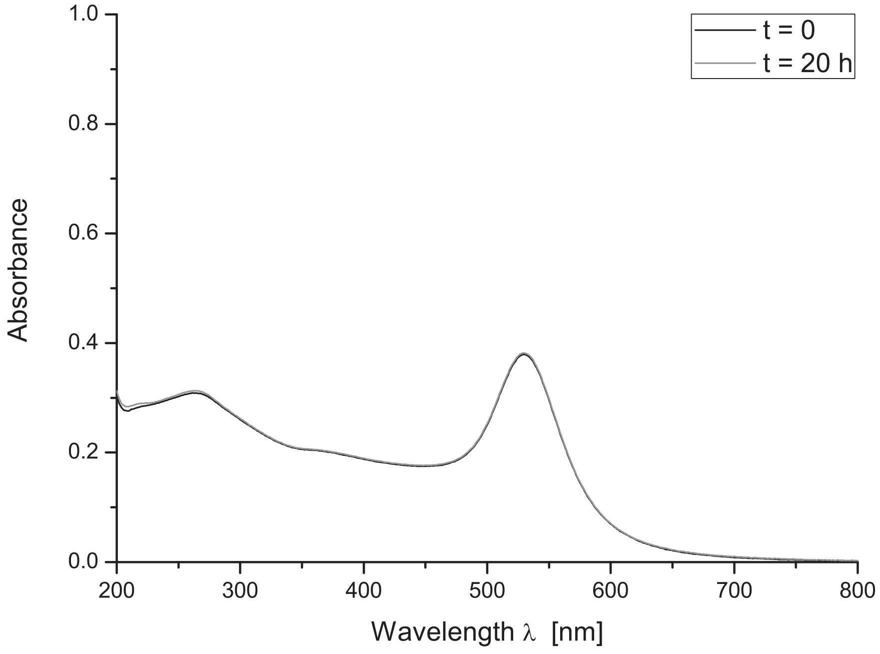

Figure S38. AuNP-5 in 1 mM phosphate buffer (pH=7.4).

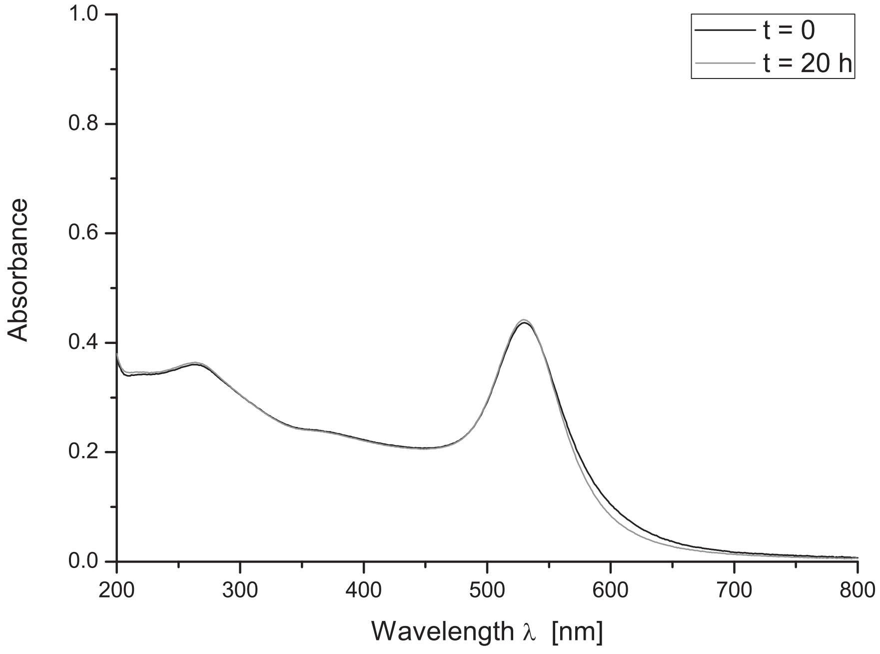

Figure S39. AuNP-6 in 1 mM phosphate buffer (pH=7.4).

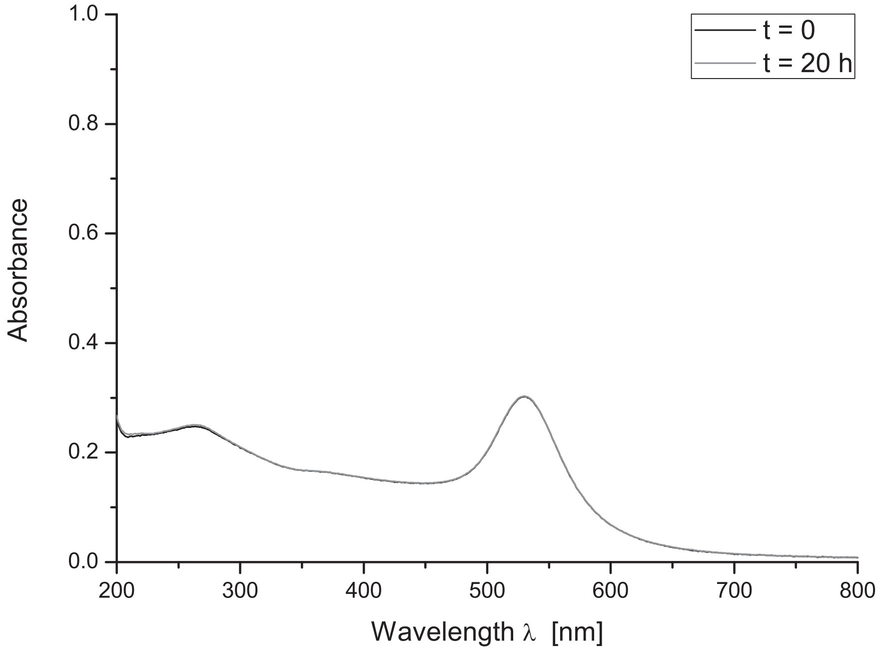

Figure S40. AuNP-7 in 1 mM phosphate buffer (pH=7.4).

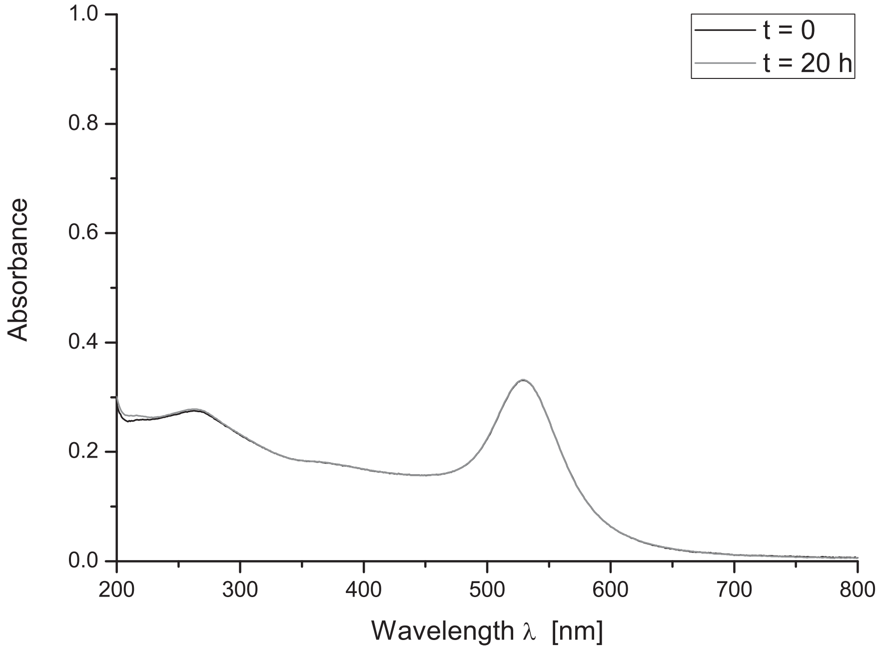

Figure S41. AuNP-8 in 1 mM phosphate buffer (pH=7.4).

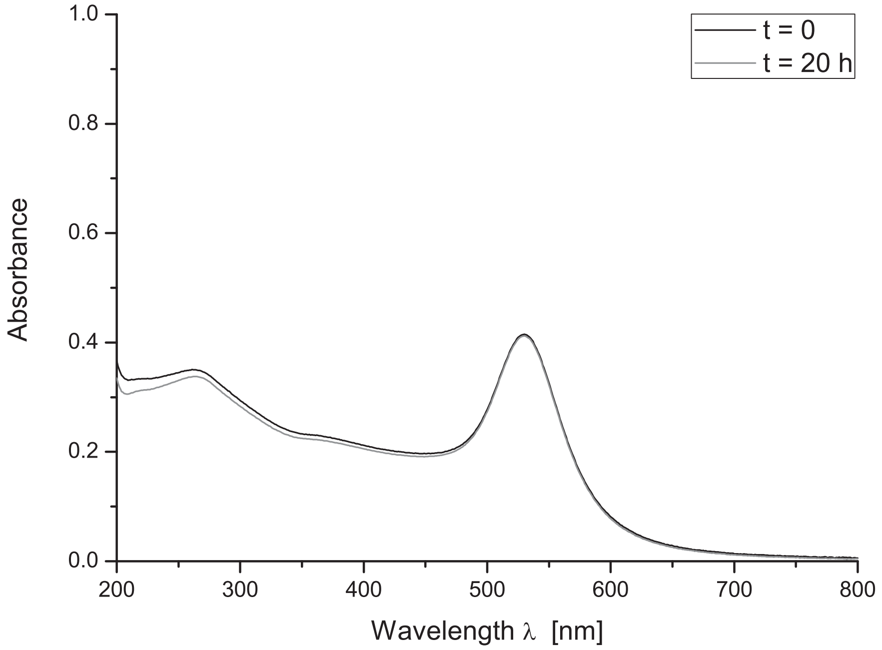

Figure S42. AuNPs synthesized following the general procedure, but without addition of oligonucleotide, in 1 mM phosphate buffer (pH=7.4).

7.5.6 Scanning Electron Microscopy (SEM) Imaging

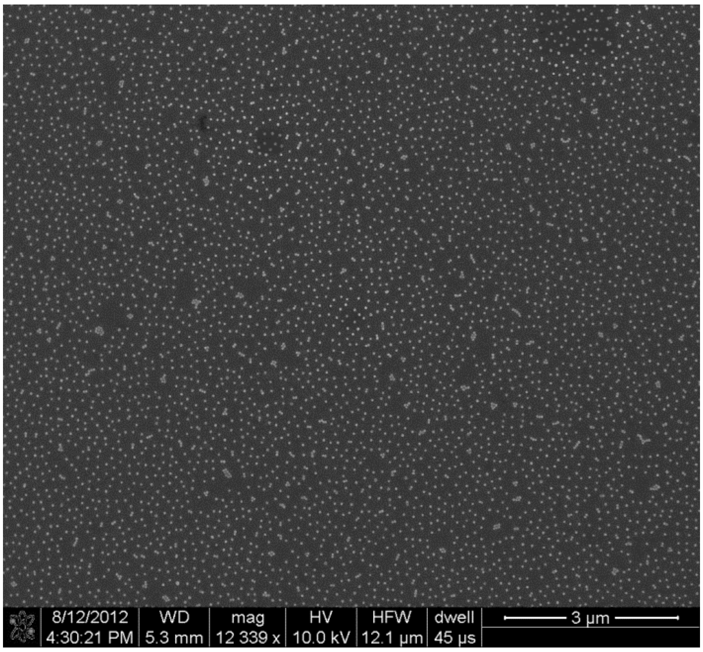

Figure S43. SEM image of surface modified with complementary PNA **7** after incubation with AuNPs **AuNP-4**.

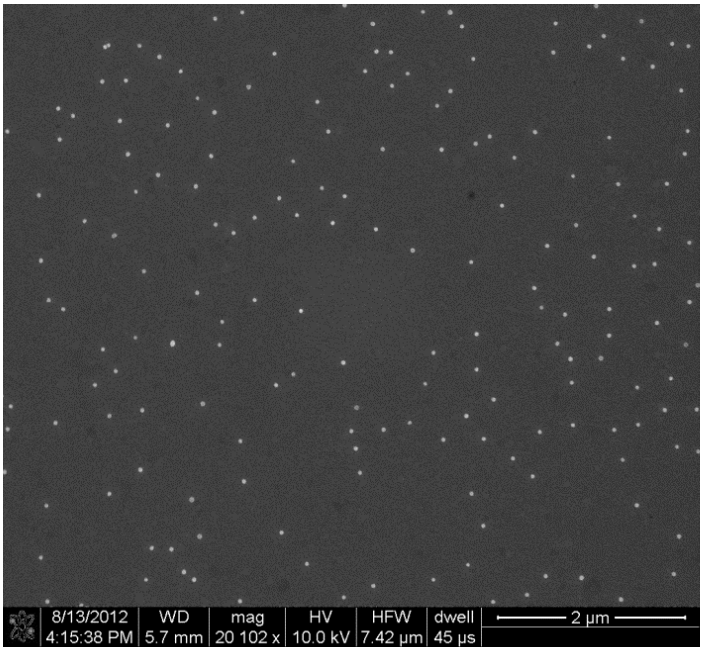

Figure S44. SEM image of surface modified with non-complementary PNA**12** after incubation with AuNPs **AuNP-4**.

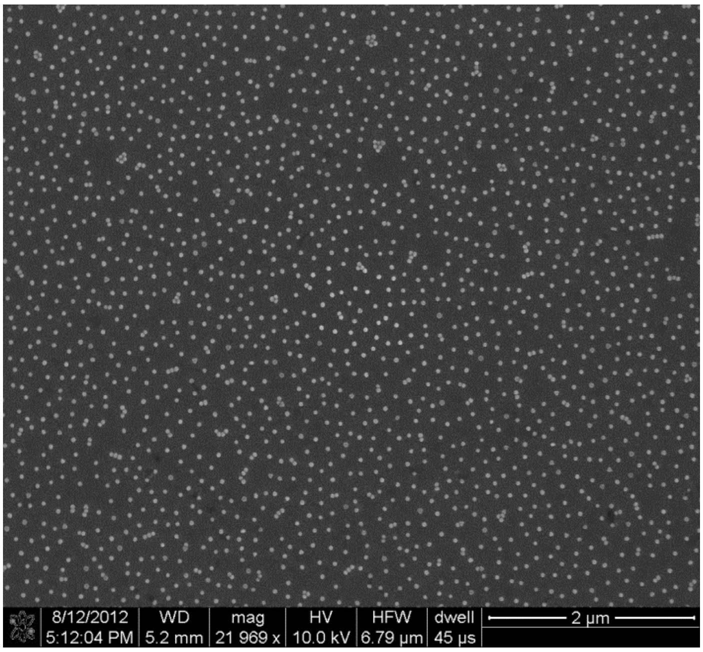

Figure S45. SEM image of surface modified with complementary PNA **7** after incubation with AuNPs **AuNP-5**.

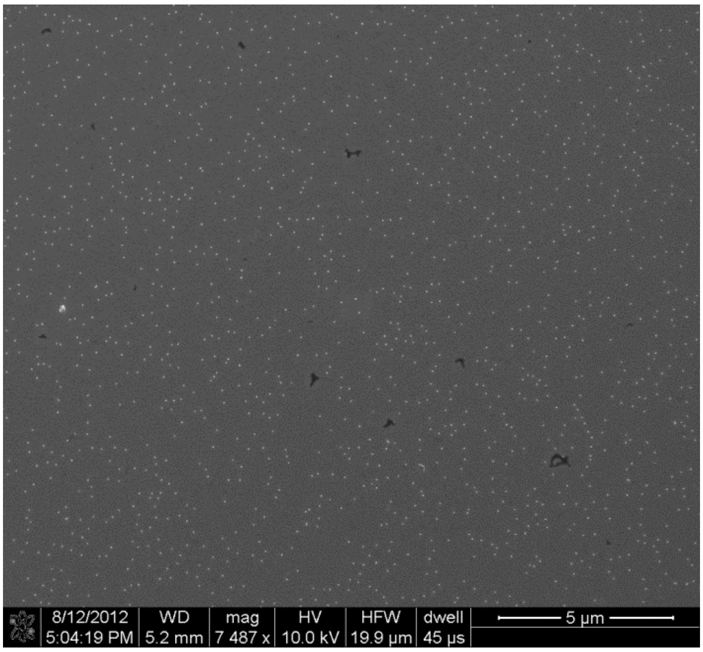

Figure S46. SEM image of surface modified with non-complementary PNA**12** after incubation with AuNPs **AuNP-5**.

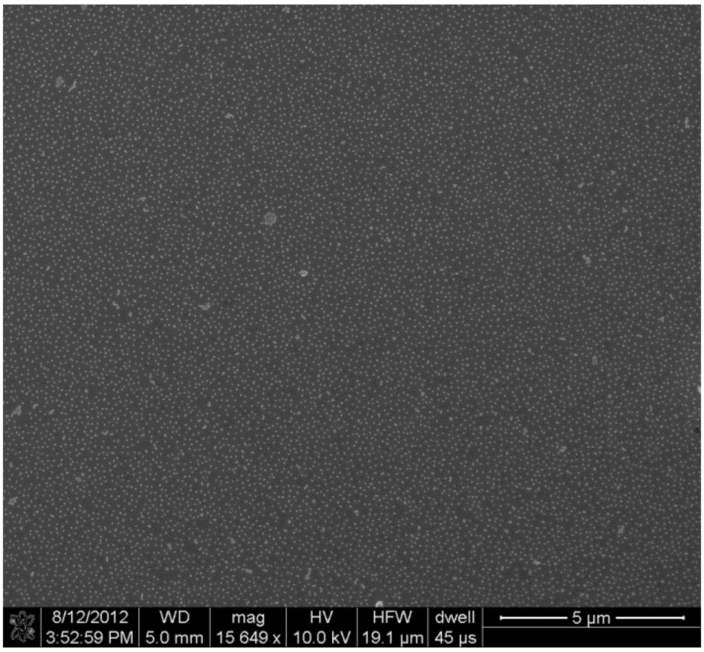

Figure S47. SEM image of surface modified with complementary PNA **7** after incubation with AuNPs **AuNP-6**.

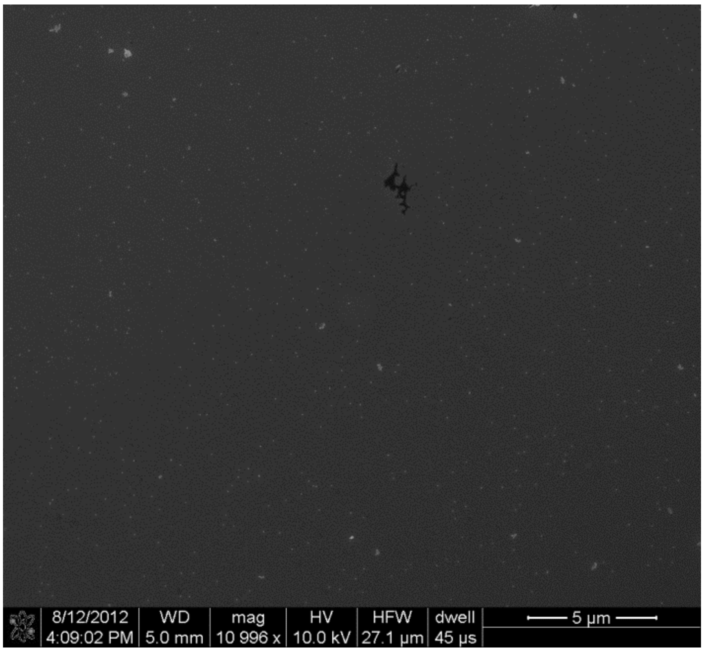

Figure S48. SEM image of surface modified with non-complementary PNA**12** after incubation with AuNPs **AuNP-6**.

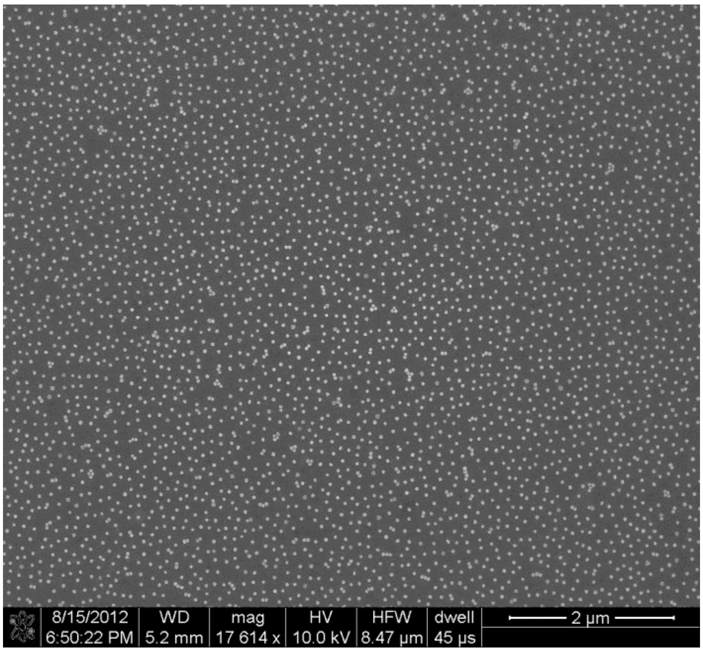

Figure S49. SEM image of surface modified with complementary PNA **7** after incubation with AuNPs **AuNP-7**.

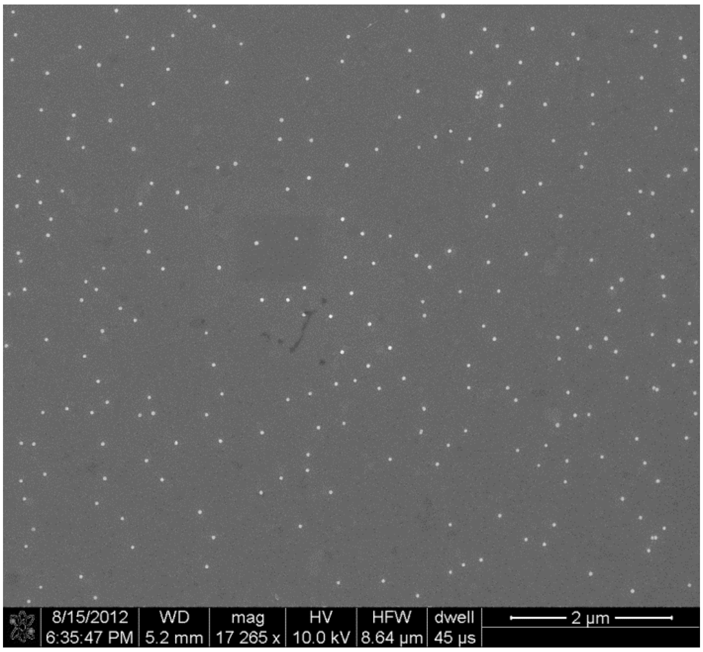

Figure S50. SEM image of surface modified with non-complementary PNA**12** after incubation with AuNPs **AuNP-7**.

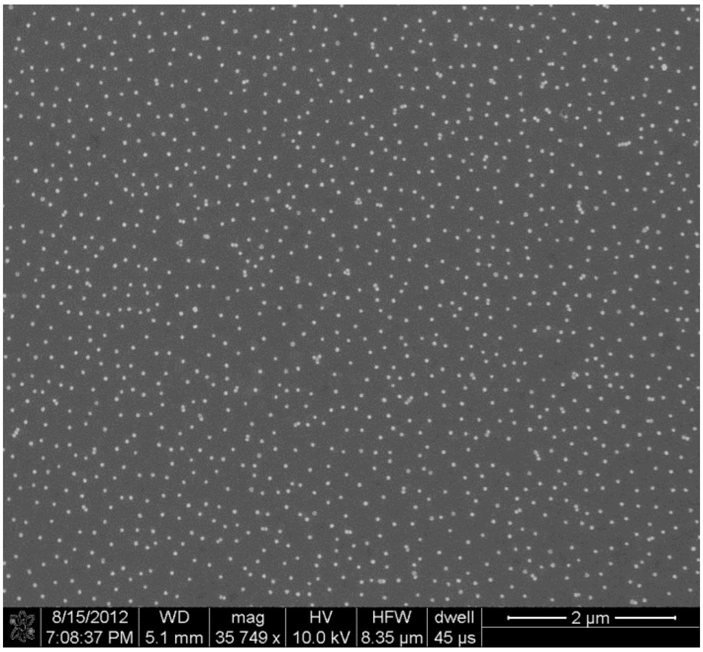

Figure S51. SEM image of surface modified with complementary PNA **7** after incubation with AuNPs **AuNP-8**.

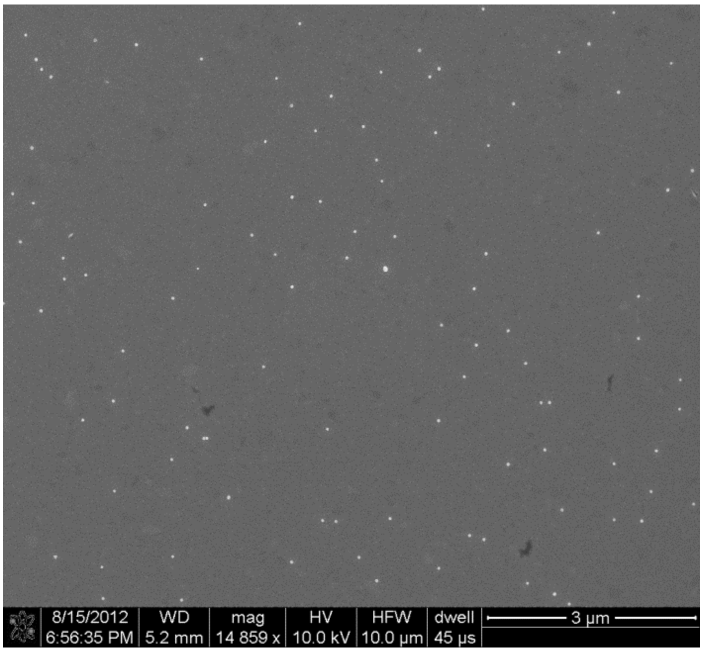

Figure S52. SEM image of surface modified with non-complementary PNA**12** after incubation with AuNPs **AuNP-8**.

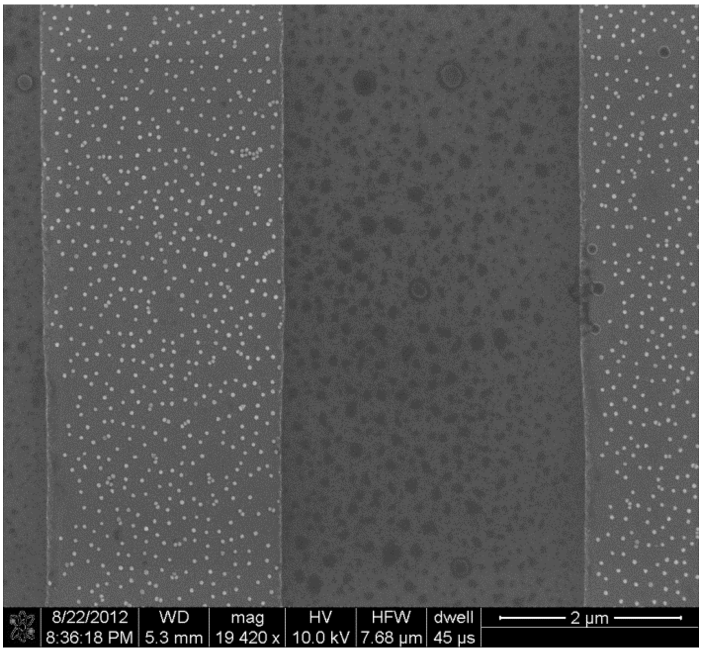

Figure S53. SEM image of micropatterned surface with complementary PNA **7** and fluoroalkyl-modified silica after incubation with AuNPs **AuNP-6**.

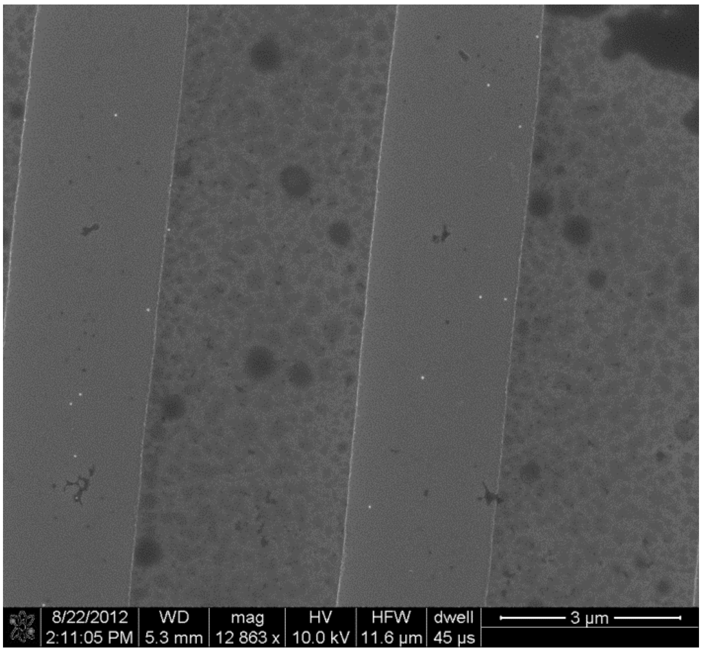

Figure S54. SEM image of micropatterned surface with non-complementary PNA **12** and fluoroalkyl-modified silica after incubation with AuNPs **AuNP-6**.

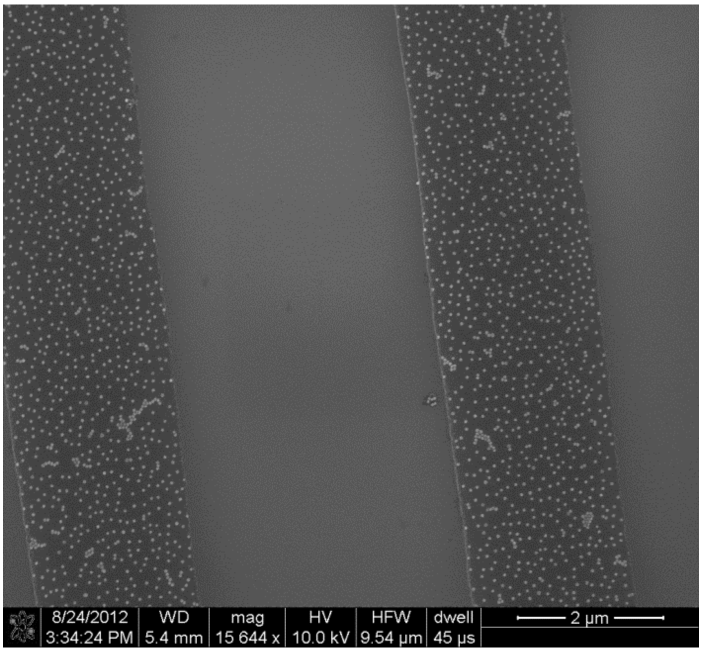

Figure S55. SEM image of micropatterned surface with complementary PNA **7** and PEG-modified silica after incubation with AuNPs **AuNP-6**.

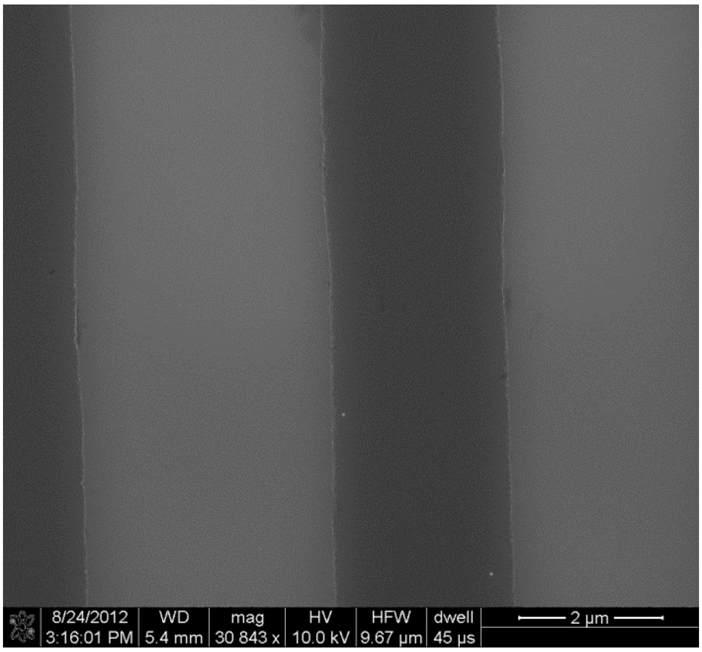

Figure S56. SEM image of micropatterned surface with non-complementary PNA **12** and PEG-modified silica after incubation with AuNPs **AuNP-6**.

7.6 References and Notes

[1] J. I. Cutler, E. Auyeung, C. A. Mirkin, *J. Am. Chem. Soc.* **2012**, *134*, 1376–1391.

[2] N. L. Rosi, D. A. Giljohann, C. S. Thaxton, A. K. R. Lytton-Jean, M. S. Han, C. A. Mirkin, *Science* **2006**, *312*, 1027–1030.

[3] a) J. D. Le, Y. Pinto, N. C. Seeman, K. Musier-Forsyth, T. A. Taton, R. A. Kiehl, *Nano Lett.* **2004**, *4*, 2343–2347; b) S. J. Tan, M. J. Campolongo, D. Luo, W. Cheng, *Nat. Nanotechnol.* **2011**, *6*, 268–276; c) S. J. Barrow, A. M. Funston, D. E. Gómez, T. J. Davis, P. Mulvaney, *Nano Lett.* **2011**, *11*, 4180–4187; d) Y. Zheng, C. H. Lalander, T. Thai, S. Dhuey, S. Cabrini, U. Bach, *Angew. Chem. Int. Ed.* **2011**, *50*, 4398–4402; e) J. Zheng, P. E. Constantinou, C. Micheel, A. P. Alivisatos, R. A. Kiehl, N. C. Seeman, *Nano Lett.* **2006**, *6*, 1502–1504; f) J. Zhang, Y. Liu, Y. Ke, H. Yan, *Nano Lett.* **2006**, *6*, 248–251.

[4] C. A. Mirkin, R. L. Letsinger, R. C. Mucic, J. J. Storhoff, *Nature* **1996**, *382*, 607–609.

[5] R. Elghanian, J. J. Storhoff, R. C. Mucic, R. L. Letsinger, C. A. Mirkin, *Science* **1997**, *277*, 1078–1081.

[6] J. Liu, Y. Lu, *J. Am. Chem. Soc.* **2003**, *125*, 6642–6643.

[7] B. M. Reinhard, S. Sheikholeslami, A. Mastroianni, A. P. Alivisatos, J. Liphardt, *Proc. Natl. Acad. Sci. USA* **2007**, *104*, 2667–2672.

[8] C. Sönnichsen, B. M. Reinhard, J. Liphardt, A. P. Alivisatos, *Nat. Biotechnol.* **2005**, *23*, 741–745.

[9] a) Y. Cao, R. Jin, C. A. Mirkin, *J. Am. Chem. Soc.* **2001**, *123*, 7961–7962; b) S. Liu, Z. Zhang, M. Han, *Anal. Chem.* **2005**, *77*, 2595–2600.

[10] M. Krishnan, N. Mojarad, P. Kukura, V. Sandoghdar, *Nature* **2010**, *467*, 692–695.

[11] N. Mojarad, M. Krishnan, *Nat. Nanotechnol.* **2012**, *7*, 448–452.

[12] P. E. Nielsen, M. Egholm, R. H. Berg, O. Buchardt, *Science* **1991**, *254*, 1497–1500.

[13] S. Tomac, M. Sarkar, T. Ratilainen, P. Wittung, P. E. Nielsen, B. Nordén, A. Gräslund, *J. Am. Chem. Soc.* **1996**, *118*, 5544–5552.

[14] R. Chakrabarti, A. M. Klibanov, *J. Am. Chem. Soc.* **2003**, *125*, 12531–12540.

[15] J. Duy, L. Connell, W. Eck, S. Collins, R. Smith, *J. Nanopart. Res.* **2010**, *12*, 2363–2369.

[16] A. Gourishankar, S. Shukla, K. N. Ganesh, M. Sastry, *J. Am. Chem. Soc.* **2004**, *126*, 13186–13187.

[17] R. Kanjanawarut, X. Su, *Anal. Chem.* **2009**, *81*, 6122–6129.

[18] T. R. Tshikhudo, Z. Wang, M. Brust, *Mater. Sci. Technol.* **2004**, *20*, 980–984.

[19] Y. Zheng, C. H. Lalander, U. Bach, *Chem. Commun.* **2010**, *46*, 7963–7965.

[20] Z. Li, R. Jin, C. A. Mirkin, R. L. Letsinger, *Nucleic Acids Res.* **2002**, *30*, 1558–1562.

[21] T. Sakata, S. Maruyama, A. Ueda, H. Otsuka, Y. Miyahara, *Langmuir* **2007**, *23*, 2269–2272.

[22] T. Axenrod, K. K. Das, H. Yazdekhasti, P. R. Dave, A. G. Stern, *Org. Prep. Proced. Int.* **1997**, *29*, 358–361.

[23] N. Hüsken, G. Gasser, S. D. Köster, N. Metzler-Nolte, *Bioconjugate Chem.* **2009**, *20*, 1578–1586.

[24] T. Stakenborg, S. Peeters, G. Reekmans, W. Laureyn, H. Jans, G. Borghs, H. Imberechts, *J. Nanopart. Res.* **2008**, *10*, 143–152.

[25] M. R. Jones, R. J. Macfarlane, A. E. Prigodich, P. C. Patel, C. A. Mirkin, *J. Am. Chem. Soc.* **2011**, *133*, 18865–18869.

[26] B. T. Houseman, M. Mrksich, *J. Org. Chem.* **1998**, *63*, 7552–7555.

[27] S.-J. Park, A. A. Lazarides, J. J. Storhoff, L. Pesce, C. A. Mirkin, *J. Phys. Chem. B* **2004**, *108*, 12375–12380.

[28] A. M. Sosniak, G. Gasser, N. Metzler-Nolte, *Org. Biomol. Chem.* **2009**, *7*, 4992–5000.

[29] a) It should be noted that in this procedure, Tween 20 was only present during the deposition of the thiols to the AuNPs. During this time, it provided additional stabilization. Afterwards, it was not needed anymore and was removed. This is in contrast to the particles described in Ref. [15]; b) K. Aslan, V. H. Pérez-Luna, *Langmuir* **2002**, *18*, 6059–6065.

[30] C. H. Lalander, Y. Zheng, S. Dhuey, S. Cabrini, U. Bach, *ACS Nano* **2010**, *4*, 6153–6161.

8 Outlook

The possibilities which PNA modified AuNPs open up in nanotechnology are exciting. For example, PNA-modified gold nanoparticles could be coupled to other PNA-modified nanoscopic objects, allowing for especially short inter-particle distances or higher binding affinities, compared to DNA-modified gold nanoparticles. To this end, we have prepared PNAs with diamine linkers for attachment to quantum dots (Figure 1). Our collaborative partners, Dr. Alison Funston and co-workers at Monash University (Australia) are currently investigating the potential of these new PNA derivatives.

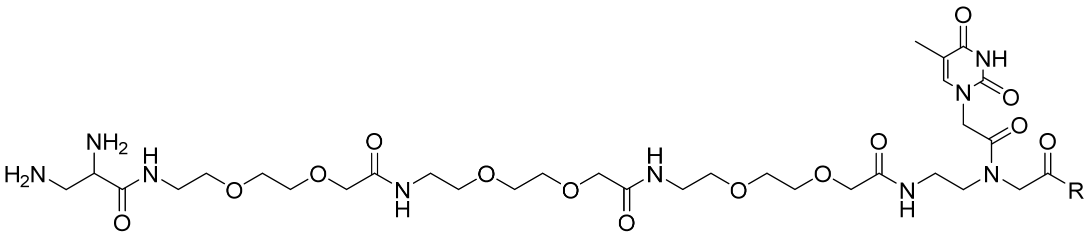

Figure 1. PNA with diamine linker. Only the base adjacent to the linker (thymine) is shown, the remaining sequence is abbreviated as R.

Additionally, further improvements of the of the PNA-modified gold nanoparticles would certainly be of interest: Due to the negative charges of the stabilizing layer which we reported (see chapter 7),[1] one of the advantages which PNA has on its own, the charge neutrality, has been lost. Consequently, there is electrostatic repulsion between the particles. Indeed, binding between gold nanoparticles functionalized with complementary PNA-sequences could not be achieved in solution. Such short-distance particle-assemblies would be appealing for the study of plasmonic phenomena.[2] Several approaches to overcome this difficulty can be envisaged (Figure 2). If trithiol linked PNAs are employed, the previously described stable PNA-functionalized nanoparticles could be subjected to an excess of a thiol reagent such as dithiothreitol (DTT; Figure 2 a). It has been shown that DTT can effectively replace monothiol substituents on gold nanoparticles, while replacing dithiol substituents only slowly, and trithiol almost not at all.[3] Consequently, the stabilizing surfactant would be desorbed from the gold surface, while the PNA would stay on the particles. Potentially, the presence of additional trithiol-linked PNAs in the solution could fill the so formed “holes” in the layer around the particles. Under the right experimental conditions, it seems possible that the PNAs stay bound to the particle only over the thiol linkage and do not adsorb *via* the bases onto the particle surface, which would lead to aggregation of the nanoparticles. Alternatively, mixing of charged and uncharged reagents could take place during the initial functionalization of the gold nanoparticles (Figure 2 b). Two surfactants, one with charges and one without, could be mixed, instead of only using a charged surfactant. The next step would again be the addition of PNAs. Also particles with a mixture of neutral PNA and charged DNA are imaginable, in which case DNA would serve as a stabilizing agent and contribute to the sequence specific binding strength.

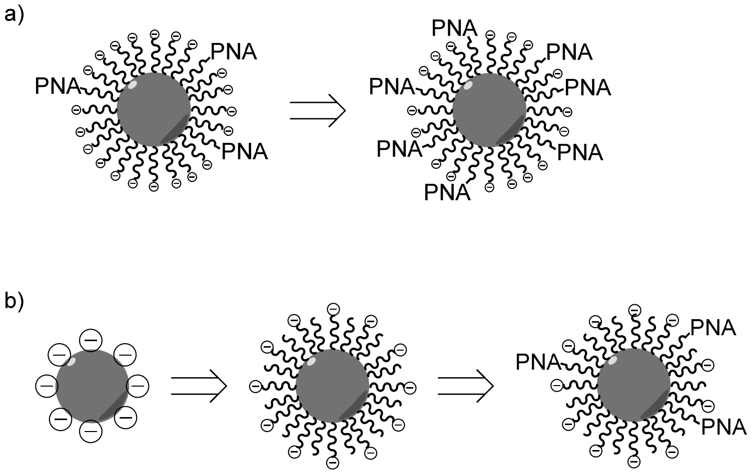

Figure 2. Possible pathways leading to stable PNA-substituted gold nanoparticles; a) starting from particles as described in chapter 7 with trithiol linked PNA, addition of a replacing agent such as DTT in large excess and PNA could replace part of the stabilizing surfactant with additional PNA strands; b) in the synthesis as described in chapter 7, the surfactant is substituted by a surfactant mixture, made up of charged and neutral molecules; the second step would be identical to the original procedure, adding again PNA.

8.1 References and Notes

[1] P. Anstaett, Y. Zheng, T. Thai, A. M. Funston, U. Bach, G. Gasser, *Angew. Chem. Int. Ed.* **2013**, *52*, 4217–4220.

[2] a) J. Zuloaga, E. Prodan, P. Nordlander, *Nano Lett.* **2009**, *9*, 887–891; b) S. J. Barrow, X. Wei, J. S. Baldauf, A. M. Funston, P. Mulvaney, *Nat. Commun.* **2012**, *3*, 1275;

[3] a) Z. Li, R. Jin, C. A. Mirkin, R. L. Letsinger, *Nucleic Acids Res.* **2002**, *30*, 1558–1562; b) B. C. Mei, E. Oh, K. Susumu, D. Farrell, T. J. Mountziaris, H. Mattoussi, *Langmuir* **2009**, *25*, 10604–10611;

Curriculum Vitae Philipp Anstätt

Personal Data

Date of birth	04.03.1986
Place of birth	Würzburg, Germany
Nationality	German

Education

04/2011-09/2014	Ph.D. studies in Chemical and Molecular Sciences at University of Zurich • Thesis topic: Photo-Activatable Organic and Organometallic Compounds for Enzyme Inhibition and Targeted Drug Delivery • Research in chemical biology • Supervision of students during their Master thesis • Supervision of lab courses for chemistry students (Bachelor and Master level)
07/2012-09/2012	Visiting Researcher at Monash University, Melbourne, Australia • Research in nanotechnology
07/2010-04/2011	Research and Teaching Assistant at ETH Zurich • Research in computational and chemical catalyst design • Composing and reading of an exercise course in physical organic chemistry
2008-2010	Studies of „Molecular Life Science (M.Sc.)“ at the University of Erlangen-Nuremberg • Master‘s thesis: Syntheses and Aggregation Behavior of Pentacene Amino Acid Hybrids • Supervision of lab courses for chemistry (Bachelor) and medicine students
2005-2008	Studies of „Molecular Science (B.Sc.)“ at the University of Erlangen-Nuremberg • Bachelor‘s thesis: Development of a New Synthetic Strategy for β2-Adrenergic Receptor Ligands
1996-2005	Wernher-von-Braun-Gymnasium Friedberg, Germany (high school)
2002-2003	Exchange year at the St. Charles High School (St. Charles, MN, USA)
1992-1996	Volksschule Stätzling-Derching, Germany (elementary school)

Publications

1. A. Leonidova,[§] **P. Anstaett**,[§] V. Pierroz, B. Spingler, S. Ferrari, G. Gasser, Induction of Cytotoxicity Through Photo-release of Aminoferrocene, **2014**, submitted ([§] these authors contributed equally).
2. **P. Anstaett**, G. Gasser, Two-Photon Uncageable Enzyme Inhibitors with Additional Targeting: Probes for Chemical Biology, **2014**, submitted.
3. A. Frei, R. Rubbiani, S. Tubafard, O. Blacque, **P. Anstaett**, A. Felgenträger, T. Maisch, L. Spiccia, G. Gasser, Synthesis, Characterization and Biological Evaluation of New Ru(II) Polypyridyl Photosensitizers for Photodynamic Therapy, *J. Med. Chem.* **2014**, accepted.
4. **P. Anstaett**, A. Leonidova, G. Gasser, Caged Phosphate and the Slips and Misses in Determination of Quantum Yields for UV-A induced Photouncaging, *ChemPhysChem* **2014**, DOI: 10.1002/cphc.201402547.
5. **P. Anstaett**, G. Gasser, *Organometallic Complexes as Enzyme Inhibitors: A Conceptual Overview* in *Bioorganometallic Chemistry* (Eds.: G. Jaouen, M. Salmain), John Wiley & Sons Ltd, in press.
6. **P. Anstaett**, G. Gasser, Peptide Nucleic Acids – An Opportunity for Bio-Nanotechnology, *Chimia* **2014**, *68*, 264–268 (invited article for the winner of the best oral presentation award at the SCS Fall Meeting).
7. **P. Anstaett**, Y. Zheng, T. Thai, A. M. Funston, U. Bach, G. Gasser, Synthesis of Stable Peptide Nucleic Acid-Modified Gold Nanoparticles and their Assembly onto Gold Surfaces, *Angew. Chem. Int. Ed.* **2013**, *52*, 4217–4220.
8. **P. Anstaett**, F. Schoenebeck, Reductive Elimination of $ArCF_3$ from Bidentate Pd^{II} Complexes: A Computational Study, *Chem. Eur. J.* **2011**, *17*, 12340–12346.

Awards and Honors

2013	Swiss Chemical Society/Metrohm Award for the Best Oral Presentation in the “Polymers, Colloids & Interfaces” section at the SCS Fall Meeting 2013
2013	Swiss Academy of Sciences/Swiss Chemical Society Travel Award
2013	Graduate School of Chemical and Molecular Sciences Travel Award, sponsored by Bruker BioSpin AG Switzerland
2008-2010	Member of the Leonardo Kolleg (institution at the University of Erlangen-Nuremberg to support the best 5% students)

Conference Attendances

1. Poster Presentation: **P. Anstaett**, G. Gasser, Two-Photon Uncaging as a More Versatile Alternative to Photodynamic Therapy, Fall Meeting of the Swiss Chemical Society **2014**, Zurich, Switzerland.
2. Poster Presentation: **P. Anstaett**, A. Leonidova, G. Gasser, Avoiding Slips in the Determination of Uncaging Quantum Yields of Organic and Organometallic Bio-active Compounds, 12th European Biological Inorganic Chemistry Conference **2014**, Zurich, Switzerland.
3. Poster Presentation: **P. Anstaett**, G. Gasser, One- and Two-Photon Uncaging For Targeted Drug Delivery, XXVth IUPAC Photochemistry Conference **2014**, Bordeaux, France.
4. Oral Presentation: **P. Anstaett**, K. Koziol, P. Hamm, G. Gasser, Two-Photon Induced Uncaging: A Tool for New Questions in Chemical Biology, Annual Retreat of the Graduate School of Chemical and Molecular Sciences **2014**, Randa, Switzerland.
5. Oral Presentation: **P. Anstaett**, Y. Zheng, T. Thai, A. M. Funston, U. Bach, G. Gasser, PNA-modified Nanoparticles: The Next Step in Self-Assembly**,** 12th International Symposium on Applied Bioinorganic Chemistry (ISABC12) **2013**,Guangzhou, China.
6. Oral Presentation: **P. Anstaett**, K. Koziol, P. Hamm, G. Gasser, Novel Cages for Two-Photon Induced Uncaging: Tools for Chemical Biology and Beyond, 5th International Meeting of the European Platform for Photodynamic Medicine (EPPM) **2013**, Ustron, Poland.
7. Oral Presentation: **P. Anstaett**, Y. Zheng, T. Thai, A. M. Funston, U. Bach, G. Gasser, Peptide Nucleic Acid Modified Gold Nanoparticles and their Assembly on Surfaces, Fall Meeting of the Swiss Chemical Society **2013**, Lausanne, Switzerland.
8. Poster Presentation: **P. Anstaett**, R. R. Tykwinski, Pentacene-Amino Acid Hybrids as Precursors for Supramolecularly Assembled Semiconductors, FUNMOLS (Fundamentals of Molecular Electronic Assemblies) Workshops **2010**, Muggendorf, Germany.
9. Attendance at the 10th Tetrahedron Symposium **2009**, Paris, France.